

Abstract

Title: Design and development of a new football shin pad

Author: Daniel William Davey

DESIGN AND DEVELOPMENT OF A NEW FOOTBALL SHIN PAD

Thesis submitted for the degree of

Doctor of Philosophy

at the University of Leicester

by

Daniel William Davey

Department of Engineering

University of Leicester

September 2001

UMI Number: U162768

All rights reserved

INFORMATION TO ALL USERS

The quality of this reproduction is dependent upon the quality of the copy submitted.

In the unlikely event that the author did not send a complete manuscript and there are missing pages, these will be noted. Also, if material had to be removed, a note will indicate the deletion.



UMI U162768

Published by ProQuest LLC 2014. Copyright in the Dissertation held by the Author.
Microform Edition © ProQuest LLC.

All rights reserved. This work is protected against
unauthorized copying under Title 17, United States Code.



ProQuest LLC
789 East Eisenhower Parkway
P.O. Box 1346
Ann Arbor, MI 48106-1346

Abstract

Title : Design and development of a new football shin pad.

Author : Daniel William Davey

This thesis describes an engineering methodology which has been applied to design a soccer shin pad to reduce the incidence of tibial fracture within the game of football.

By extrapolating statistics detailing the cause of tibial fracture within the County of Leicestershire it is estimated that approximately 3000 footballers sustain a broken leg each year in the UK. The vast majority of fractures are 'low energy' and result in the formation of a single crack in the tibia. This demonstrates that the re-design of shin pads has potential to reduce the number of fractures for even a relatively small decrease in loading during the impact event.

An experimental test rig has been developed with an impacting mass and geometry that simulates a football tackle. This test method significantly improves on previous investigations by including a pressure sensing array between the padding materials and synthetic leg. Preliminary experimentation demonstrated that for a two layer system, consisting of a stiff outer shell with a foam substrate, subjected to an impact of fixed mass and velocity, there must be an optimal material combination which provides the minimal peak load on the leg, and therefore reduces the probability of tibial fracture as a result of impact. These experiments provided useful data for a combination of prospective materials for impacts of low velocity. To achieve realistic impact velocities, computational Finite Element Analysis (FEA) has been used.

Analysis was carried out by applying non dimensional groupings, derived from text book theory to experimental and FEA results. This led to a definitive equation that allowed the characteristics of an impact, typical of a football tackle, to be predicted. Using this equation, materials were selected to manufacture a prototype, which was subsequently put through a rigorous test regime.

To gauge the effectiveness of the prototype performance, seven commercially available pads were also tested. In comparison with the branded shin pads the prototype reduced the peak load at the point of impact by between 13.5 and 36.7%, and the peak pressure experienced beneath the pad by between 21.5 and 51.3%. These results prove the performance of the prototype to be superior to that of the established commercially available pads, and the magnitude of these reductions suggest a significant proportion of tibial fractures could be avoided.

ACKNOWLEDGEMENTS

I would like to thank my supervisor Professor A. R. S. Ponter and also Mr C. Morrison for their advice and guidance for the duration of my research. I would also like to thank Mr G. O'Conner and all the technical staff for all their help. Finally I would like to thank Dr J. Hardy for his help with the medical aspects of the project.

Index

Development of experimental equipment with particular attention to the measurement of a dynamic shin area pressure sensing array. **pages**

Chapter 1 1 - 10

Introduction

1.0 Shin pads and impact protection in sport.	1
1.1 Current safety standards for shin pads in the UK.	3
1.2 Research methodology.	6
1.3 Contents of the thesis.	8
Chapter 1 References.	10

Chapter 2 11 - 59

Properties of the lower leg with particular reference to bone.

2.0 Introduction.	11
2.1 Soccer Injuries and Tibial Fracture.	13
2.2 Mechanical properties of long bones.	17
2.3 Viscoelasticity of Bone.	20
2.4 Mode of Fracture.	24
2.5 Tibial geometry.	27
2.6 Previous experimentation on bone.	28
2.7 Tibial Impact Dynamics.	36
2.7.1 Summary of investigation into wave phenomena, as a result of impact induced in the lower leg.	37
2.8 Further serious injuries that occur as a result of impact in the game of soccer.	39
2.9 Biomechanics of Kicking.	42
2.10 Summary of previous work on shin pads.	45
2.11 Comparison of influence for force attenuation, load spreading and energy absorption on shin pad effectiveness.	49
2.12 Conclusions.	52
Chapter 2 References.	55

Chapter 3 **60 - 104**

Development of experimental equipment with particular attention to the development of a dynamic thin film pressure sensing array.

3.1 Introduction.	60
3.2 Football impact measurement requirements.	62
3.3 Instrumentation to measure the pressure between contact surfaces.	65
3.3.1 Force Sensing Resistors (FSR's).	68
3.4 Basic Evaluation of sensor behaviour.	70
3.4.1 Sensor response to static loading.	70
3.4.2 Sensor response to dynamic loading.	73
3.5 Software and hardware used in conjunction with sensors.	79
3.6 Development of visualisation software used in conjunction with FSR's.	81
3.7 Accuracy validation tests for sensors under dynamic loading.	85
3.8 Basic Test Method.	86
3.9 Conclusions.	103

Chapter 4 **105 - 130**

Materials testing results.

4.0 Introduction.	105
4.1 Range of materials tested.	106
4.2 Test Method for flat plate testing.	109
4.3 Typical results obtained.	112
4.4 Summary of initial testing results and explanation of material behaviour.	115
4.5 Conclusions.	129

Chapter 5	131 - 159
Finite Element Analysis.	
5.1 Introduction.	131
5.2 Finite Element Analysis (FEA).	133
5.2.1 Pre-processing.	134
5.2.2 Running the Simulation.	135
5.2.3 Post Processing.	136
5.3 The model.	137
5.3.1 Model geometry.	137
5.3.2 Impact Simulation.	140
5.3.3 Simulation of material behaviour	142
5.4 Detailed comparison of results obtained through FEA, and testing carried out in Chapter 4.	147
5.5 Conclusions.	158
Chapter 5 References.	159

Chapter 6 **160 - 202**

Theoretical work.

6.1 Introduction to theoretical model.	160
6.2 Timoshenko's solution.	162
6.3 Experimental Method.	165
6.4 Creation of theoretical model.	168
6.4.1 Dealing with the non-linear behaviour of foams.	171
6.5 Comparison of experimental results to basic Timoshenko result.	175
6.6 Applying a Dynamic Solution to the data.	180
6.6.1 Significance of derived formulae.	183
6.7 Adding criteria to the solution to obtain optimum material properties.	189
6.7.1 The first criterion.	189
6.7.2 Proof by application of equation derived using the first criterion.	192
6.7.3 The second criterion.	196
6.8 Adjustments required to make equation 6.18 applicable to human tibia.	198
6.9 Conclusions.	201
Chapter 6 References.	202

Chapter 7

201 - 204

Concluding remarks and suggestions for further work.

7.1 Conclusions.

201

7.2 Suggestions for further work.

202

7.2.1 Suggestions for further work on shoe pad design.

202

7.2.2 Suggestions for other work.

203

Summary of abbreviations

201 - 204

Chapter 7 203 - 231

Development and Manufacture of Prototype.

7.0 Introduction. 203

7.1 Design Considerations. 204

7.2 Material selection. 210

7.2.1 Cellular material selection. 210

7.2.2 Outer Shell material selection. 214

7.3 Manufacture of prototype. 226

7.4 Conclusions. 230

Chapter 7 References. 231

Chapter 8 232 - 250

Testing of prototype and comparison with commercially available shin pad performance.

8.1 Introduction. 232

8.2 Revised test method. 233

8.3 Analysis of performance of prototype by comparison of experimental results to behaviour predicted using theoretical solution. 239

8.4 Summary of key results obtained from pad tests. 242

8.5 Analysis and comparison of shin pad performance. 245

8.6 Conclusions. 250

Chapter 9 251 - 260

Concluding remarks and suggestions for further work.

9.1 Conclusions. 251

9.2 Suggestions for further work. 257

9.2.1 Suggestions for further work on shin pad design. 257

9.2.2 Suggestions for other work. 260

Summary of abbreviations 261 - 264

Index of Appendices

Due to the size and graphical nature of the appendices they are contained on the accompanying CD.

Appendix A 265 - 272

A1 MRI scans of human lower leg

Appendix B 273 - 300

B1 Piezoresistance 273 - 276

B2 C++ Array visualising program 277 - 284

B3 Dynamic analysis of a shin pad supported by a beam 285 - 294

B4 Analysis with a deformable impactor 295 - 300

Appendix C 301 - 312

C1 Materials Testing Results

Appendix D 313 - 331

D1 Abaqus Input File 313 - 322

D2 Comparison of experimental and simulation results 323 - 331

Appendix E 332 - 347

E1 FEA Results 332 - 334

E2 detailed manipulation of Timoschenko solution 334 - 340

E3 application of dynamic solution to theoretical results 341 - 343

E4 examples testing validity of derived equations 344 - 347

Appendix F 348 - 349

F1 Diagrams of tools

Appendix G 350 - 365

G1 Shin pads tested and key results

Chapter 1

Introduction

1.0 Shin pads and impact protection in sport.

Shin pads are used to protect the wearer against injury in the game of soccer and generally consist of a stiff shell material, either made from one continuous plate or a number of splints covering a layer of soft foam material. It is a breach of Football Association law to play in a competitive soccer game without them, irrespective of the age of participant or standard of competition. It is shown in section 1.1 that although it is compulsory to wear pads of some sort there are no guidelines to what level of protection the pads should offer.

From a manufacturers' perspective, shin pads are clearly seen as a low technology item within the market place and have a price structure in the range 5 to 20 pounds sterling. In comparison, football boots retail at a much higher price and are seen as a high cost potentially performance enhancing piece of equipment. As such, it is fair to assume a much larger sum of any sport manufacturers research and marketing budget is apportioned in directions other than the shin guard. The lack of a recognised testing procedure or liability of manufacturer for injury as a result of sub standard pads mean it is unlikely that the low technology, low cost design procedure for soccer shin pads will change without a shift in the legal framework.

Football shin pads are relatively unique in the field of sport protection in general. Consider the impact protection devices in other sports such as cricket or American football. These have the advantage that they can be fairly large, as mobility in these particular sports is not as important as in the game of soccer and therefore

large amounts of padding may be inserted into the pads. Intuitively the properties of these materials must have a much larger range over which they are effective at preventing injury in comparison to a guard that, for the purpose of practicality, has an upper limit of approximately one centimetre thickness. Football is a contact sport which regularly involves impact comprising of large mass and velocity, particularly in the event of a sliding tackle and it is therefore of significant concern that the shin pad performs to the optimum of its ability offered by its limited thickness. This highlights the potential importance of engineering a pad to maximise the level of protection against injury to loads that typically occur within the game of soccer.

• PFD which is neither simple or complex in design - Where injury could be severe.

• PFD of 'complex design' - Where injury could result in death or irreversible damage.

Football shin pads are currently included in the PFD of simple design.

grouping. The illustration (provided to assist the CE marking) is shown in Figure 1.4.

All information from the Shin and Ankle Trade Association (SATA) on marking

procedures and guidelines is valid as of 15 June 2016.

As can be seen for PFD of 'simple design' all aspects are the responsibility of the manufacturer. This clearly states the responsibility that perhaps the product may define their own testing procedures and standards to which they test their product.

The Department of Health and Safety (HSE) are aware that there is an error in the categorisation of shin pads and have moved to amend the classification (as of 21

1.1 Current safety standards for shin pads in the UK.

Despite the legal requirements to wear football shin pads, the standard of protection which a pad is required to provide to the wearer is not clearly stipulated; a problem highlighted in section 1.0.

Since July 1995, it has been illegal to place on the market in the European Union, personal protective equipment (PPE) that is not CE marked. However, this standard may be considered deceptive for certain items. PPE is grouped into three sub-sections that are defined as follows.

- PPE of 'simple design'. - Resultant injury minor.
- PPE which is neither 'simple or complex in design'. - Where injury could be severe.
- PPE of 'complex design'. - Where injury could result in death or irreversible damage.

Football shin pads are currently included in the PPE of simple design grouping. The attestation procedure to obtain the CE marking is shown in figure 1.1. All information from the Shoe and Allied Trade Association (SATRA) on testing procedure and guidelines is valid as of 15 June 1998^[1.1].

As can be seen for PPE of 'simple design' all sections are the responsibility of the manufacturer. This effectively means the company that produces the product may define their own testing procedure and standard to which they test their product.

The Department of Trade and Industry (DTI) are aware that there is an error in the categorisation of shin pads and have moved to amend the classification (as of 20

April 1998^[1,2]) to the second group, PPE which is neither 'simple or complex in design'. This requires that to obtain the safety certificate, an independent approved body must test the product using an EC specified testing method. However, the reclassification of products normally takes upwards of five years and until this takes place there is no minimum standard to which a commercially available pad must legally conform.

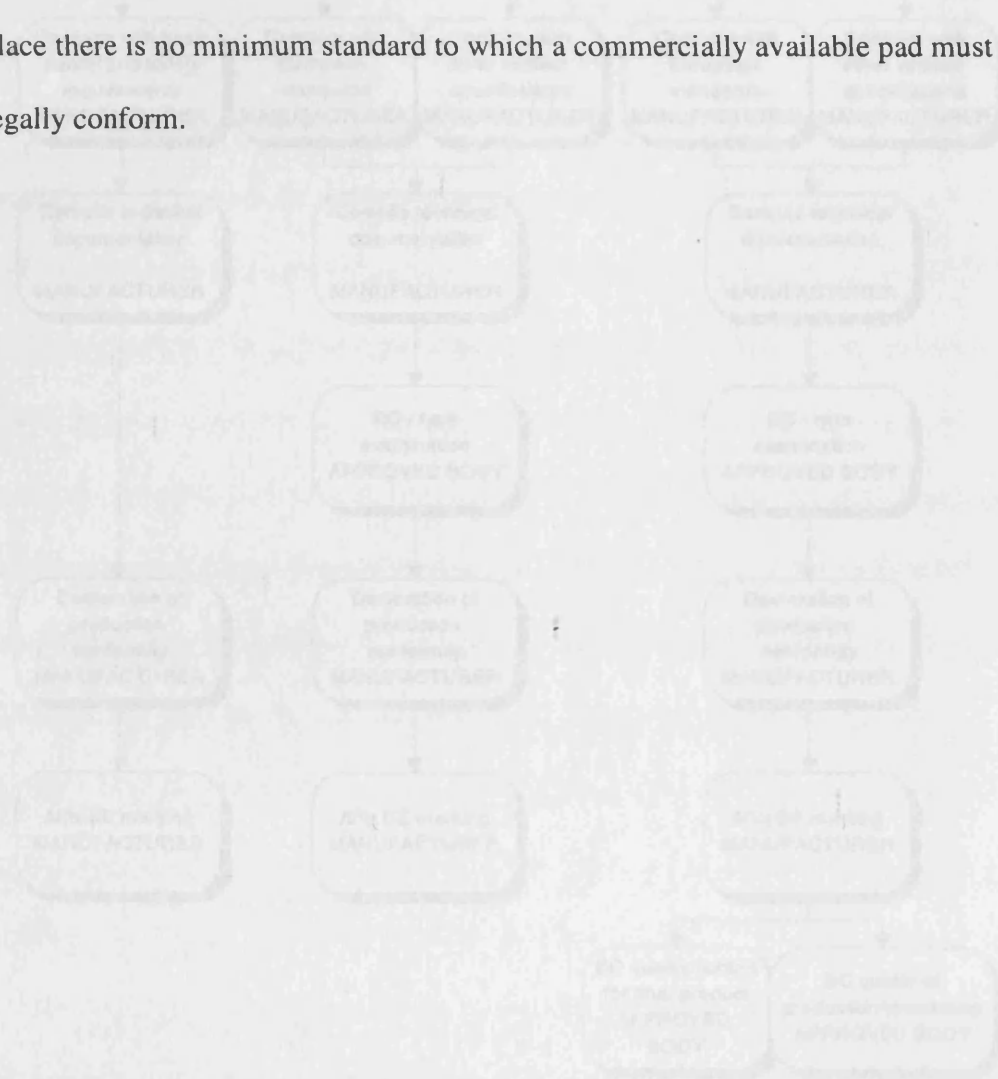
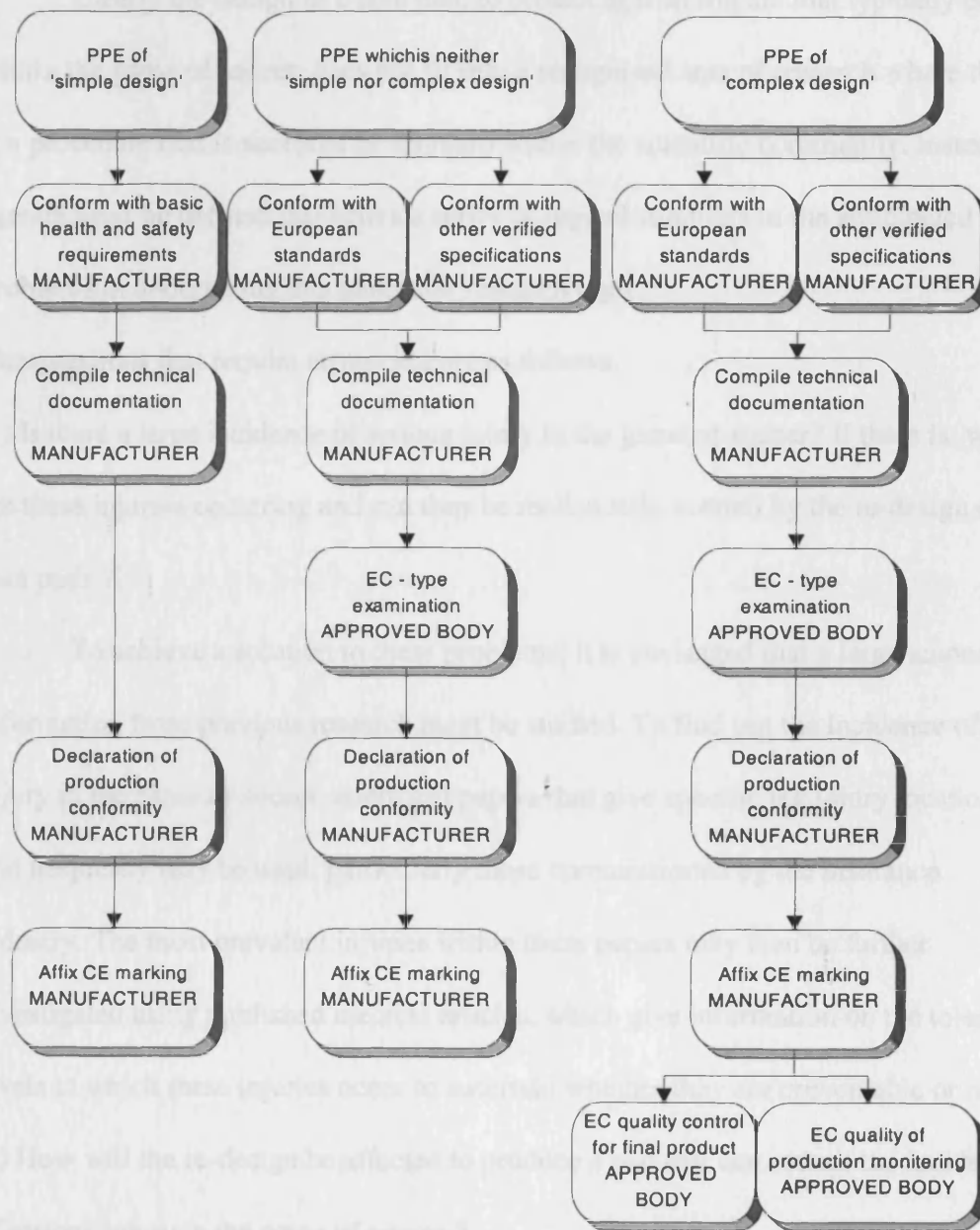


Figure 1.1 Showing the attestation procedures to obtain the CE mark for the three categories of PPE. The responsibility for each sub-section is shown in capitals.



1.2 Research methodology.

Clearly the design of a shin pad, to protect against impact that typically occurs within the game of soccer, does not fit into a recognised area of research where there is a procedure that is accepted as standard within the scientific community. Instead an agenda must be defined that offers a series of logical solutions to the anticipated problems in undertaking this particular research topic.

The questions that require answering are as follows.

1) Is there a large incidence of serious injury in the game of soccer? If there is, why are these injuries occurring and can they be realistically averted by the re-design of shin pads ?

To achieve a solution to these problems, it is envisaged that a large amount of information from previous research must be studied. To find out the incidence of injury in the game of soccer, statistical papers that give specific leg injury locations and frequency may be used, particularly those commissioned by the insurance industry. The most prevalent injuries within these papers may then be further investigated using published medical articles, which give information on the tolerance levels at which these injuries occur to ascertain whether they are preventable or not.

2) How will the re-design be affected to produce a pad that can reduce the incidence of serious injury in the game of soccer ?

This will be achieved through a combination of experimental and theoretical programmes. The experimental procedure will be based on the types of injury that are most frequently observed within available literature and previous research into the subject of football shin pads and impact in general. A test rig may be set up that

provides an impact that is comparable to that which occurs in a game of football. This equipment will be instrumentalised using either standard or customised devices at locations where the most relevant information may be accumulated.

Further work will be based on the most applicable text book theory which will allow impact and material characteristics to be expressed in significant non-dimensional groupings. Using the experimentally obtained data in conjunction with these groups the behaviour of an idealised shin pad, in terms of material characteristics and geometry may be defined. A prototype pad will be constructed based on these findings and tested in direct comparison with a range of commercially available pads from the leading manufacturers, to quantify the level of improvement achieved.

1.3 Contents of the thesis.

A scientific approach is required to follow the methodology presented in section 1.2. This may be summarised as reference to previous research, the development of an experimental method to quantify the performance of shin pads, as well as any potential pad materials and the detailed analysis of the results generated using this technique. The successful completion of this agenda may be used to create an engineered pad which will reduce the incidence of serious injury within Association football. The work is presented within the thesis as follows:

Chapter 2 An assessment of the capacity of the tibia to withstand forces induced by impact while carrying functional loading. This section is approached using available literature on the strength of bone and the biomechanics of kicking. Reference is also made to the previous research into the performance of shin pads. This combination of information is used to gain an understanding of the characteristics that cause serious injury with particular reference to tibial fracture.

Chapter 3 Design and construction of a test rig which allows accurate experimental measurements of those characteristics which are discovered to be of importance in the causation of injury .

Chapter 4 A study of the relative performance of lightweight materials when subjected to impact loading through the evaluation of materials and design of typical commercially available shin pads. These tests are carried out using equipment developed in chapter 3.

Chapter 5 The development of an accurate Finite Element Analysis (FEA) model to allow accelerated testing of prospective materials at velocities which are beyond the experimental set up.

Chapter 6 The creation of a theoretical model which suggests idealised material properties for the guard. This section expands on the standard theoretical behaviour of plates on elastic foundations using the experimental results achieved in chapters 4 and 5.

Chapter 7 The definition of an improved shin pad design using inexpensive materials obtained by applying the method derived in chapter 6.

Chapter 8 An experimental comparison of the performance of available shin pads and the prototype guard developed in chapter 7.

Chapter 9 Conclusions and suggestions for further work.

References

[1.1] Minutes of CE marking of personal protective equipment workshop. 15 June 1998.

SATRA safety product centre, Wyndham Way, Northampton.

Telephone: 01536 410 000

Website: www.satra.co.uk

[1.2] Minutes of DTI PPE working group meeting of 20 April 1998.

DTI, 1 Victoria Street, London SW1H 0ET

Telephone: 020-7215-5000

Chapter 2

Properties of the lower leg with particular reference to bone

2.0 Introduction

This chapter incorporates information taken from previous research in three key areas: the incidence of tibial fracture in the game of soccer, the mechanical properties of the tibia and previous research into shin pad design. The research is concerned only with the tibia as the load bearing capacity of the fibula is small in comparison with the larger bone and the location of the fibula deep within the leg surrounded by soft tissue makes it less vulnerable to impact.

To validate the necessity of this research it must be shown there is sufficient evidence that the frequency of tibial fractures in the modern game of football to justify the re-design of soccer shin guards. To gauge the prevalence of such injury, a study of available literature on soccer injuries has been carried out. Further to the analysis of published statistical occurrence of tibial fracture, investigation of medical documents is required to associate the type of fracture with the loading history to gain an understanding of what loading the tibia experiences during a football tackle and whether this type of loading can be better controlled by an improved shin pad. The mechanical properties of bone, specifically the tibia must be researched to gain an understanding of the limits to which it may be loaded. This will provide important information to aid the design process.

A full summary of relevant previous experimentation on the tibia is also included in this chapter along with a geometrical analysis of my own tibia bone measured and photographed using an MRI scan. This allows the moment of area of

the tibia to be calculated, identifying sections of the bone structure particularly susceptible to certain types of loading. Within this chapter, literature concerning the biomechanics of kicking has been studied to gauge the velocity and mass of a typical impact that occurs during a football game to provide values to aid in the design of an experimental test rig. Finally, previous research into shin pad design and performance is assessed to aid in the design of an experimental test rig, and gain insight into how modern shin pads behave under impact.

Effectively this section of the work first sets out to prove that a tibial fracture problem exists in the game of soccer. It then moves on to try to understand why this problem exists by studying both the geometrical and mechanical properties of the bone. Crucially, this chapter attempts to draw specific ultimate values of load to fracture for the tibia bone that are essential in the design methodology undertaken in later chapters. It also investigates typical impact loads in the game of soccer and previously used shin pad test methods to aid in the future design of a realistic test rig.

2.1 Soccer Injuries and Tibial Fracture.

Research into the frequency and severity of injury in soccer is common. All literature available agrees that the majority of soccer injuries are to the lower extremities, with published studies giving leg injury rates of between 70-88% of all soccer injuries.^{[2.1] [2.2] [2.3] [2.4]} Of these leg injuries there is again agreement as to the most frequent types of injury; ankle ligament damage closely followed by knee ligament damage, the majority of which are minor sprains and strains.

There is however a differing opinion as to the frequency of tibial fracture. For example Pardon^[2.5] reports the most typical and frequent injury is fracture of the shaft of the tibia. In a paper concerning accidents in the French Rhone Alps area^[2.6] reported to the insurance company 6.2% of all injuries were leg fractures. In another report concerning major injuries in Norwegian football,^[2.7] 13% of serious injuries were leg fractures. Another study concerning a male soccer league containing 12 teams over a period of one season^[2.3] produced a figure of 4% of injuries being leg fractures.

In contrast, other studies^{[2.8] [2.9]} dispel leg fractures as rare and insignificant. If all injuries, including minor strains, cuts and bruises are recorded, the number of serious injuries such as fracture are small in comparison, which tends to lead to a trivialisation of the more serious injuries. Football is a contact sport and minor injuries are commonplace, however studies that concern themselves solely with more serious injury for the insurance industry (Roaas)^[2.7], (Berger-Vachon)^[2.8] do indicate there is a significant incidence of tibial fracture.

As evidence concerning the importance of tibial fracture in the game of soccer is contradictory dependant on the source, the subject has been approached from an alternative perspective. Sport is by far the commonest cause of tibial fracture in Leicester,^[2.10] and soccer causes over 85% of such injuries.

The study into the epidemiology of all tibial fractures sustained in the city of Leicester using a recognised statistical approach as recommended by Van Mechelen^[2.11] showed a surprisingly large amount of the injuries were sustained by amateur footballers. In the first year of the study, 140 patients with a fractured tibia were admitted to the three hospitals serving the city (dealing with a population of 918,000). A breakdown of the cause of injury in 1992 is shown in table 2.1.

Table 2.1. Breakdown of cause of tibial fracture in Leicestershire in 1992.

Cause of tibial fracture	Number of injuries	Percentage of total
Fall	38	27.14%
Sport in General	54	38.57%
(Due to Football)	(47)	(33.57%)
Crush	5	3.57%
Pedestrian	19	13.57%
Road Traffic Accident	6	4.28%
Cycling Accident	1	0.71%
Motorcycle Traffic Accident	17	12.14%
Total	140	100%

In 1993, a further 53 (39%) fractures occurred during a football match. This indicates that the incidence of fracture due to football was not unusually high in 1992.

The cost to society of this injury is high, not only for medical treatment and statutory sick pay, but also from a loss of productivity and taxes. In Leicester, the calculated cost for the 47 fractures in 1992, arising from hospital stay, initial treatment, outpatient visits and statutory sick pay was £126,000. Extrapolating this

data, and assuming the same incidence of this injury nationally, this represents a minimum estimated annual cost of £7,700,000 ^[2.12].

Upon this evidence, the large proportion of injuries to footballers demands attention. The wearing of shin pads is legally mandatory in a soccer match ^[2.13] yet football is the commonest cause of the injury. This suggests current commercially available shin pads do not provide the required standard of protection to safeguard against tibial fracture.

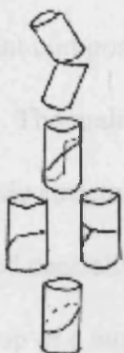
The specific type of fracture obtained as a result of soccer injury was further investigated by Cattermole *et al* ^[2.10]. In the study, she investigated the circumstances in which tibial fracture occurred for the 100 footballers who received such an injury during the period of the study. By observing the different types of fracture, the mechanism of injury may be defined.

Cattermole *et al*'s research shows the commonest cause of fracture is three point bending. The results of the study show 57% of fractures were transverse and as a result of pure bending, 24% of injuries were butterfly and arose as a result of bending and compression, 11% were oblique and resulted as a combination of compression, bending and torque, 5% were spiral and as a direct result of torque and 3% were comminuted (shattering of tibial shaft) and cannot be classified. In all cases, fracture initiated at the point of contact. A diagram showing how the fractures may be classified is shown in figure 2.1 below.

From these results Cattermole *et al* concludes the typical footballers fracture is caused by three point bending. The assumption Cattermole *et al* makes, that there is only one injury mechanism, possibly over simplifies the situation. These results

suggest there are two clear mechanisms of injury. The first results in the transverse fractures, and occurs almost purely as a result of bending loading. This implies the impact to the tibia occurs when the leg is raised from the ground and occupied in a kicking or running motion. The second results in oblique, butterfly and spiral fractures and occurs when the weight bearing leg is impacted. The specific type of fracture is dependant on the amount of torque present.

Figure 2.1 Fracture patterns and associated loading conditions.

	Fracture Pattern	Load	% of injury
	Transverse	Bending	57
	Spiral	Torsion	5
	Oblique transverse (butterfly)	Axial compression and bending	24
	Oblique	Axial compression, bending and torsion	11

2.2 Mechanical properties of long bones.

Bone is made up of organic cells, fibres and inorganic minerals. It differs from any other part of the body by having a high proportion of inorganic minerals. The bone mineral crystals, largely consisting of calcium and phosphate, are embedded in collagen fibres. The crystals are extremely small (in the region of 50 Ångstroms) and may be considered as short fibres embedded in a collagen matrix. The crystals are so small that there is little chance of a Griffith crack initiating. Any cracks that form do so only under very high stresses and are arrested when they reach the collagen which deforms, but does not rupture. Bone is essentially a good example of a fracture resistant composite medium.

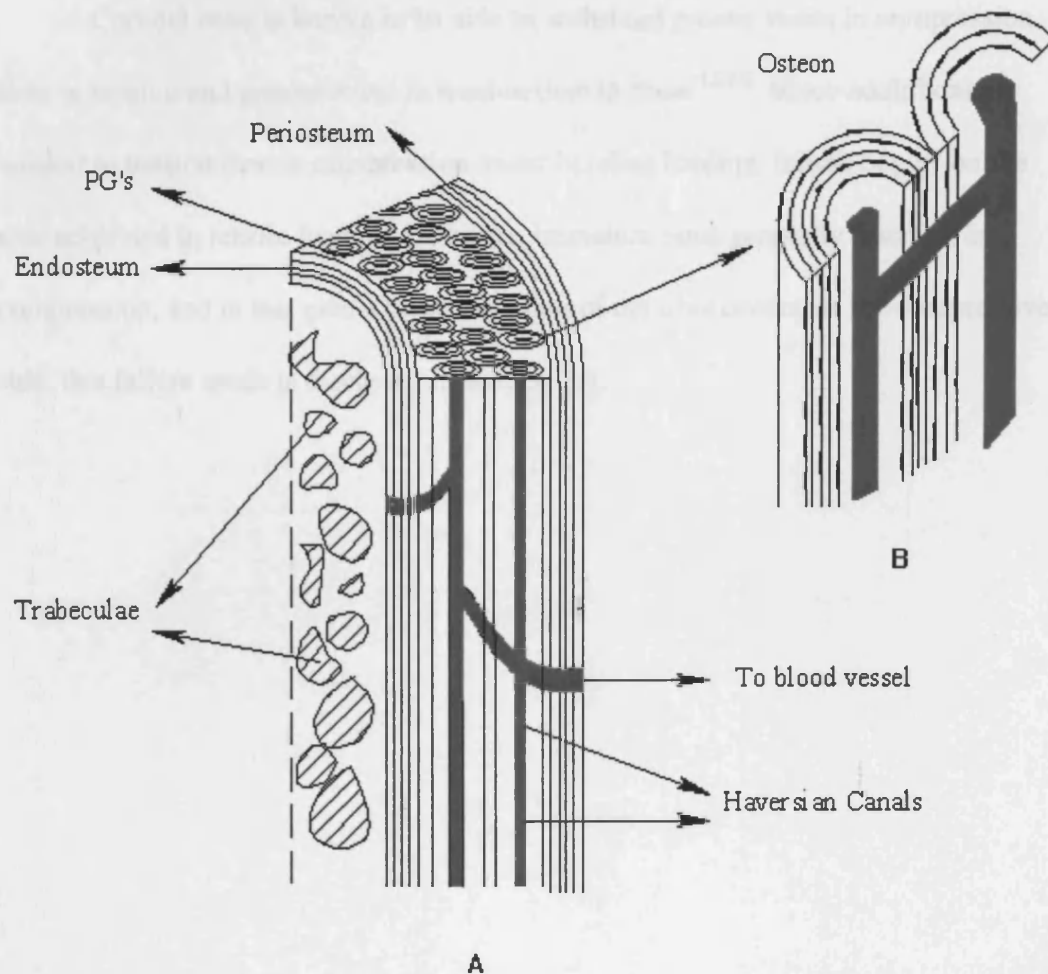
The main components of bone are shown in figure 2.2. At a microscopic level the basic structural component of bone is the osteon which is shown in figure 2.2B. Located centrally in each osteon is a canal that contains blood vessels and nerves. It is made up of a number of lamellae consisting of the mineralised collagen. Along the boundaries of the lamellae are small gaps which allow nutrients from the central blood vessel to circulate.

Surrounding each osteon is a narrow region of a gelatine like substance called proteoglycans (PGs). The collagen fibres are able to interconnect from one lamella to another but do not cross the boundary provided by the PGs.

At the macroscopic level there are two types of bone. The outer shell of cortical bone surrounds cancellous bone. The two types of bone are biomechanically equivalent except for their density and porosity. Cortical bone has a porosity of between 5 and 30% and cancellous bone has a porosity of 30 to 90%. Cortical bone

also has a higher density of approximately 2.0 kgm^{-3} whereas cancellous bone density ranges from $0.25\text{-}0.8 \text{ kgm}^{-3}$.^[2,14]

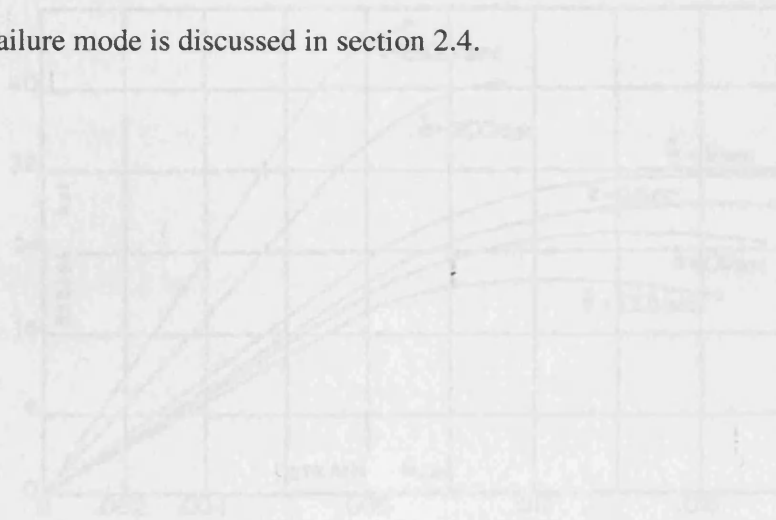
Figure 2.2 The main components of bone.



The bones are surrounded by an outer fibrous membrane called the periosteum and a thinner inner membrane called the endosteum which separates the bone from the central cavity, which contains the marrow.

Due to the porosity of cancellous bone, it has a large capacity for energy storage. Cancellous bone does not fracture until a strain of approximately 75% whereas cortical bone is much more brittle and will fracture as the strain exceeds 2% [2.14].

Cortical bone is known to be able to withstand greater stress in compression than in tension and greater stress in tension than in shear [2.14]. Since adult bone is weaker in tension than in compression under bending loading, failure begins on the side subjected to tensile loading. However, immature bone generally fractures in compression, and in this case a buckle fracture of the tibia occurs on the compressive side, this failure mode is discussed in section 2.4.

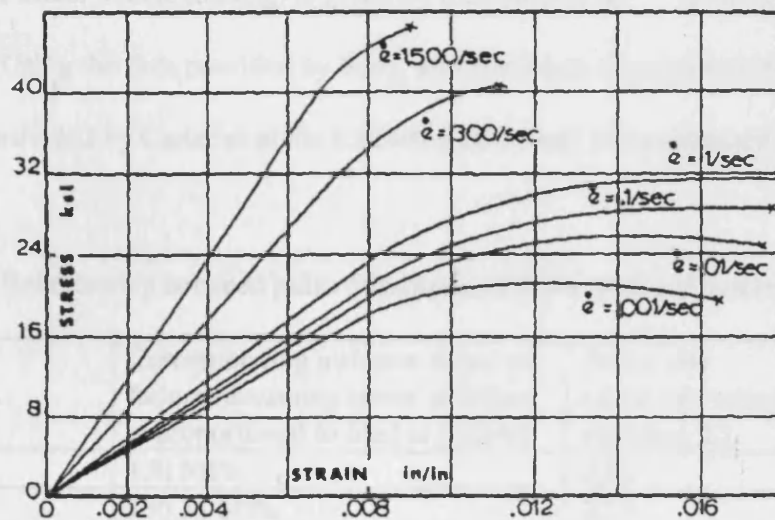


King *et al.* [2.14] showed the human tibial load-to-fracture tolerance level increases from 7340 N to 8430 N to 8900 N for increasing pulse durations of 30, 2, and 1 ms respectively, in comparison to a static tolerance level of approximately 7000 N (Patrick *et al.* [2.15]) under impact testing.

2.3 Viscoelasticity of Bone.

Bone is a viscoelastic material (see Figure 2.3 below), that is stiffer and sustains a higher load without fracture when loads are applied at a higher rate. (McElhaney)^[2.15].

Figure 2.3 Stress Strain curve for the human tibia for increasing strain rates (strain rates given in reciprocal seconds). Bone samples taken from the shaft of a 24 year old male specimen. Reproduced from 'Dynamic response of bone and muscle tissue.' (McElhaney)^[2.15]



King *et al*^[2.16] showed the human cadaver femur bone fracture tolerance level increases from 7340 N to 8450 N to 8900 N for decreasing pulse durations of 50, 3, and 1 ms respectively, in comparison to a static tolerance level of approximately 7000N (Patrick *et al*^[2.17]) under impact testing.

The relationship between the stress to failure (in MPa) and strain rate for human bone is given by Carter^[2,18] by:

$$\sigma_{ult} = 147 \dot{\epsilon}^{0.055} \quad \text{equation 2.1}$$

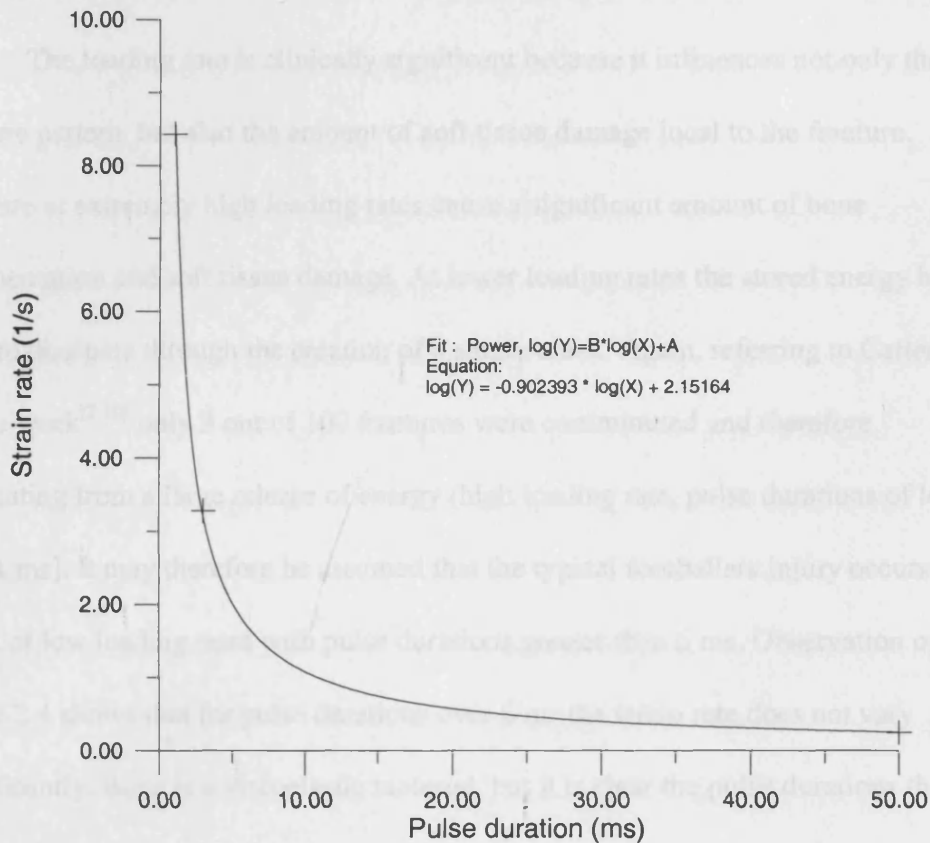
Where $\dot{\epsilon}$ is the strain rate is given in reciprocal seconds and σ_{ult} is the stress at failure (MPa). Assuming the ultimate stress to failure is directly proportional to the maximum axial load at failure, an attempt may be made to express the pulse durations in terms of strain rates using equation 2.1. The ultimate stress at failure for the femur (adult bone under tensile loading) is given by Burnstein *et al*^[2,19] to be approximately 130 MPa. Using the data provided by King, and Burnstein in conjunction with the equation provided by Carter *et al* the following table may be constructed.

Table 2.2 Relationship between pulse duration and strain rates for human bone.

load	Corresponding ultimate stress to failure (assuming stress at failure is proportional to load at failure)	Strain rate calculated using equation 2.1	Pulse duration
7000 N	130 MPa	0.01	static load
7340 N	136.31 MPa	0.25	50 ms
8450 N	156.93 MPa	3.28	3 ms
8900 N	165.29 MPa	8.43	1 ms

We may now plot the relationship between pulse times and strain rate as shown in figure 2.4 below.

Figure 2.4 Graphical representation of relationship between strain rate and impact pulse duration for the human femur bone.



The fact there are only three available data points makes the fitting of the curve difficult, but the data does indicate that there are three basic thresholds. Pulses of 1ms or less appear to drastically affect the strain rate and ultimately the load required to fracture the tibia. Pulses in the intermediate range of 1ms to 5 ms have an appreciable effect on the strain rate and the ultimate strength of the bone, but this effect results in relatively small increases in ultimate strength (observe curves for strain rates of 0.1/sec and 1/sec in figure 2.3). Pulses of 6 ms or greater behave increasingly as a static loadcase. This analysis has been carried out on the femur rather than the tibia as information was available only for the larger bone. It is

assumed that the tibia exhibits a similar relationship between strain rate and pulse duration.

The loading rate is clinically significant because it influences not only the fracture pattern, but also the amount of soft tissue damage local to the fracture.

Fracture at extremely high loading rates cause a significant amount of bone fragmentation and soft tissue damage. At lower loading rates the stored energy has time to dissipate through the creation of a single crack. Again, referring to Cattermole *et al's* work^[2.10] only 3 out of 100 fractures were comminuted and therefore originating from a large release of energy (high loading rate, pulse durations of less than 1 ms). It may therefore be assumed that the typical footballers injury occurs as a result of low loading rates with pulse durations greater than 6 ms. Observation of figure 2.4 shows that for pulse durations over 6 ms the strain rate does not vary significantly. Bone is a viscoelastic material, but it is clear the pulse durations that occur as a result of impact in soccer do not relate to strain rates high enough to significantly affect the fundamental material characteristics derived under static loadcases. This is particularly important as the value for the elastic modulus used in chapter 7 to calculate the stiffness of the tibia and therefore the required stiffness of the pad is based on data obtained using a static loadcase.

2.4 Mode of Fracture.

In 1985, Carter and Caler ^[2.20] produced a model that suggested bone failed in tension after a certain amount of damage has occurred in the region of fracture. They loaded bone to a tensile stress that did not fracture the bone and held it at this stress. The bone subsequently fractured, suggesting bone accumulates damage while it is stressed and will fracture when a critical amount of damage has occurred. This model was corroborated by subsequent work by Currey ^[2.21] ^[2.22]. At high loading rates the stress in the bone stays constant for only a short time and thus little damage accumulates before a higher stress level is attained. This possibly explains the viscoelastic behaviour of bone.

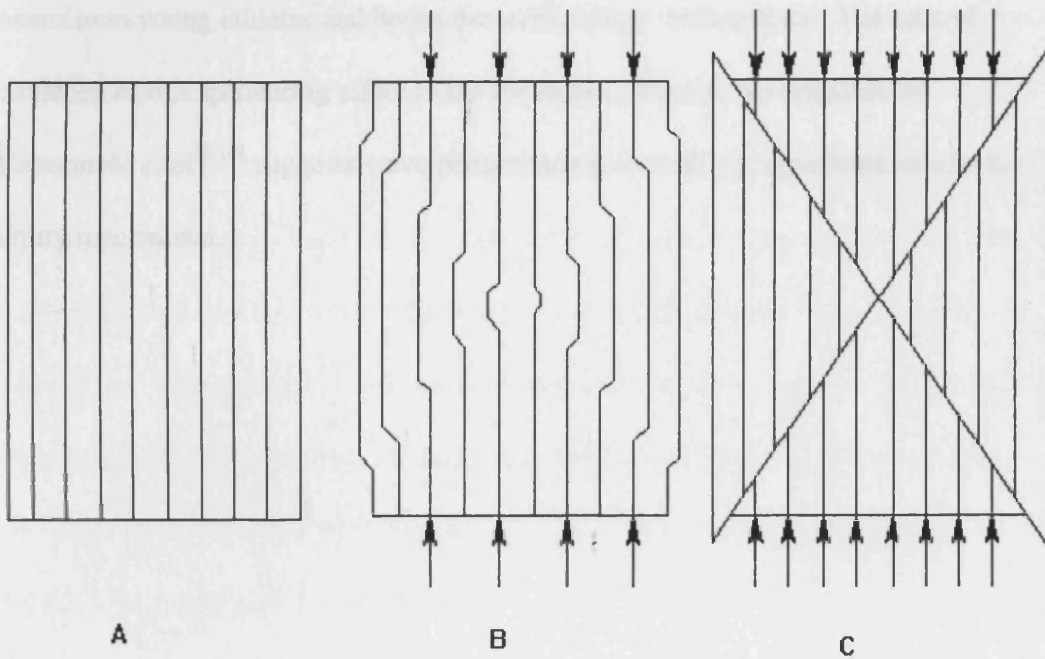
Work on fracture in compression indicates failure occurs by a different means. Frost *et al* ^[2.23] and Chumney ^[2.24] showed that when bone is strongly compressed, lines of shear are produced at angles of approximately 30° to the direction of application. This mode is thought to be as a result of the buckling of lamella in the bone. Again, similar modes of failure occur in composite materials such as carbon fibre reinforced plates, where buckling of the fibre is accompanied by shear deformation of the matrix. As the compressive forces are increased, the bone cracks along these lines of shear. These lines also have a tendency to initiate at stress concentrators such as blood vessels. Their formation is shown in Figures 2.5 A, B and C.

Figure 2.5 Shear strains caused by buckling of the lamellae in the bone.

A) Block of bone with central stress concentrator.

B) The bone is subjected to a compressive load, the lamellae buckle starting at the stress concentrator spreading out at 30° to the line of application of the force.

C) The shear lines turn into cracks as the force becomes greater.



Research into failure by fatigue has been carried out by McElhaney^[2,15] who placed a section of human tibia under cyclic loading with frequencies approaching 1500 cycles per second. He concluded bone failure under these loading conditions was typified by the formation of multiple vertical splinters. This is also characteristic of tibial fatigue fractures caused by cyclic loading which occurs due to excessive exercise in young athletes and hence the terminology 'shin splints'. The lack of evidence of this splintering effect in the footballers fracture investigated by Cattermole *et al*^[2,10] suggests wave phenomena do not play a significant role in the injury mechanism.

2.5 Tibial geometry.

The geometry of the tibia bone provides a problem in relation to loading when an impact occurs in a football game. The resistance to bending loading of any material is described by the area moment of inertia. The resistance to torsional loading is described by the polar moment of inertia. The moment of area of my own tibia has been measured at 6 intervals using the output from an MRI scan that was undertaken. The results are presented in detail in Appendix A1. Work by Minns^[2.25] showed that the minimum moment of area occurred between 70 and 80% of the distance along the tibia. This is supported by the findings observed in Appendix A1 where the minimum moment of area is observed between 75 and 90% of the distance along the tibia. Frankel and Burnstein^[2.26] showed the polar moment of area was at a minimum 70% of the distance along the tibia. Unfortunately this part of the tibia, just above the ankle, is where the centre of the football lies, and is where a tackle would logically be aimed. This explains why there is such a high incidence of tibial fracture in football. The characteristics of the game ensure that impact is likely to occur at the most vulnerable point on the tibia. This is compounded by the likelihood that the player is also sprinting at the time and the tibia may be experiencing high loading as a result of body weight, increasing the possibility of fracture. In short, the tibia is not designed for football.

2.6 Previous experimentation on bone.

The mechanical properties of bone, specifically the tibia must be researched to gain an understanding of the limits to which it may be loaded. This will provide important information to aid the design process detailed in chapter 6.

There has been a large amount of research into the mechanical properties of bone. Unfortunately there has been no uniformity of method which has led to a wide range of recorded material properties. For example, some tests use embalmed human cadavers, others use fresh. In the first case, the embalming process has been shown to drastically affect the mechanical behaviour of bone. Furthermore, most human cadavers are in the 60-80 year old range and the mineralogy of their bones is very different to those of an age who play football regularly. Another method is to machine a slice of tibia bone from the surface of a cadaver which results in the makeup of the bone being predominantly cortical. Other studies use animal bone, but do not relate these results to human bone.

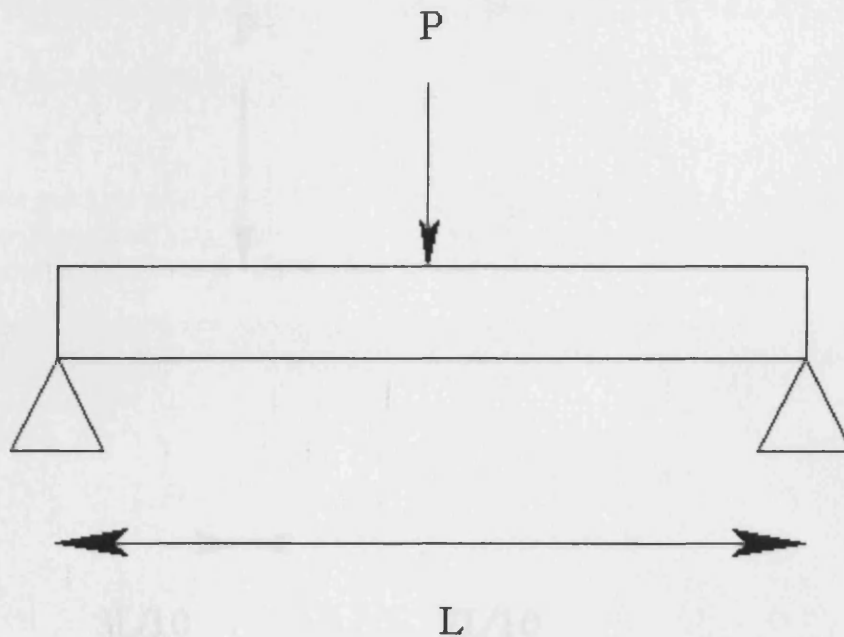
As previously discussed, bone may be classified as a composite material. Composites are notoriously difficult to quantify in terms of material constants, due to the variability from one specimen to another. All the work tends to consider loading in only one mode i.e. pure tension, compression or bending, and fracture is unlikely to occur naturally under those circumstances. All of these factors combine to produce a range of values dependant on the source, experimental technique, cadaver age and storage conditions. A summary of properties extracted from various papers was presented in a paper by Currey^[2.15]. The approximate properties of the tibia using data from this paper is shown in Table 2.3 below.

Table 2.3 Mechanical properties of the tibia.

	Direction of Loading	Stress (MPa)
Compressive strength	Parallel to long axis	167-205
	Perpendicular to long axis	117-156
Tensile strength	Parallel to long axis	98-127
	Perpendicular to long axis	10
Shear strength		78
Modulus of Elasticity		15000

Cattermole *et al*^[2.10] has shown 95% of fractures occurred either completely or at least partially as a result of bending. As this is clearly the predominant factor causing tibial fracture within the game of soccer, particular attention must be made to literature considering this particular fracture mode. Nyquist^[2.27] conducted dynamic impact tests on unembalmed human tibias to investigate tibial fracture as a result of three point bending. The conclusion of this research is that a bending moment of approximately 320 Nm for male tibia and 280 Nm for females results in fracture for tests conducted mid-span on the tibia with the tibial shaft mounted on supports 250 mm apart. We can manipulate these results to obtain the peak load for failure, a value that is much easier to experimentally monitor within a test situation. The impact situation considered by Nyquist is shown in figure 2.6 below.

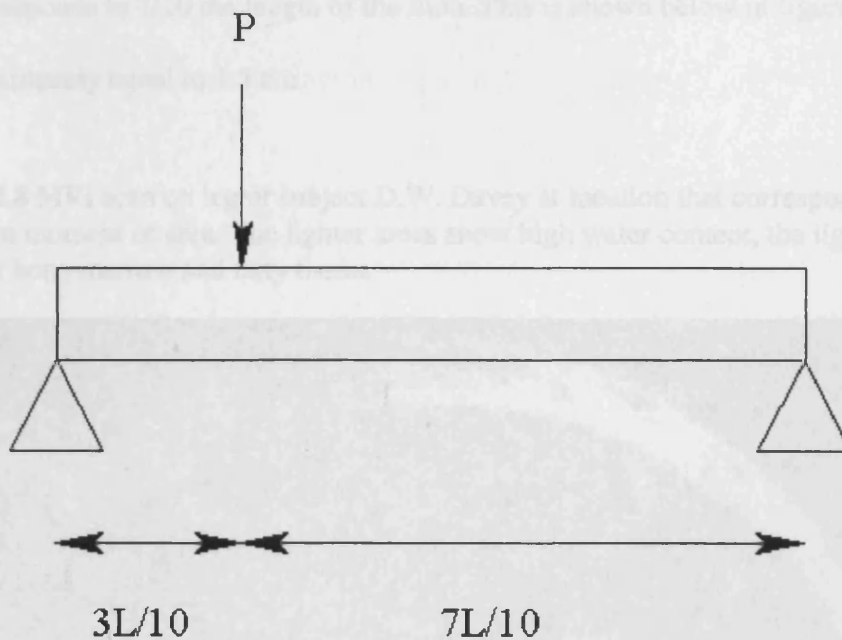
Figure 2.6 Nyquist's test method



The maximum bending moment is given by $M = PL/4$ which indicates a peak sustainable load of 5100N for the male tibia and 4500N for a female tibia. However, as previously mentioned, the typical footballers fracture does not occur mid-span, but 70% along the tibia down from the knee where it has been highlighted that there is a geometrical weakness to impact. It must be evaluated whether a load applied at this particular location has a significant effect on the impact tolerance of the tibial shaft.

The football impact situation is shown in figure 2.7 below.

Figure 2.7 Typical football impact situation.



Maximum bending Moment $M = \frac{21PL}{100}$ equation 2.2

From general beam bending theory

$$\sigma = \frac{My}{I}$$
 equation 2.3

Substituting equation 2.2 into 2.3 we obtain

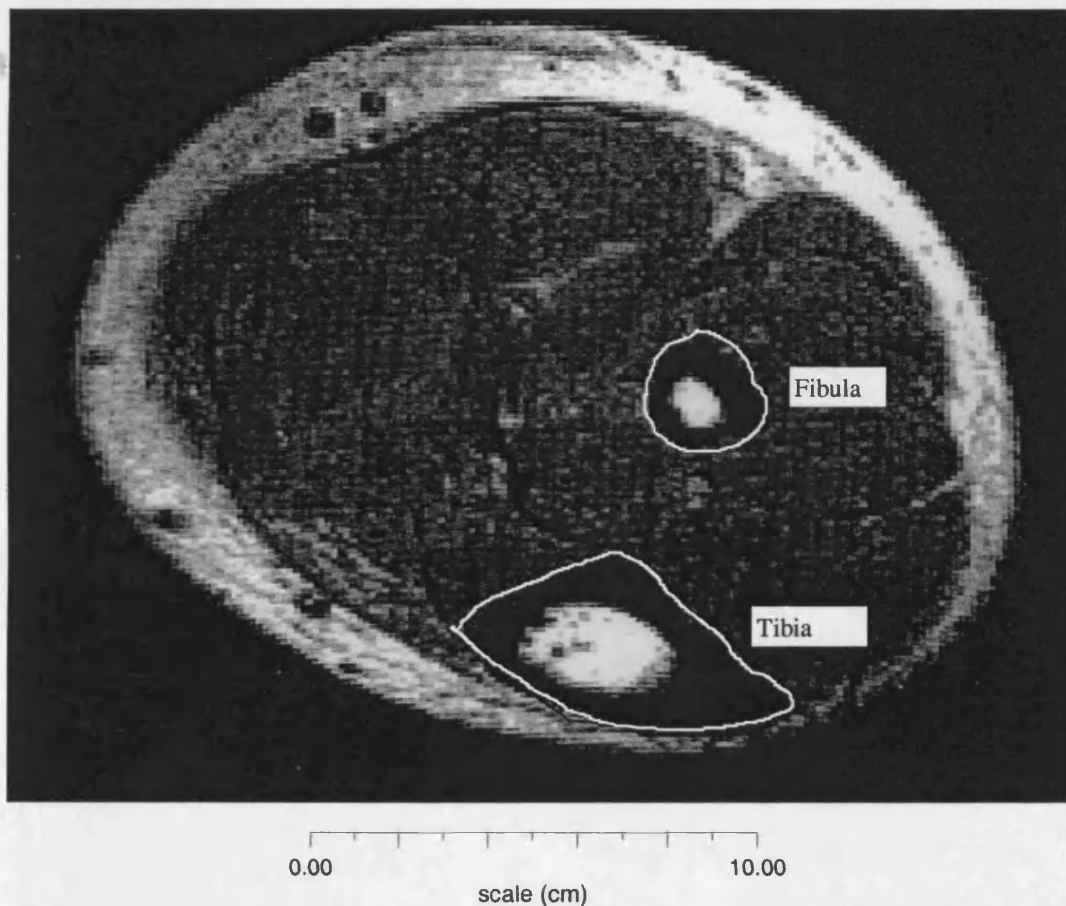
$$\sigma = \frac{21PLy}{100I}$$
 equation 2.4

At 70% of the distance along the tibia Minns^[2,25] gives the average polar moment of inertia as $3 \times 10^{-8} \text{ m}^4$. This value compares well to that calculated using the geometry of my own shin as given in Appendix A1 (value calculated for 75% of distance along tibial shaft is $2.8 \times 10^{-8} \text{ m}^4$).

We know that bone fails in tension before compression so the fracture initiates on the tensile side. From table 2.3 the average tensile stress at failure $\sigma = 112 \text{ MPa}$.

The average distance from the neutral axis y is calculated using a slice of my own leg that corresponds to $7/10$ the length of the tibia. This is shown below in figure 2.8 and is approximately equal to 1.5 cm.

Figure 2.8 MRI scan on leg of subject D.W. Davey at location that corresponds to minimum moment of area. The lighter areas show high water content, the lightest areas are bone marrow and fatty tissue.



Substituting these values into equation 2.4, leads to a maximum tolerable load of 4300N which is 84% of the load sustainable mid-span. This suggests that impact at the geometrically weakest point on the tibia causes fracture to occur at a slightly lower value than it would if it occurred mid-span. However, the average age of Nyquist's ^[2.27] subjects was 55.7 years (11 subjects ranging from 43-64) and these

results clearly do not represent the active footballers age group. Studies by Mather [2.28] and Yamada [2.29] have shown that cadavers taken from the elderly exhibit decreased strength, in terms of ultimate stress to failure.

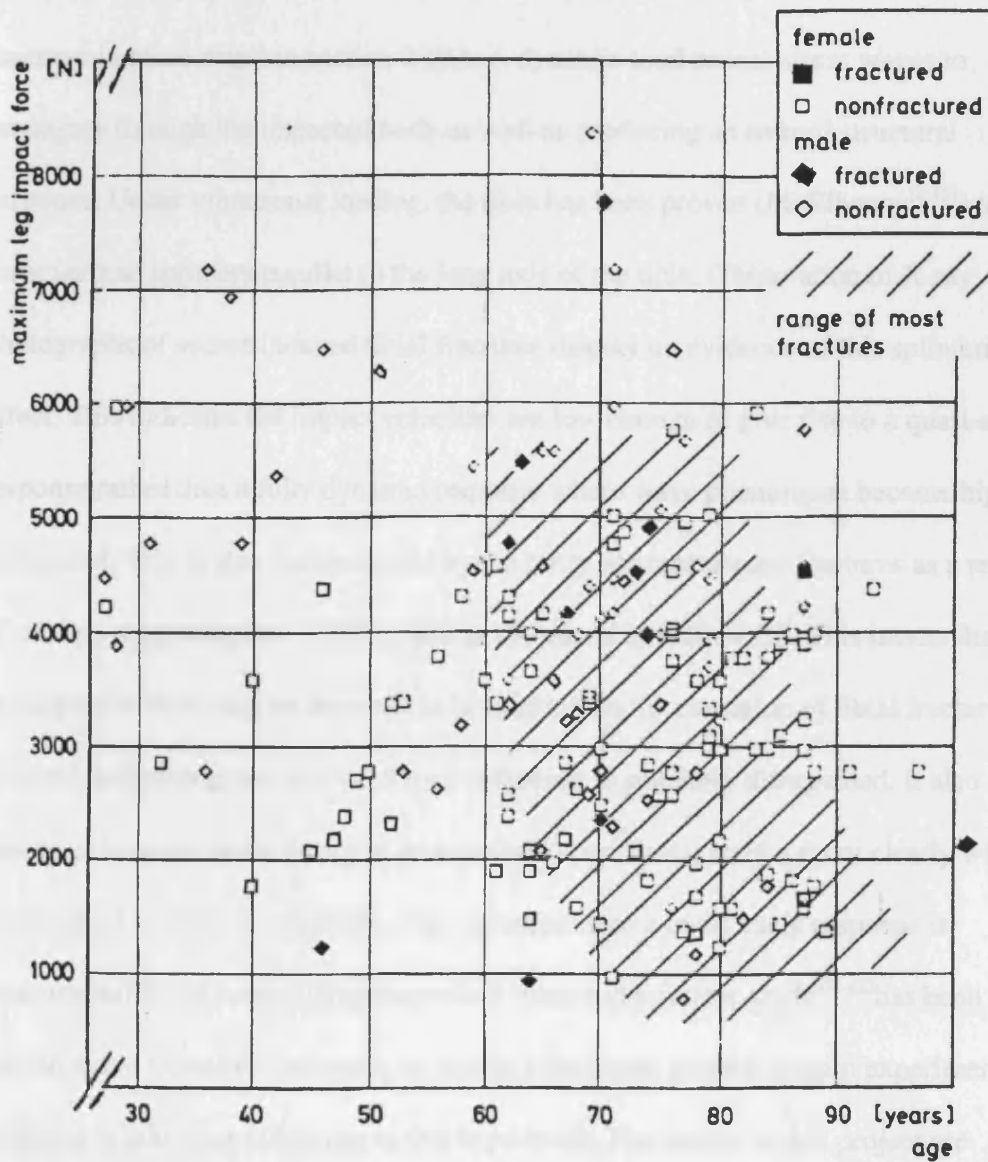
Addressing the problem of patellar pain in older adult athletes, it is particularly comparable to the football injury situation as it involves a patellar dislocation on the distal third of the lower leg. The paper is particularly significant as over 200 subject cadavers were tested over an age range of 20 to 80 years of age. The final results result is shown below in figure 2.9 below. As has been seen, under the age of 60 no fractures occur, even though there is a peak load of over 7000N in some cases and this suggests the calculated value of 1375N may be a conservative value. Most fractures do occur between loads of 6000 and 10000N which supports the value calculated from Biomechanics work, but significantly this is for the age group of 60 years.

The evidence presented within this section shows tibial fracture is available literature generally indicates a range of values of 5000N. This value must be viewed as a rather conservative one as the work by Knapik [2.30] suggests that below the age of 60 years athletes may be able to withstand loads in excess of 10000N. However, the lack of a comprehensive study indicates that the lower value is accepted as standard within this thesis. The value is of particular importance as it is used within chapter 6 in the creation of a formula that defines the idealised behaviour of a shin pad.

An attempt has been made to find literature that concentrates on subjects of an age more likely to regularly play football. The most comprehensive tibial impact test results are provided by Kramer *et al* ^[2.30]. The paper addressed the problem of pedestrians in urban traffic accidents. It is particularly comparable to the football impact situation as it simulates car bumper impact on the distal third of the lower leg. The paper is particularly significant as over 200 subject cadavers were tested over an age range of 20 to 90 years of age. The most notable result is shown below in figure 2.9 below. As can be seen, under the age of 60 no fractures occur, even though there is a peak load of over 7000N in some cases and this suggests the calculated value of 4300N may be over conservative. Most fractures do occur between loads of 4000 and 5000 N which supports the values calculated from Nyquists work, but significantly this is for the age group of 60 plus.

The evidence presented within this section shows tibial fracture in available literature generally initiates at around a value of 5000N. This value must be viewed as a rather conservative one as the work by Kramer^[2.30] suggests that below the age of 60 years the tibia may be able to withstand loads in excess of 7000N. However, the lack of a comprehensive study conducted on younger bone dictates that the lower value is accepted as standard within this thesis. The value is of particular importance as it is used within chapter 6 in the creation of a formula that defines the idealised behaviour of a shin pad.

Figure 2.9 Plot of peak impact load against age of cadavers, the shaded area shows the range of most fractures. Reproduced from 'Fracture Mechanism of Lower Legs Under Impact Load.' (Kramer *et al*^[2,30])



2.7 Tibial Impact Dynamics

An impact typical of that which occurs in a football match is clearly dynamic in nature with a reported duration of between 4 and 6 ms^[2.31] (This literature is assessed in more detail in section 2.10.). A dynamic load causes stress waves to propagate through the impacted body as well as producing an overall structural response. Under vibrational loading, the tibia has been proven (McElhaney^[2.15]) to form vertical splinters parallel to the long axis of the tibia. Observation of X-ray photographs of soccer induced tibial fractures display no evidence of this splintering effect. This indicates the impact velocities are low enough to give rise to a quasi-static response rather than a fully dynamic response where wave phenomena become highly influential. This is also demonstrated by the rarity of comminuted fractures as a result of soccer, suggesting low loading rates as discussed in section 2.3. This means that vibrational effects may be assumed to be minimal in the causation of tibial fracture in football and throughout this work their influence is generally disregarded. It also allows us to apply static theory to understand experimental results more clearly which is discussed in detail in chapter 6. This assumption of a quasi static response is fundamental to the forthcoming theoretical work and a further study^[2.32] has been carried out at Leicester University as part of a final year project, to gain experimental evidence to add more substance to this hypothesis. The results of this project are presented in detail in section 2.7.1.

2.7.1 Summary of investigation into wave phenomena, as a result of impact induced in the lower leg.

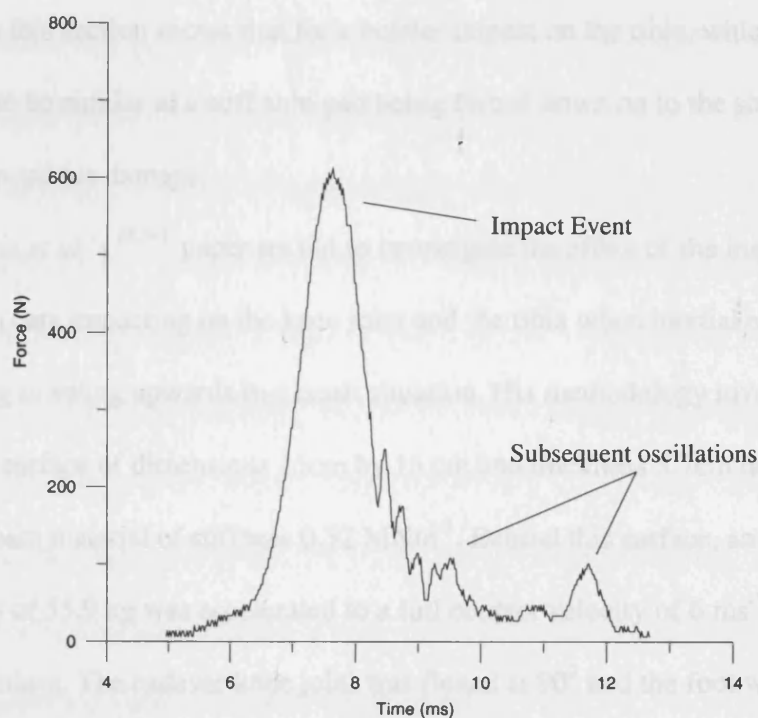
A project investigation ^[2.32] was set up to produce a synthetic limb with similar material properties to that of the human lower leg, to gauge the significance of wave phenomena in the tibia under impact loading. The model shin was set up to have a realistic overall bending stiffness, so that when an impact occurred a mode of vibration similar to that induced in a human leg should occur. To duplicate the stiffness of the tibia required the cross sectional area of the wooden 'leg' to be small in the area just above the tibia. Unlike the human limb, the synthetic tibia included no soft tissue at the ankle and knee joints which led to an inflexible leg much more fragile than a real tibia.

The artificial tibia was constructed from Lignum Vitae which is an exotic hardwood with a comparable elastic modulus (approximately 20 GPa compared to 15 GPa for human bone) and an unusually high density ($1.25\text{-}1.3 \text{ Mgm}^{-3}$) which is reasonably close to that for human bone ($1.8\text{-}2.1 \text{ Mgm}^{-3}$). The surrounding muscle mass was simulated using gelatine.

The tibia was instrumented using strain gauges attached centrally at the top, middle and bottom of the wooden tibia. A load cell was also situated within the impactor to measure the impulsive loading applied to the tibia. The key results obtained from this work show that for an impact on the artificial leg, oscillations are induced, but these are quickly damped out, resulting in only two or three peaks subsequent to the initial impact. The oscillations were relatively small and directly proportional to the applied load, with the first oscillation after impact consistently of a

magnitude less than 10% of the peak load recorded during impact as shown in figure 2.10 below. Although these tests were carried out at very low impact velocities, typically in the range of 2 to 2.8 ms⁻¹ due to the fragile nature of the limb, they do suggest oscillations in the lower leg are small and quickly damped out. This work is further supported by Gadd *et al* ^[2,33] who researched the tolerance of superficial tissue to impact. Analysis of the force deflection curves indicated that the energy dissipation rate of soft tissues exceeds 70%, suggesting the soft tissue in the leg acts as an excellent damper. This work adds experimental support to the hypothesis introduced in section 2.7, that wave phenomena do not have a significant influence in the causation of tibial fracture for an impact that typically occurs within a football match.

Figure 2.10. Output from strain gauge located centrally on Horta's synthetic leg.



2.8 Further serious injuries that occur as a result of impact in the game of soccer.

Although focused on the prevention of tibial fracture, any shin pad re-design must be carried out in a manner that ensures other forms of serious injury, that transpire as a result of impact are also avoided. Possibly the most serious injury a footballer can sustain is torn ankle or knee ligaments. This is a particularly severe injury due to the limited regenerative capacity associated with ligamentous tissue. Although generally associated with twisting, there is strong evidence presented in a paper by Viano *et al* ^[2.34] that torn ligaments also occur as a result of impact to the tibia. The obvious solution to the fracture problem introduced in section 2.6 is to use a stiff pad that spreads the load and minimises tibia bending. However, the evidence discussed in this section shows that for a bolster impact on the tibia, which may be considered to be similar to a stiff shin pad being forced down on to the shin, there is a risk of ligamentous damage.

Viano *et al* 's ^[2.34] paper set out to investigate the effect of the instrument panel within cars impacting on the knee joint and the tibia when inertial effects cause the lower leg to swing upwards in a crash situation. His methodology involved the use of a contact surface of dimensions 15cm by 15 cm and thickness 5.7cm made from a section of foam material of stiffness 0.32 MNm^{-1} . Behind this surface, an axially guided mass of 55.9 kg was accelerated to a full contact velocity of 6 ms^{-1} by a free falling pendulum. The cadaver knee joint was flexed at 90° and the foot was in contact with the ground prior to impact. The centre of the impactor was aimed at a point 15 cm down from the top of the tibial shaft as shown in figure 2.11 and was

instrumented with an accelerometer. The tests were carried out on three female and four male cadavers. All female subjects exhibited comminuted fractures of the tibia/fibula whereas two male subjects, suffered no serious injury and two sustained tears to the posterior cruciate ligament (shown in figure 2.11 below) . Crucially, these tests involved peak loads with an average value of 5.15 kN which is a similar load to that required to fracture the tibia as discussed in section 2.6. Effectively, in the case of the male subjects if the full burden was applied as a point load fracture, would be the likely outcome, but by spreading the load towards the knee joint, ligament damage has been induced instead.

Further tests were carried out by Viano *et al*^[2.34], solely on ligamentous tissue using a servocontrolled test machine which translated the tibia axially through a distance of 5 cm relative to the femur. It was found that the ligaments snapped after a lateral displacement of 2.26 cm at a peak load of 2.48 kN.

Figure 2.11 Viano^[2,34] test method and location of posterior crutiate ligament.

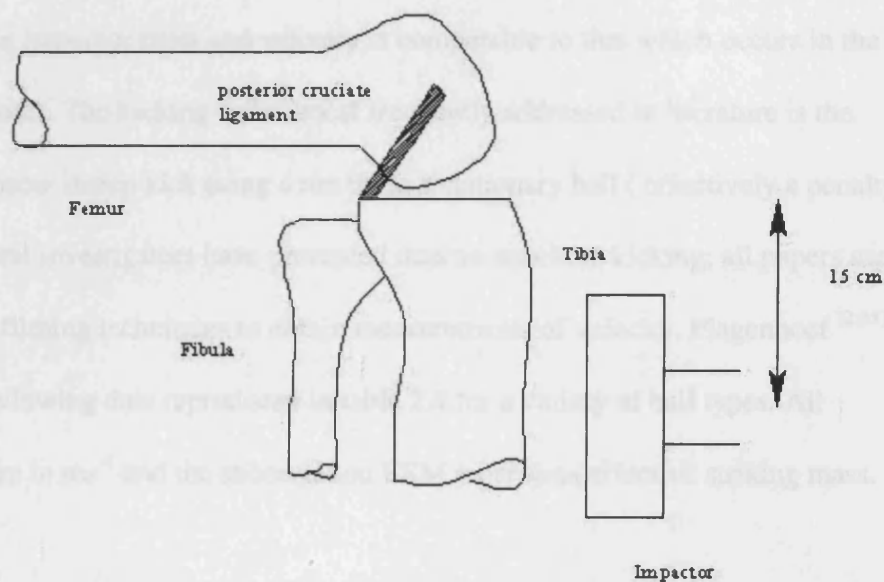


Table 2.4 Velocity and mass of impactor for stationary kick (Flagstaff)

Type of ball and impact direction	ball velocity (m/s)	ball velocity (km/h)	ESM (kg)
American football - kicking - side approach	29.1	24.1	3.9
Soccer ball - rolling - side approach	29.1	23.8	3.9
Soccer ball - stationary - side approach	27.9	21.3	3.2
Soccer ball - cross	26.8	20.3	3.3
Soccer ball - kicking - straight approach	26.7	19.3	3.2
American football - toe strike - straight approach	24.9	19.8	2.6
American football - kicking - straight approach	24.9	19.3	2.6
Soccer ball - stationary - straight approach	23.8	16.3	2.4

The effective striking mass (ESM) is an arbitrary factor. The value can range from the mass of the foot (0.9 kg for a 73 kg male subject), to the mass of the foot and lower leg (4.29 kg) up to 14.23 kg for the mass of the whole leg. The ESM is calculated using conservation of momentum, i.e. the foot impact velocity and the

2.9 Biomechanics of Kicking.

To accurately simulate a football tackle in the form of a test rig it is important that both the impactor mass and velocity is comparable to that which occurs in the game of soccer. The kicking action most frequently addressed in literature is the maximal soccer instep kick using a run up to a stationary ball (effectively a penalty kick). Several investigators have presented data on maximal kicking; all papers use high speed filming techniques to obtain measurements of velocity. Plagenhoef^[2,35] gives the following data reproduced in table 2.4 for a variety of ball types. All velocities are in ms^{-1} and the abbreviation ESM represents effective striking mass.

Table 2.4 Velocity and mass of impactor for stationary kick.(Plagenhoef)

Type of ball and impact location	ball velocity (ms^{-1})	foot velocity (ms^{-1})	ESM (kg)
American football - instep - side approach	29.1	24.1	3.9
Soccer ball - rolling - side approach	29.1	23.8	3.9
Soccer ball - stationary - side approach	27.9	21.5	3.2
Soccer ball - cross	26.8	20.3	3.2
Soccer ball - rolling - straight approach	26.7	19.8	3.2
American football - toe poke - straight approach	24.9	19.8	2.6
American football - instep - straight approach	24.9	19.5	2.6
Soccer ball - stationary - straight approach	23.8	16.3	2.4

The effective striking mass (ESM) is an important factor. This value can range from the mass of the foot (0.9 kg for a 72 kg male subject), to the mass of the foot and lower leg (4.29 kg) up to 14.23 kg for the mass of the whole leg. The ESM is calculated using conservation of momentum, as the foot impact velocity and the

football mass (0.45 kg), along with initial ball velocity is measured experimentally for all studies.

A further study was carried out by Asami and Nolte^[2.36] into the kicking action of 19 German professional footballers. The results are summarised in table 2.5.

Table 2.5 Velocity and mass of impactor for stationary kick. (Asami and Nolte^[2.36])

ball velocity (ms^{-1})	mean 29.9	range 21.5 to 34.0
foot velocity before impact (ms^{-1})	mean 28.3	range 25.8 to 31.1
foot velocity after impact (ms^{-1})	mean 15.5	range 12.7 to 18.6
ESM (kg)	mean 1.02	range 0.80 to 1.26

A further test was performed by Taylor and Broad^[2.34] using three subjects in 1982, results are shown in table 2.6.

Table 2.6 Velocity and mass of impactor for stationary kick. (Taylor and Broad^[2.34])

	ball velocity (ms^{-1})	foot velocity (ms^{-1})	ESM (kg)
subject 1	27.96	21.81	2.93
subject 2	25.83	22.68	1.70
subject 3	26.7	21.01	1.42

From these three sets of data there appears to be an anomaly concerning the variation in stated values for the ESM. If we analyse the figures, we can see that the ESM for the three sets of data ranges from 0.8 kg to 3.9 kg. All papers give foot impact velocities and ball velocities which are reasonably close to each other. Both Plagenhoef and Taylor chose to omit the velocity of the foot after contact from their papers, a crucial factor in the calculation of the ESM. In reference to table 2.6 it can

be seen that subject 1 and 3 exhibit almost exactly the same football and foot velocities, but the ESM varies by a factor of 2. As such, the results for both the Plagenhoef and Taylor research must be treated with suspicion. It was decided to take an average of the findings of the three authors, but by eliminating the Plagenhoef data for non soccer (as this would involve differing ball masses) and moving ball situations the effect of this questionable data is minimised and a value of 1.3 kg is obtained for the mean striking mass.

The main problem concerning the overall relevance of this data is the impact velocity for a player running up to a stationary ball and hitting it as hard as possible would be expected to be much higher than those obtained in a tackle situation (fair or foul). However, the measured effective masses involved would be anticipated to be similar and this presents a useful guide for the prospective mass of the impactor for an experimental simulation of a football tackle. Nyquist^[2,27] produced non-comminuted impact fractures in cadavers at kinetic energy levels ranging from 92 to 282 Joules and comminuted fractures in the range of 135 to 762 Joules. Using the effective mass calculated as 1.3 kg, the lowest non-comminuted fracture corresponds to an impact velocity of just under 12 ms^{-1} .

To sum up the findings of this section, a typical football kick involves a mass of approximately 1.3 kg, and a kick which causes fracture does so at a minimum velocity of approximately 12 ms^{-1} .

2.10 Summary of previous work on shin pads.

Shin pads have been infrequently mentioned in publications, and very few studies have attempted to assess their efficiency.

Philippens and colleagues^[2.31] attempted to study the efficiency of various commercially available shin pads in Holland in 1989. They set up test methods for shin guards simulating conditions experienced during a soccer match. The stiffness of the shin pads were assessed, followed by impact testing using a spring loaded impactor. The impact force time history was measured using a piezoelectric device which was situated centrally, directly beneath the impactor in a wooden shin prosthesis. The peak impact force was then compared for various shin pads against that recorded for an impact with no pad present. The work by Philippens *et al* concluded that the peak impact force is reduced by between 40 and 70% by the use of a shin pad and that the reduction showed no direct correlation to the stiffness.

Bir *et al* ^[2.38] tested eleven pads commercially available in the United States using a similar method to that used by Philippens. The impactor in this test was a free swinging pendulum which was allowed to collide with a fixed, instrumented Hybrid III crash test dummy leg. The instrumentation consisted of load cells at both knee and ankle joints within the dummy. The control for comparison in this study was a healthy physically active 26 year old man who was subjected to an impact with a peak load of 2300N. There is no information on how the athlete was instrumented. The response of the dummy leg under impact was compared to that for the volunteer and results were adjusted to achieve congruity. Again, the peak impact force was then compared for various shin pads against that for the uncovered dummy leg. The tests were carried

out at 0⁰, 20⁰ and 38⁰ Celsius. Again, a significant reduction in the peak force was noted of between 40 and 77% and there was no significant evidence of temperature dependence.

Possibly the most informative of the papers provided on this subject has been written by Lees and Cooper^[2.39]. They carried out testing on a range of pads using the test method employed by the British Standards Institution to evaluate cricket pads (BS6183 Part 1^[2.40]). This method uses an impactor of mass of 5 kg instrumented with an accelerometer which is dropped from 400 mm on to a wooden leg, upon which the tested pads were placed. The key results obtained were a reduction in peak impact force of between 40 and 60 %, an increase in impact duration of between 30 and 40 % and a reduction in the impact energy absorbed by the leg of up to 20 %. The level of performance showed no correlation to the price of the pad. Crucially, within this paper the authors try to interpret how the shin pads behave using these results. It is concluded that shin pads prevent injury by means of shock absorption, spreading the load over a larger surface area and modifying the load time history of the impact event.

The results from these three papers do show the importance of shin guards to attenuate the forces experienced by the lower extremities during the course of a soccer match, with all reports concluding the peak impact load is reduced by a minimum of 40 % by the use of a pad. However, only the Lees paper offer any insight into the fundamental behaviour of shin pads and none attempt to improve on the basic design.

A similar test to those carried out by Phillipens and Bir is suggested by Woods^[2.41] and again a force cell is the preferred measuring device. A mass of 5 kg is

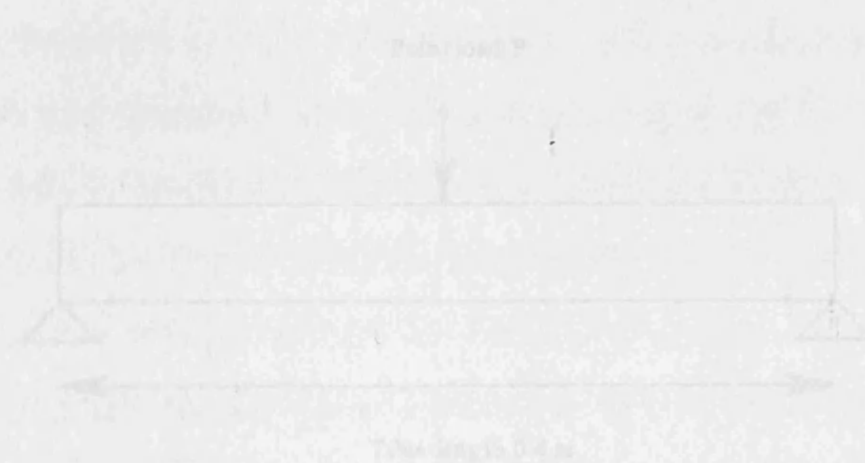
dropped from various heights onto a curved steel plate, with a thin covering layer of leather to simulate skin situated between the pad and the plate. The whole apparatus is mounted on a central load cell. Unfortunately, further to presenting his ideal test he presents no actual meaningful results and there is no explanation as to why a mass of 5 kg is chosen. The impact energies at which tests are conducted are of 12.5, 25 and 50 Joules which relate to heights of 25, 50 and 100 cms and impact velocities of 2.2, 3.13 and 4.43 ms^{-1} . None of these values compare with those obtained through analysis in the previous section of available literature, which suggest an impacting mass of 1.3 kg and velocity of 12 ms^{-1} which relates to an impact energy of 92 Joules. Surprisingly the method defined by Woods is the basis for the test performed by SATRA^[1.1] in an advisory capacity to award the CE mark for personal protective equipment (PPE), the standard discussed in chapter 1.

The key problem with this research is the instrumentation used. In each case a dummy leg of sorts is mounted on a load cell. There is a large contact surface between the pad and the leg through which the impact energy may be transmitted. The impact energy is turned from a concentrated load at the point of impact to a pressure distribution beneath the pad. The load cell provides the total force/time history for the impact, it does not however give any indication of how this load is spread. In real terms, a large impact force spread over the whole contact surface represents less threat of potential injury than a lesser force that stays highly localised (although the work of section 2.8 suggests care must be taken that the loads applied at the knee and ankle joints do not cause ligament damage). Lees highlights this spreading of the impact is

one of the basic ways a pad helps in the avoidance of injury and an experimental method to monitor this phenomenon should be included in any experimental set-up.

Evidence presented within section 2.1 shows the key to fracture avoidance is the minimization of the average bending moment on the distal shaft. Continuing with the beam analogy for the pedicle system, first introduced within section 2.6, a comparison of the system for an infinitely stiff pad and a pad that is elastic where E_p is the modulus of the pad, effectively an impact with no stiff pad present) may be made to assess the effect of the pad on the bending moment at the distal end of the shaft.

Figure 2.12 Beam analogy for centrally loaded distal shaft with pad of zero stiffness.

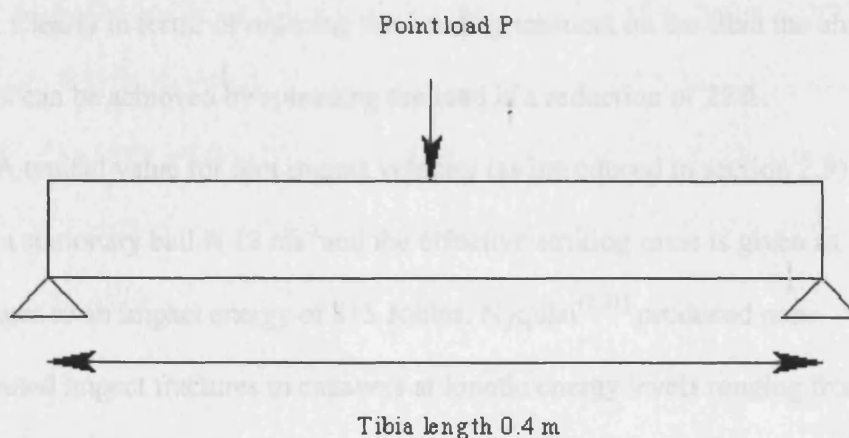


For a peak load that induces fracture (approximately 3000 N) as depicted in section 2.6, applied centrally on a shaft of length 0.4 m as shown in figure 2.12, the bending moment is given by 300 Nm.

2.11 Comparison of influence for force attenuation, load spreading and energy absorption on shin pad effectiveness.

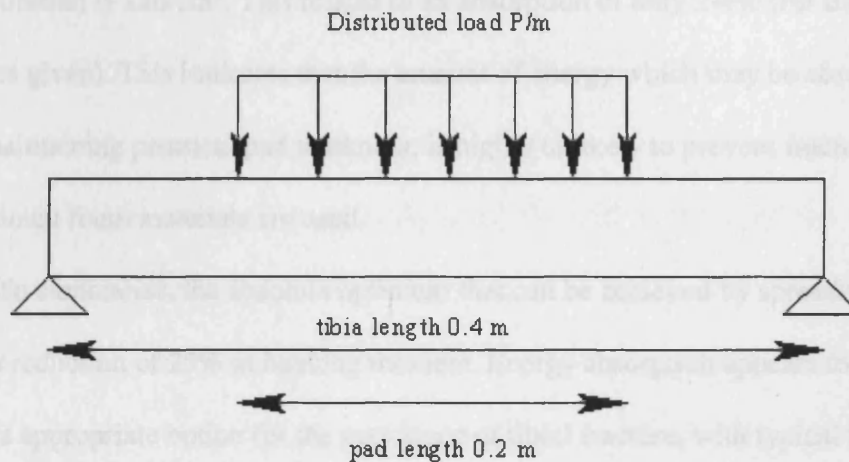
Evidence presented within section 2.1 shows the key to fracture avoidance is the minimisation of the overall bending moment on the tibial shaft. Continuing with the beam analogy for the pad/tibia system, first introduced within section 2.6, a comparison of the system for an infinitely stiff pad and a point load (a situation where there is no spreading of load, effectively an impact with no shin pad present) may be made to assess the maximum achievable effect of spreading the load.

Figure 2.12 Beam analogy for centrally impacted tibial shaft with pad of zero stiffness.



For a peak load that threatens fracture (approximately 5000 N as discussed in section 2.6) applied centrally to a tibia of length 0.4m as shown in figure 2.12, the bending moment is given by 500Nm.

Figure 2.13 Beam analogy for centrally impacted tibial shaft with pad of infinite stiffness.



For an identical load of 5000N distributed equally over the length of a hypothetical shin pad of length 0.2 m as shown in figure 2.13 the bending moment is given by 375Nm. Clearly in terms of reducing the bending moment on the tibia the absolute limit that can be achieved by spreading the load is a reduction of 25%.

A typical value for foot impact velocity (as introduced in section 2.9) for a kick on a stationary ball is 12 ms^{-1} and the effective striking mass is given as 1.3 kg. This relates to an impact energy of 315 Joules. Nyquist^[2.27] produced non-comminuted impact fractures in cadavers at kinetic energy levels ranging from 92 to 282 Joules and comminuted fractures in the range of 135 to 762 Joules. Using these values the energy to be absorbed to avoid fracture is approximately 223 Joules (315 - 92). For two typical elastomeric foams; polyester and polyethylene, the energy absorbed per cubic meter is $3.9 \times 10^4 \text{ Jm}^{-1}$ and $6.4 \times 10^4 \text{ Jm}^{-1}$ respectively. (Ashby and Gibson^[2.42]). To achieve the required energy absorbency level of 223 Joules would require over 5700 cm^3 of polyester foam and 3480 cm^3 of polyethylene foam. For a

hypothetical pad of practical dimensions with a length 20 cm, width 10 cm and thickness 0.6 cm, the volume of available foam (assuming the load is spread over the whole volume) is 120 cm^3 . This relates to an absorption of only 2-4% (for the two examples given). This indicates that the amount of energy which may be absorbed while maintaining practical pad thickness, is highly unlikely to prevent fracture if conventional foam materials are used.

To summarise, the absolute optimum that can be achieved by spreading the load is a reduction of 25% in bending moment. Energy absorption appears to be an even less appropriate option for the avoidance of tibial fracture, with typical foam materials absorbing less than 5% of the energy required. In contrast, literature discussed in section 2.10 showed the peak load on the tibia, and therefore the peak bending moment was reduced by up to 77% for superior performing shin pads. This clearly sets an early precedent in the direction of subsequent work contained within this thesis. The observation and understanding of how a shin pad attenuates the load time history is clearly the most encouraging approach from which the problem of tibial fracture within the game of soccer may be solved.

2.12 Conclusions.

Previous research as introduced within this chapter has been considered to gain an understanding of the frequency of tibial fracture in the game of soccer. By extrapolating statistics detailing the cause of tibial fracture within the County of Leicestershire it is estimated that approximately 3000 footballers sustain a broken leg each year in the UK. This indicates that the injury is significant and justifies the re-design of shin pads undertaken within this thesis.

The loading conditions that cause tibial fracture have also previously been researched, with the conclusion that most of the fractures are caused by bending loading and cracks initiate on the opposite side to the point on the tibia where contact with the impacting body is made. Consideration of the geometry of the tibia shows the tibia has a specific weakness to bending loading at approximately 70 % of the vertical distance between ankle and knee. This is also the usual position of the centre of the football when located on the ground and logically is where a tackle would be aimed. This goes some way to explaining why there are so many fractures within the game.

The specific values at which fracture initiates has also been investigated at length. Unfortunately the lack of a standard test method, coupled with the variability of properties from one bone specimen to another has led to a range of published values rather than a specific quantity. However, bone generally fails at a stress of 112 MPa in tension, 180 MPa in compression and has an elastic modulus of 15 GPa. Further evidence shows that the tibia fails under load of approximately 5000 N applied mid span, although this value is considered to be conservative. Bone is a viscoelastic material but the pulse durations that occur as a result of impact in soccer

do not relate to strain rates high enough to significantly affect the fundamental material characteristics derived under static loadcases.

Available literature discussed within this chapter suggests the fractures that occur as a result of football are not highly influenced by wave phenomena. The strongest evidence in support of this conclusion is the nature of the fracture patterns. If the fractures were completely or even partially due to vibrational effects there would be evidence of splintering parallel to the long axis of the tibia.

In the attempt to reduce the localised bending, which has been shown to be the predominant cause of fracture a stiff guard could be used. Care must be taken to ensure the stiffness is not such that a significant proportion of the load is transferred to the ankle and knee joints. It has been proven that posterior cruciate ligaments tear under impact at a load of approximately 2.5 kN and it would be expected that serious damage may occur at loads of lesser magnitude.

Consideration of literature on the biomechanics of kicking indicates a mass of approximately 1.3 kg is involved in a typical tackle. Further analysis involving the energy required to fracture the tibia suggests a minimum impact velocity of 12 ms^{-1} would cause a non-comminuted fracture. Clearly these values are important in the design of a pertinent test rig.

Previous experimentation on football shin pads generally show very limited experimental techniques; involving a single load measurement device located either within the impactor or the supporting medium. Impacts are compared for situations with, and without shin guards in place. Results show commercially available pads reduce the peak load on the tibia by between 40 and 75 % and that shin pads prevent

injury by means of shock absorption; spreading the load over a larger surface area and modifying the load time history of the impact event. Comparison of the scope of improvement achievable using these three methods indicates that the modification of the load time history is clearly the most encouraging approach to minimising the incidence of tibial fracture within the game of soccer. These results are particularly important in the context of developing an experimental test rig and suitable instrumentation to monitor these three modes of behaviour. The design of such a test rig is considered in detail in chapter 3.

[2.4] Watson A.W.

Incidence and type of knee symptoms in football. Analysis of four types of sport.
American Journal of Sports Medicine 1982;10:137-143.

[2.5] Pridan ET

Lower extremity site of onset of acute soccer injuries.
The Physician and Sportsmedicine 1979;8:43-48.

[2.6] Berger, Jackson JJ

Knee accidents in the French Alps. Alps soccer association.
Journal of Sports Medicine 1986;3:66-77.

[2.7] Rognes A, Nilsson S

Major injuries in Norwegian football.
British Journal of Sports Medicine 1979;13:3-5.

[2.8] Chalmers J, Gilman J, Maher M, Oberg P, Lippman SG

Incidence of soccer injuries and their relation to training and team success.
Journal of Sports Medicine 1977;1:53-67.

[2.9] Friedl T, and Lloyd EW

An overview of common soccer injuries.
Journal of Sports Medicine 1992;16:269-273.

References

- [2.1] Backous DD, Friedl KE, Smith NJ, Parr TJ, Carpine WD Jnr
Soccer injuries and their relation to physical maturity.
American Journal of Diseases in Children 1988; 142:839-842
- [2.2] Ekstrand J, Gillquist J
The Avoidability of Soccer Injuries.
International Journal of Sports Medicine 1983;4:124-128
- [2.3] Maehlum S
Football injuries in Oslo: a one year study.
British Journal of Sports Medicine 1984;18:186-190
- [2.4] Watson AW
Incidence and nature of sports injuries in Ireland. Analysis of four types of sport.
American Journal of Sports Medicine 1993;21(1):137-143
- [2.5] Pardon ET
Lower extremities are site of most soccer injuries
The Physician and Sportsmedicine 1977;5:43-48
- [2.6] Berger-Vachon G
Soccer accidents in the French Rhone-Alpes soccer association.
Journal of Sports Medicine 1986;3:69-77
- [2.7] Roaas A, Nilsson S
Major Injuries in Norwegian Football.
British Journal of Sports Medicine 1979;13:3-5
- [2.8] Ekstrand J, Gillquist J, Moller M, Oberg B, Liljedah SO
Incidence of soccer Injuries and their relation to training and team success.
Journal of Sports Medicine 1983;11:63-67
- [2.9] Fried T, and Lloyd GJ
An overview of common soccer injuries.
Journal of Sports Medicine 1992;14:269-275

[2.10] Cattermole HR, Hardy JRW, Gregg PJ
The footballers fracture.
Journal of Sports Medicine 1996;30:171-175

[2.11] Van Mechelen W, Hlobil H, Kemper HCG.
Incidence, severity, aetiology and prevention of Sports Injuries. A review of
Concepts. Journal of Sports Medicine. 1992; 14: 82-99

[2.12] Hardy JRW, Richardson JB, Gregg PJ
The footballers fracture.
Paper presented to inaugural meeting of British Orthopaedic Sports Trauma
Association at the British Orthopaedic Association. 13 April 1994. Abstract: Journal
of Bone Joint Surg. 1994; 76-B(Suppl & III): 141-142

[2.13] The Football Association
The Referee's chart and Player's guide to the laws of Association Football.
London: Macmillan, 1999.

[2.14] Currey JD
The Mechanical Properties of Bone.
Journal of Clinical Orthopaedics 1970;73:210-231

[2.15] McElhaney JH
Dynamic Response of bone and muscle tissue.
Journal of Applied Physiology 1966 ;31(4):1231-1236

[2.16] King JJ, Fan WRS, Vargovick RJ.
Femur Load Injury Criteria - A Realistic Approach
17th STAPP Car Crash Conference 1973 SAE730984, 423-438

[2.17] Patrick LM, Kroell CK, Mertz HJ
Forces on the human body in simulated crashes.
9th STAPP Car Crash Conference
Minneapolis: Nolte Centre for continuing education
University of Minnesota, 1995.

- [2.18] Carter DR, Caler WE
A cumulative damage model for bone fracture.
Journal of Orthopaedic Research 1985;3:84-90
- [2.19] Burnstein AH, Currey JD, Frankel VH, Reilly DT
The ultimate properties of bone tissue: the effects of yielding.
Journal of Biomechanics 1972;5:35-43
- [2.20] Carter DR, Caler WE
A cumulative damage model for bone fracture.
Journal of Orthopaedic Research 1985;3:84-90
- [2.21] Curry JD
Strain Rate and Mineral content in fracture models of bone.
Journal of Orthopaedic research 1988 ;6:32-38
- [2.22] Currey JD
Strain rate dependence of the mechanical properties of reindeer antler and the cumulative damage model of bone fracture.
Journal of Biomechanics 1989;22:469-475
- [2.23] Frost HM, Roth A, Villanueva AR
Physical characteristics of bone II. Biphasic elastic behaviour of fresh human bone.
Henry Ford Hospital Medical Bulletin 1961;9:153-156
- [2.24] Chamy A, Tschantz P
Mechanical influences on bone remodelling. Experimental research on Wolff's law.
Journal of Biomechanics 1972;5:173-180
- [2.25] Minns RJ, Bremble GR, Campbell
The Geometrical properties of the human tibia.
Journal of Biomechanics 1975 ;8:253-255
- [2.26] Frankel VH and Burnstein AH
Load capacity of tubular bone.
In Biomechanics and related Bioengineering Topics.
Edited by Kenedi RM 1965
Pergamon Press Oxford 381-396

[2.27] Nyquist GW, Cheng R, EL-Bohy AAR, King AI
Tibia Bending: strength and response.
29th STAPP Car Crash Conference 1985 SAE851728, 273-286

[2.28] Mather BS
Variation with age and sex in strength of the femur
Journal of Medical and Biological Engineering 1968;6:129-134

[2.29] Yamada H
Strength of Biological Materials
Edited by Evans FG
Williams and Wilkins Baltimore 1970
Chapter 3, 19-73

[2.30] Kramer M, Burrow K, Heger A
Fracture Mechanism of Lower Legs Under Impact Load.
17th STAPP Car Crash Conference 1973 SAE730966, 81-100

[2.31] Philippens M and Wismans J.
Shin Guard impact protection.
Proceedings of 1989 International I. R. C. O. B. I. Conference on the Biomechanics of impacts. 65-76.

[2.32] Horta P
Simulation of the dynamic properties of the human tibia.
University of Leicester Engineering Department
Final Year Project Report 1998.

[2.33] Gadd C. W., Nahum A. M., *et al*
Tolerance and Properties of Superficial Soft Tissue in Situ
Paper 700910, Proceedings of Fourteenth Staap Car Crash Conference, p33, New
York: Society of Automotive Engineers, Inc., 1970

[2.34] Viano D, Culver C, Haut R, Melvin J, Bender M, Culver R, Levine R
Bolster Impacts to the Knee and Tibia of Human Cadavers and an Anthropomorphic
Dummy.
22nd STAPP Car Crash Conference 1978, 347-357

[2.35] Plagenhoef S
Patterns of Human Motion (1971)
Englewood Cliffs, N.J.
Prentice-Hall
Chapter 8. Throwing and kicking.

[2.36] Asami T, Nolte V
Analysis of powerfull ball kicking
Journal of Biomechanics 1983 ;8B:695-700

[2.37] Taylor J, Broad T
Unpublished Report
Sports Biomechanics Laboratory Report
Liverpool Polytechnic 1982

[2.38] Bir CA, Cassatta SJ and Janda DH.
An Analysis and comparison of soccer shin guards.
Clinical Journal of Sports Medicine. 1995. 5; 95-99

[2.39] Lees A, Cooper S
The Shock Attenuation Characteristics of Soccer Shinguards.
Unpublished Report
Liverpool John Moores University.
School of Human Sciences internal report number. 19945

[2.40] British Standards Institution
Protective equipment for cricketers
BS 6183; Part 1. 1981.

[2.41] Woods RI.
Thoughts on shin pad testing.
Unpublished Report
Cambridge University Engineering Department internal report. 1994.

[2.42] Ashby M.F, Gibson L.J
Cellular Solids: structure and properties
Pergammon Press 1988 page 236

Chapter 3

Development of experimental equipment with particular attention to the development of a dynamic thin film pressure sensing array.

3.1 Introduction

Having validated that there is a serious problem concerning tibial fracture in the game of soccer, the next task is to develop equipment to firstly simulate a football tackle, and then add instruments to this equipment to measure the most significant of the impact characteristics. Building on the evidence amassed in chapter 2, the key attributes of the impact, with respect to preventing tibial fracture, are in descending order of importance; load attenuation, load spreading and energy absorption. The characteristics required for measurement are clear, but careful choice of instrumentation must be made with the ultimate aim of achieving the optimal sensor set-up, in terms of both locality and performance.

This chapter also deals with the basic equipment used to simulate the impact that occurs in the game of soccer. Of obvious importance is the medium upon which the pads are placed to be tested. Clearly an assessment of the influence of this material must be carried out to decide whether an accurate model of the leg is required to recreate the desired impact situation.

Evidence ((Taylor(1982)^[2.34],Plagenhoef(1971)^[2.35],Asami(1983)^[2.36],Nyquist, 1985^[2.27]) in available literature has suggested that an impacting mass of 1.3kg and velocity of approximately 12 ms^{-1} threatens fracture of the tibia. A test rig able to deliver an impact of such magnitude, or failing this, provide the most rigorous

examination possible must be designed to allow testing of a range of prospective materials, current shin pads and any future prototype that may be developed.

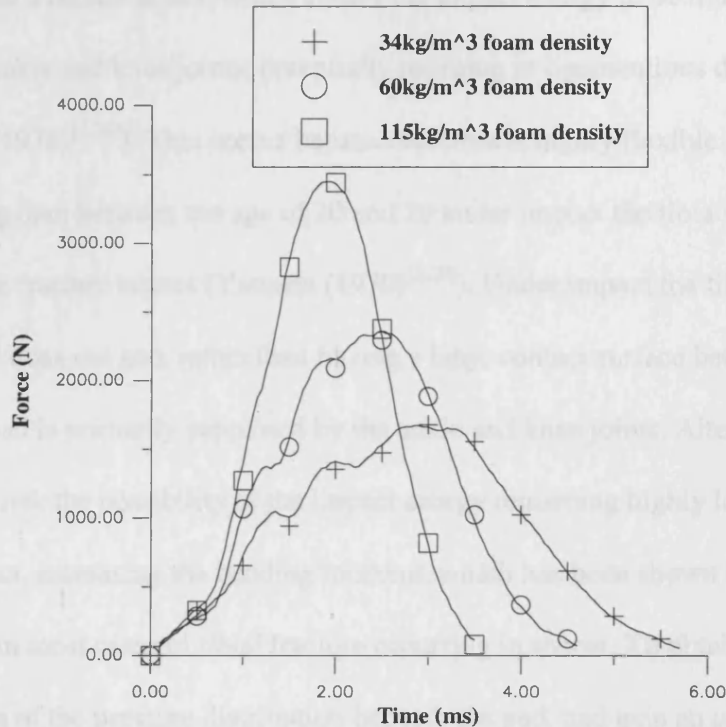
The overall objective of the work in this section is to concentrate on the most important characteristics of the impact, with reference to causing injury.

Instrumentation must be assimilated to allow these characteristics to be accurately measured in a laboratory environment, on test equipment that simulates a football tackle as closely as possible.

3.2 Football impact measurement requirements.

In the understanding of impact, of paramount importance are the devices used to record and measure the data from the collision. As previously discussed in chapter 2 section 2.1, the commonest cause of fracture is bending loading, with crack initiation occurring beneath the point of impact, on the side of the tibia under tensile loading. The key aspect of the response is the control of the impulse (the integral of the force with time) imparted to the pad/leg system as shown in section 2.11. For successive impacts of similar impactor mass and velocity, basic mechanics dictates that the impulse must be identical. However, the force time history for the impact is strongly material sensitive. Effectively, the pattern of the force time history has a constant area beneath it, but may have very different patterns, in terms of peak loading and impact duration. This is shown in figure 3.1 below, for three impacts of equal mass and impact velocity, but conducted upon three different foam materials. The impacts were conducted using a 1m drop weight tower which is shown in figure 3.7. For each separate impact, the impactor was released from the same height and was of the same mass. The impactor was instrumented with a load cell and it is the output from this device which is shown on figure 3.1.

Figure 3.1 Force time history of impact on three differing foams, measured at the point of impact using a load cell.



As can clearly be seen, the impulse which is represented by the area beneath the curve is equivalent for the three differing materials. However the force time histories are very different. These characteristics are easily interpreted; an impact spread over a short period of time has a larger peak load than that spread over a longer period of time. Clearly the case where the peak force is the lowest represents the least threat of injury if we analogue this to a shin pad situation.

Also discussed in chapter 2 is the possibility of injury avoidance through the spreading of the impact load over a larger surface area. Although this has been shown to have less promise than the manipulation of the load time history, a potential reduction of 25% cannot be ignored. The impact energy is turned from a point load at the boot tip to a pressure distribution beneath the pad. Intuitively, the pattern of

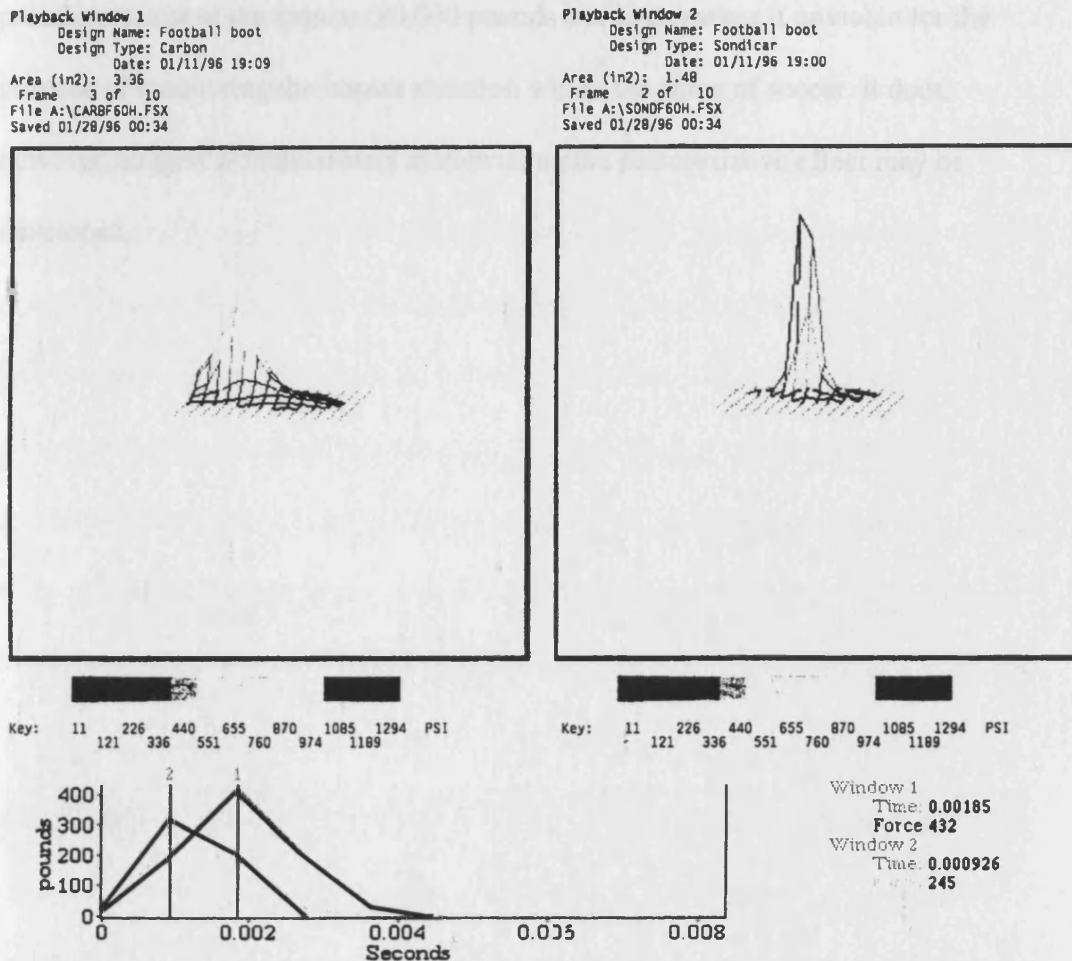
distribution is material sensitive and varies between two extremes. Stiff guards are likely to create a bolster effect, which causes the impact energy to be transferred towards the ankle and knee joints, potentially resulting in ligamentous damage (Viano et al (1978)^[2.34]). This occurs because the tibia is highly flexible and for a healthy young man between the age of 20 and 29 under impact the tibia will deflect 10 mm before fracture occurs (Yamada (1970)^[2.29]). Under impact the tibia bends while the pad does not and, rather than having a large contact surface between pad and leg, the pad is primarily supported by the ankle and knee joints. Alternatively flexible pads risk the possibility of the impact energy remaining highly localised at the point of impact, increasing the bending moment, which has been shown in chapter 2 to be critical in most cases of tibial fracture occurring in soccer. To obtain a full representation of the pressure distribution beneath the pad, and gain an understanding of the spread of load, it is required that data is recorded at a number of locations between the pad and the leg.

The effectiveness of a shin pad to absorb the impact energy which may occur within a football game, as highlighted in section 2.1.1, is extremely limited; nevertheless instrumentation to monitor such data will be included within the experimental set up for the purpose of completeness.

3.3 Instrumentation to measure the pressure between contact surfaces.

To analyse the pressure distribution between two contact surfaces for a dynamic loading situation there are very few options for accurate measurement. Resistive and semiconductor strain gauges are not sensitive to forces normal to their axis. There are similar problems with piezoelectric films, with the added problem that if strained in one direction the readings on other axes are affected. Although there are other methods of measurement, such as load cells, these devices are large and intrusive and affect the dynamic response of the system. However, recent developments within the piezoresistive semiconductor field has led to the development of a new sensing option which is ideal for insertion between two surfaces to measure compressive stress. The most comprehensive equipment currently on the market is produced by Tek-scan of the USA. The dynamic sensing array is grid based with 100 sensing locations and a maximum sampling rate of 100 kHz. The machine was acquired for a demonstration and the output for an impact on two shin pads is shown in figure 3.2.

Figure 3.2 Output from Tek-scan sensor array for impacts conducted on two shin pads.



You can see the higher pressures in the composite material easily by the 3-d display. And, the magnitude of force is almost double. However, the contact area is much smaller while the carbon spreads the load over a wider contact area. Contact area is 3.36 versus 1.48 square inches.

3.3.3 As can be seen, even set to the fastest sampling rate, only three points are recorded during the impact event. The fact the sampling rate is slow, coupled with the prohibitive cost of the system (80,000 pounds sterling), makes it unviable for the purpose of monitoring the impact situation within the game of soccer. It does, however, suggest a measurement system using the piezoresistive effect may be developed.

Figure 3.3 is the lighter material, the other with a semiconductive material such as the dark material. The semiconductive material forms a resistive path between the electrodes and the electrical resistance of this material is proportional to the lateral pressure applied. The resistance falls exponentially decreasing resistance in current when a pressure is applied normal to the sensor surface.

Figure 3.3 Force Sensitive Resistor (FSR) 1991. Acceleration gun diameter. Total gun 7.62mm diameter. Tail length 31.25 mm.

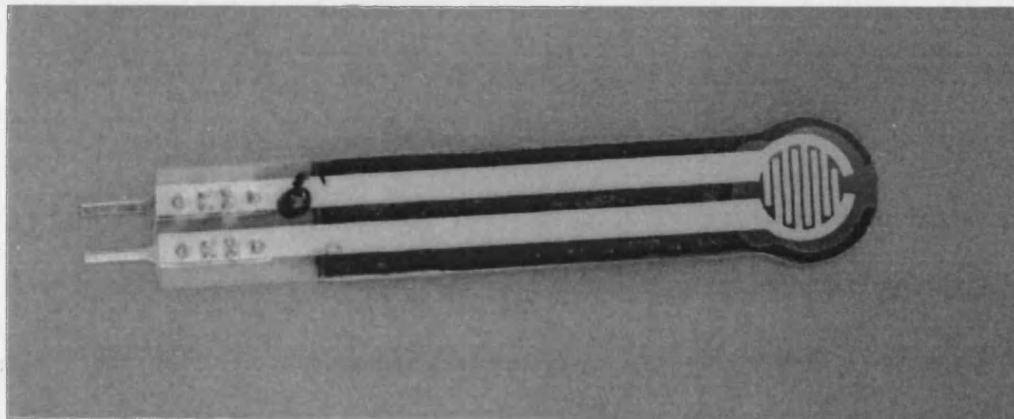


The term piezoresistive refers to this change of resistance due to pressure. A common cause of this is the change in the nature of the valence and conduction bands of electrons in certain some conductive crystals. A further explanation of the principles of piezoresistivity may be found in appendix B1.

3.3.1 Force Sensing Resistors (FSR's).

Simple static and dynamic testing of Force Sensing Resistors (FSR's) a piezoresistive product developed by Interlink Electronics, has shown the device to be suitable for the measurement of pressure between contact surfaces. A picture of a FSR with dimensions is shown in figure 3.3 below. The FSR is basically two polymer sheets laminated together. One sheet is coated with interdigitating electrodes seen on figure 3.3 as the lighter material, the other with a semiconductive material seen as the dark material. The semiconductive material forms a resistive path between the electrodes and the electrical resistance of this material is proportional to the lateral pressure applied. The sensors exhibit an exponentially decreasing resistance to current when a pressure is applied normal to the sensor surface.

Figure 3.3 Force Sensing Resistor (FSR 149). Active area 4 mm diameter. Total area 7.62 mm diameter. Tail length 31.24 mm.



The term piezoresistance refers to this change of resistivity due to pressure. It occurs as a result of the anisotropic nature of the valence and conduction bands of electrons in certain semiconductor crystals. A section explaining the principles of piezoresistivity may be found in appendix B1.

The FSR is not established as a standard measurement device and its unfamiliarity necessitates a full characterisation of its properties to firstly, ensure confidence in the results obtained using the device as a measurement tool and secondly, to enable suitable supporting equipment and software to be developed. Evaluation of the FSR to both static and dynamic loading, was carried out and a method of validation was devised before the sensors could be used with assurance.



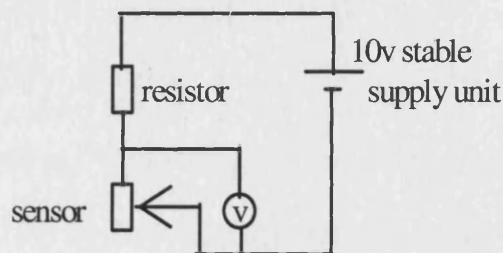
The sensor was first placed in a test machine (Hounsfield Tensometer) with a specially modified air pressure platen system, and loaded up to a maximum value of 11.00N in 11 increments of 1.00N. For each increment the change in the voltage across the sensor was measured using a digital voltmeter. The experiment was repeated to assess whether the voltage readings could be reproduced for further loading/unloading cycles. The value of the resistors connected in the potential divider circuit was also varied to investigate the effect on the output from the FSR. The experiment was repeated for more than one sensor to see whether there were any differences in results city from one to another. The output graphs are shown in Figure 1.5 and 1.6 below.

3.4 Basic Evaluation of sensor behaviour

3.4.1 Sensor response to static loading

To assess the FSR response to static loading, a potential divider circuit was set up across the sensor as shown in figure 3.4.

Figure 3.4 Potential divider circuit.



The sensor was then placed in a test machine (Hounsfield Tensometer) with a specially modified compression platen system, and loaded up to a maximum value of 1100N in 11 increments of 100N. For each increment, the change in the voltage across the sensor was measured using a digital voltmeter. The experiment was repeated to assess whether the voltage readings could be reproduced for further loading/unloading cycles. The value of the resistor connected in the potential divider circuit was also varied to investigate the effect on the output from the FSR. The experiment was repeated for more than one sensor to see whether there were any differences in sensitivity from one to another. Two sample results are shown in figures 3.5 and 3.6 below.

Figure 3.5 Voltage output from the sensors connected in potential divider circuit with a 1.2k ohm resistor, loaded up to 1100N in increments of 100N.

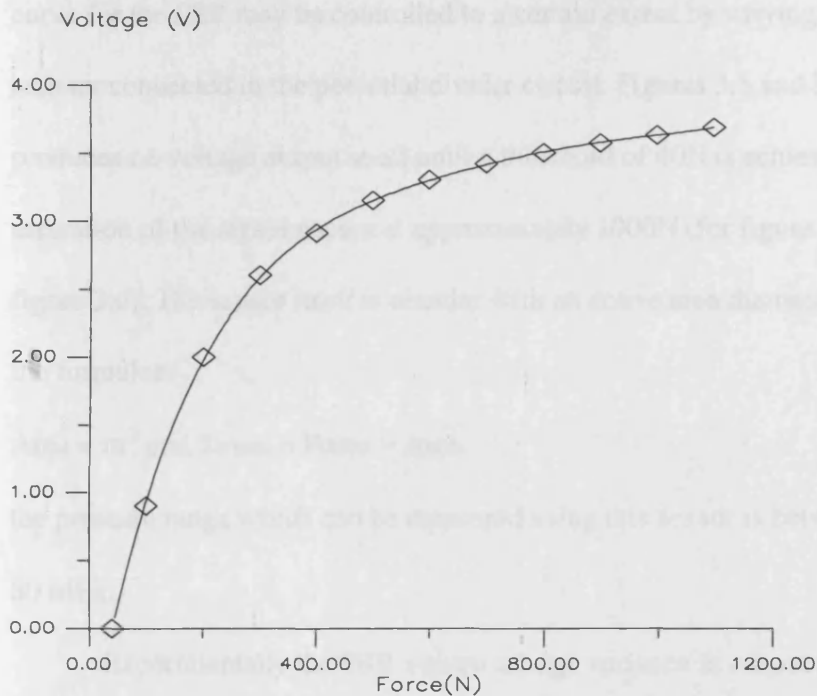
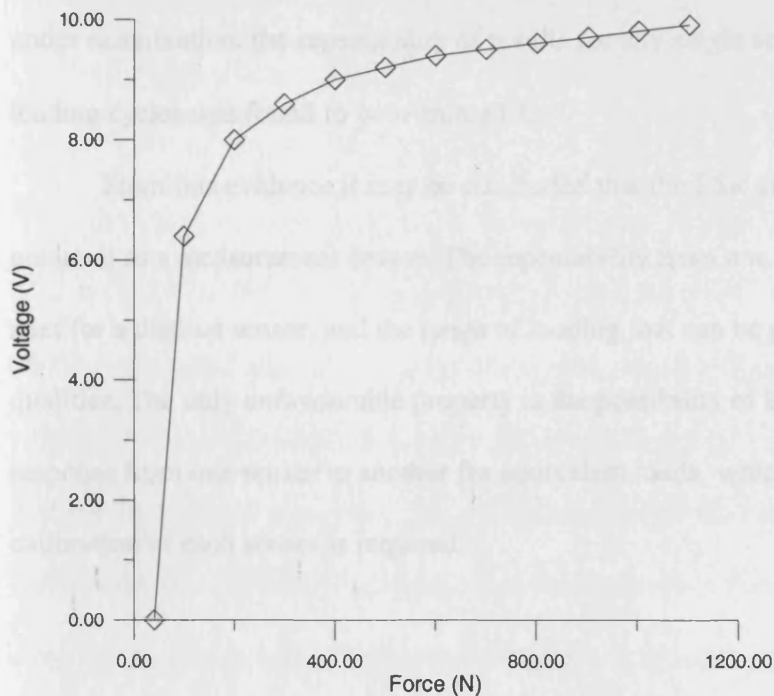


Figure 3.6 Voltage output from the sensors connected in potential divider circuit with a 40k ohm resistor, loaded up to 1100N in increments of 100N.



As can be seen from the results, for the static loading, the steepness of the curve for the FSR may be controlled to a certain extent by varying the value of the resistor connected in the potential divider circuit. Figures 3.5 and 3.6 show the FSR produces no voltage output at all until a threshold of 40N is achieved, and the saturation of the signal occurs at approximately 1000N (for figure 3.5, lower value in figure 3.6). The sensor itself is circular with an active area diameter of 4 mm. Using the formulae:

$$\text{Area} = \pi r^2 \text{ and Stress} = \text{Force} \div \text{Area}$$

the pressure range which can be measured using this sensor is between 6 MPa and 80 MPa.

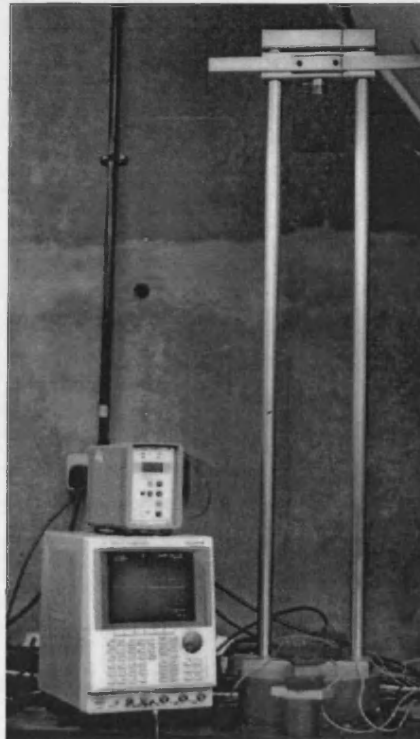
Experimentally the FSR's show a large variance in output for different sensors with the same circuit and loading conditions. The manufacturers' technical specifications gives the repeatability from one sensor to another as $\pm 15\%$. However, under examination, the repeatability of results for any single sensor for subsequent loading cycles was found to be within $\pm 1\%$.

From this evidence it may be concluded that the FSR shows excellent potential as a measurement device. The repeatability from one loading cycle to the next for a distinct sensor, and the range of loading that can be measured are notable qualities. The only unfavourable property is the possibility of large variation in response from one sensor to another for equivalent loads, which suggests individual calibration of each sensor is required.

3.4.2 Sensor response to dynamic loading

A basic drop weight test, as shown in figure 3.7 below, was used to provide the dynamic analysis. A Kistler load cell (washer type 9021A) was placed between the slider and the threaded impactor and tightened so the force cell was slightly pre-loaded. This in turn was connected via an amplifier to the first channel on an oscilloscope. The calibration chart for the load cell is shown in figure 3.8.

Figure 3.7 Basic equipment for dynamic sensor testing.



A potential divider circuit, similar to that shown in figure 3.4 was used with a 1.2k ohm resistor connected in parallel with the sensor. The voltmeter was removed to allow connections to be made to a second channel on the oscilloscope. The sensor was placed on a flat metal base with a 5 mm diameter cylindrical platen completely covering the active area and secured directly beneath the impactor. The metal base

was clamped as securely as possible to avoid vibration. The impactor, which has a mass of 1.3 kg, was dropped from a height of 20 cm. The data recorded on the oscilloscope was then transferred to a file on the computer via an IEEE connection port. The programme 'Grapher for Windows' was used to process the results.

Figure 3.8 Calibration curve for load cell.

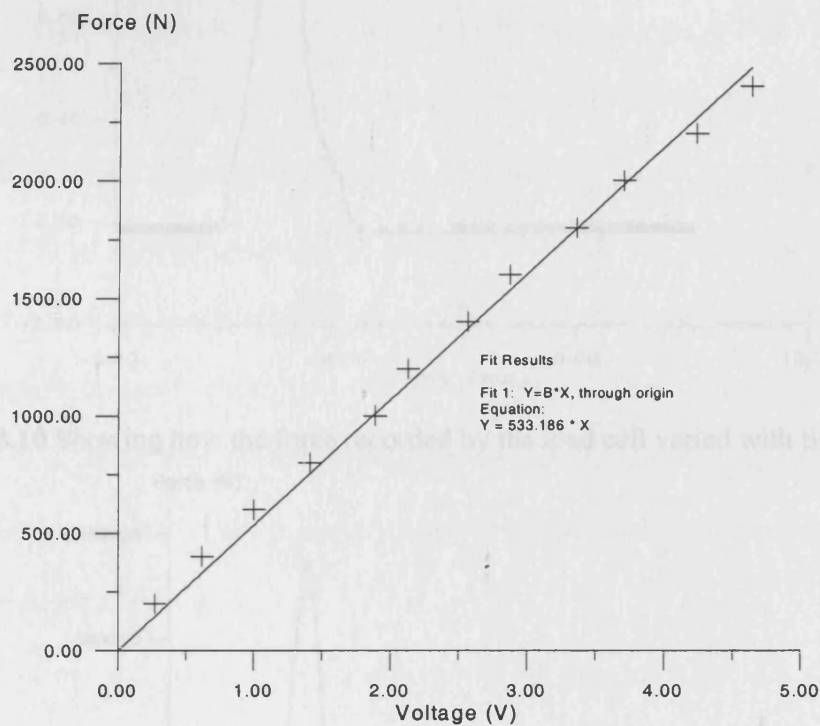


Figure 3.9 Voltage measured across the sensor during impact event.

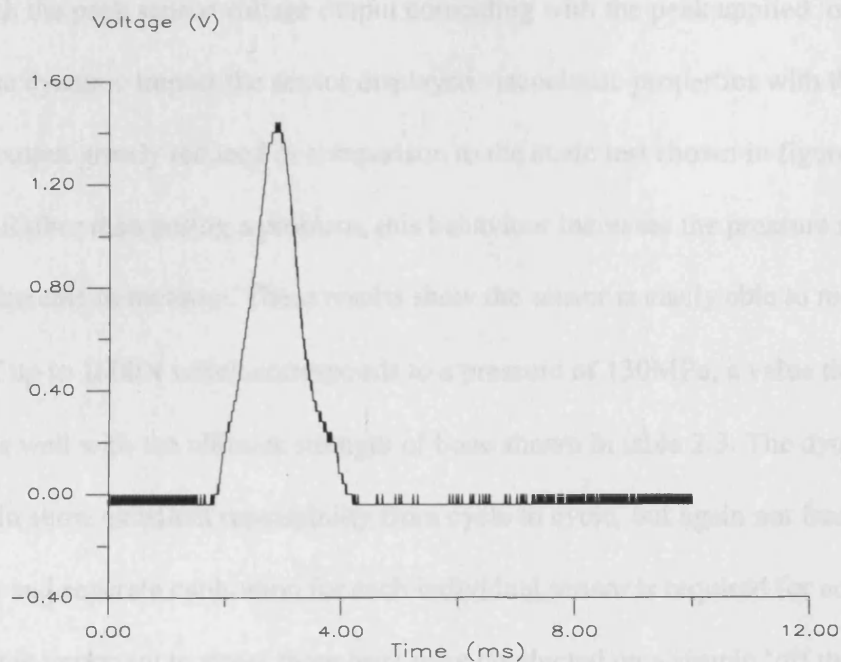
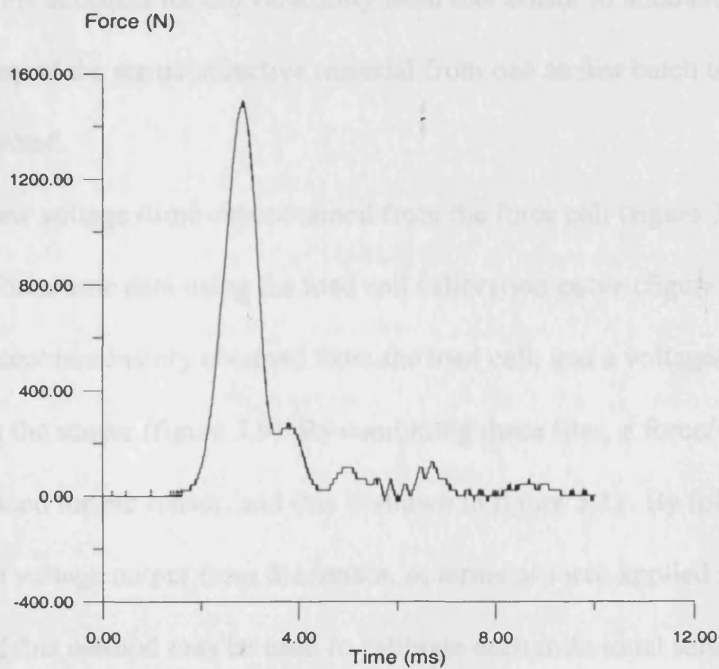


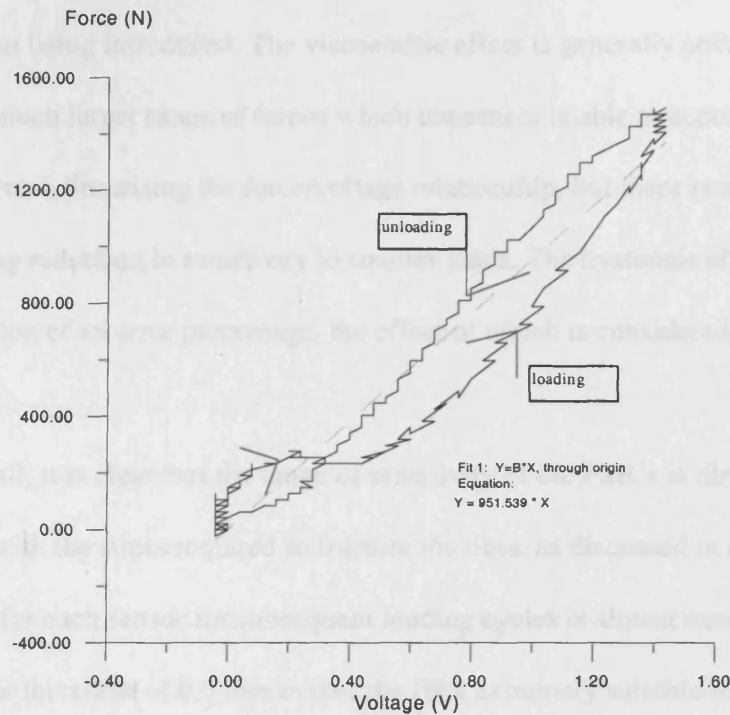
Figure 3.10 Showing how the force recorded by the load cell varied with time.



As can be seen by comparing figures 3.9 and 3.10, there is no delay in reaction time, with the peak sensor voltage output coinciding with the peak applied load. Under the dynamic impact the sensor displayed viscoelastic properties with the voltage output greatly reduced in comparison to the static test shown in figures 3.5 and 3.6. Rather than posing a problem, this behaviour increases the pressure range the sensors are able to measure. These results show the sensor is easily able to record forces of up to 1600N which corresponds to a pressure of 130MPa, a value that compares well with the ultimate strength of bone shown in table 2.3. The dynamic tests again show excellent repeatability from cycle to cycle, but again not from sensor to sensor and separate calibration for each individual sensor is required for accurate results. It is important to stress these tests were conducted on a simple 'off the shelf' component. This accounts for the variability from one sensor to another, as deviation in the chemistry of the semiconductive material from one sensor batch to another would be expected.

The raw voltage /time data obtained from the force cell (figure 3.10) was converted to force/time data using the load cell calibration curve (figure 3.8). This left two files; a force/time history obtained from the load cell, and a voltage/time history obtained from the sensor (figure 3.9). By combining these files, a force/voltage curve could be obtained for the sensor, and this is shown in figure 3.11. By following this procedure, the voltage output from the sensor, in terms of force applied may be calculated and this method may be used to calibrate each individual sensor.

Figure 3.11 Force/voltage output from sensor obtained by combining figures 3.9 and 3.10.



The most important effect observed under dynamic testing is the sensors exhibit a much more linear variation of voltage with pressure at this speed which can clearly be seen in figure 3.11. Further observation of figure 3.11 shows there is a hysteresis effect between the loading and unloading cycle. Taking an average of the loading and unloading curves provides an error percentage of within $\pm 12\%$ from the straight line approximation.

Evidence amassed through testing shows that the dynamic sensor behaviour is significantly more complex than for the static load case. Both viscoelastic and hysteresis effects are induced (both are commonly associated with polymeric

materials, and are possibly characteristic of the polymer coating covering the semiconductive material rather than the active material itself), with the sensor voltage output both reduced and linearised, and a deviation between loading and unloading voltage output being introduced. The viscoelastic effect is generally advantageous, providing a much larger range of forces which the sensor is able to accurately measure and also linearising the force/voltage relationship, but there is an accompanying reduction in sensitivity to smaller loads. The hysteresis effect causes the introduction of an error percentage, the effect of which is considered within section 3.7.

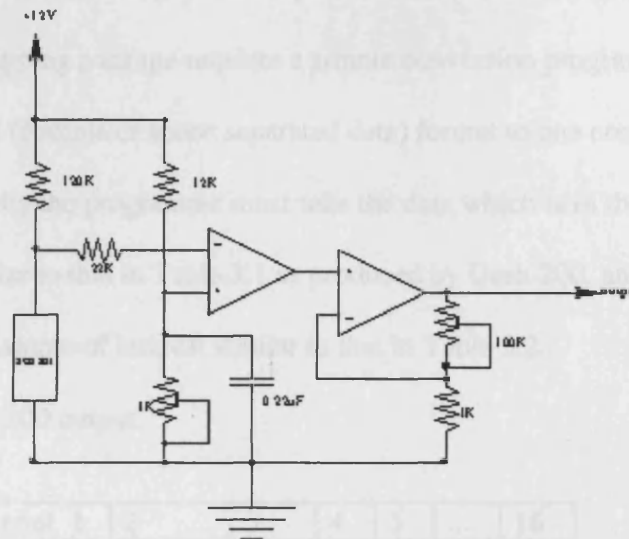
Overall, it is clear that the range of sensitivity of the FSR's is directly comparable with the stress required to fracture the tibia, as discussed in chapter 2. The repeatability for each sensor for subsequent loading cycles is almost exact and the modest sensor thickness of 0.5 mm makes the FSR extremely suitable for measuring loads between contact surfaces.

3.5 Software and hardware used in conjunction with sensors

The next task was to develop the circuitry in which to include the FSR's and software to be used in conjunction with them to allow visualisation of the pressure distributions.

The viscoelastic effect, although useful in increasing the peak pressure measurable by the sensors, makes smaller pressures harder to distinguish. To deal with this, an amplifier circuit is required to allow the output voltage from the sensors to be adjusted. A diagram of the circuit to which each individual sensor is attached is shown in figure 3.12. Importantly it contains two operational amplifiers. The input to the first is simply the output from the potential divider circuit. The value of the resistors are specifically chosen to allow maximum sensitivity to values expected to cause fracture (approximately 130 MPa). The output from this amplifier then goes into the second op-amp which effectively produces a gain of 1 to 100. The output is then connected to a channel on an Analogue to Digital Converter which samples the signal. The resistor and capacitor in parallel simply act as a filter to reduce the noise in the circuit.

Figure 3.12 Circuitry incorporating sensors. Developed by David Dryden, a technician based within the University of Leicester Electrical Engineering department.



Of critical importance is the speed of sampling. If the sampling is not sufficiently fast, the characteristics of the impact, particularly the peak load could be missed. This problem is clearly evident on the Tek-Scan plots in figure 3.2. To deal with the required speed a PC226 Analogue to Digital converter with 16 channels and a maximum sample rate of 750 kHz was connected to the sensors. The board has an extremely high sampling rate, but is unable to sample all channels simultaneously, so channel 16 is dealt with fifteen time units after channel 1. The A/D card (an Amplicon PC226) is controlled by the programme DASH200 which allows the sample rate and duration to be monitored. The ASCII file which is produced by DASH200 is then converted to a format compatible with the three dimensional mapping package Surfer for Windows by a programme which was subsequently written. The programme (written in C++ language) may be found in Appendix B2, with a detailed description of the important commands and how they work.

3.6 Development of visualisation software used in conjunction with FSR's.

To allow visualisation of the output from the sensors within a three dimensional mapping package requires a simple conversion programme, to turn the data from ASCII (comma or space separated data) format to one compatible with Surfer. Essentially the programme must take the data which is in the format of one large array similar to that in Table 3.1 as produced by Dash 200, and write a file for any individual sample of interest similar to that in Table 3.2.

Table 3.1 Dash 200 output.

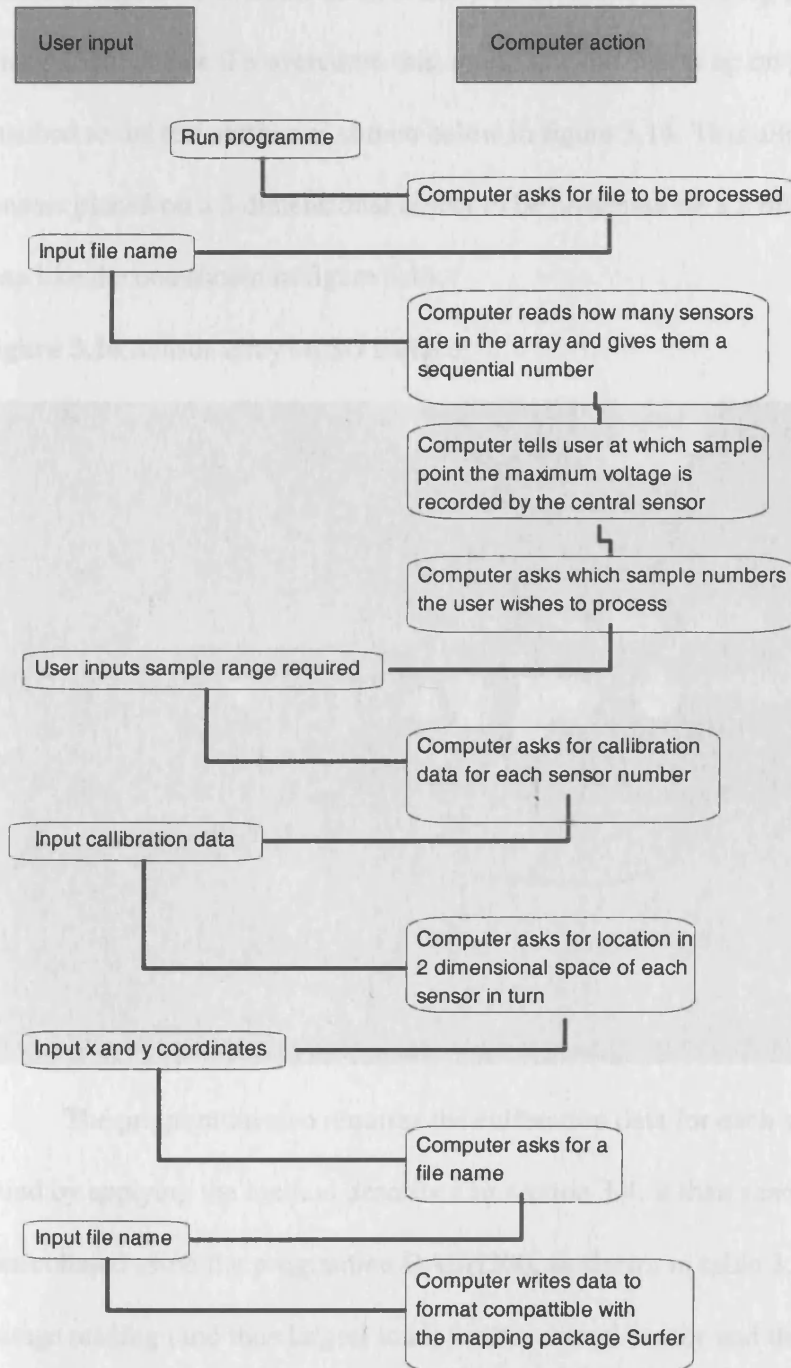
	channel 1	2	3	4	5	...	16
sample 1	x volts	y volts	etc.				
2	z volts						
3	etc.						
4							
...							

Table 3.2 C++ programme output.

	x co-ord	y co-ord	force (N)
channel 1	x meters	y meters	z Newtons
2	etc.		
3			
...			
16			

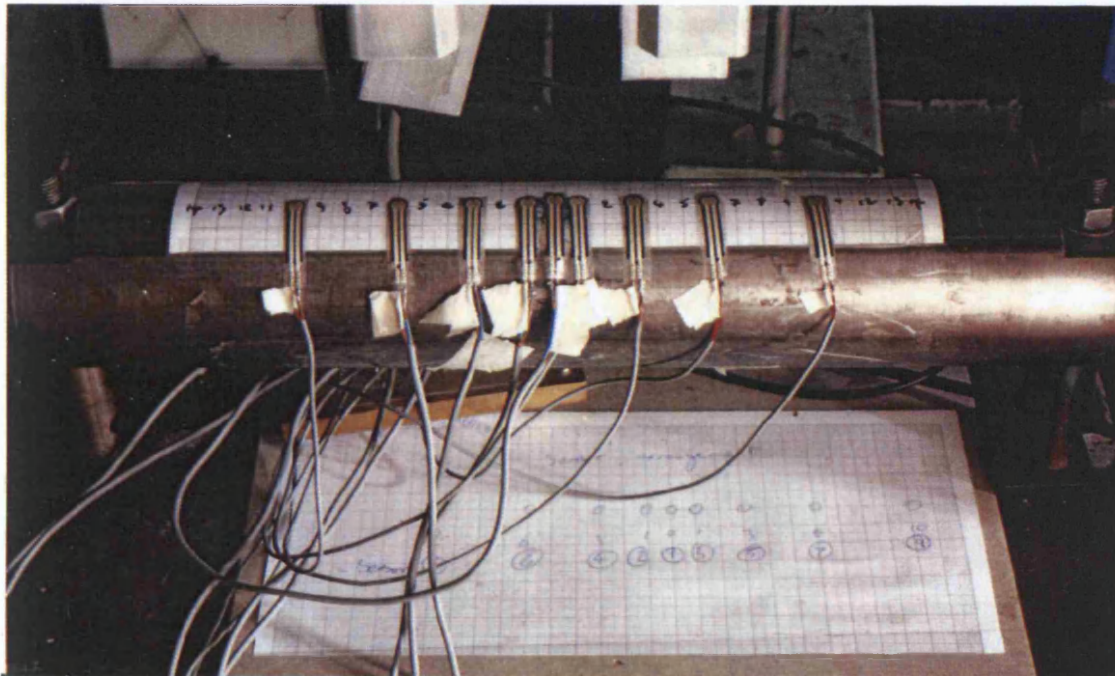
To achieve this, a certain amount of extra information is required and an interactive front end to the programme poses a number of questions to the user to acquire this data. The sequence of questions is shown in figure 3.13 below.

Figure 3.13 Flow chart showing operational procedure for C++ programme.



As can be seen in figure 3.13, the programme requires that the location of each sensor is stipulated in terms of its x and y co-ordinate, but the leg is a three dimensional object. To overcome this, a grid may be drawn up on graph paper and attached to the test surface as shown below in figure 3.14. This allows results from sensors placed on a 3 dimensional object to be presented on a 2 dimensional contour map like the one shown in figure 3.14.

Figure 3.14 Sensor array on 3D surface

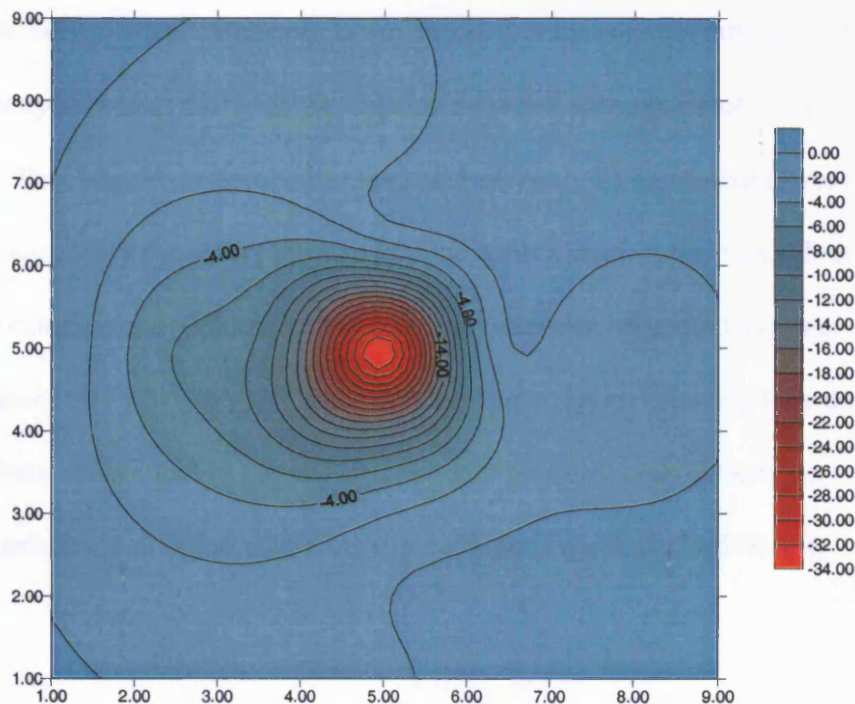


The programme also requires the calibration data for each sensor which is found by applying the method described in section 3.4. It then searches the array of data collated using the programme DASH200, as shown in table 3.1 for the largest voltage reading (and thus largest load) for the central sensor and the sample at which this occurs is then told to the user. The user is then asked for which samples he

wishes to observe the pressure distribution. The programme then writes the pressure contour files for each sample as shown in Table 3.2.

From this, the mapping package Surfer for Windows may be used to visualise the pressure distribution at any sample. An example of a typical output from the mapping package Surfer, for the peak response of the sensor array is shown below in figure 3.15. A bezier function is used to interpolate between the 13 known values. This particular function was chosen as it produces symmetrical circular contours around the point of impact which is the geometry of pressure anticipated. The actual sensor array used to obtain this contour map is shown in figure 3.18. The 'diamond' arrangement of the sensors tended to cause all other smoothing functions to be unrealistically angular in appearance.

Figure 3.15 Typical Surfer map representing the stress over a 80mm square region for an array of sensors. The x and y co-ordinates are given in cm, the contours are given in MPa the values of which are negative representing compressive stress.



3.7 Accuracy validation tests for sensors under dynamic loading.

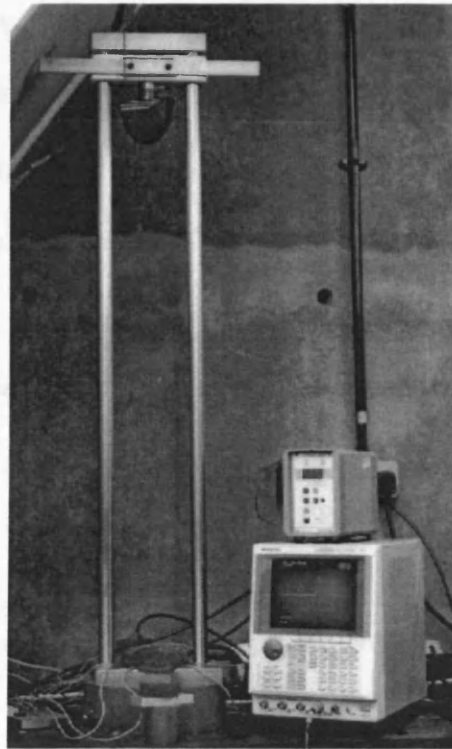
As previously discussed, it is important that it is confirmed that the sensors and the calibration technique explained in section 3.4.2 is shown to be accurate enough to allow confidence in the experimental results. This has been achieved by comparing the combined sum of impulses for the sensor array to the impulse recorded by the load cell at the point of impact. A sensor array identical to that shown in figure 3.18 was set up, and a foam material was placed on top of the array and impacted using the drop weight tower shown in figure 3.16. A trace similar to those shown in figure 3.1 was recorded by the load cell, and a set of corresponding curves were obtained for the thirteen sensors. Equilibrium dictates that the impulse applied at the point of impact will equal the total impulse the material imparts to the sensor array. Validation tests were carried out for a number of test materials (these materials are introduced in detail within chapter 4) which would typically be expected to be within a commercially available shin pad. It was found that the sum of impulses recorded by the sensors was within $\pm 20\%$ of the impulse recorded at the point of impact by the load cell. This large error percentage is almost certainly a cumulative effect associated with the inaccuracy caused by the straight line approximation for the calibration of each individual sensor. Clearly the sensor array may not be treated as a high accuracy measurement tool when they are grouped to create an array, however they do provide a useful inexpensive tool in the understanding of pressure distributions between contact surfaces, a situation where instrumentation is particularly difficult.

3.8 Basic Test Method.

Following on from the development and satisfactory validation of the pressure measurement system, the rest of the apparatus which incorporates more established instrumentation may be defined. To provide the impact there are two obviously discernible avenues of approach; discharging a projectile at the pad with a high initial velocity, or dropping an impactor from a suitable height onto the test material using gravity to accelerate the impactor. Both methods have their merits, for example if a device similar to a cricket bowling machine is used the ball may be fired at up to 30 ms^{-1} which is well in excess of that required to fracture the tibia (as discussed in section 2.9). Contrastingly, to attain the minimum velocity to fracture the tibia of 12 ms^{-1} the impactor would have to be dropped from 7.5 meters if gravity alone is used as the accelerator. However, precise control of the impact location for a projectile is difficult. This is particularly disadvantageous with respect to locating the sensor array beneath the test material. Although it is difficult to attain the impact velocity required, the use of a drop weight tower has been decided as the optimum set-up. The tower option allows exact control of the point of impact and also permits the impactor to be instrumented with a load cell which has already been shown to display the load time history of the impact extremely well. Significantly it has been proven in section 2.11 that the measurement of the load time history is the most crucial aspect of all impact characteristics.

Initial experimentation has been carried out using the equipment shown below in figure 3.16.

Figure 3.16 Drop weight test apparatus.

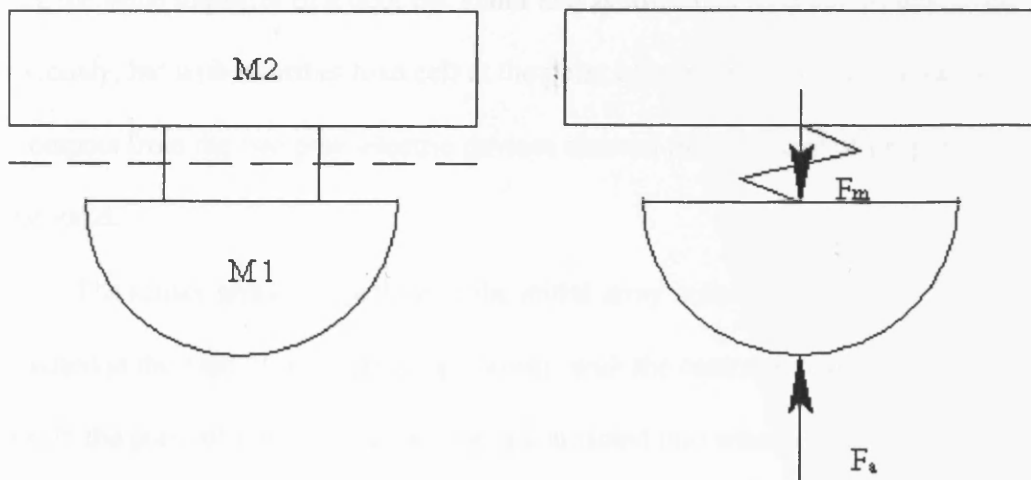


The equipment consists of a one meter drop weight tower, the base of which is clamped to minimise vibration. To create a realistic striking geometry, the impactor is a boot tip filled with resin which screws into the slider. The resin used is Ebalta tooling resin (type SG140/PUR11) which, once set, forms an extremely solid material. The reason for the choice of this particular resin which causes the impactor to be very stiff in direct comparison with a human foot, is discussed later within this section. A Kistler load cell (type 9021A) is sandwiched between the boot tip and the slider, and connected via an amplifier (Kistler type 5011) to an oscilloscope, allowing the force at the boot tip during the impact to be calculated. The combined mass of the boot, slider and load cell is 1.35 kg this compares well to the effective mass of the lower leg when occupied in a kicking action calculated in section 2.9, using three

separate reports on the biomechanics of kicking. The height of the tower limits the maximum impact velocity to 4 ms^{-1} which is significantly lower than the minimum velocity expected to fracture the tibia of 12 ms^{-1} , again calculated in section 2.9. The low impact velocity achievable using the tower requires significant improvement. This is achieved through computer simulation of the impact event and is addressed in detail in chapter 5.

As the load cell is located between two masses, the reading from the cell is not the true load at the point of impact. Consider the situation shown in figure 3.17 below.

Figure 3.17 Left, diagram of load cell sandwiched between two masses. Right, system analogised as two separate masses. F_a is the true impulsive load whereas F_m is the load measured by the force cell.



If we assume the impulse and the peak load measured is proportional to that occurring at the boot tip we obtain the expressions

$$C \int F_a dt = \int F_m dt \quad \text{equation 3.1}$$

$$CF_a^{\max} = CF_m^{\max} \quad \text{equation 3.2}$$

where C is a constant F_a is the actual load, F_m is the measured load, F_a^{\max} is the true peak impact load and F_m^{\max} is the maximum measured load. From basic mechanics force equals the product of mass times acceleration.

$$F_a = (M_1 + M_2) \frac{dv}{dt} \quad \text{equation 3.3}$$

$$F_a - F_m = M_1 \frac{dv}{dt} \quad \text{equation 3.4}$$

Where M_1 is the mass beneath the measured load and M_2 is the mass above, equations 3.2, 3.3 and 3.4 give.

$$C = \frac{M_1 + M_2}{M_2} \quad \text{equation 3.5}$$

This result has been proven experimentally by conducting a drop weight test using the same impactor of a boot tip, slider and sandwiched load cell as described previously, but with a further load cell at the point of impact. A direct comparison of the outputs from the two piezoelectric devices showed this constant of proportionality to be valid.

The sensor array (the pattern of the initial array is shown in figure 3.18 below) is located at the base of the drop weight tower, with the central sensor located directly beneath the point of impact. Each sensor is connected into what is essentially a potential divider circuit shown in figure 3.12. This initial array geometry has been chosen to acquire increased readings in the region adjacent to the initial point of contact of the impactor on the pad material, as it is logical to expect the pressure to vary most in this zone.

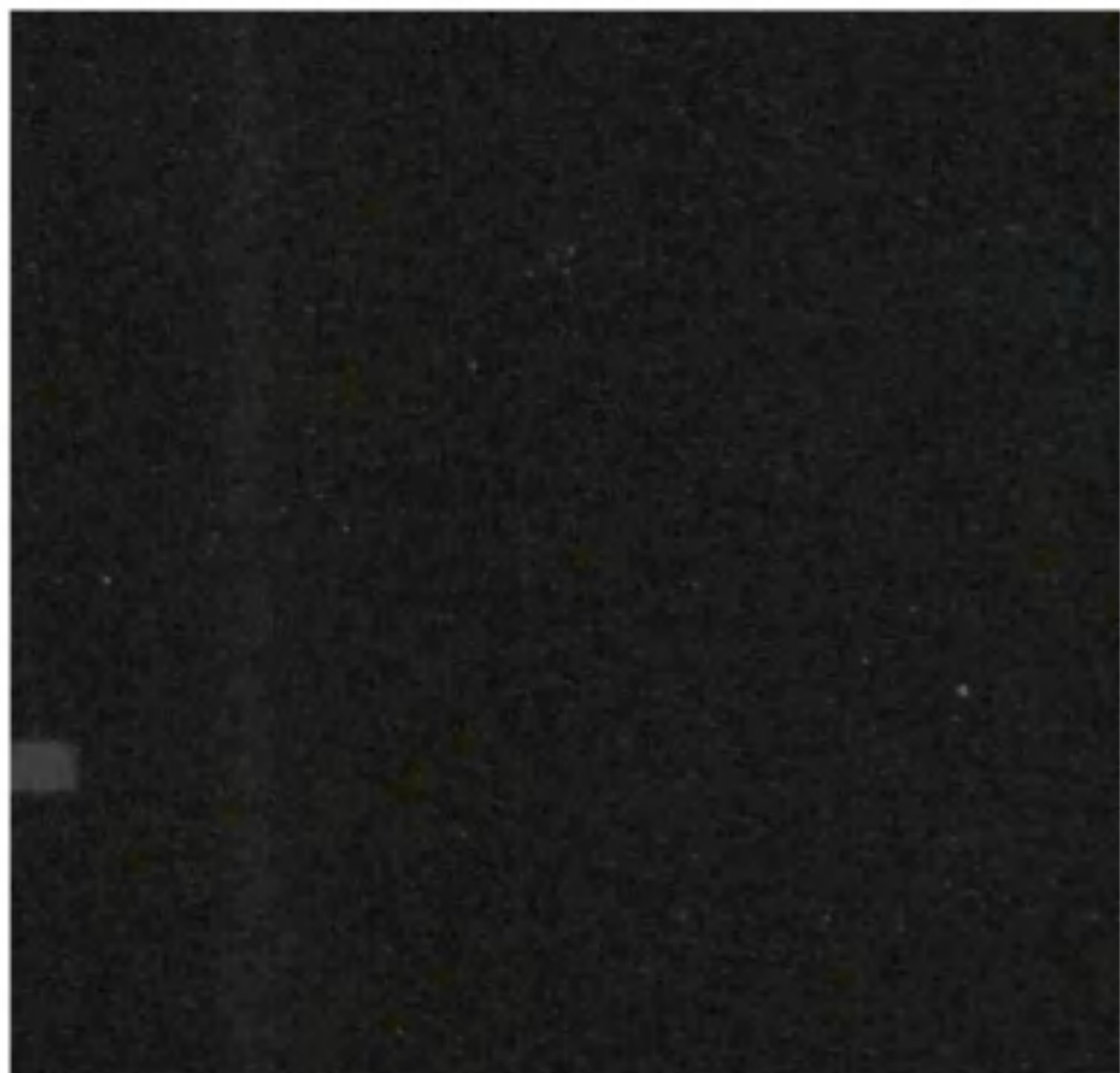
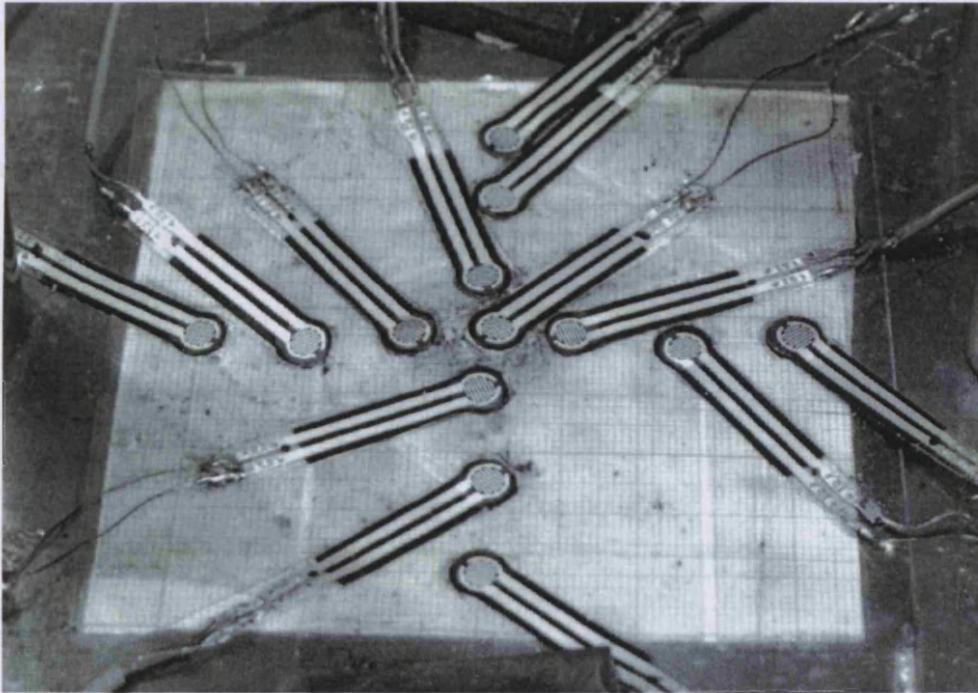


Figure 3.18 Sensor array.

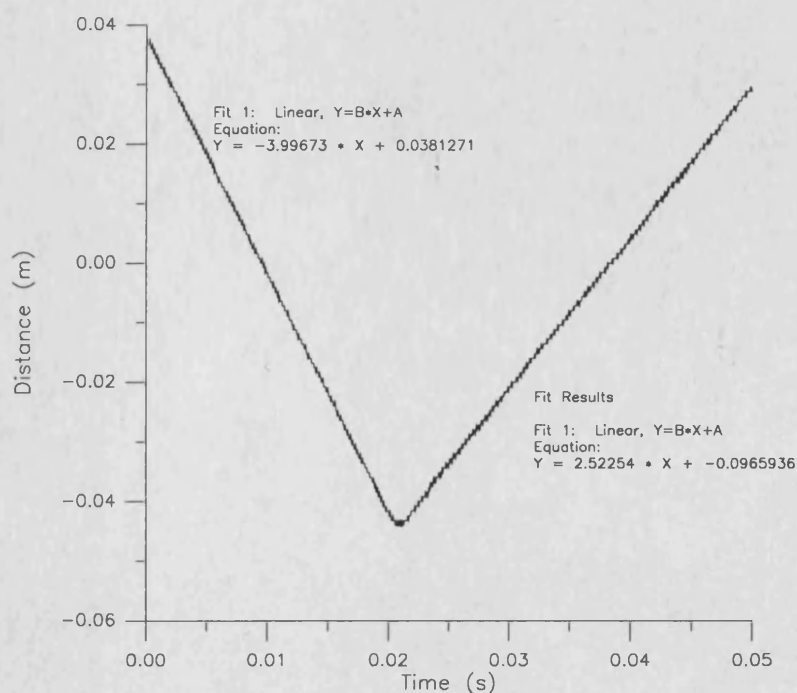


As pressure is applied normal to the sensor, the device resistance decreases and thus the voltage applied across the sensor is varied. The voltage is recorded using an analogue to digital converter (an Amplicon PC226). It is controlled by the programme DASH200 which allows the sample rate and duration to be monitored and adjusted. The data is converted from a voltage/time history to a pressure/time history using previously obtained calibration data for each sensor. Essentially this experimental set up allows us to monitor how the test materials affect the impulse at the point of impact, and also how the material combination transmits and spreads the load over the underlying surface.

Located adjacent to the drop weight tower is a laser aimed at the horizontal bar attached to the slider as shown in figure 3.16 above. The purpose of the inclusion of this device is firstly to allow the velocity of the impactor to be measured to ensure

all impact velocities are comparable, and secondly to allow the displacement of the test materials to be calculated. The laser accurately measures distances by means of triangulation, a method where the laser beam is aimed at a target with a sensor measuring the angle at which the beam is reflected. The laser gives an output of 1 Volt for every 0.1 metre in distance that the target is removed from the point of laser beam emission. By connecting the laser to a second channel on the oscilloscope the displacement/time history (a typical output is shown below in figure 3.19) of the impact may be recorded. From this the terminal velocity of the boot prior to impact may be calculated.

Figure 3.19 Output from laser.

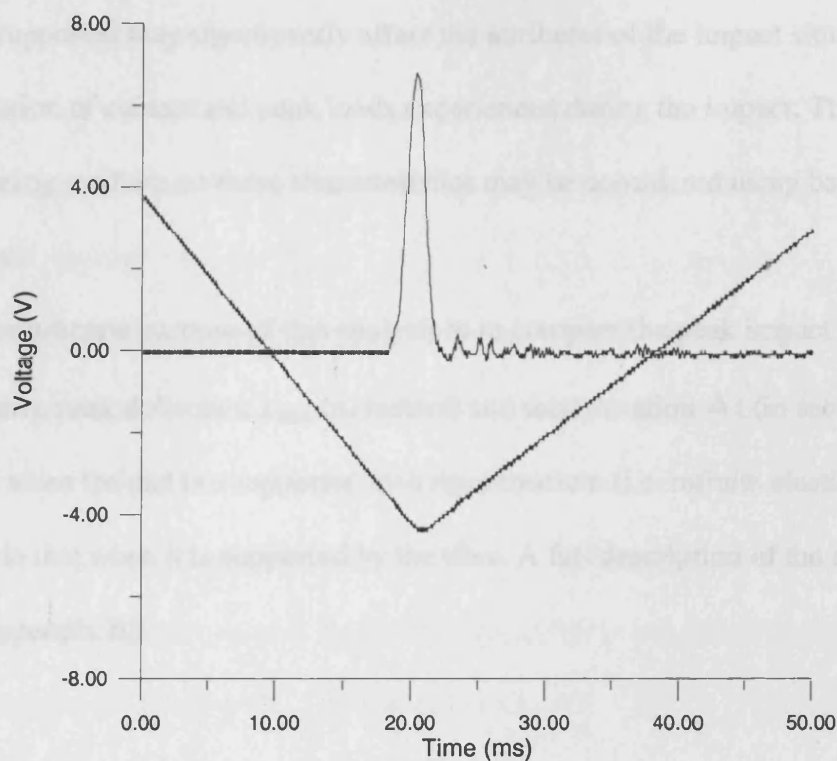


By measuring the slope of displacement/time curve, impactor velocity may be measured. For the impact shown in figure 3.19 above, the impact velocity is 4.0 ms^{-1} and the rebound velocity is 2.52 ms^{-1} . This also allows the total energy absorbed by the pad materials and the underlying surface to be calculated.

More importantly, the displacement/time history may be used in conjunction with the force/time history to calculate how much a test material deforms under impact.

Consider the oscilloscope output, as shown below in figure 3.20. The output is the raw data obtained directly from the oscilloscope, with no calibration carried out to turn the voltage into either a force or displacement for the load cell and laser respectively. The data has been presented in this way specifically to allow them to be presented graphically on the same scale.

Figure 3.20 Output from laser and load cell plotted on same axes.



It is reasonable to assume that the force recorded by the load cell is zero at the first instance of contact, and that the force recorded is a peak at maximum displacement. By comparison to the output from the laser between the point in time when contact is first made and when the peak load occurs, the distance the test material displaces under the impact may be measured. Although this quantity of lateral displacement may not be particularly useful in relation to the causation of injury discussed in chapter 2, it is fundamental in the application of a theoretical behavioural model which is discussed in chapter 6.

Used as a whole, this apparatus allows the response of a layered material, typical of a shin guard, to be examined in an idealised and controlled experiment which does not, however, include the dynamic response of the leg itself. This

provides a potential problem, as the surface on which the layered material (or shin guard) is supported may significantly affect the attributes of the impact situation; such as the duration of contact and peak loads experienced during the impact. The effect of the supporting medium on these characteristics may be considered using basic mechanics.

The ultimate purpose of this analysis is to compare the peak impact load P_{\max} (in Newtons), peak deflection x_{\max} (in meters) and total duration Δt (in seconds) for an impact when the pad is supported by a rigid medium (i.e. infinite elastic modulus) to that when it is supported by the tibia. A full description of the analysis is given in appendix B3.

B. The geometry of the impactor

The key results are as follows:

The ratio of the peak force P_{\max} to the peak force P_{\max}^{rigid} for a pad supported by a rigid medium is given by:

$$\frac{P_{\max}}{P_{\max}^{\text{rigid}}} = \sqrt{\frac{1}{1 + 2\lambda}}$$

Where P_{\max}^{rigid} is the peak force for a pad supported by a rigid medium.

and λ is defined as:

The ratio of the impactor's mass m to the mass of the pad M is given by:

supported by a rigid medium is given by:

$$\lambda = \frac{m}{M}$$

Key assumptions within analysis:

- 1) The tibia behaves as a simply supported beam.
- 2) The impactor is infinitely stiff and does not deform during impact.
- 3) The intensity of the reaction of the substrate is directly proportional to the deflection of the pad.
- 4) The mass of the pad is negligible in comparison with the mass of the impactor.
- 5) The beam deforms as a result of the point load at the site of impact; in essence the spreading of the load by the pad is neglected to allow simple beam bending theory to be applied.
- 6) The impact velocity is equal to the rebound velocity (purely elastic deformation).
- 7) The geometry of the impulse is sinusoidal in nature.

The key results are as follows.

The ratio of the peak impact load for a pad supported by the tibia to that supported by a rigid medium is given by:

$$\frac{P_{\max}}{P_{\max E \rightarrow \infty}} = \sqrt{\frac{1}{1+X}} \quad \text{equation 3.6}$$

Where $P_{\max E \rightarrow \infty}$ is the peak load in Newtons when the beam is made from an infinitely stiff material

The ratio of the impact duration for a pad supported by the tibia to that supported by a rigid medium is given by:

$$\frac{\Delta t}{\Delta t_{E \rightarrow \infty}} = \sqrt{1+X} \quad \text{equation 3.7}$$

Where $\Delta t_{E \rightarrow \infty}$ is the impact duration in seconds when the beam is made from an infinitely stiff material.

The ratio of the maximum total deflection for a system with a pad supported by the tibia to a pad supported by a rigid medium is given by:

$$\frac{y_{\max}}{y_{\max E \rightarrow \infty}} = \sqrt{1 + X} \quad \text{equation 3.8}$$

Where $y_{\max E \rightarrow \infty}$ is the peak deflection in meters when the beam is made from an infinitely stiff material

$$X = \left(\frac{2L^3kab}{48(EI)_L} \right)$$

where:

L is the length of the tibia in meters

k is the modulus of the foundation (units Nm^{-3}) which is given by the elastic modulus of the foam material in Newtons per meter squared, divided by the thickness of the foam material in meters.

2a is the length of the pad outer shell material in meters.

b is the width of the pad outer shell material in meters.

$(EI)_L$ is the minimum value for the modulus of elasticity for the supporting medium in Newtons per meter squared, multiplied by the minimum moment of area in meters to the fourth power over the length of the beam.

Substituting typical values for the tibia into X

L (length of tibia)= 0.45 m

E (elastic modulus of tibia)= $15 \times 10^9 \text{ Nm}^{-2}$

I (Minimum second moment of area for tibia given in Appendix A1) = $4 \times 10^{-8} \text{ m}^4$

we obtain:

$$X = (31.6 \times 10^{-6})kab$$

For the elastomeric foams experimented upon within this thesis k typically ranges from 1×10^8 to $1 \times 10^9 \text{ Nm}^{-3}$. Assuming a pad length ($2a$) of 0.2 m and pad width (b) of 0.1 m values typical of a standard sized shin pad, X corresponds to a value ranging between 63 and 630. Referring to the plots shown below in figure 3.21, evidently there is a considerable difference in the peak load P_{\max} , the duration of the impact Δt , and the total peak deflection x_{\max} for a pad supported on an infinitely stiff medium ($(EI)_L$ is infinite and therefore $X=0$) to that supported by the tibia (X is in the range 63 to 630 dependant on the materials that make up the pad). To address this requires either the supporting medium to accurately simulate the behaviour of the tibia, or a correctional factor to be introduced into the experimental results if the stiffness of the medium is significantly different to that of the tibia.

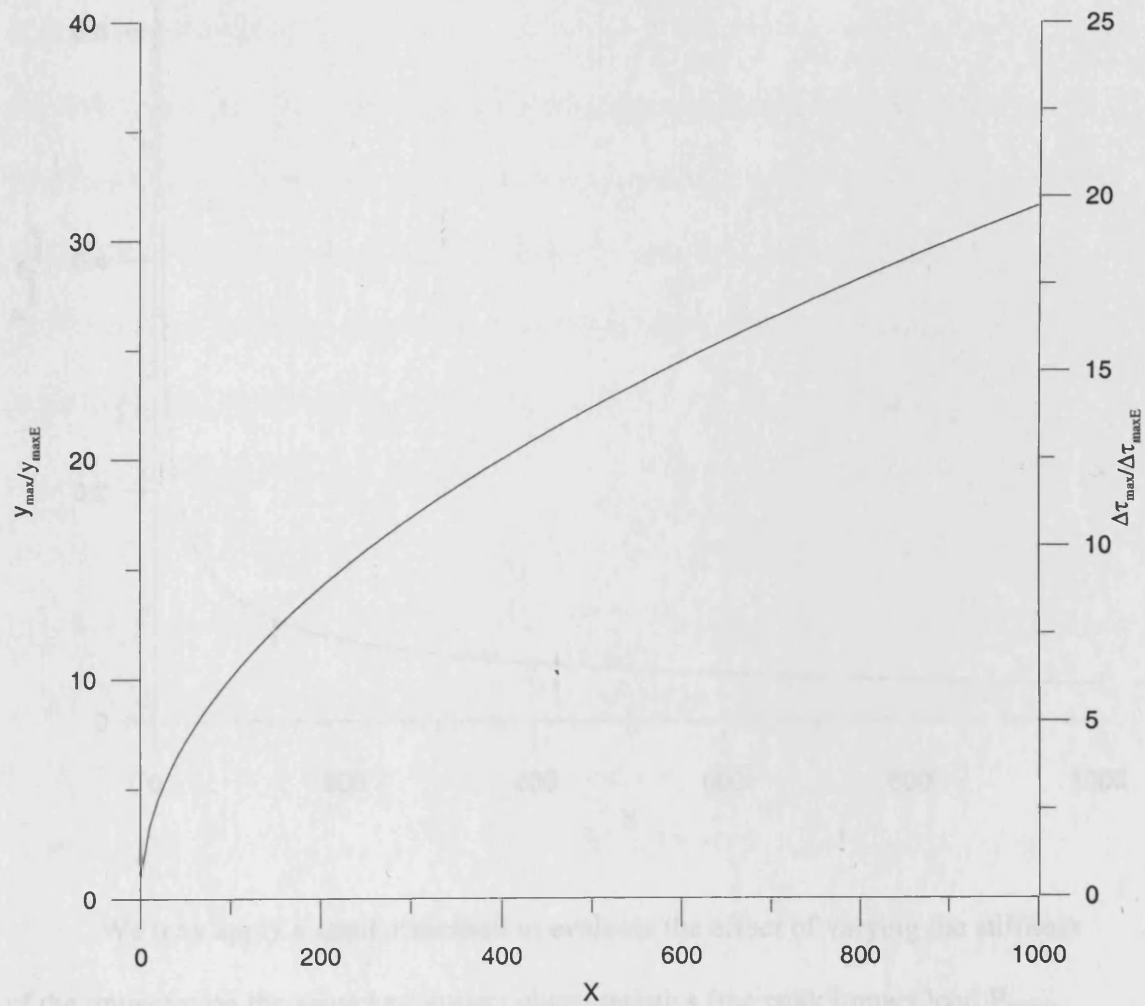
For the following reasons a stiff supporting medium has been chosen for initial experimentation. These are:

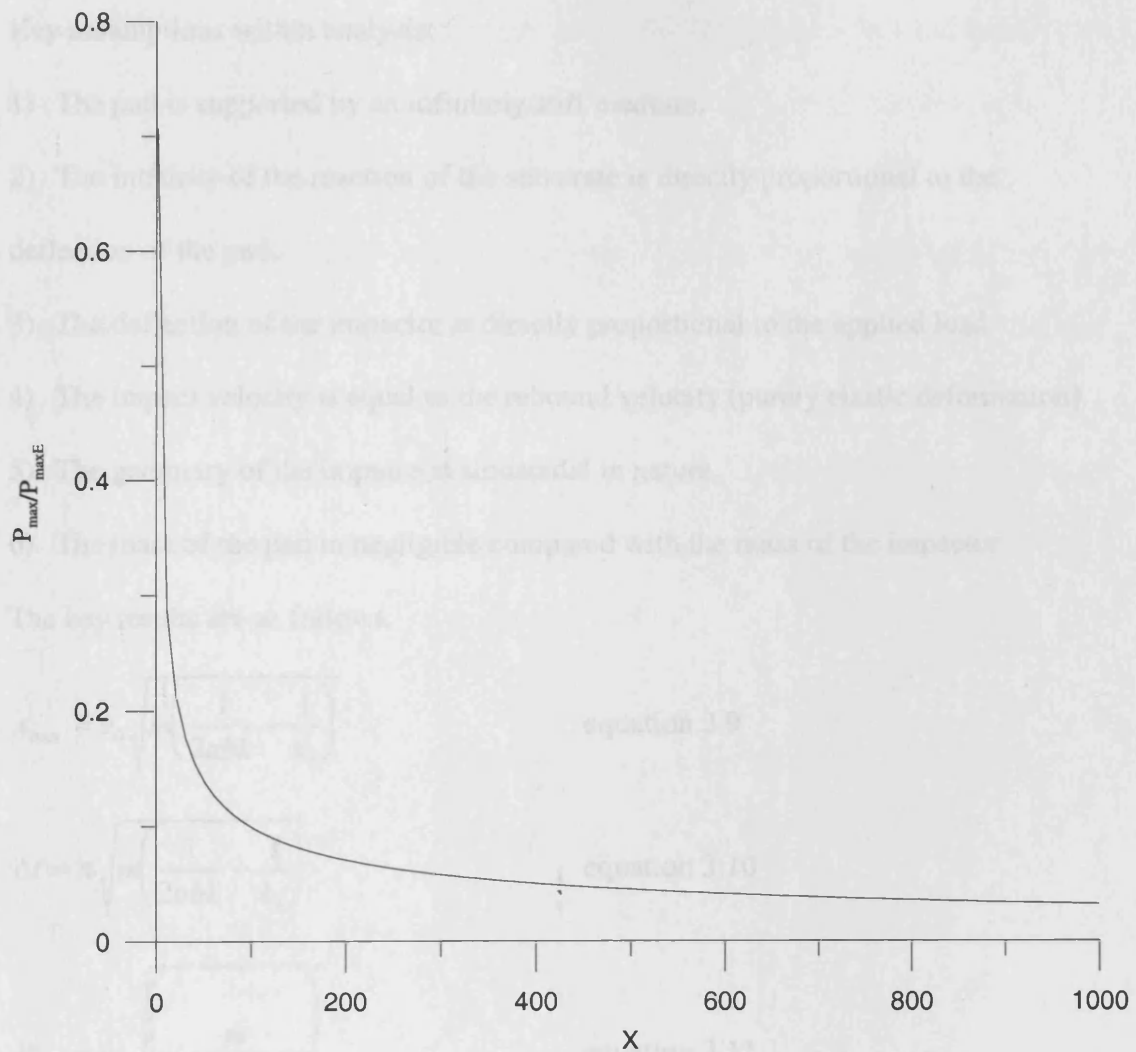
- 1) To create a synthetic leg that behaves as a human tibia is an incredibly difficult task. The complexity of long bone behaviour has been highlighted within chapter 2, and an attempt to recreate these characteristics would be a severe drain on resources in terms of both finance and time.
- 2) Once an accurate synthetic leg is created, early testing would be likely to cause damage to the leg and subsequent results would be affected.

3) Most importantly, the apparatus designed within this chapter relies on a 1 meter drop weight tower to provide the impact. This produces impact velocities much reduced from those that occur within a football match (typical values given in section 2.9). To provide results at velocities unattainable within the laboratory, it is envisaged that a large volume of results will be generated through computer simulation. It is much easier to model a rigid supporting medium within a FEA simulation (dealt with in chapter 5) than it is to include an inelastic (in the case of the tibia at the onset of yield) deformable solid.

The work in this thesis therefore concentrates on the performance of the pad materials omitting the effect of tibial stiffness. A model which describes the behaviour for an infinitely stiff impactor, impacting a pad supported by an infinitely stiff medium is therefore developed. The factor X is re-introduced within chapter 6 in an attempt to adapt the model to be specific to an impact on a beam with material properties representative of the tibia.

Figure 3.21 Graphs showing how the value of X effects the characteristics of the impact.





We may apply a similar method to evaluate the effect of varying the stiffness of the impactor on the same key impact characteristics (the peak impact load P_{\max} , peak deflection x_{\max} and total duration Δt). The analysis is detailed in full in appendix B4.

Key assumptions within analysis:

- 1) The pad is supported by an infinitely stiff medium.
- 2) The intensity of the reaction of the substrate is directly proportional to the deflection of the pad.
- 3) The deflection of the impactor is directly proportional to the applied load.
- 4) The impact velocity is equal to the rebound velocity (purely elastic deformation).
- 5) The geometry of the impulse is sinusoidal in nature.
- 6) The mass of the pad is negligible compared with the mass of the impactor.

The key results are as follows.

$$x_{\max} = v_0 \sqrt{m \left(\frac{1}{2abk} + \frac{1}{k_1} \right)} \quad \text{equation 3.9}$$

$$\Delta t = \pi \sqrt{m \left(\frac{1}{2abk} + \frac{1}{k_1} \right)} \quad \text{equation 3.10}$$

$$P_{\max} = v_0 \sqrt{\frac{m}{\frac{1}{2abk} + \frac{1}{k_1}}} \quad \text{equation 3.11}$$

where:

m is the total mass of the impactor in kilograms.

v_0 is the terminal impactor velocity in meters per second.

k_1 is the constant of proportionality (assuming a linear relationship) between load and deflection for the impactor in Newtons per meter.

a, b and k are as defined in the preceding analysis.

Clearly for an infinitely stiff impactor ($k_1 \rightarrow \text{infinity}$), there is no effect on the key results. However as the stiffness of the impacting body is reduced, there is an increasing effect on the significant characteristics. For a finite value of k_1 , P_{\max} (equation 3.11) is clearly reduced, whereas both the duration of the impact Δt and the total deflection y_{\max} of the impactor and pad material is increased (equations 3.10 and 3.9 respectively). Again in anticipation of creating a computer simulation, the impactor, like the supporting medium has been made as stiff as possible, as discussed previously within this section to allow an uncomplicated analysis.

3.9 Conclusions

Previous work discussed in section 2.10 focused on the impulsive loading using imitation legs mounted on load cells which gave no information on the locality of the impact induced stresses on the leg. This has been shown to be of some importance within chapter 2, where impact has been shown to induce high loading at the extremities of the pad (for a pad of high bending stiffness) which may risk ligamentous damage. The work in this section has concluded the use of piezoresistive sensors offers the best solution to the problem of monitoring the locality of the impact. Used in tandem with an A/D board, 16 sensors may be located at any stipulated position between pad and leg. Clearly the sensors may not be treated as a high accuracy device (results in section 3.7 suggest the total impulse measured by the array of sensors is within $\pm 20\%$ of the actual impulse), but they do provide a useful inexpensive tool in the understanding of pressure distributions between contact surfaces.

The sensors exhibit good output duplication from one loading cycle to the next, although the lack of repeatability for different sensors requires individual calibration. A sensor array sandwiched between the test material and a synthetic leg therefore allows the influence the test material has on the impact to be monitored in terms of both magnitude and locality.

The rest of the equipment chosen is standard and needs no comprehensive evaluation. To allow accurate control of the point of impact, a drop weight tower has been decided upon as the means to produce the impact. It also has the advantage that a load cell may be located within the impactor to allow the impulse at the point of

impact to be accurately measured. To simulate a kick similar to that which occurs in a football game, the impactor is a resin filled boot tip of comparable mass to that experimentally measured by literature that assessed the biomechanics of kicking discussed in section 2.9.

A basic analysis on the behaviour of an idealised tibia with covering pad under impact loading has concluded that the stiffness of the aforementioned synthetic leg supporting the pad may significantly affect the properties that are being experimentally measured. To allow comparable results to be generated through FEA (dealt with in chapter 5), an unrealistically stiff medium is used to support the pad. However a factor is introduced within chapter 6 to adapt the results to be specific to an impact on a beam with material properties representative of the tibia. The stiffness of the impactor has also been shown to have a significant effect on results. To again simplify FEA simulation the boot tip has also been made as stiff as possible.

The apparatus that has been developed allows the response of a layered material to be examined in an idealised and controlled experiment, which should enable the behaviour of various materials and shin pads to be evaluated under conditions not too dissimilar to those which occur in the game of soccer. The key attributes with respect to causing injury to the lower leg may be measured, and an understanding of material properties desirable to minimise the risk of injury may therefore be affected.

Chapter 4

Materials testing results.

4.0 Introduction.

Having completed the development of the equipment required to analyse impact in the game of soccer, an initial assessment of materials, typical of those found within shin pads, may now be made. This section aims to experimentally show that the hypothesised behaviour (first discussed in section 3.2) of a reduction of the impulsive peak load and peak stress beneath the test materials occur as a result of spreading the impact over time and dispersing the pressure over area respectively. Intuitively, the first needs a cushioning layer and the second a stiff layer. This appears to be the basic design concept that is applied to the majority of the shin pads commercially available and an assessment of the effectiveness of designing pads in this way will be able to be made. To this end, a range of shell stiffness coupled with foam materials of differing density may be tested to gain an understanding of the coupled behaviour of such materials. As discussed in chapter 2, particular reference must be made to the peak load which causes three point bending, as this has been proven to be directly responsible for the largest proportion of fractures.

Effectively, this section of the work presents sample results which are analysed to obtain an understanding of typical modes of behaviour for conventional shin pads under impact loading.

4.1 Range of materials tested.

A preliminary experimental study has been conducted with an outer shell of a stiff material covering a foam layer, the prevalent material combination for a modern shin pad. Two outer shell materials, polycarbonate of 2 mm, 3 mm and 4 mm thickness and a $[\pm 45]_{16}$ woven carbon fibre laminate of 2.45 mm thickness, were selected to obtain a range of outer shell stiffness. The experiments were designed to demonstrate a range of behaviour by varying both the stiffness of the foam and the flexural and compressive stiffness of the outer layer. The elastic modulus is equal to 2.5 GPa for the polycarbonate and 47 GPa for the carbon fibre laminate. The elastic modulus for the laminate has been assumed to be isotropic, this assumption is justified through observation of experimental results in section 4.4. Plots showing the distribution of stress beneath the padding materials for experiments that include the laminate shell are symmetrical about the point of impact; producing a circular pattern. If the laminate material was highly direction dependant a more complex stress pattern would occur.

These materials produce a range of bending stiffness (proportional to Eh^3 where h is the layer thickness) which differ by a factor of 18.8 from the thinnest polycarbonate to the carbon fibre layer.

A chart showing the plate stiffness is given below in table 4.1. The shell materials dimensions have been selected to have a much lower bending stiffness than the tibia (the minimum bending stiffness of the tibia is 900Nm, the stiffness of the tibia is analysed in detail in chapter 7). This has been decided principally because the

drop weight tower is only 1 metre in height, limiting the impact velocity to a value much reduced from that required to cause fracture. Bending has been concluded in chapter 2 to cause the majority of fractures, and it is this phenomenon that is necessary to experimentally duplicate, hence the relatively low stiffness in comparison to the tibia. Each shell material was tested with closed cell polyethylene foams of 34 kgm^{-3} , 47 kgm^{-3} , 60 kgm^{-3} , 79 kgm^{-3} and 115 kgm^{-3} density manufactured by Zotefoam. The stress strain characteristics of these foams, up to a strain of 85% are shown in figure 4.1 below. These plots were obtained using a standard compression machine, where the displacement of a known cross section of each foam was recorded under a steadily increasing load.

Table 4.1 outer shell characteristics

Shell Material	shell thickness	Elastic Modulus (E)	Plate stiffness (D)
polycarbonate	2 mm	2.69 GPa	1.6 Nm
polycarbonate	3 mm	2.69 GPa	6.66 Nm
polycarbonate	4 mm	2.69 GPa	15.78 Nm
carbon fibre laminate	2.45 mm	46.7 GPa	62.89 Nm

Figure 4. 1 Stress strain characteristics for range of foams tested.

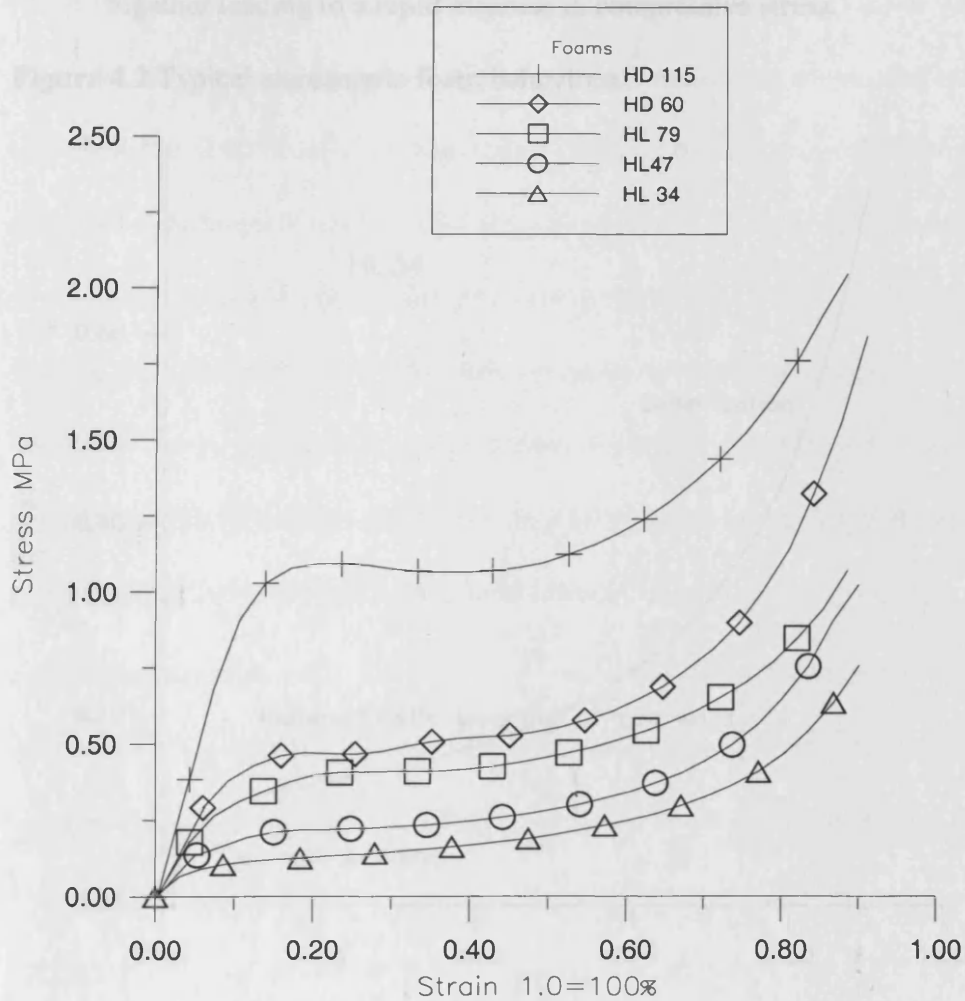
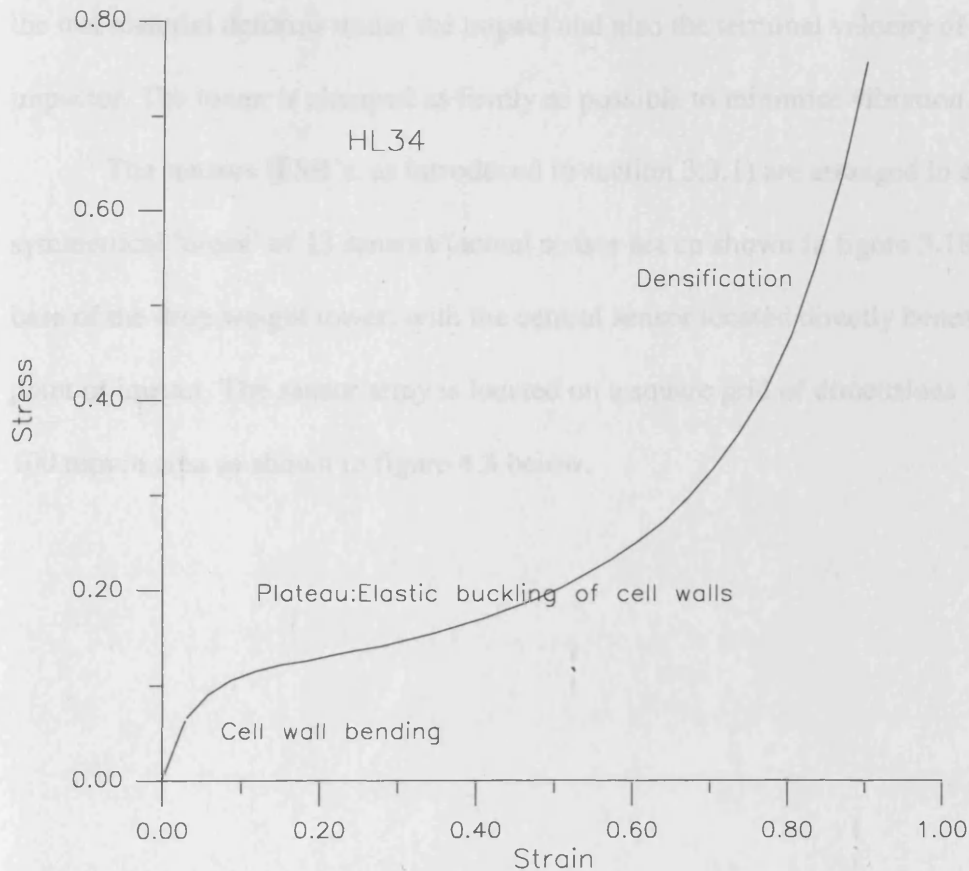


Figure 4.2 shows the compressive stress strain curve for HL34. The characteristics may be broken down into three distinguishing sections.

- At small strains the foam deforms in a linear elastic manner due to cell wall bending
- This is followed by a plateau of deformation at almost constant stress, caused by the elastic buckling of the cell walls

- Finally there is a region of densification where the cell walls crush together leading to a rapid increase in compressive stress.

Figure 4.2 Typical elastomeric foam behaviour.



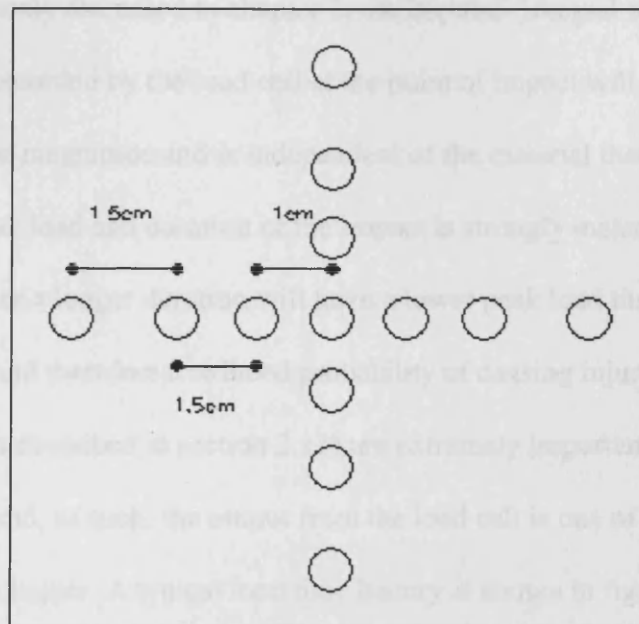
4.2 Test Method for flat plate testing.

Testing has been limited to a 'flat plate' investigation to remove geometrical effects from the results and allow full concentration on the material response. A basic drop weight test was used to simulate the 'kick'. The apparatus used is described in detail in section 3.8. Essentially it consists of a 1 metre drop weight tower which provides the impact. The impactor itself is a boot tip which is instrumented with a

load cell to monitor the impulse applied to the test materials. A sensor array is positioned at the foot of the tower, upon which the test materials may be placed to monitor how the material spreads the impact. A laser is used to measure the distance the test material deforms under the impact and also the terminal velocity of the impactor. The tower is clamped as firmly as possible to minimise vibration.

The sensors (FSR's, as introduced in section 3.3.1) are arranged in a symmetrical 'cross' of 13 sensors (actual sensor set up shown in figure 3.18) at the base of the drop weight tower, with the central sensor located directly beneath the point of impact. The sensor array is located on a square grid of dimensions 100 mm x 100 mm in area as shown in figure 4.3 below.

Figure 4. 3 Sensor array

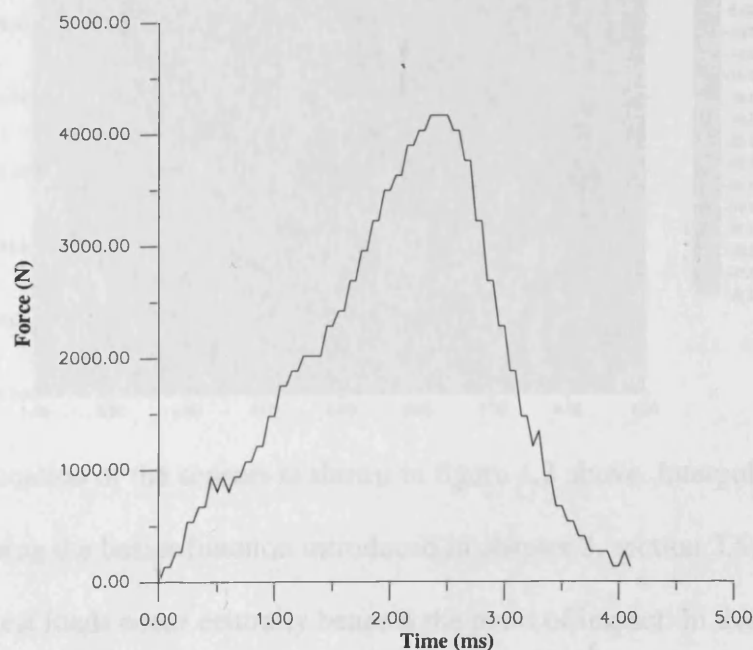


The foams tested were of equal volume with a 100 x 100mm surface area and 6 mm depth, and the shells had a surface area of 100 x100 mm and thickness already stipulated in section 4.1. The shell material was attached to the foam using a layer of double sided tape covering the whole of the shell surface, placed on top of the sensor array and impacted. All drop weight tests were from a height of 80 cm, which resulted in an impact velocity of approximately 4 ms^{-1} . This velocity was measured using the laser targeted at a point on the impacting body.

4.3 Typical results obtained

As previously discussed in chapter 3, the impulse (integral of force with respect to time) recorded by the load cell at the point of impact will be equal for impacts of similar magnitude and is independent of the material that is being struck. However, the peak load and duration of the impact is strongly material sensitive. An impact spread over a longer duration will have a lower peak load than that with a shorter duration and therefore a reduced probability of causing injury. These characteristics (as described in section 2.11) are extremely important with respect to injury causation and, as such, the output from the load cell is one of the key results presented in this chapter. A typical load time history is shown in figure 4.4 below.

Figure 4.4 Load time history for 2mm polycarbonate shell with HD115 foam beneath, measured using output from load cell within the impactor.



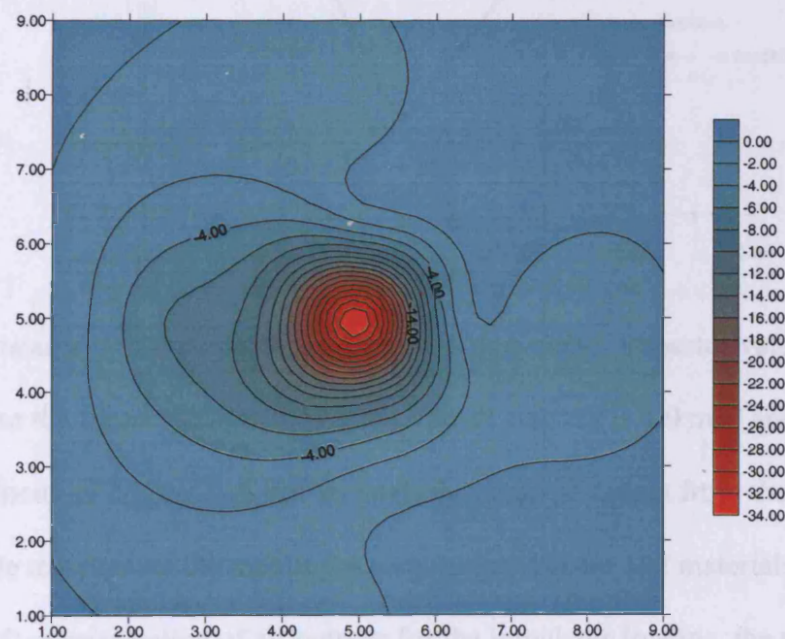
Consider figure 4.4 above. The force begins to increase from zero as contact between impactor and impacted body initiates. This force continues to increase until

C

the downward motion of the impactor is arrested, at which point the peak load is recorded. As the impactor rebounds from the target, the load ramps down until it reaches zero, when physical contact between the boot tip and the pad is broken.

The corresponding peak pressure distribution (occurring at the same instant the peak load is recorded as shown in figure 4.4 above) between the test material and the supporting medium for the same test is shown below in figure 4.5.

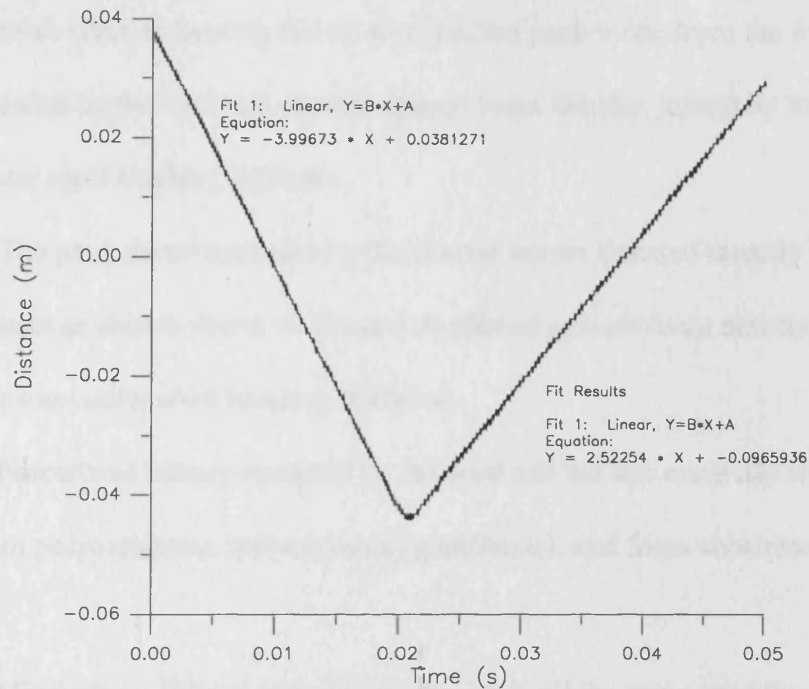
Figure 4.5 Corresponding stress distribution recorded using sensor array as shown in figure 4.3, interpolation carried out using bezier function as discussed in section 3.5.1. The x and y co-ordinates are given in cm, the contours are given in MPa, the values of which are negative representing compressive stress.



The location of the sensors is shown in figure 4.3 above. Interpolation is carried out using the bezier function introduced in chapter 3, section 3.5.1. As can be seen, the largest loads occur centrally beneath the point of impact. In this particular test, the stress stays highly localised with little or no load being recorded at the extremities of the test material.

The displacement/time history of the impact is recorded by the laser. A typical output is shown in figure 4.6 below

Figure 4.6 Output from laser.



By measuring the slope of displacement/time curve, impactor velocity may be measured. For the impact shown above, the impact velocity is 4.0 ms^{-1} and the rebound velocity is 2.52 ms^{-1} . A further analysis using the output from the load cell may be made to calculate the maximum displacement of the test materials.

A full representation of all outputs for the impulsive loading, the pressure distributions and impactor displacement are given in appendix C1. A summary of the more interesting results and the interpretation of these findings is given in the next section.

4.4 Summary of initial testing results and explanation of material behaviour characteristics.

Graphical results presented in this section are as follows.

Figure 4.7 Peak force at boot tip for all tests i.e. the peak value from the force/time history recorded by the load cell plotted against foam density, joined by lines of constant outer shell bending stiffness.

Figure 4.8 The peak stress recorded by the central sensor (located directly beneath the point of impact as shown above in figure 4.3) plotted against foam density, joined by lines of constant outer shell bending stiffness.

Figure 4.9 Force/time history recorded by the load cell for test materials with an outer shell of 2mm polycarbonate (lowest bending stiffness), and foam substrate of varying density.

Figure 4.10 Force/time history recorded by the load cell for test materials with an outer shell of 2.45 mm carbon fibre laminate (highest bending stiffness), and foam substrate of varying density.

Figure. 4.7 Peak force at boot tip for all material combinations

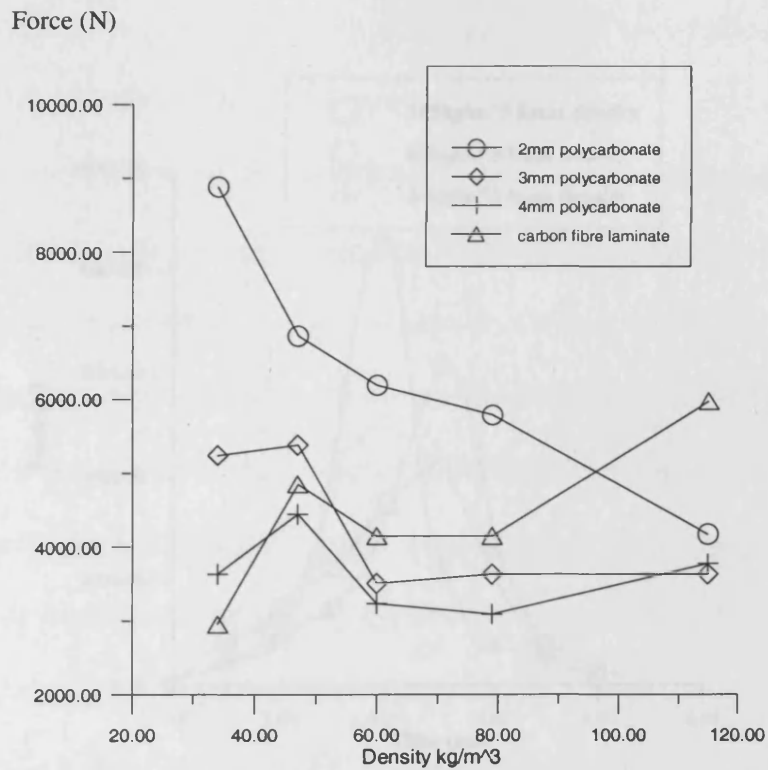


Figure 4.8 Stresses recorded by central sensor for all material combinations

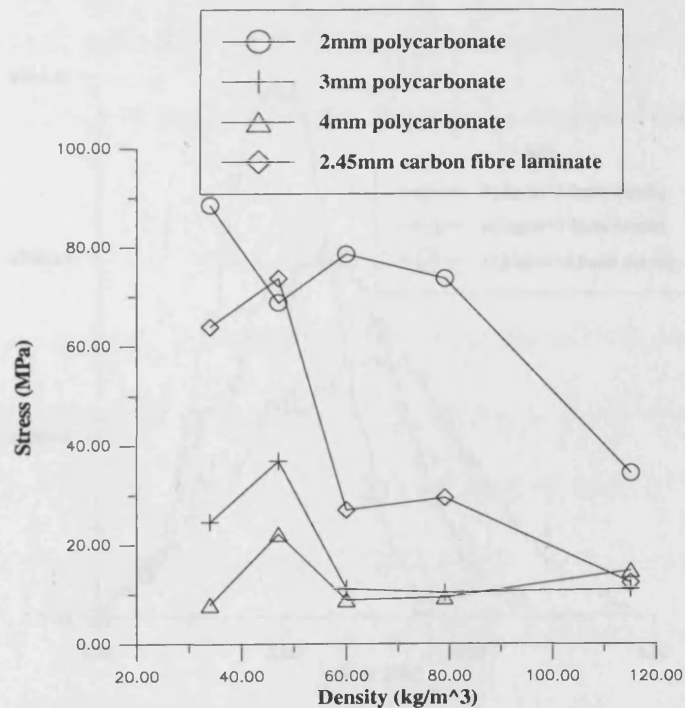


Figure 4.9 Force/time history at boot tip for foams with 2 mm polycarbonate shell

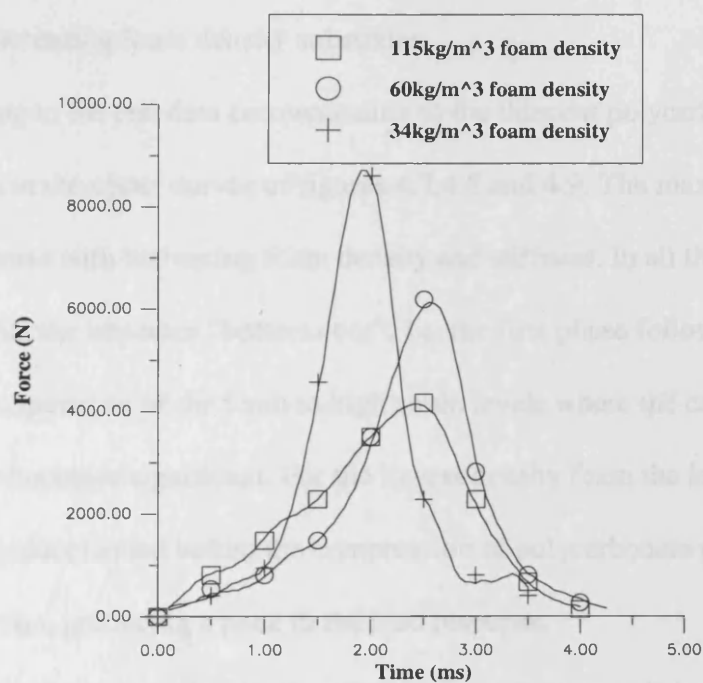
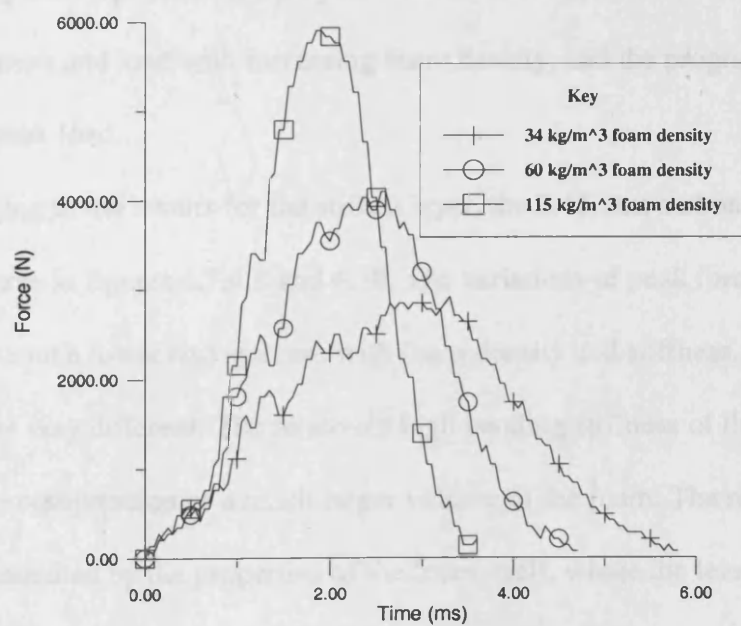


Figure 4.10 Force/time history at boot tip for foams with 2.45 mm carbon fibre shell



Observing the graphs detailed above (figs 4.7-4.10), it can be seen that there is a contrasting impactor response for materials of various outer shell stiffness when coupled with increasing foam density substrates.

Referring to the test data corresponding to the thinnest polycarbonate layer (2 mm), as shown in the upper curves of figures 4.7, 4.8 and 4.9. The maximum force and stress decrease with increasing foam density and stiffness. In all these cases it is hypothesised that the impactor "bottoms out", i.e. the first phase following impact involves the compression of the foam to high strain levels where the compression of the stiffer layer becomes significant. For the lowest density foam the impactor has only moderately decelerated before the compression of polycarbonate provides the major deceleration, producing a peak in the load response.

For stiffer foams, the deceleration during the initial phase is increased, delaying the peak and reducing its magnitude. However, the deceleration remains dominated by the response of the polycarbonate. This explains the reduction of the maximum stress and load with increasing foam density, and the progressive delay in time to the peak load.

Turning to the results for the stiffest layer, the 2.45 mm carbon fibre, shown as the lower curve in figures 4.7, 4.8 and 4.10. The variations of peak force and stress in this case are much lower and increase with foam density and stiffness. The behaviour in this case is very different. The relatively high bending stiffness of the carbon fibre results in the compression of a much larger volume of the foam. The response now becomes dominated by the properties of the foam itself, where the least dense foam produces the lowest deceleration and the longest response times. As the foam density

increases the deceleration increases, the response time is reduced and the maximum stress and load increases.

In support of this hypothesised behaviour, the displacement results obtained using the laser may be presented. To obtain the displacement of the test materials the method detailed in section 3.8 is used. The displacement/time history for the impactor is compared to the load/time history. This allows the instant where contact between impactor and test material initiates, and also the instant of peak load and therefore peak displacement to be observed. The distance which the impactor travels between these two points in time is the distance the test material is displaced.

Displacement/time histories over period of first contact to peak load are as follows.

Figure 4.11 2 mm polycarbonate shell with 34 kgm^{-3} foam substrate.

Figure 4.12 2 mm polycarbonate shell with 115 kgm^{-3} foam substrate.

Figure 4.13 2.45 mm carbon fibre laminate shell with 34 kgm^{-3} foam substrate.

Figure 4.14 2.45 mm carbon fibre laminate shell with 115 kgm^{-3} foam substrate.

Figure 4.11 2 mm polycarbonate shell with 34 kgm^{-3} foam substrate.

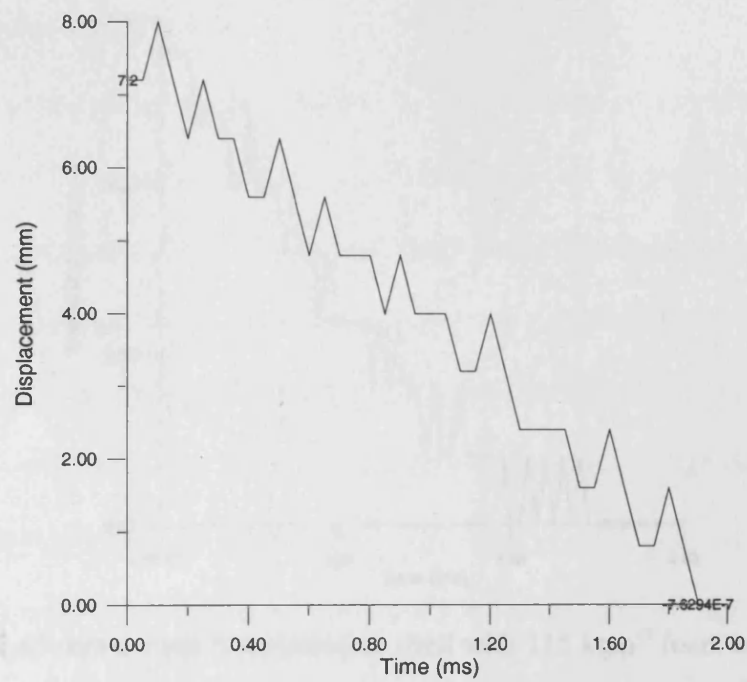


Figure 4.12 2 mm polycarbonate shell with 115 kgm^{-3} foam substrate.

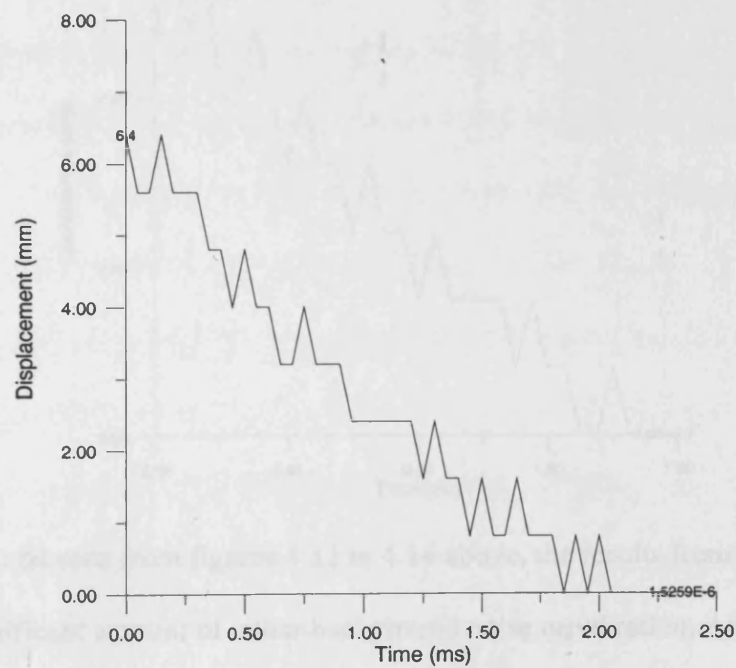


Figure 4.13 2.45 mm carbon fibre laminate shell with 34 kgm⁻³ foam substrate.

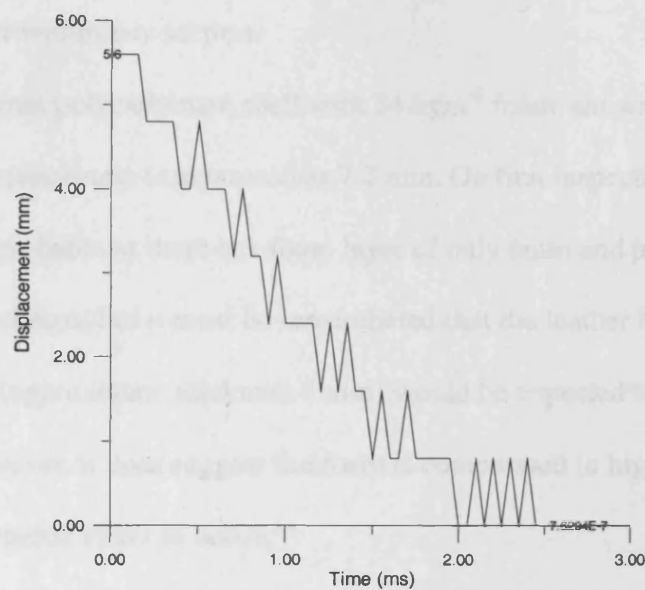
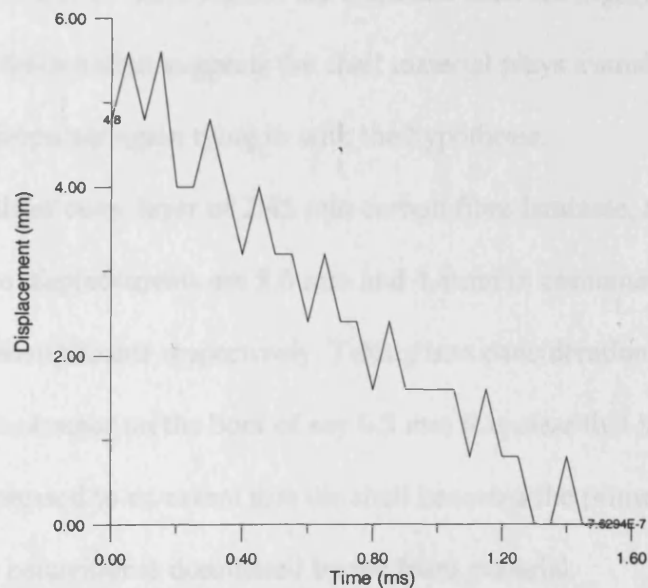


Figure 4.14 2.45 mm carbon fibre laminate shell with 115 kgm⁻³ foam substrate.



As can be seen from figures 4.11 to 4.14 above, the results from the laser include a significant amount of either background noise or vibration. Attempts were made to filter the signal and clamp the laser emitter as tightly as possible to eliminate these two possibilities with no visible improvement. Although these results may not

be as accurate as initially hoped, they do support the 'bottoming out' behaviour introduced earlier within this section.

For the 2mm polycarbonate shell with 34 kgm^{-3} foam, shown above in figure 4.11, the total displacement is measured as 7.2 mm. On first inspection this result seems highly improbable as there is a foam layer of only 6mm and polycarbonate layer of 2mm thickness, but it must be remembered that the leather from which the boot tip is made (approximate thickness 2 mm) would be expected to deform as well as the foam. However, it does suggest the foam is compressed to high strains causing the previously detailed effect to occur.

The maximum displacement for the polycarbonate with 115 kgm^{-3} foam, shown in figure 4.12 is 6.4 mm. Again, the foam and shell are highly compacted, but the smaller total deformation suggests the shell material plays a smaller part in decelerating the impactor again tying in with the hypothesis.

For the stiffer outer layer of 2.45 mm carbon fibre laminate, shown in figures 4.13 and 4.14, the displacements are 5.6 mm and 4.8mm in combination with the 34 and 115 kgm^{-3} density foams respectively. Taking into consideration the likely deformation of the leather on the boot of say 0.5 mm it is clear that in both cases the foam is not compressed to an extent that the shell becomes the prime decelerating medium, and the behaviour is dominated by the foam material.

The results presented up to this point have been obtained primarily using the load cell instrumentated impactor, a test method that has already been used by Phillipens(1989)^[2.31], Bir et al (1995)^[2.38], Lees^[2.39] and Woods(1994)^[2.41], as discussed in chapter 2. The component of the equipment which significantly

improves on the aforementioned research is the thin film sensor array that measures the stress distributions beneath the test material.

Stress distribution results presented in this section are as follows. All plots are on axes in cm with stress contours in negative MPa representing compression.

Figure 4.15 Surfer plot for 2 mm polycarbonate shell with 34 kgm^{-3} density foam.

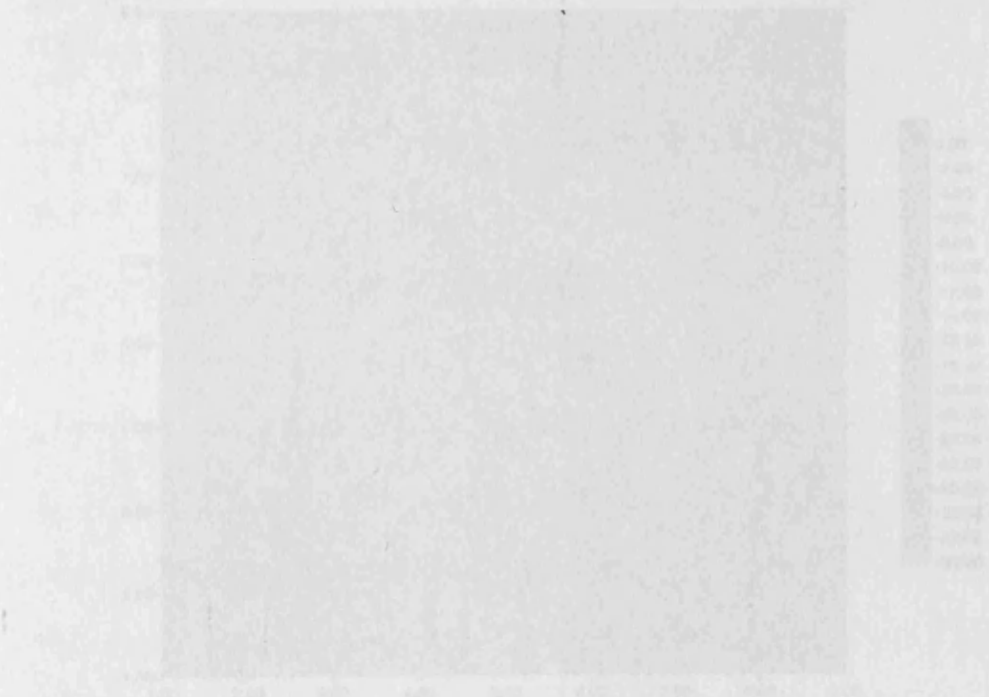
Figure 4.16 Surfer plot for 2 mm polycarbonate shell with 115 kgm^{-3} density foam.

Figure 4.17 Surfer plot for 2.45 mm carbon fibre laminate shell with 34 kgm^{-3} density foam.

Figure 4.18 Surfer plot for 2.45 mm carbon fibre laminate shell with 115 kgm^{-3} density foam.

Figure 4.19 Surfer plot for 2.45 mm carbon fibre laminate shell with 60 kgm^{-3} density foam.

Figure 4.16 Surfer plot for 2 mm polycarbonate shell with 115 kgm^{-3} density foam



C

Figure 4.15 Surfer plot for 2 mm polycarbonate shell with 34 kgm⁻³ density foam

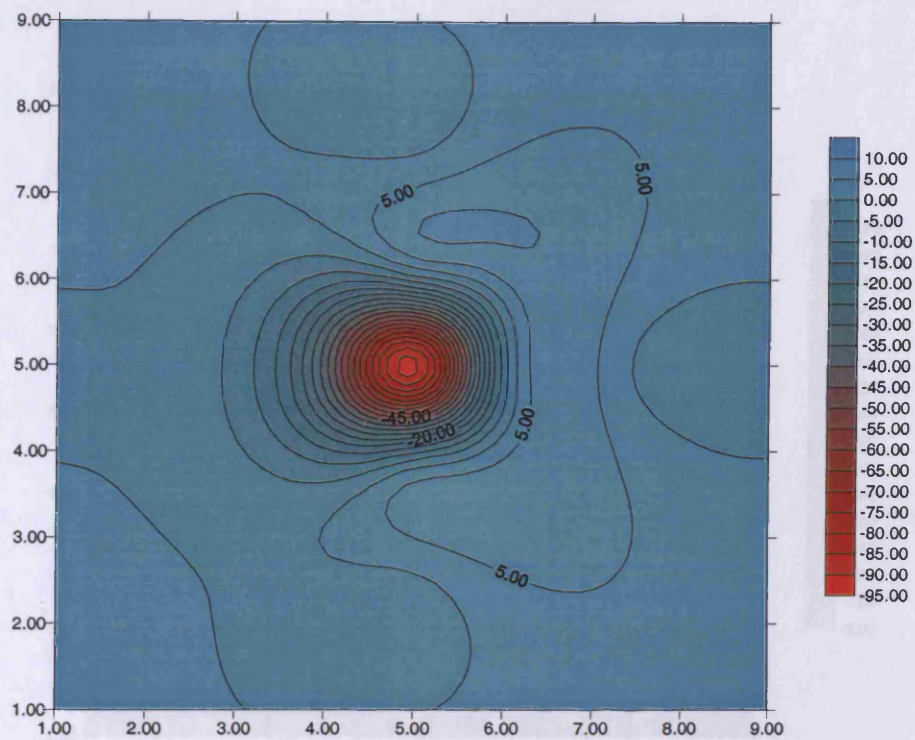
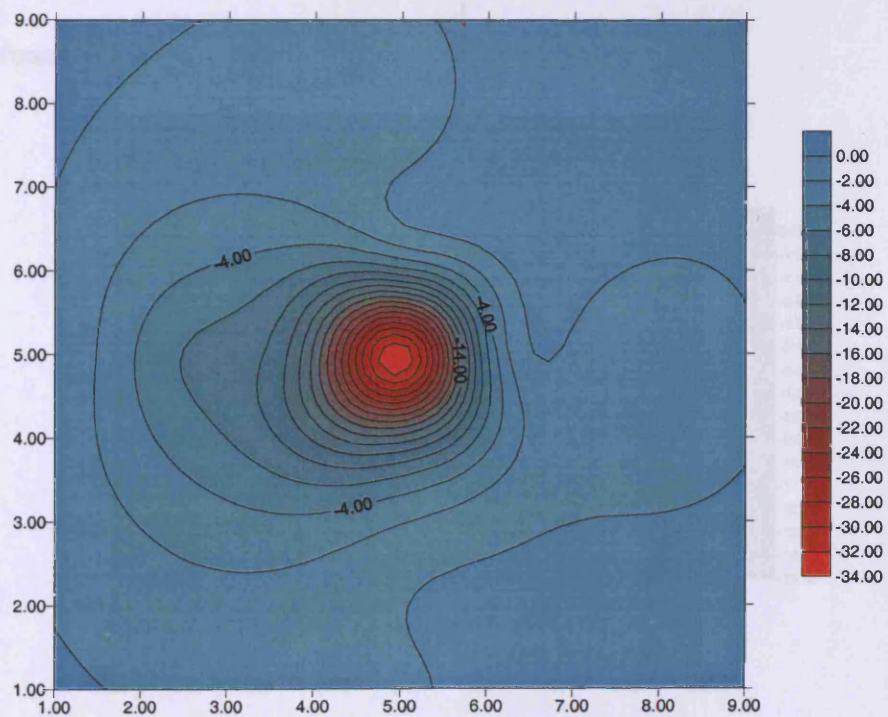
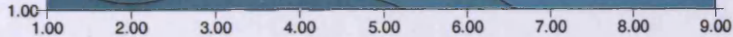


Figure 4.16 Surfer plot for 2 mm polycarbonate shell with 115 kgm⁻³ density foam

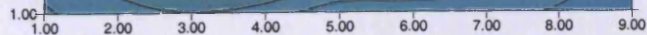


C

foam



density foam



C

Figure 4.19 Surfer plot for 2.45 mm carbon fibre laminate shell with 60 kgm^{-3} density foam.

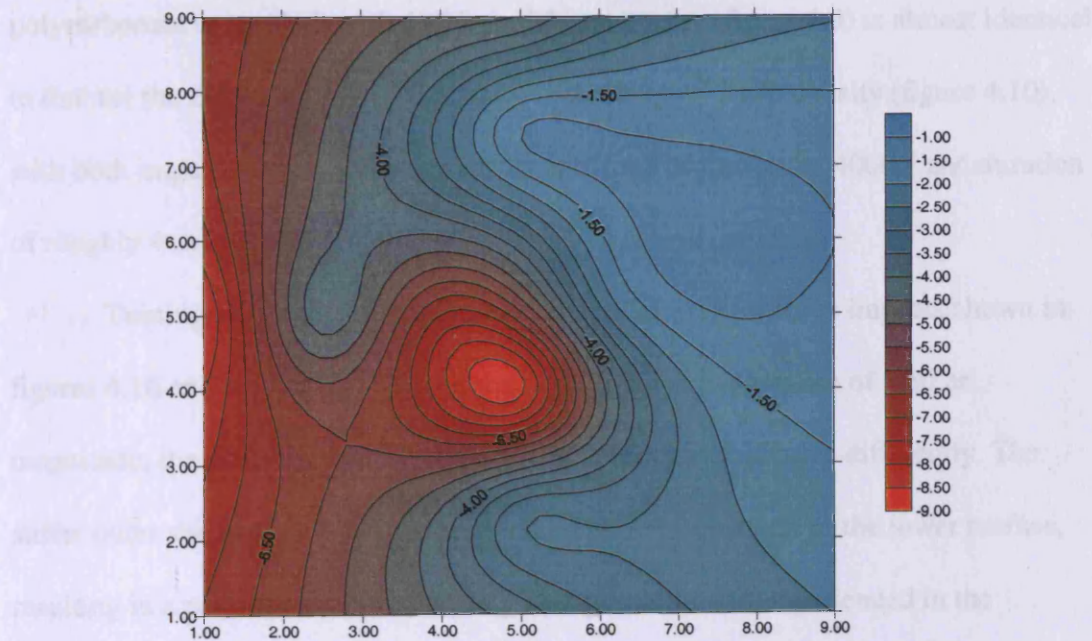


Figure 4.19 shows the surfer plot for the combination of the 2mm polycarbonate with the lowest density foam HL34. As expected, the stress pattern stays highly localized beneath the point of impact. In comparison to the highest density foam with the least stiff polycarbonate shell (3-variation in figure 4.16) it can be seen that the impact has been spread over a very similar, but slightly larger area. It is concluded that the foam decelerates the impact over a much larger extent before the polycarbonate takes on the role, and this results in a much reduced peak stress.

The corresponding surfer plots for the outer shell of 2.45 mm carbon fibre with the low density HL34, and higher density HD15 foams, are shown in figures

To illustrate just how important the sensor array is, a comparison between figures 4.9 and 4.10 shows that the impactor force/time history for the 2mm polycarbonate outer shell with 115 kgm^{-3} foam density (figure 4.9) is almost identical to that for the 2.45mm carbon fibre shell with 60 kgm^{-3} foam density (figure 4.10), with both impacts experiencing a peak impact load of just under 4000N and duration of roughly 4ms.

Turning to the corresponding stress distributions for these impacts shown in figures 4.16 and 4.19, it can be seen that although the impacts are of similar magnitude, the differing materials distribute the impact load very differently. The stiffer outer shell spreads the pressure over a larger proportion of the lower surface, resulting in a peak stress approximately one quarter of that experienced in the situation with the more flexible shell material.

Figure 4.15 shows the surfer plot for the combination of the 2 mm polycarbonate with the lowest density foam HL34. As expected, the stress pattern stays highly localised beneath the point of impact. In comparison to the highest density foam with the low stiffness polycarbonate shell (2 mm) shown in figure 4.16, it can be seen that the impact has been spread over a very similar, but slightly larger area. It is postulated that the foam decelerates the impactor to a much larger extent before the polycarbonate takes on the role, and this results in a much reduced peak stress.

The corresponding Surfer plots for the outer shell of 2.45 mm carbon fibre with the low density HL34, and higher density HD115 foams, are shown in figures

4.17 and 4.18 respectively. For both cases, the stiff outer shell spreads the impact over a much larger area with the result that no 'bottoming out' occurs.

In this impact situation, the overall stiffness of the shell/substrate system is crucial. As can be seen, the stiffer system (laminated shell with 115 kgm^{-3} foam substrate) spreads the impact over a larger area than the more flexible system in a similar way to the previous example (for the 2mm polycarbonate shell with 115 and 35 kgm^{-3} density foams). What becomes crucial in this instance is the duration of the impact. The higher stiffness of the system causes the duration of the impact to be much shorter, thus increasing the peak load. This is evident by observation of figure 4.10. Effectively, the stiffer system is better at distributing the load, but the ergonomics of the impulse are such that this loading is more substantial at its peak, causing a larger peak stress to occur beneath the test material.

A full set of results for all material combinations measured by the load cell, sensor array and laser may be found in appendix C1. Observation of the stress plots for the tests with the laminated shell shows the deformation of the shell material is reasonably symmetrical about the point of impact producing a circular pattern for all tests. This shows the assumption of isotropic properties is reasonable, as high directional dependency would induce a more complex stress pattern.

4.5 Conclusions

These preliminary results demonstrate that a simple two layer system is capable of a wide range of responses when subjected to dynamic impact. However, these responses also show that for a two layer system, consisting of a stiff outer shell with a foam substrate, subjected to a specific impact loading, there must be an optimal material combination which provides the minimal bending moment on the leg, and therefore reduces the probability of tibial fracture as a result of said impact. These initial tests show there must clearly be a balance between two extremes to obtain this ideal:

- if the foam material is overly pliant, the 'bottoming out' situation occurs leading to high loading on the tibia.
- if the shell/foam combination is too stiff, the impact duration is much reduced again leading to higher loading on the tibia.

Chapter 6 deals with the solution of this problem by applying experimental results discussed in this chapter, with further results obtained through computational Finite Element Analysis (the topic of chapter 5) to Timoshenko's theoretical work for the prediction of the behaviour of a plate on an elastic foundation under static loading.

Before Timoshenko's solution may be applied, it is required that more experimental results are generated at impact velocities which are closer to those experienced during the game of soccer. It is also necessary to improve the accuracy of the displacement measurements which are key to the application of this method. This work will be addressed within chapter 5.

The results presented within this chapter also show that the test method used in previous research (Phillipens(1989)^[2.31], Bir et al (1995)^[2.38], Lees^[2.39] and Woods(1994)^[2.41]), is not sufficient to fully enable the loading the leg undergoes, beneath a shin pad, to be assessed. This is clearly illustrated within the preceding section where almost identical impulsive loading have been shown to provide very different stress distributions beneath the test material. This is particularly significant as the current test used by SATRA (as discussed in chapter 1) relies solely on the measurement and comparison of the impulsive loading. Unfortunately, literature which defines injury causation in terms of stress distributions on the surface of the lower leg has not been encountered. The complexity of the lower leg (as shown in chapter 2) makes it extremely difficult to put forward a model that predicts how the shape and concentration of the stress contours may cause injury without supporting experimental evidence. As such, the information provided by the stress plots is not utilised to its full potential.

Chapter 5

Finite Element Analysis

5.1 Introduction.

The tests carried out on typical shin pad materials in chapter 4 were largely a success in terms of capturing the impact characteristics, using the instrumentation developed in chapter 3. The only minor disappointment was the inability of the laser to accurately measure the distance the 'pad' materials displace under impact. Unfortunately, the accurate measurement of this quantity is crucial to the application of theory for the behaviour of a plate on an elastic foundation, which is presented in chapter 6. This theory is important as it is used to create a design tool for the development of a new shin pad. To address this void of information, unattainable through experimental methods, focus has been transferred to computer simulation methods, through the Finite Element Analysis (FEA) procedure. FEA allows the response of any material to be predicted under any type of loading. The geometry of the problem, any boundary conditions and loadcases are defined in the form of a computer programme, which when run, simulates all conditions and characteristics that transpire within the physical problem. Before an FEA model may be used to calculate the missing displacement data, it must be validated that it is closely imitating the experimental conditions. To achieve this, the accuracy of the simulation must be confirmed, by comparison of modelled results to those obtained using the load cell and sensor array. Once the results mirror those obtained experimentally, the FEA may then be used to expand on the data obtained in chapter 4, by carrying out further impacts at higher velocities than those physically possible, due to limitations

imposed by the height of the drop weight tower. This allows velocities to be attained which are more realistic in comparison to those regularly experienced in the game of soccer. By using computational methods, it was also hoped to confirm the hypothesised 'bottoming out' effect for the low density foams coupled with low stiffness shells discussed in chapter 4.

which involves the minimisation of strain energy potential. The Rayleigh-Ritz^[11] method defines that for a system of equilibrium in a body, the total potential energy of the system must be at a minimum.

The first step in the FEA is to separate the boundary of the body into smaller sub sections or 'finite elements', each of which represents a discrete portion of the whole structure. As the complexity of the problem increases to those of number of finite elements, applied loads, geometry, boundary conditions and material properties, the differential equations required to define the situation become more complex and numerous and it is necessary to use a computer to assist in solving these equations. Computational FEA is an established method which may be applied to a variety of engineering problems. For the purpose of this research it has been used solely for stress analysis.

The basic steps required for the computational simulation of a model is shown in the flow diagram in figure 3.1.

5.2 Finite Element Analysis (FEA)

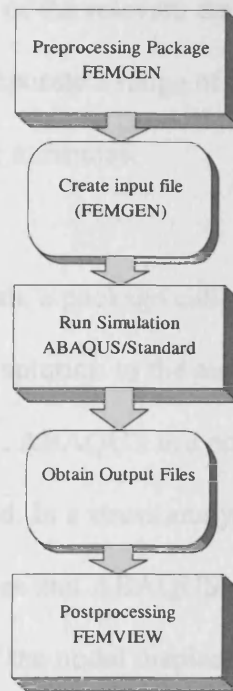
Finite Element Analysis (FEA) is essentially used to describe a method for the numerical procedure of solving differential equations.

The components of a classical solution are Equilibrium, Compatibility and the Constitutive law. However, FEA approaches problems using variational methods which involves the minimisation of strain energy potential. The Raleigh-Ritz^[5.1] method defines that for a condition of equilibrium in a body, the total potential energy of the system must be at a minimum.

The first step in any FEA is to separate the geometry of the body into smaller sub sections, or 'finite elements', each of which represents a discrete portion of the whole structure. As the complexity of the problems increase in terms of number of finite elements, applied loads, geometry, boundary conditions and material properties, the differential equations required to define the situation become more complex and numerous and it is necessary for a computer to be used to solve these equations. Computational FEA is an established method which may be applied to a variety of engineering problems. For the purpose of this research it has been used solely for stress analysis.

The basic steps required for the computational solution of a model is shown in the flow diagram in figure 5.1.

Figure 5.1 Important steps required in computational FEA



5.2.1 Pre-processing

The pre-processing stage defines a model of the physical problem to be analysed. To create the model, an option of the pre/post processing package Femgv, called Femgen, is used. This allows the model to be constructed initially by creating points in three dimensional space. These are joined to form lines which in turn can be made into surfaces, and then solid bodies to create any shape that is required. Material properties, loading conditions and any constraints to movement may also be added. Once the model geometry has been created, the 'finite elements' must be defined. These elements are created by joining up node points in the body to create individual blocks. The collection of elements and nodes is known as the mesh. The model is then written to the mesh solution form, in which all the data contained in the model is

written to an input file which is ready for the second stage of the process. The input file generally does not contain all of the relevant data required for an accurate model, and the file may be edited to incorporate a range of user options and sub-routines defining more complex behaviour attributes.

5.2.2 Running the Simulation

For the solution of the mesh, a package called ABAQUS is used. The simulation is the stage in which a solution to the numerical problems, defined in the pre-processing stage, are obtained. ABAQUS is a powerful engineering tool that is based on the finite element method. In a stress analysis, the displacements of the nodes are the fundamental variables that ABAQUS calculates. The strain energy density is then defined in terms of the nodal displacements and from this, the internal energy is calculated by integrating the elemental energies over the volume of the body using Gaussian integration. The minimisation of the energy within the system using the Raleigh-Ritz method may then be carried out to obtain a solution to the mesh. For a full explanation of how ABAQUS calculates the displacement, stress and strain within a simulation, reference should be made to the ABAQUS user manuals.

5.2.3 Post Processing

For any particular simulation, ABAQUS generates huge volumes of data in tabular form for each element in the model. Realistically, it is very difficult to interpret the results in this particular format. It is usual to run a post processing programme to allow the results to be viewed graphically. To create these graphical results, the output files from the ABAQUS simulation are processed and viewed using another option of the package Femgy called Femview.

5.2.4 Model Geometry

The simulation of a dynamic impact on a fixed material requires significant computer facilities. To reduce the demand on the computer facilities and run time, the model geometry has been simplified to an axisymmetric analysis. This effectively reduces the problem from three to two dimensions by modelling a plane through the component with mesh elements representing a complete 360 degree ring, as shown below in Figure 5.2.

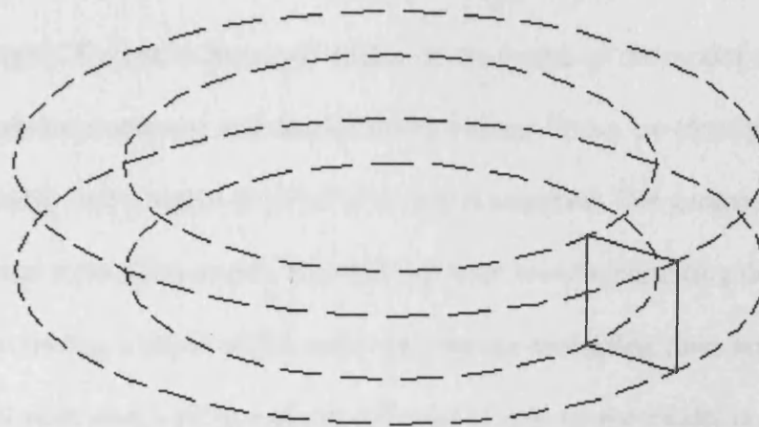
5.3 The model

The accuracy of any computational FEA is governed by how the model is defined. The element type, shape and overall number of elements used in the mesh all have an effect. The greater the mesh density the more accurate the results. However, this is accompanied by an increase in computational time and effort. Care must be taken not to exceed the limitations of the computing facilities. The extent of the approximations made in the model in terms of geometry, material behaviour, boundary conditions and loading, also determines how well the numerical simulation matches the physical problem. The ABAQUS input file generated to simulate the impact situation described in chapter 4 is given in appendix D1, with explanatory notes to describe the important features of the programme. The key impact attributes modelled will now be considered along with details of any assumptions made which may cause the simulation results to differ from the corresponding experimental ones.

5.3.1 Model geometry.

The simulation of a dynamic impact on a foam material requires significant computational effort. To reduce the demand on the computer facilities and run time, the model geometry has been simplified to an axisymmetric analysis. This effectively reduces the problem from three to two dimensions by modelling a plane through the component with each element representing a complete 360 degree ring, as shown below in figure 5.2.

Figure 5.2 Three dimensional geometry represented by a single axisymmetric element.

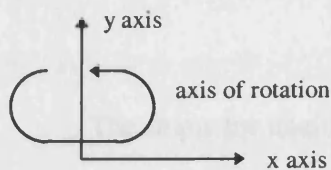
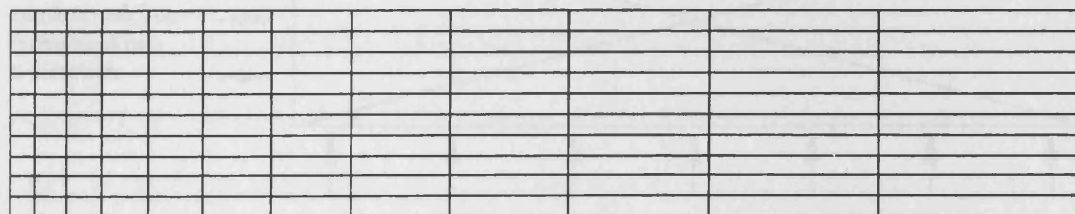


The test materials were set up as rectangular blocks in the experimental situation (of dimensions discussed in chapter 4 section 4.3), but an axisymmetric model is, in effect, cylindrical rather than cubic in nature. Assuming the effect of the impact at the edges of the plate, distant from the central point of impact, is nominal, the behaviour of the model is assumed to be reasonably close to that experienced experimentally. As a result of this assumption, the test materials have a surface area of 0.01m^2 , and the simulation materials have a surface area of 0.0079 m^2 . The model geometry may also be cut in half along the central line of symmetry to again cut down on the computational effort. A diagram showing the geometry of the model, along with the meshing which was generated using Femgen (the pre processing package), is shown below in figure 5.3. Each element is defined as a rectangular 'block' constructed from four nodes which are located at each corner.

The bottom surface of the geometry has a length of 50 units (one unit on the model is one millimetre on the test material). This is broken up into 12 vertical

columns of elements, with the element located furthest to the right of the diagram (figure 5.3) having a width eight times greater than that furthest to the left. The elements located between these two outer members gradually increase in magnitude from left to right. The mesh density is higher at the centre of the model as this is where the maximum stresses and displacement occurs. These are clearly the most important results, and a higher level of accuracy is required. The geometry has a depth of 10 horizontal rows of elements, with the top four rows representing the shell material, each having a depth of 0.5 units, and the six remaining rows representing the foam material with each having a depth of 1 unit (1 unit on the model is equal to 1 mm on the test material). The element type is defined within the ABAQUS input file as CAX4, which is the standard four noded axisymmetric element for stress analysis.

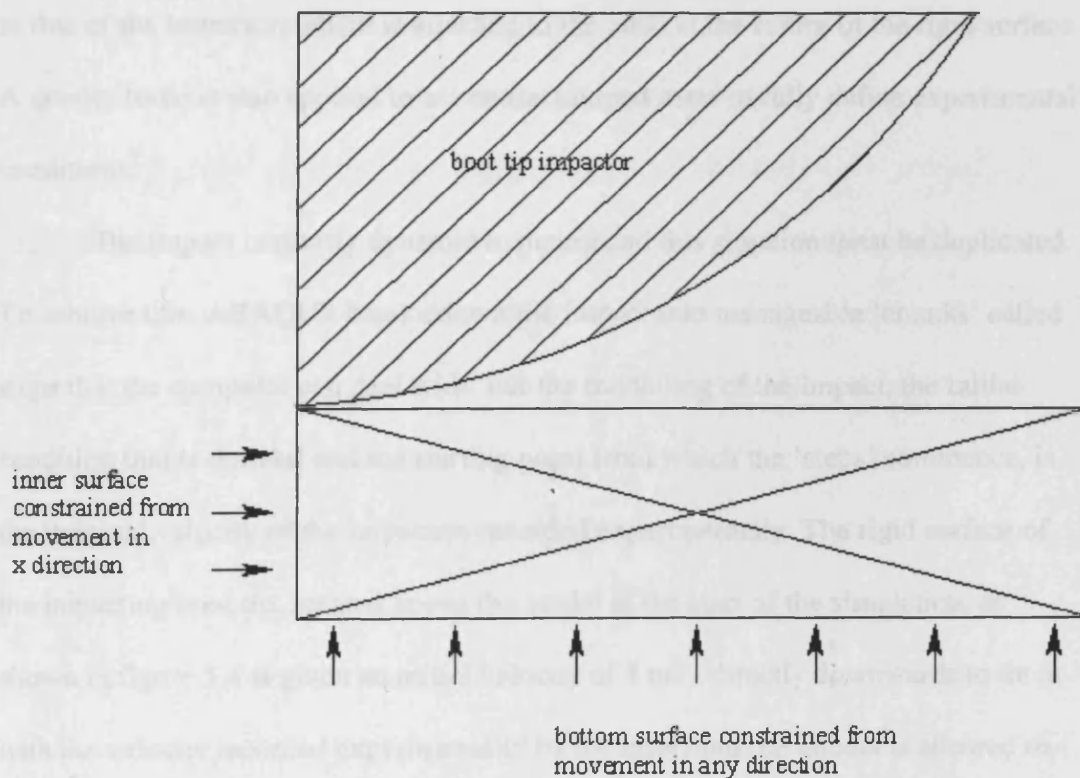
Figure 5.3 Diagram of mesh.



5.3.2 Impact Simulation

The pre processing package Femgen defines the mesh as shown in figure 5.3, which represents the geometry of the test materials. However, this does not fully define the experimental impact conditions. A full representation of the impact situation is shown below in figure 5.4.

Figure 5.4 Full representation of impact situation.



The impactor itself, shown above as the hatched boot tip, is defined as a rigid surface i.e. a geometric structure that cannot deform, but may translate or rotate. The surface has a single reference node and variables such as displacement are associated singularly with this node. In the model, the rigid surface is simply circular in nature and of 50 mm radius, to simulate the approximate shape of the boot tip used on the

test rig, with the reference node located at the centre of the arc. ABAQUS does not calculate stiffness or stresses within the rigid body, as it is always the master surface of the contact pair. The rigid surface is initially defined as being a small distance above the axisymmetric model to give an initial condition of no contact between the rigid surface and the pad materials.

Inertial effects are included in the model by defining a lumped mass identical to that of the impactor, which is attached to the node at the centre of the rigid surface. A gravity force is also applied to act on the lumped mass to fully define experimental conditions.

The impact is clearly dynamic in nature and this situation must be duplicated. To achieve this, ABAQUS breaks down the impact into manageable 'chunks' called steps that the computer can deal with. For the modelling of the impact, the initial condition that is defined and the starting point from which the 'steps' commence, is the terminal velocity of the impactor, recorded experimentally. The rigid surface of the impacting boot tip, located above the model at the start of the simulation, as shown in figure 5.4 is given an initial velocity of 4 ms^{-1} directly downwards to tie in with the velocity recorded experimentally by the laser, and the impact is allowed to proceed from this point. The computer will then step forward a unit of time into the impact and attempt to achieve a state of equilibrium. If it is unable to achieve this, it will return to the starting point and attempt to obtain equilibrium for a smaller increment of time. The starting point for each general step is the deformed state at the end of the previous step, once a state of equilibrium has been obtained. Therefore, the state of the model evolves in a sequence of general steps as it responds to the

conditions experienced in each phase. As a result, a series of points in time for which the impact characteristics are computed will emerge as the impact evolves.

The bottom surface of the model is constrained from movement in any direction to simulate the effect of the firm metal base supporting the test materials in the experimental set-up. The inner surface of the model is confined from movement in the x direction and rotation about the y axis to simulate the effect of the symmetrical half of the materials not defined in the model. Effectively all the components of the impact have been simulated. The only assumption further to that previously discussed concerning the axisymmetric geometry is the impacting body and the surface supporting the test material are absolutely rigid. In the experimental situation a certain amount of deformation would occur on each of these surfaces although realistically this is expected to be small due to the selection of rigid materials, and unlikely to have a significant effect on the results.

5.3.3 Simulation of material behaviour

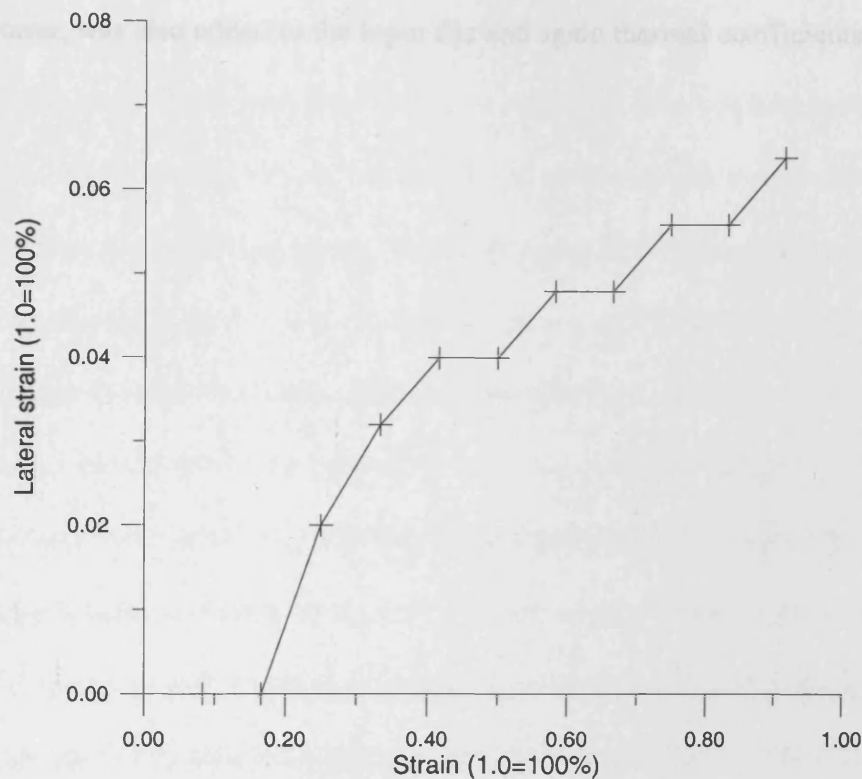
The basic analysis performed by ABAQUS is for a linearly elastic system, where it is assumed that there is a linear relationship between the applied load and the deflection, and when this load is removed the body returns to its original shape. This is an accurate representation for the polycarbonate outer shell material, which is defined in the model by inputting values for the elastic modulus, Poisson's ratio and density. Temperature coefficients are omitted, as all tests are carried out at room temperature. The elastic modulus was determined using a simple bending test to measure the central deflection of a polycarbonate beam under increasing load. Simple beam bending theory was then used to calculate the modulus of elasticity. The

Poisson's ratio was obtained by consulting the Cambridge Material Selector; a computerised material database, and the density was acquired by weighing a known volume of the polycarbonate material. The carbon fibre laminate was modelled in exactly the same way, with the assumption being made that it exhibited isotropic properties. This has been carried out as the detailed modelling of laminate behaviour, coupled with a dynamic analysis, put an excessive strain on the computing facilities available. This assumption should not unduly affect the results as it is the bending of the material that is the property of particular interest, rather than the phenomena associated with the absorption of energy under impact such as delamination or fibre pull out. This linear relationship does not hold for foamed polymers (observe typical stress strain curves shown in figure 4.1). This presents a problem because the integration technique used by ABAQUS (Gaussian Integration) is only exact for linear functions. The problem is overcome by approaching non linear problems incrementally. The stress/strain characteristics are broken down into sections which are small enough to essentially be treated as linear. These increments are added to give the solution for the non linear material.

ABAQUS has a specific method for defining the strain energy potential of an elastomeric foam material which requires the definition of certain material parameters. These values are calculated by ABAQUS using actual test data input from laboratory tests. Data may be added in tabular format directly into the input file for uniaxial test data in compression or tension, equibiaxial test data in compression or tension, shear test data, planar test data in compression or tension, and volumetric test data. For the purpose of this analysis, data has been input in terms of stress for

increasing values of strain, up to a maximum of approximately 90% for the foam materials measured under compression. This method has previously been successfully used by Williams (1995)^[5.2] who modelled the behaviour for a range of elastomeric foamed polymers, called Microvon, manufactured by Dunlop under static and dynamic compressive loadcases. In his ABAQUS input file, the lateral strain, along with the stress, were tabulated for regular increments of 5% from 5-75% strain. For the modelling of the foams (HD35, HL47, HD60, HL79 and HD115 produced by Zotefoam) tested in chapter 4, the lateral strains were measured using a video extensometer. The method involves the aiming of a video camera at a sample of foam under compression. The camera is attached to a computer which has software enabling the lateral movement of the foam sample to be measured. This is carried out for a succession of increasing compressive strains, and allows the lateral strain of the foam to be calculated over a range of compressive stresses. The curve obtained for the foam HD115 (which exhibited the largest lateral strains) is shown in figure 5.5 below.

Figure 5.5 Lateral strain for HD115



When it was attempted to include the lateral strain data within the dynamic simulation, the increment from one time step to the next (described in section 5.3.2) required to obtain a state of equilibrium dropped to below $1.0\text{E-}10$ seconds. This caused the programme to run for excessive durations and fill available disk space before completion of the programme. To attain sensible running times, it became necessary to assume a Poisson's ratio of zero. This is not an unreasonable assumption, as a compressive strain of approximately 85% results in a maximum lateral strain of only 6% (for HD115, corresponding lateral strain for HL34 of 3%), as shown in figure 5.5 above.

5.4 Detailed comparison of results obtained through FEA, and testing carried out in Chapter 4.

The purpose of this particular section is to draw a detailed comparison between the results obtained through experimental and computational methods. This correlation is crucial, as displacement results are taken solely from the simulation due to experimental inaccuracy. The accurate measurement of this displacement is fundamental to the theoretical solution applied in chapter 6, to obtain a model which defines how various material properties affect the impact characteristics. It is therefore imperative that there is confidence the simulation is mirroring the experimental situation. To this end, a detailed comparison of results obtained using the two methods will now be given for a range of characteristics. One detailed example for a single material combination is given within the body of this section, along with more general results for the whole range of materials tested. A further three detailed examples may be found in Appendix D2. The four examples cover the full range of materials tested, with the low stiffness 2 mm polycarbonate shell coupled with the lowest and highest density foams (35 and 115 kgm⁻³) and the highest stiffness laminate shell again coupled with the extremes of foam stiffness (35 and 115 kgm⁻³).

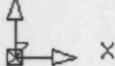
Experimentally, four key characteristics of the impact are observed; the stress distribution measured by the sensor array, the force applied by the impacting body monitored by the load cell, the duration of the impact which is also recorded by the load cell and the deflection of the material measured by the laser. Each of these

quantities will now be compared for both simulation and experiment for the combination of a 2 mm polycarbonate shell coupled with 34 kgm^{-3} foam (HL34).

The nodes on the mesh shown in figure 5.3 are numbered as shown in figure 5.6 below, results presented refer directly to these points on the model

Figure 5.6 Mesh node numbers.

113	164	115	114	113	112	111	110	109	108	107	106	105
104	103	102	101	100	99	98	97	96	95	94	93	92
91	90	89	88	87	86	85	84	83	82	81	80	79
78	77	76	75	74	73	72	71	70	69	68	67	66
65	64	63	62	61	60	59	58	57	56	55	54	53
52	51	50	49	48	47	46	45	44	43	42	41	40
39	38	37	36	35	34	33	32	31	30	29	28	27
26	25	24	23	22	21	20	19	18	17	16	15	14
13	12	11	10	9	8	7	6	5	4	3	2	1



All displacement/distance measurements are in mm, all stress measurements are in MPa, all time measurements are in seconds and all force measurements are in Newtons, values given for stipulated nodes correspond to the locations shown on figure 5.6.

Figure 5.7 Force/time history recorded at boot tip.

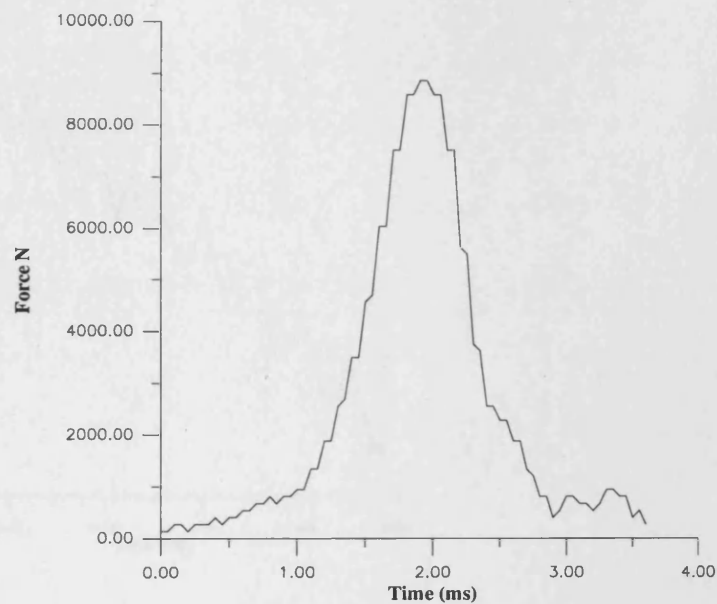


Figure 5.8 Simulated displacement (mm)/time (seconds) history for impacting body.

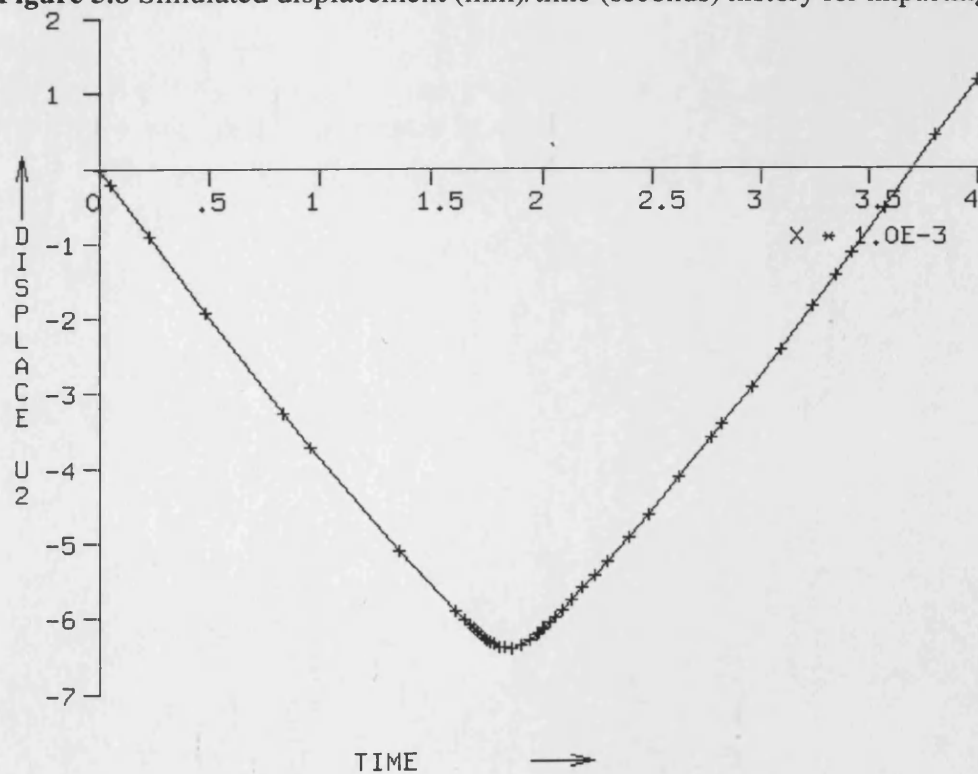


Figure 5.9 Experimentally obtained displacement of impacting body while in contact with the pad, measured by the laser.

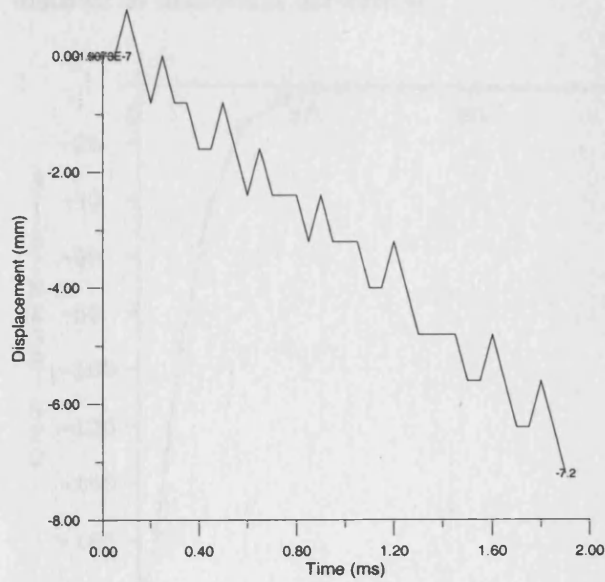


Figure 5.10 Simulated stress (MPa) along bottom surface (node 13 at 0, node 1 at 50, which corresponds to a line drawn radial from the centre of the pad to the edge) at instance of maximum deflection

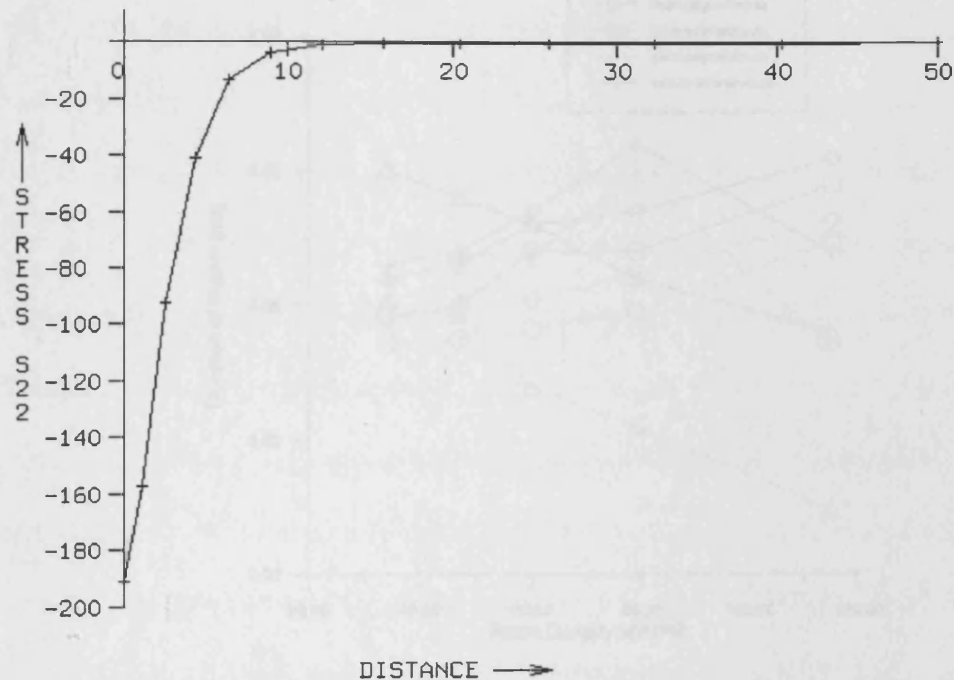


Figure 5.11 Stress recorded by sensors at maximum deflection for line of sensors moving radial from central to outer sensor.

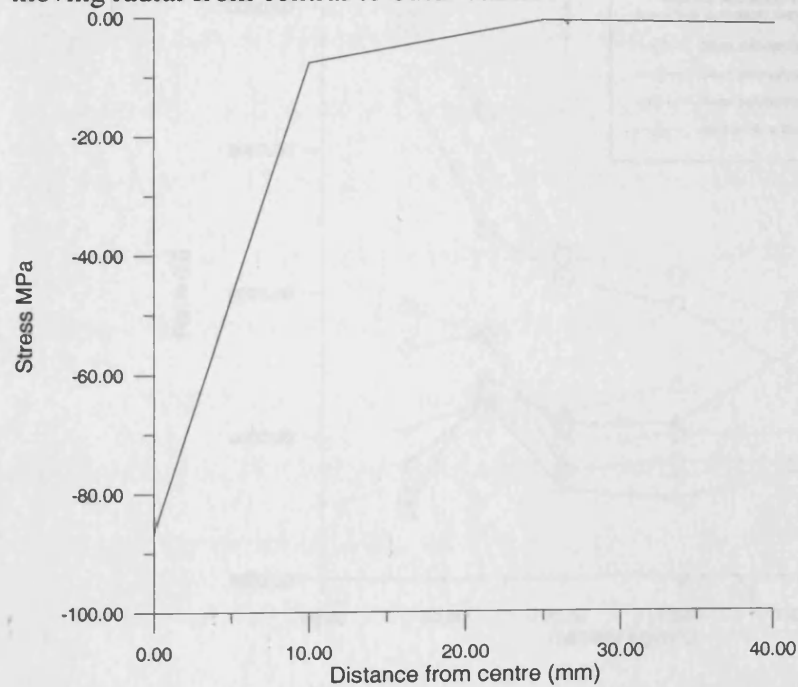


Figure 5.12 Comparison of impact duration for simulated and experimental results.

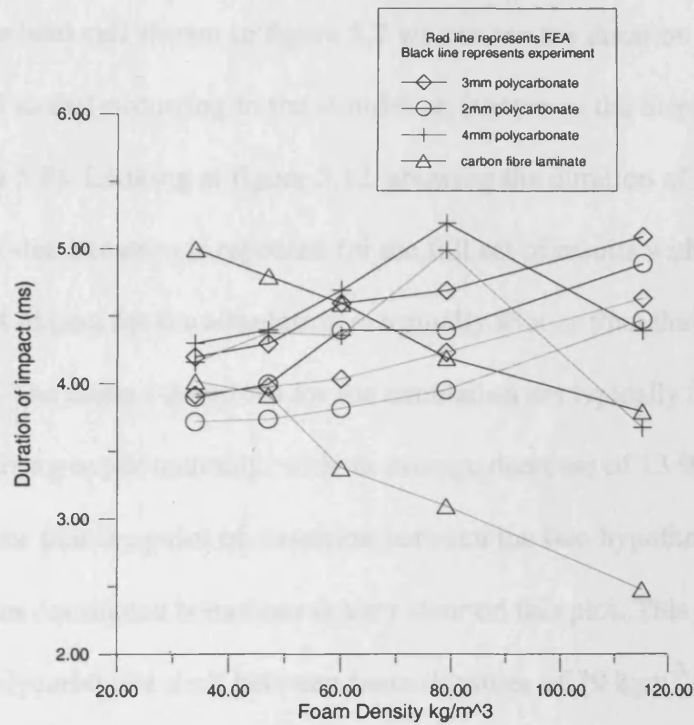
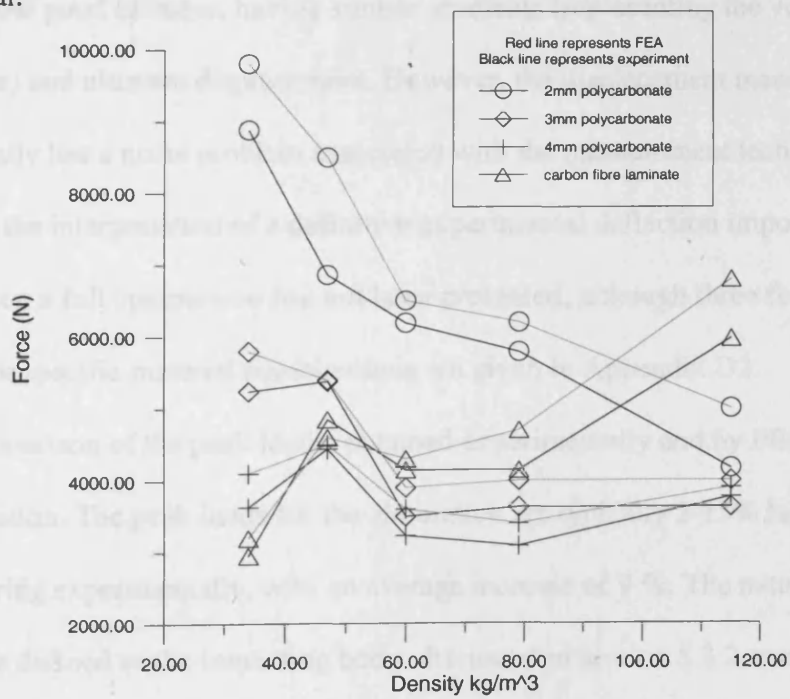


Figure 5.13 Comparison of peak impact force for all results, both simulated and experimental.



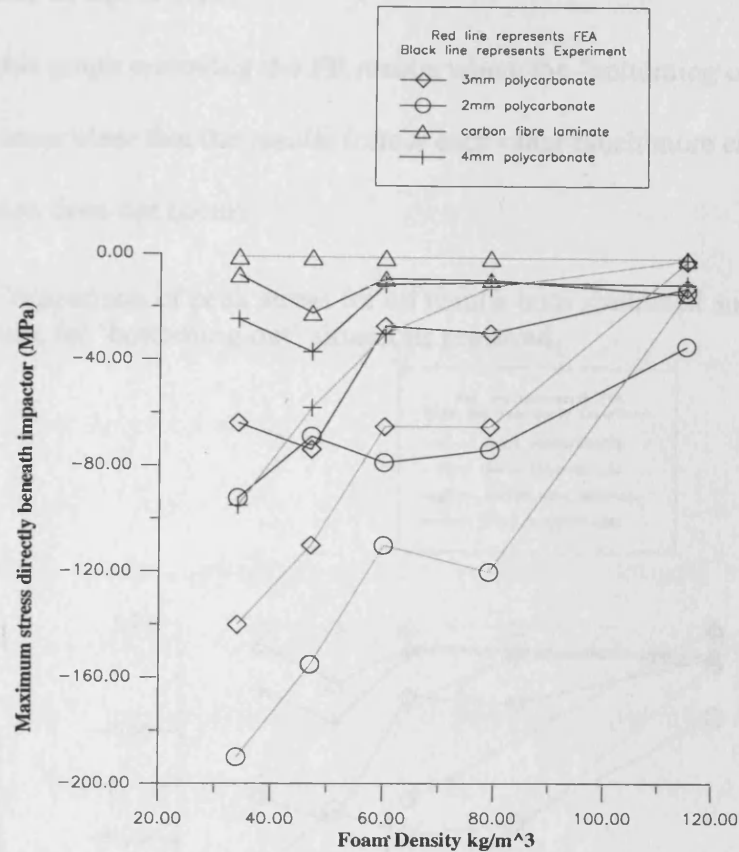
If we analyse the force/time history at the point of impact, experimentally measured by the load cell shown in figure 5.7 we can see the duration of the impact is almost identical to that occurring in the simulation (shown as the displacement/time history in figure 5.8). Looking at figure 5.12, showing the duration of all impacts, it can be seen that this situation is repeated for the full set of results with the total duration of impact for the simulation marginally shorter than that which occurs experimentally. The impact durations for the simulation are typically 8-35 % shorter than those occurring experimentally, with an average decrease of 13 %. It is interesting to note that the point of transition between the two hypothesised situations of shell and foam dominated behaviour is very clear on this plot. This clearly occurs for the 4 mm polycarbonate shell between foam densities of 79 kgm^{-3} and 115 kgm^{-3} .

The displacement/time histories for experiment (figure 5.9) and model (figure 5.8) also show good likeness, having similar gradients (representing the velocity of the impactor) and ultimate displacement. However, the displacement measured experimentally has a noise problem associated with the measurement technique used. This makes the interpretation of a definitive experimental deflection impossible, and for this reason a full comparison has not been presented, although three further examples for specific material combinations are given in Appendix D2.

Comparison of the peak loads, obtained experimentally and by FEA show good correlation. The peak loads for the simulation are typically 2-15% larger than those occurring experimentally, with an average increase of 9 %. The nature of the rigid surface defined as the impacting body, discussed in section 5.3.2, means ABAQUS does not calculate any results on the surface, and results for the force/time

history are unable to be presented graphically in Femgv. Instead, the peak load may be calculated by summation of the reactive force along the bottom surface (nodes 1 to 13), at the instance of maximum deformation. From equilibrium, the total of these forces are equal to the load being applied at the point of impact. Figure 5.13 shows the results for the peak load are comparable with the forces observed in the simulation, again being slightly higher than those obtained experimentally. This is consistent with the shorter impact duration shown in figure 5.12, as, to obtain a constant impulse, the peak load would have to be higher. This shortening of the impact period, and resultant increase in loading, is conceivably due to the definition of the impactor as an infinitely stiff surface. It must be noted that a shortened impact duration and larger peak load would intuitively suggest a larger peak deformation is occurring within the FEA model.

Figure 5.14 Comparison of peak stress occurring centrally for all results, both simulated and experimental.



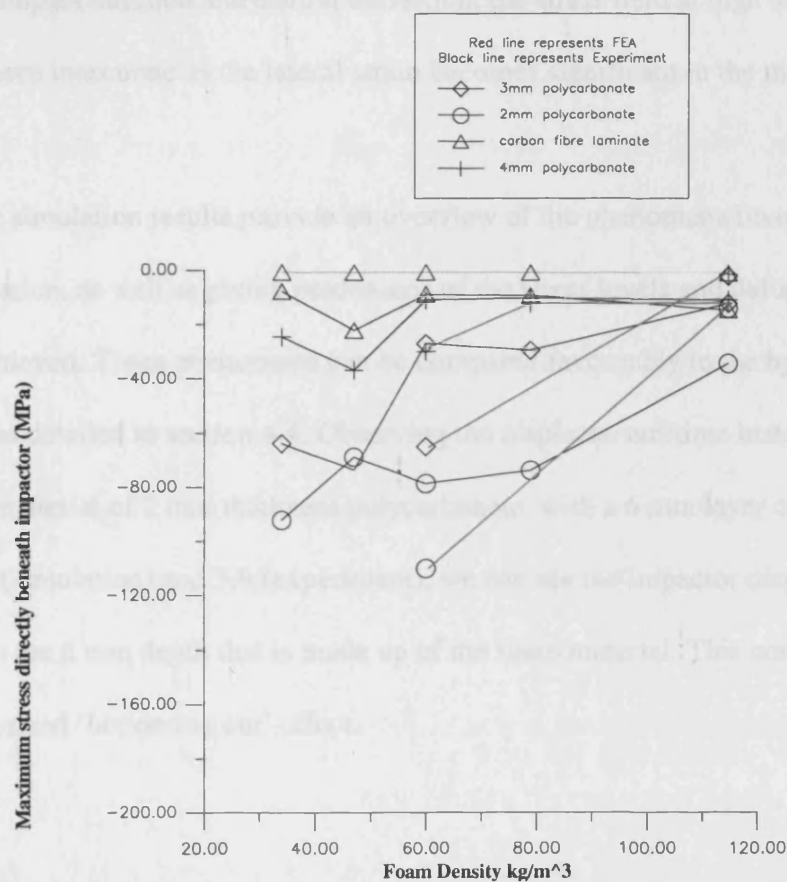
Moving on to compare the peak stresses measured by the sensor array to those occurring in the simulation, there is clearly a more appreciable difference than the results previously considered. The stress along the bottom surface occurring within the simulation (figure 5.10) is clearly much larger than that occurring experimentally (figure 5.11). A slightly larger stress would have been expected as this would tie in with the shorter impact time and larger peak load observed for the simulation.

Concentrating on the comparison of the stresses recorded by the central sensor to

those experienced over the same region on the FEA simulations, the difference is clearly definable in figure 5.14.

If we re plot this graph removing the FE results where the 'bottoming out' effect occurs, it becomes clear that the results follow each other much more closely when full compression does not occur.

Figure 5.15 Comparison of peak stress for all results both simulated and experimental with FEA results for 'bottoming out' situations removed.



The crux of the differing results lie with the assumption that the Poisson's ratio for the foamed polymer is defined in the ABAQUS input file as being zero. At

lower strain levels this has experimentally been shown to be a reasonable assumption, as discussed in section 5.3.2. However, at high strain levels, in the range of 85 - 100%, the material would be expected to behave increasingly like a solid polymer as densification occurs. For example, solid rubber typically has a Poisson's ratio of 0.5. The polymer that makes up the foam would be expected to have a similar value in its solid state. This shows that while the simulation successfully mirrors the experimental peak load, impact duration and central deflection, the stress field at high strains becomes more inaccurate as the lateral strain becomes significant in the material behaviour.

The simulation results provide an overview of the phenomena involved in the impact situation, as well as giving predictions of the stress levels and deformation patterns achieved. These phenomena can be compared favourably to the hypothesised behaviour as detailed in section 4.4. Observing the displacement/time history for an outer shell material of 2 mm thickness polycarbonate, with a 6 mm layer of HL34 in figures 5.8 (simulation) and 5.9 (experiment), we can see the impactor displaces further than the 6 mm depth that is made up of the foam material. This corroborates the hypothesised 'bottoming out' effect.

5.5 Conclusions

Differences between simulation and experimental results for load, duration of impact and deflection of pad material are small (on average within 13 %). The fact the duration of the impact is shorter and the peak load is higher for the simulation is consistent with the assumption of an infinitely rigid surface as the impacting body. In reality, the flexibility of the impactor would contribute to the deceleration of the impact, leading to longer impact durations as discussed in section 3.8. The stress results for the simulation are once again higher, but in situations where large compressive strains are experienced, these results become disproportionately greater. This may again be explained by considering the assumptions that were made when defining the model. The foamed polymer was assumed to have a Poisson's ratio of zero for all strains, an action that was necessary to enable practical run times. Experimentally it has been proven that lateral strains are low at strains of up to 85% (typically 3-6%), but beyond this the polymer would be expected to behave as it does in solid rather than cellular form, at which point the Poisson's ratio would become significant (possibly as high as 0.5).

Essentially, this section of the work has proven the results obtained through computer simulation to be a fairly reliable substitute for those obtained experimentally. This is particularly important for defining the deflection of the impacted body, a characteristic which was unobtainable through experimental means. It also allows the generation of data at impact velocities in excess of those attainable using the drop weight tower described in chapter 4.

References

[5.1] *Vibration for Engineers*

Edited by: Dimarogonas A. D. and Haddad S

Published by Prentice-Hall International 1992

The Raleigh-Ritz method, Section 10.6 Page 489

[5.2] Williams J.M.

Mechanical Behaviour of Flexible Polyurethane Foams

PhD. Thesis

University of Leicester 1995

Chapter 6

Theoretical work

6.1 Introduction to theoretical model.

In the design and development of a new shin pad, it is imperative that a full understanding of the behaviour of materials, in the specific impact situation of powerful kicking in a football game, is obtained. With the development of the test equipment, as described in chapter 3, we have a powerful tool in comparing the behaviour of an infinite number of materials. The purpose of this section of work is to obtain a theoretical solution, which relates the material properties of the pad to the impact characteristics observed within chapter 4.

The methodology used in this section is to first identify standard text book theory that describes the impact situation reasonably well. The solution selected is based on work by Timoshenko^[6.1], who derived a formula for the behaviour of a finite plate supported by an infinitely large elastic medium under a static load case. The solution must then be expanded from its basic form to a solution for a finite plate on a finite elastic foundation, which is in turn supported by a rigid surface under a dynamic load case. This may be achieved using the experimental values obtained from the testing detailed in chapter 4, and computer simulation techniques as described in chapter 5. By organising the Timoshenko solution into non-dimensional groups, and substituting the actual experimental responses into these groupings, it is hoped to obtain a mathematical function that defines the experimental behaviour in terms of material properties, geometry and impactor characteristics.

Essentially the method applied within this chapter attempts to modify the basic Timoshenko theory, so it may be applied to the more complex experimental situation. From this, a predictive model which anticipates the response of any materials under any load case may then be developed. By applying criterion which focus on the maximum tolerable loads sustainable by the tibia discussed in chapter 2, and experimental behaviour discussed in chapter 4, it is hoped that specific material constants, in terms of both foamed polymer and outer shell materials, may be derived within the model to obtain the minimum risk of injury to any specified load case.

4. The supporting reaction is initially zero and increases during impact.

5. The impact velocity is equal to the rebound velocity (purely elastic deformation occurs).

6. The geometry of the impactor is assumed as a cone.

The general solution for a plate on an infinite elastic foundation under a central point load has been calculated by Timoshenko^{14,15} and giving series terms of x greater than $x^2/4$

$$\frac{w}{\delta} = A \left(1 - \frac{x^2}{64} \right) + B \left(x^2 - \frac{x^4}{96} \right) + C \left(1 - \frac{x^2}{64} \right) \ln(x) + D \left(x^2 - \frac{x^4}{96} \right) \ln(x) + \frac{5x^4}{3456}$$

For a full explanation of how this equation has been derived refer to Timoshenko^{14,15}

where

A, B, C and D are constants

w is the deflection of the plate at x , δ is the maximum deflection which is given by the radial distance x from the centre of the plate, divided by the characteristic length l

6.2 Timoshenko's solution

Key assumptions within analysis carried out within this chapter:

- 1) The solution for the static situation of a plate on an elastic foundation is applicable to the quasi static phenomenon exhibited experimentally within chapter 4.
- 2) The impactor is infinitely stiff and does not deform during impact.
- 3) The intensity of the reaction of the substrate varies linearly with the deflection of the pad.
- 4) The supporting medium is infinitely stiff and does not deform during impact.
- 5) The impact velocity is equal to the rebound velocity (purely elastic deformation occurs).
- 6) The geometry of the impulse is sinusoidal in nature.

The general solution for a plate on an infinite elastic foundation under a central point load has been calculated by Timoshenko^[6.1] as (ignoring series terms of x greater than x^6):

$$\frac{w}{l} = A\left(1 - \frac{x^4}{64}\right) + B\left(x^2 - \frac{x^4}{576}\right) + G\left(1 - \frac{x^4}{64}\right)\ln(x) + H\left(\left(x^2 - \frac{x^4}{576}\right)\ln(x) + \frac{5x^6}{3456}\right)$$

For a full explanation of how this equation has been derived refer to Timoshenko^[6.1].

where:

A, B, G and H are constants

w is the deflection of the plate at x , a non-dimensional term which is given by the radial distance r from the centre of the plate, divided by the characteristic length l

$$x = \frac{r}{l}$$

The characteristic length l is a function that defines a radial distance from the centre of the plate, over which the impact has a significant influence on the deformation of the material and is governed by the ratio of plate stiffness to foam stiffness.

$$l = 4\sqrt{\frac{D}{k}}$$

D the stiffness of the plate and is given by $D = \frac{E^p t}{12(1-\nu)}$

E^p is the elastic modulus of the plate in Nm^{-2} , t is the thickness of the plate in meters and ν is its Poisson's ratio.

k is the modulus of the foundation (the stiffness per unit thickness) and is given by

$$k = \frac{E^f}{h}$$

E^f is the elastic modulus of the foam in Nm^{-2} , and h is the thickness of the foam in meters.

Applying boundary and geometry conditions associated with a circular plate, the constants G and H may be calculated and expressions for A and B may be substituted into the equation to arrive at the following expression:

$$\frac{w}{l} = \frac{P}{8\pi k l^3} f_1\left(\frac{a}{l}\right) g_1(x) + \frac{P}{8\pi k l^3} f_2\left(\frac{a}{l}\right) g_2(x) + \frac{P}{8\pi k l^3} g_4(x) \quad \text{equation 6.1}$$

$$g_1(x) = 1 - \frac{x^4}{64}, \quad g_2(x) = x^2 - \frac{x^6}{576}, \quad g_4(x) = \left(x^2 - \frac{x^6}{576}\right) \ln(x)$$

$f_1\left(\frac{a}{l}\right)$ and $f_2\left(\frac{a}{l}\right)$ are functions of the outer radius of the plate (a) divided by the

characteristic length (l)

The maximum deflection occurs at a radial distance from the centre of $r = 0$, which subsequently causes $x = 0$. Substituting $x = 0$ into equation 6.1 gives:

$$g_1(x) = 1, \quad g_2(x) = 0, \quad g_4(x) = 0$$

Using the term w_0 to define the deflection at the centre of the plate we obtain the equation:

$$w_0 = \frac{P}{8\pi kl^2} f_1\left(\frac{a}{l}\right) \quad \text{equation 6.2}$$

For the special case of an infinitely large plate ($a = \infty$), the central deflection w_{inf} is given by:

$$w_{inf} = \frac{P}{8kl^2} \quad \text{equation 6.3}$$

A full derivation of these equations may be found in appendix E2.

6.3 Experimental Method.

To experimentally obtain the central deflection w_0 , an axisymmetric FE model was set up, the accuracy of which has been verified in chapter 5. Previous tests concerned with foam thickness of 6 mm exhibited two behavioural trends; impact domination by the shell material and impact domination by the foam material. From the point of view of creating a theoretical model, the definition of two behavioural modes within said model is obviously much more difficult than that for one mode. What has emerged from the experimental work is that when the shell material is the prime decelerator within the impact, larger peak loads are generated. This indicates that this mode of behaviour is an extremely undesirable characteristic within a prospective shin pad. It is therefore necessary to eliminate this data from the model, and concentrate on the design of a new shin pad using the mode of behaviour where the foam material principally decelerates the impacting body. There is also a problem concerning the accurate modelling of shell dominated behaviour associated with the assumption of zero Poisson's ratio. Clearly, to obtain accurate FEA results, the influence of Poisson's ratio generated at high strains must be eliminated.

To ensure both foam dominated behaviour and accurate FEA modelling, the foam in the simulations must not compress by more than 80%, where experimentally Poisson's ratio has been proven to be virtually zero. To solve this problem, it was decided to repeat the experimental procedure described in chapter 4 with an important difference. By increasing the foam layer thickness to 12 mm, it was hoped the undesirable mode of behaviour would be eliminated, and data exclusively for the foam dominated behaviour would be collected.

A table showing the comparison of peak loads (sum of all reaction forces on bottom surface in the FEA) and duration of the impacts for equivalent experimental and FEA tests is shown in table 6.1.

Table 6.1

Material combination	Peak load (N) from simulation	Peak load (N) from tests	Duration of impact (ms) from simulation	Duration of impact (ms) from tests
2 mm poly + 12 mm HL34	8740	1800	8.3	9.02
2 mm poly + 12 mm HL47	1953	1900	7.75	8.44
2 mm poly + 12 mm HD60	2324	2020	6.57	7.3
2 mm poly + 12 mm HL79	2452	2050	7.4	8.14
2 mm poly + 12 mm HD115	3256	2900	5.06	5.84
3mm poly + 12 mm HL34	2313	1600	9.2	9.5
3mm poly + 12 mm HL47	1948	1900	7.37	7.94
3mm poly + 12 mm HD60	2527	2220	6.11	6.72
3mm poly + 12 mm HL79	2444	1900	7.1	7.9
3mm poly + 12 mm HD115	3466	2900	4.53	5.26
4mm poly + 12 mm HL34	2203	1600	8.62	8.46
4mm poly + 12 mm HL47	1976	2000	6.85	7.34
4mm poly + 12 mm HD60	2848	2450	5.44	6.22
4mm poly + 12 mm HL79	2611	1820	6.37	7.54
4mm poly + 12 mm HD115	3670	3220	4.18	4.68
2.45mm cf + 12 mm HL34	2237	1800	7.45	7.66
2.45mm cf + 12 mm HL47	1904	2240	5.86	5.98
2.45mm cf + 12 mm HD60	3571	3080	3.94	4.82
2.45mm cf + 12 mm HL79	2875	2300	4.83	6.08
2.45mm cf + 12 mm HD115	5265	4150	3.04	3.66

Table abbreviations:

poly = polycarbonate

cf = carbon fibre laminate

As can be seen, results again follow each other closely, with the impact durations being shorter and the peak loads being higher, as observed in chapter 5.

This is hypothesised to be an effect associated with the definition of the impactor as an infinitely rigid surface in the simulation. The results presented in table 6.1 also interestingly show that for the lowest density foam (H34), coupled with the lowest stiffness material (2 mm polycarbonate), the peak load recorded indicates the 'bottoming out' effect is occurring in the simulation, but not experimentally. This suggests the deflection recorded within the simulation is slightly higher than that which occurs experimentally, an eventuality that is again consistent with the rigid surface assumption. However, impacts for all other material combinations showed no evidence of 'bottoming out', and may therefore be used to define the theoretical model.

Further impacts were carried out using FEA only. The impactor speed was doubled from 4ms^{-1} to 8ms^{-1} , and the thickness of the foam substrate was set to 40 mm to avoid undesirable closure of the foam. All materials used previously, along with impactor shape and mass, remained constant. Tables showing all the results generated are given in appendix E1.

A considerable amount of data for the desirable behavioural mode has now been obtained through computational methods, with appreciable variations of materials and impact velocities. The next task is to make some progress in assimilating this data to provide a comprehensive method of predicting the behaviour of any combination of materials under any loading conditions.

6.4 Creation of theoretical model

The creation of a theoretical model may be achieved by manipulating the equations given in section 6.2, to derive non-dimensional groups of variables which are significant in the behaviour of a plate on an elastic foundation. These dimensionless parameters allow limited experimental results to be applied to situations involving different physical dimensions and different material properties. The FEA results in table 6.1 and appendix E1 provide these results, and through simple mathematical procedures, a relationship for the experimental behaviour, in terms of the dimensionless groups, may be obtained.

From section 6.2 the central deflection (w_0) for a circular plate on an elastic foundation is given by:

$$w_0 = \frac{P}{8\pi k l^2} f_1\left(\frac{a}{l}\right) \quad (6.2)$$

For the special case of an infinitely large plate ($a=\infty$) the central deflection w_{inf} is given by:

$$w_{\text{inf}} = \frac{P}{8\pi k l^2} \quad (6.3)$$

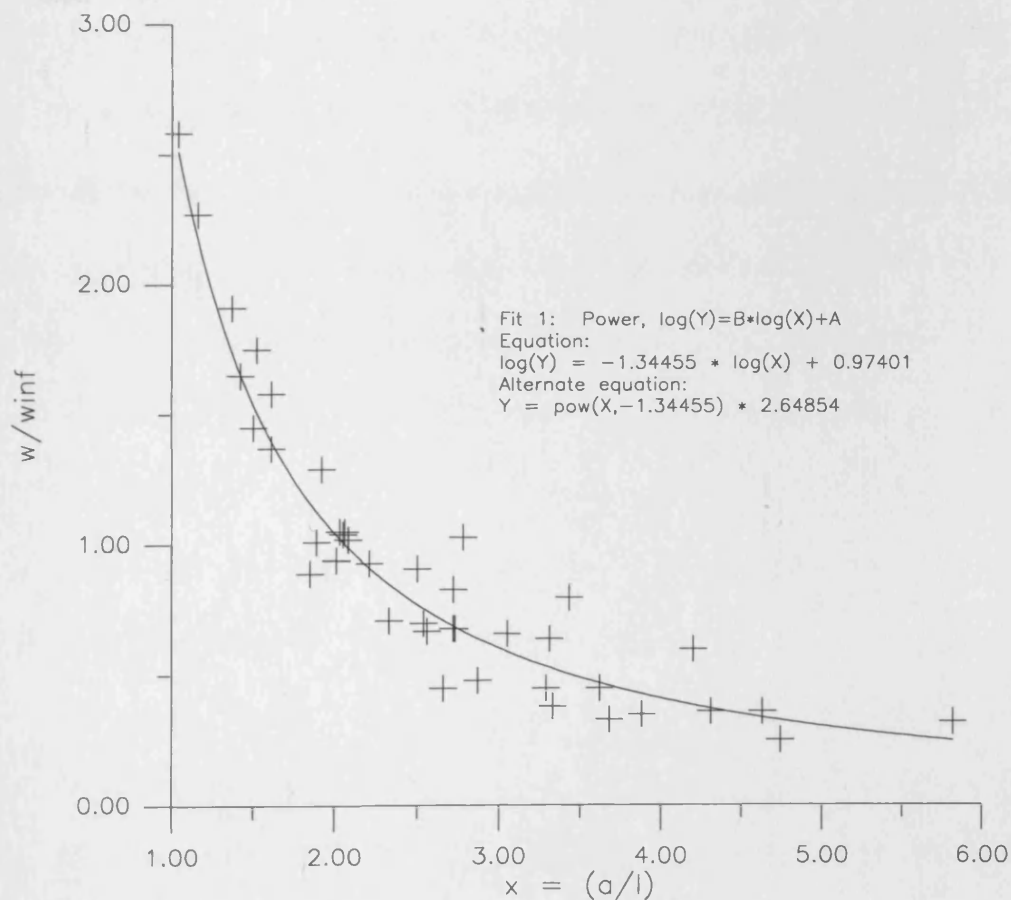
If we now divide equation 6.2 by equation 6.3 we obtain:

$$\frac{w_0}{w_{\text{inf}}} = \frac{1}{\pi} \left(f_1\left(\frac{a}{l}\right) \right) \quad \text{equation 6.4}$$

Equation 6.4 is a non-dimensional expression. From this, a non-dimensional plot may be obtained by dividing the experimentally obtained w_0 by the theoretical central displacement calculated for an infinite plate of otherwise identical properties,

to obtain a graphical solution for $(f_1(a/l))$. To calculate the central deflection for an infinite plate, a value for k given by E^f/h is required. However, referring back to section 4.2, it can be seen that elastomeric foams do not have a linear stress / strain relationship, which makes the definition of the E^f value difficult. The method used to obtain a single value of E^f is given in section 6.4.1.

Figure 6.1 Non-dimensional plot to obtain graphical solution for $(f_1(a/l))$



The data points are shown as crosses, and the best fit is shown by the solid line.

From the non-dimensional plot the following equation is obtained:

$$\frac{w_0}{w_{\text{inf}}} = 2.65x^{-1.34} \quad \text{equation 6.5}$$

If we compare this to the solution previously derived:

$$\frac{w_0}{w_{\text{inf}}} = \frac{1}{\pi} \left(f_1 \left(\frac{a}{l} \right) \right) \quad (6.4)$$

this gives $(f_1(a/l)) = 2.65\pi x^{-1.34}$

Therefore, for the experimental situation, the central deflection may be defined as:

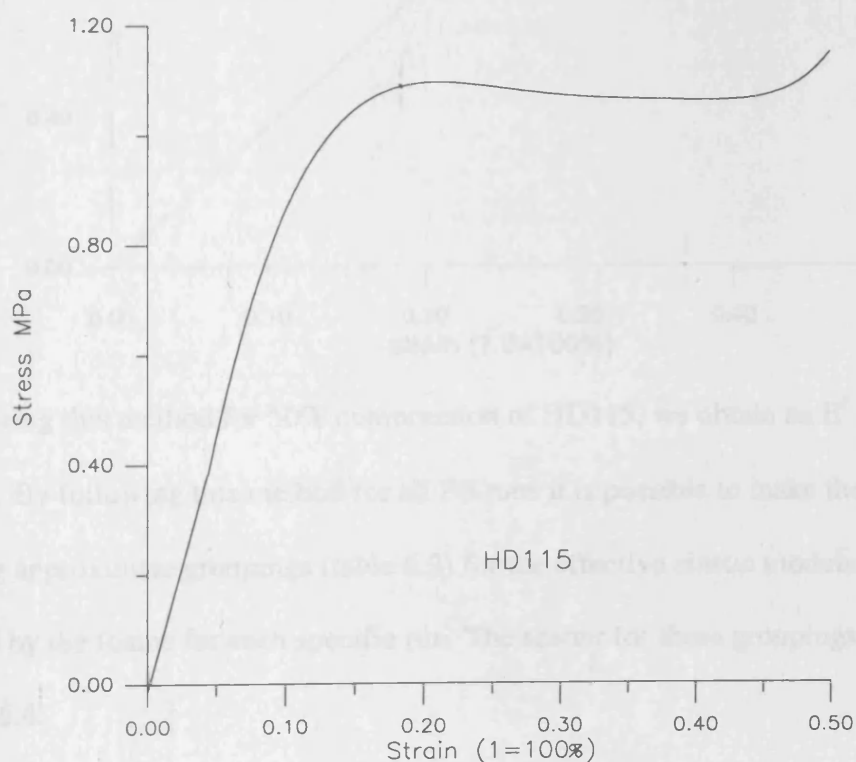
$$w_0 = \frac{2.65P}{8\pi kl^2} \left(\frac{a}{l} \right)^{-1.34} \quad \text{equation 6.6}$$



6.4.1 Dealing with the non-linear behaviour of foams.

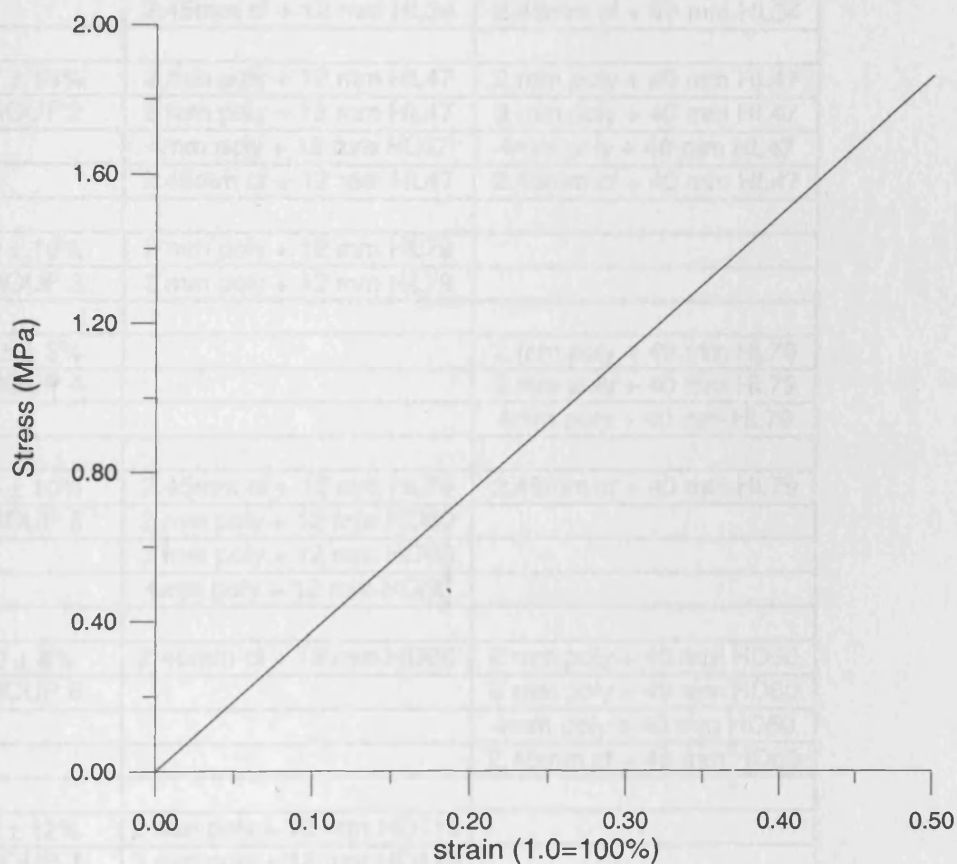
The non-linearity of the stress / strain curves provides a problem in defining an elastic modulus for the foams. It was found an average value for E^f , taken over the whole range of the stress/strain curve, led to excessive error for situations of low and high strain. It was decided to use the area beneath the curve, up to the strain experienced in each individual FE run, and re-plot this as a straight line, with the E^f value calculated as the gradient of this equivalent plot. An example of the method is shown below in figures 6.2 and 6.3. Effectively by using this method, the two plots exhibit identical energy usage (represented by the area under the curves) to obtain the same central deflection, but a definite elastic modulus is now defined.

Figure 6.2 Plot for HD 115 up to 50% compression. Area beneath curve 0.455 MPa.



Equating areas beneath curves, we obtain a straight line equivalent shown below in figure 6.3.

Figure 6.3 Equivalent plot for HD115 up to 50% strain. Area beneath curve 0.455 MPa.

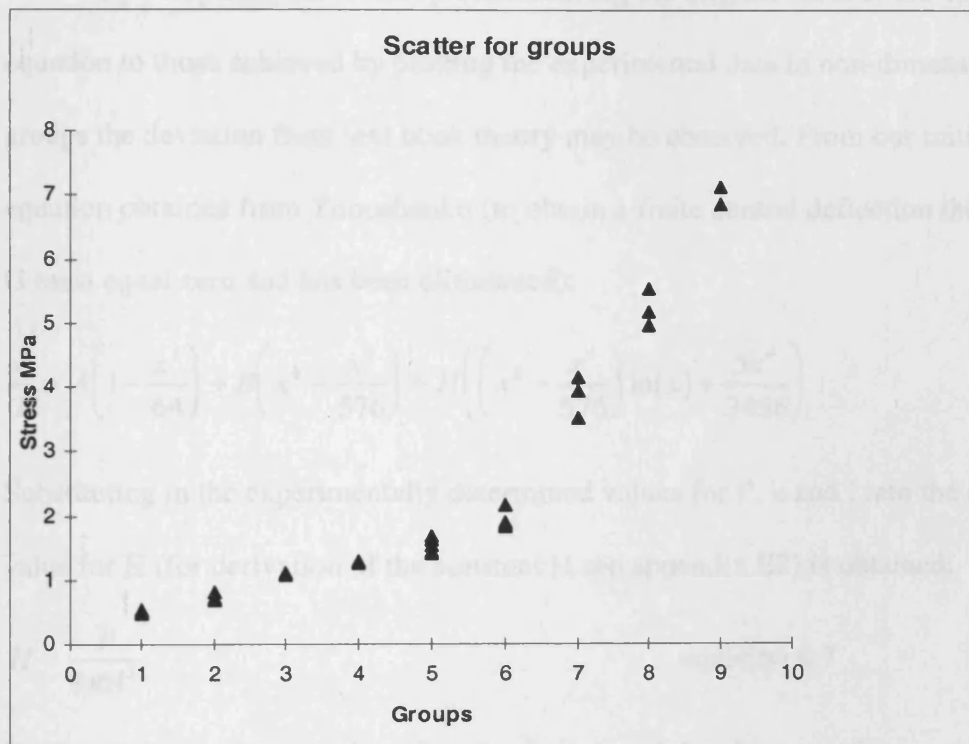


Using this method for 50% compression of HD115, we obtain an E^f value of 3.64MPa. By following this method for all FE runs it is possible to make the following approximate groupings (table 6.2) for the effective elastic modulus exhibited by the foams for each specific run. The scatter for these groupings is shown in figure 6.4.

Table 6.2 Elastic modulus groupings with the maximum percentage error to the nearest one percent.

Approximate E MPa	3.8ms ⁻¹ run	8ms ⁻¹ run
0.5 ± 6%	2 mm poly + 12 mm HL34	2 mm poly + 40 mm HL34
GROUP 1	3 mm poly + 12 mm HL34	3 mm poly + 40 mm HL34
	4mm poly + 12 mm HL34	4mm poly + 40 mm HL34
	2.45mm cf + 12 mm HL34	2.45mm cf + 40 mm HL34
0.7 ± 14%	2 mm poly + 12 mm HL47	2 mm poly + 40 mm HL47
GROUP 2	3 mm poly + 12 mm HL47	3 mm poly + 40 mm HL47
	4mm poly + 12 mm HL47	4mm poly + 40 mm HL47
	2.45mm cf + 12 mm HL47	2.45mm cf + 40 mm HL47
1.0 ± 10%	2 mm poly + 12 mm HL79	
GROUP 3	3 mm poly + 12 mm HL79	
1.25 ± 3%		2 mm poly + 40 mm HL79
GROUP 4		3 mm poly + 40 mm HL79
		4mm poly + 40 mm HL79
1.5 ± 10%	2.45mm cf + 12 mm HL79	2.45mm cf + 40 mm HL79
GROUP 5	2 mm poly + 12 mm HD60	
	3 mm poly + 12 mm HD60	
	4mm poly + 12 mm HD60	
2.0 ± 8%	2.45mm cf + 12 mm HD60	2 mm poly + 40 mm HD60
GROUP 6		3 mm poly + 40 mm HD60
		4mm poly + 40 mm HD60
		2.45mm cf + 40 mm HD60
4.0 ± 12%	2 mm poly + 12 mm HD115	
GROUP 7	3 mm poly + 12 mm HD115	
	4mm poly + 12 mm HD115	
5.0 ± 10%		2 mm poly + 40 mm HD115
GROUP 8		3 mm poly + 40 mm HD115
		4mm poly + 40 mm HD115
7.0 ± 3%	2.45mm cf + 12 mm HD115	2.45mm cf + 40 mm HD115
GROUP 9		

Figure 6.4 Showing the data scatter for each individual group



6.5 Comparison of experimental results to basic Timoshenko result.

By comparing the results predicted using the original form of the Timoshenko equation to those achieved by plotting the experimental data in non-dimensional groups the deviation from text book theory may be observed. From our initial equation obtained from Timoshenko (to obtain a finite central deflection the constant G must equal zero and has been eliminated):

$$\frac{w}{l} = A\left(1 - \frac{x^4}{64}\right) + B\left(x^2 - \frac{x^4}{576}\right) + H\left(\left(x^2 - \frac{x^4}{576}\right)\ln(x) + \frac{5x^6}{3456}\right)$$

Substituting in the experimentally determined values for P , k and l into the equation, a value for H (for derivation of the constant H see appendix E2) is obtained:

$$H = \frac{P}{8\pi kl^3} \quad \text{equation 6.7}$$

The bending moment and shear force at the edge of the plate must be equal to zero, giving the boundary conditions given in equations 6.8 below:

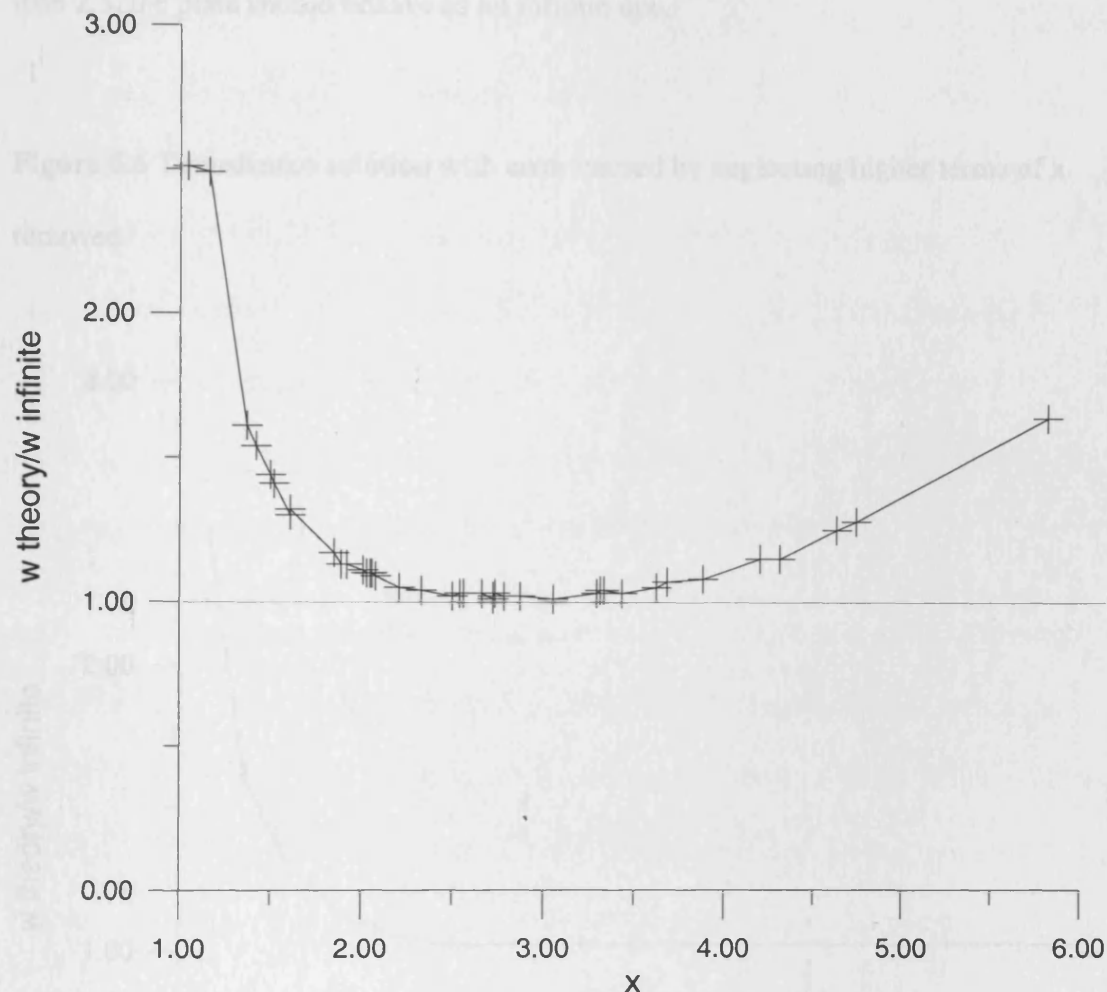
$$\left(\frac{d^2w}{dr^2} + \nu \frac{1}{r} \frac{dw}{dr}\right)_{r=a} = 0$$

equations 6.8

$$\frac{d}{dr}\left(\frac{d^2w}{dr^2} + \nu \frac{1}{r} \frac{dw}{dr}\right)_{r=a} = 0$$

Using equations 6.7 and 6.8, we can calculate the outstanding constants A and B and, therefore, the corresponding theoretical deflections for our experimental values for P , k and D . These are plotted on the figure 6.5 below.

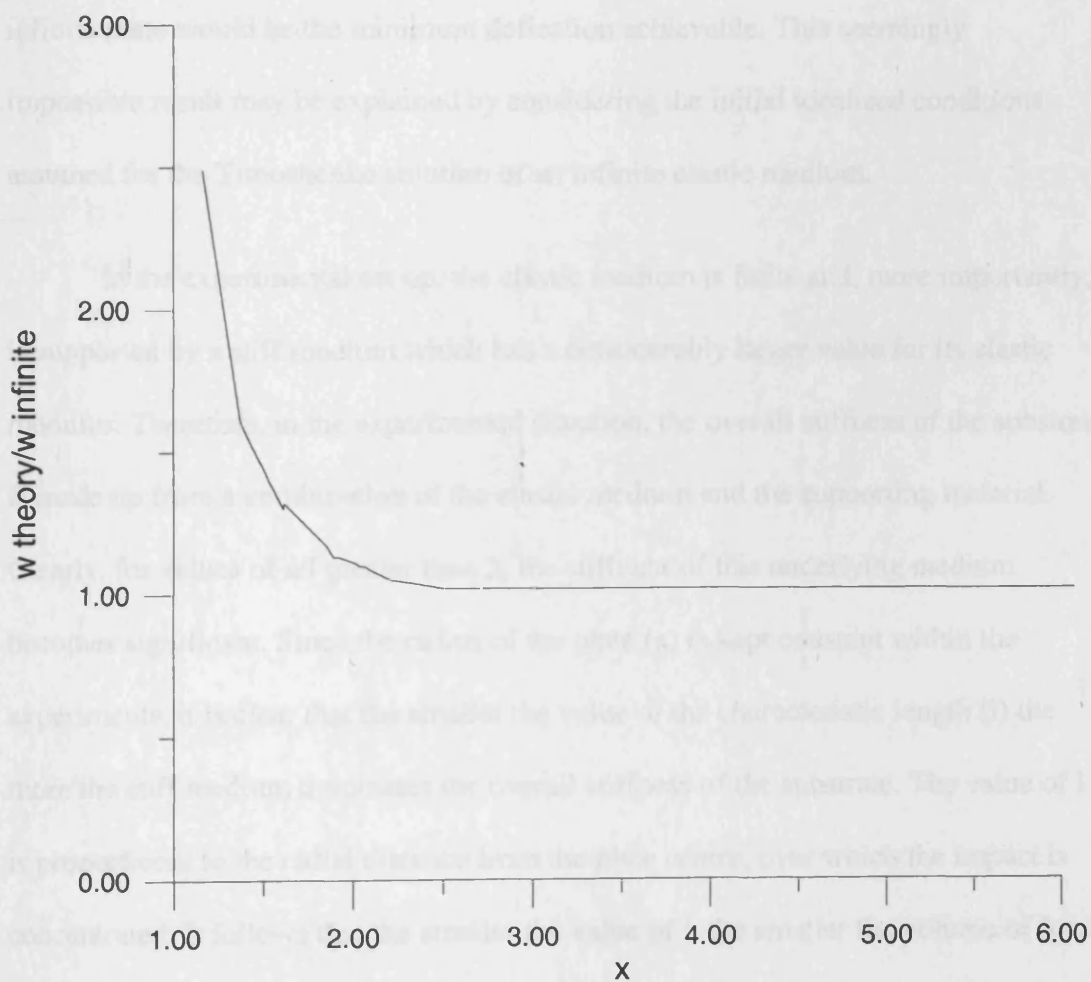
Figure 6.5 Graph showing the results obtained using the unmanipulated Timoshenko solution in conjunction with the experimental data.



Essentially, we can see from the plot in figure 6.5 that the theoretical displacement approaches the displacement for an infinite plate as x reaches 2.5. Thereafter it begins to drift away again. Clearly as x gets larger the solution should converge on one. The solution begins to drift because an error is introduced into the solution by our initial neglect of series terms greater than x^6 . As x gets larger the error increases and this explains the drift away from 1. Essentially, the graph may be replotted as shown in figure 6.6, which may be in turn be interpreted to indicate that if

the ratio between the characteristic length and the radius of the plate becomes greater than 2.5, the plate should behave as an infinite one.

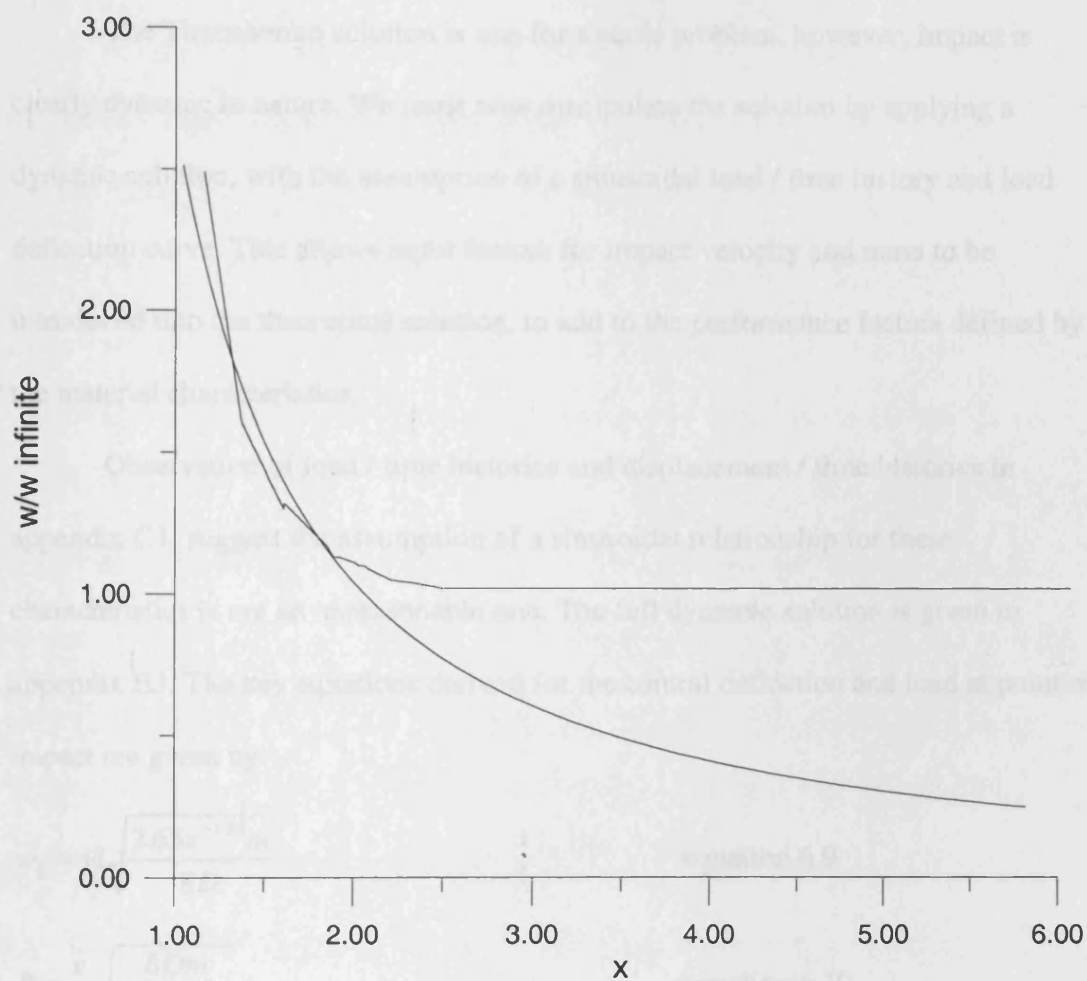
Figure 6.6 Timoshenko solution with error caused by neglecting higher terms of x removed.



If we now compare the plots for our experimental results and the theoretical results as shown in figure 6.7, an anomaly is observed. For $x < 2$ the two sets of results follow each other closely, but thereafter they begin to diverge, with the theoretical solution equating to the infinite plate solution, whilst the experimental solution suggests central deflections increasingly lower than that for an infinite plate as x continues to increase. This situation should be impossible, as the deflection for an infinite plate would be the minimum deflection achievable. This seemingly impossible result may be explained by considering the initial idealised conditions assumed for the Timoshenko solution of an infinite elastic medium.

In the experimental set up, the elastic medium is finite and, more importantly, is supported by a stiff medium which has a considerably larger value for its elastic modulus. Therefore, in the experimental situation, the overall stiffness of the substrate is made up from a combination of the elastic medium and the supporting material. Clearly, for values of a/l greater than 2, the stiffness of this underlying medium becomes significant. Since the radius of the plate (a) is kept constant within the experiments, it is clear that the smaller the value of the characteristic length (l) the more the stiff medium dominates the overall stiffness of the substrate. The value of l is proportional to the radial distance from the plate centre, over which the impact is concentrated. It follows that the smaller the value of l , the smaller the volume of foam which is affected by the impact, and the foam therefore becomes less significant.

Figure 6.7 Comparison of Timoshenko and experimental solutions.



The Timoshenko theory has been used to develop an equation that defines the experimental behaviour through arrangement into non-dimensional groups. This equation presents a solution that is fundamentally different to the initial theory.

6.6 Applying a Dynamic Solution to the data.

The Timoshenko solution is one for a static problem, however, impact is clearly dynamic in nature. We must now manipulate the solution by applying a dynamic solution, with the assumption of a sinusoidal load / time history and load deflection curve. This allows input factors for impact velocity and mass to be introduced into the theoretical solution, to add to the performance factors defined by the material characteristics.

Observation of load / time histories and displacement / time histories in appendix C1, suggest the assumption of a sinusoidal relationship for these characteristics is not an unreasonable one. The full dynamic solution is given in appendix E3. The key equations derived for the central deflection and load at point of impact are given by:

$$w_0 = vl\sqrt{\frac{2.65x^{-1.34}m}{8D}} \quad \text{equation 6.9}$$

$$P = \frac{v}{l}\sqrt{\frac{8Dm}{2.65x^{-1.34}}} \quad \text{equation 6.10}$$

$$\Delta t = \pi l\sqrt{\frac{2.65x^{-1.34}m}{8D}} \quad \text{equation 6.11}$$

where

v = impact velocity

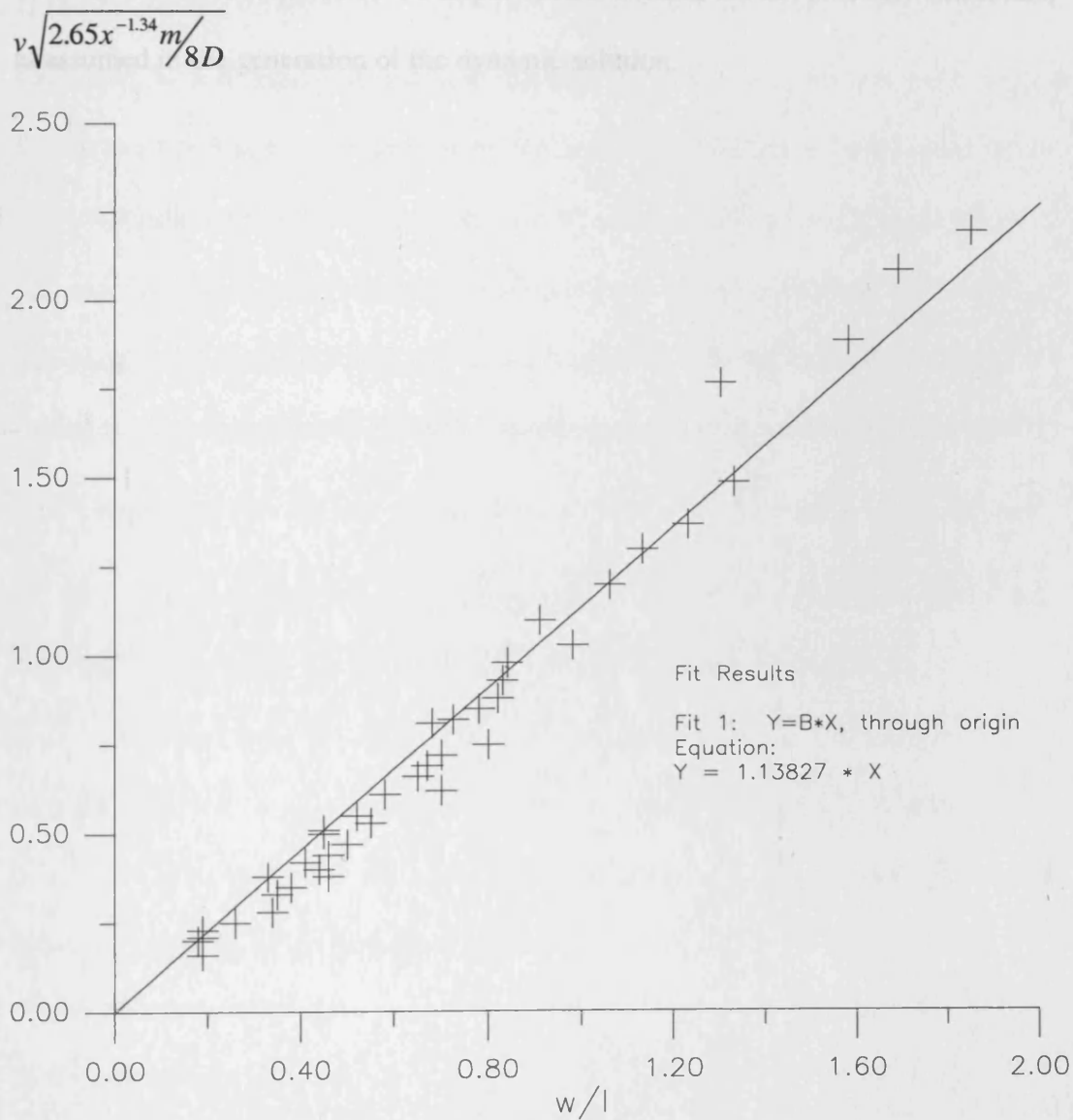
m = mass of impactor

P = load at point of impact

Δt = duration of impact

The validity of this relationship may be tested using the experimental data, this is plotted in figure 6.8.

Figure 6.8 Plot of experimental data to validate dynamic solution for w_0 .



Our initial dynamic solution gives:

$$w_0 = \nu l \sqrt{\frac{2.65x^{-1.34}m}{8D}} \quad (6.9)$$

However, from the plot we can see the relationship must be adjusted to:

$$w_0 = 0.88vl \sqrt{\frac{2.65x^{-1.34}m}{8D}} \quad \text{equation 6.12}$$

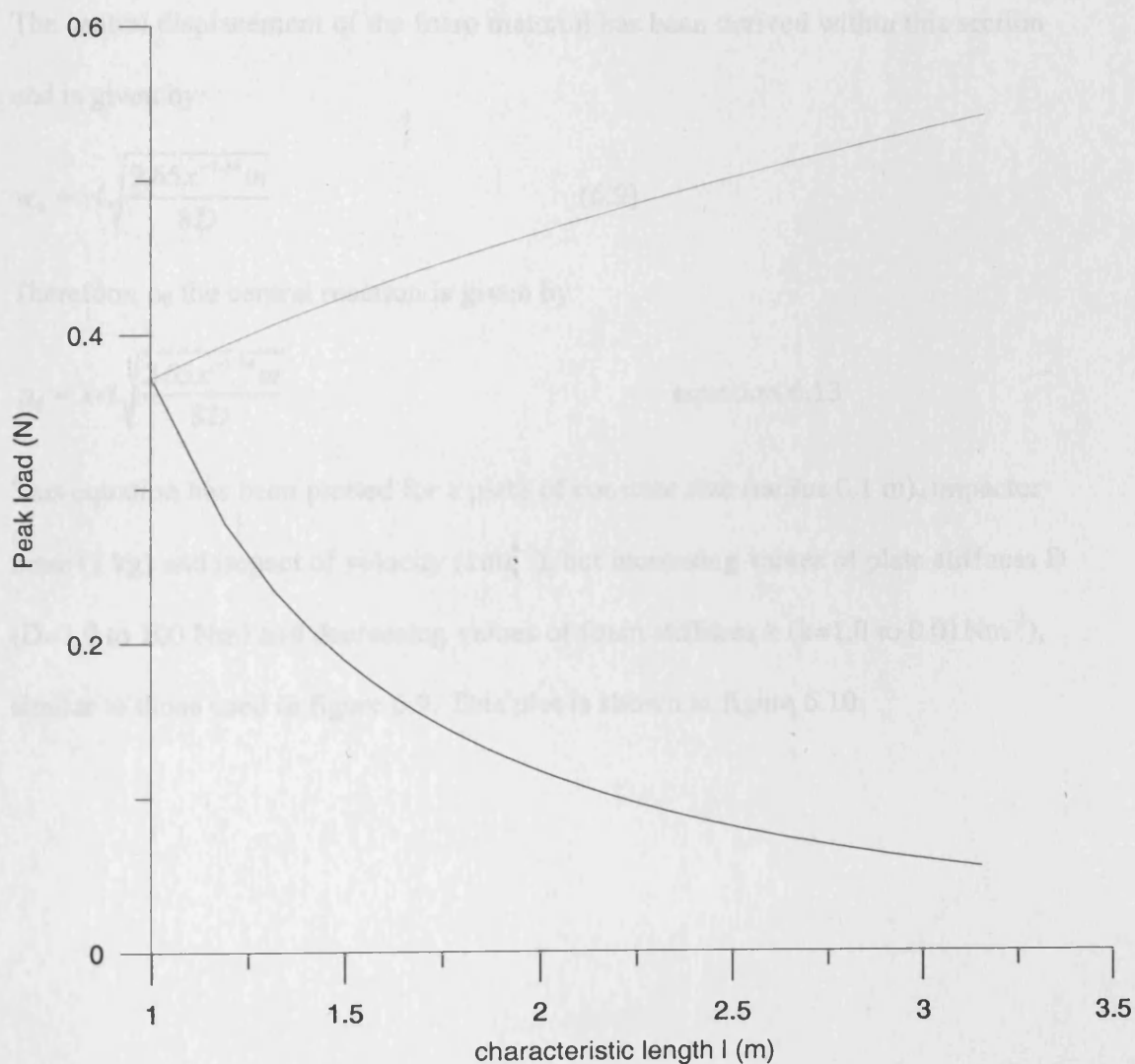
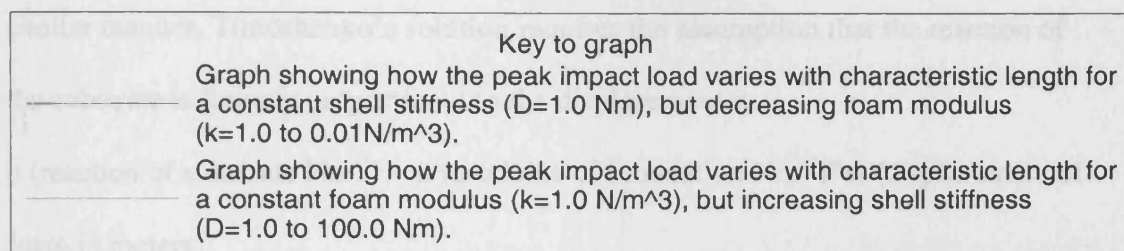
This adjustment is required as the impact characteristics are not precisely sinusoidal, as assumed in the generation of the dynamic solution.

6.6.1 Significance of derived formulae.

As detailed in chapter 2, shin pads prevent injury by means of shock absorption, spreading the load over a larger surface area and modifying the load / time history of the impact event. Returning to the equations which describe shin pad behaviour, we may now evaluate how varying the individual terms that make up these equations affect these two important methods through which shin pads reduce injury.

Consider a plate of unit size (radius 0.1 m), impactor mass (1 kg) and impact velocity (1ms^{-1}). Through observation of equation 6.10, it is apparent that the minimisation of the peak impact load may be achieved by manipulating the value of the foam and plate stiffness. The effect of carrying out these two alternatives on the peak impact load for constant values of l ($l = \sqrt[4]{D/k}$), but increasing values of plate stiffness D ($D=1.0$ to 100 Nm), and decreasing values of foam stiffness k ($k=1.0$ to 0.01Nm^{-3}) is plotted in figure 6.9. The range of D has been selected to tie in with those values used experimentally. The corresponding range of k has been selected to provide a reasonable scale on the plots shown in figures 6.9 and 6.10. The plots are intended to show the effect of varying the material characteristics in principle, rather than over the range of experimental values.

Figure 6.9 Effect of varying plate and foundation stiffness on peak impact load.



The area over which the impact load is spread may also be considered in a similar manner. Timoshenko's solution requires the assumption that the reaction of the substrate is linearly proportional to the displacement w .

p (reaction of substrate Nm^{-2}) = k (modulus of foundation Nm^{-3})* w (displacement of foam in meters)

The central displacement of the foam material has been derived within this section and is given by:

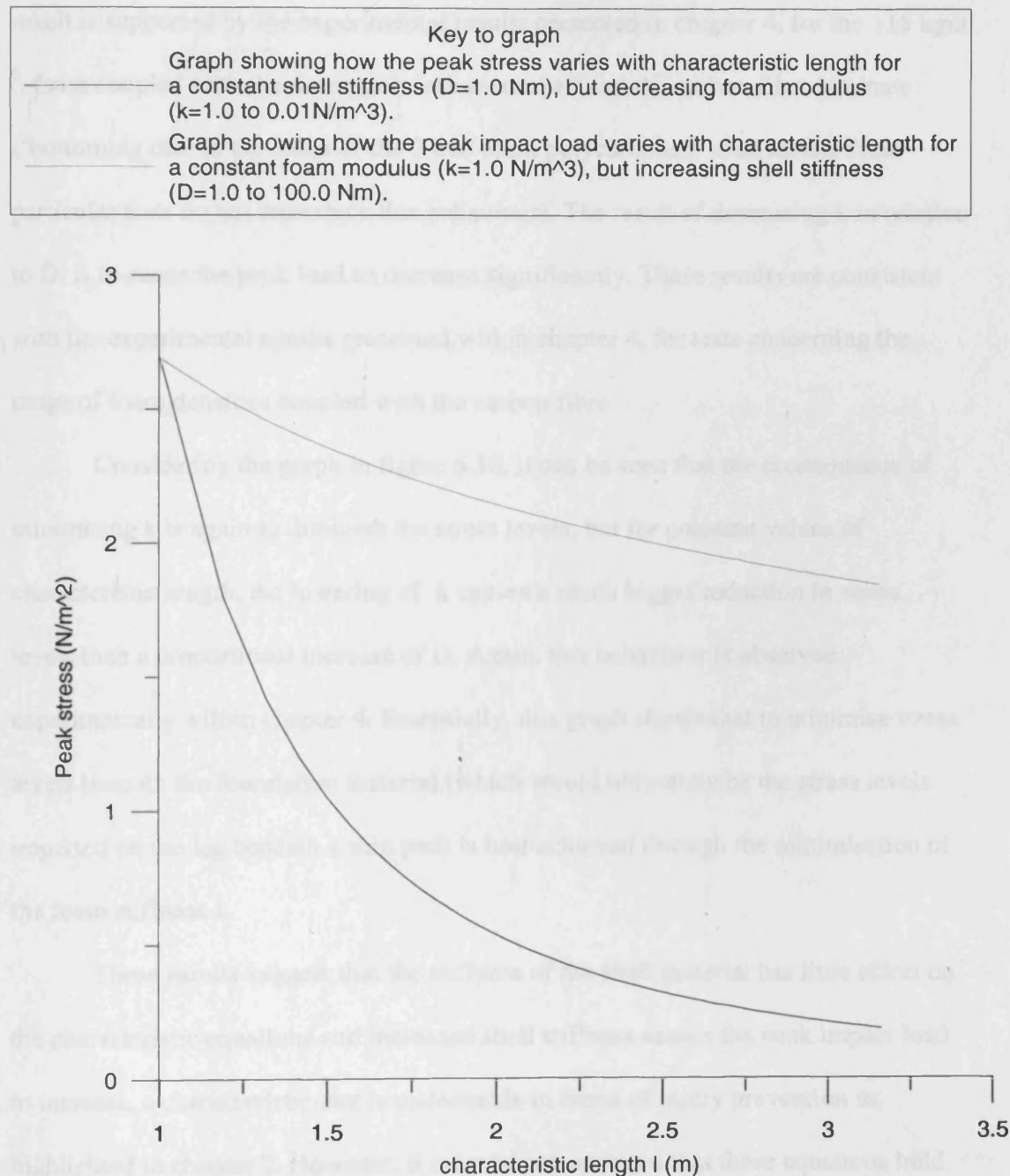
$$w_0 = vl \sqrt{\frac{2.65x^{-1.34}m}{8D}} \quad (6.9)$$

Therefore, p_0 the central reaction is given by

$$p_0 = kvl \sqrt{\frac{2.65x^{-1.34}m}{8D}} \quad \text{equation 6.13}$$

This equation has been plotted for a plate of constant size (radius 0.1 m), impactor mass (1 kg) and impact of velocity (1ms^{-1}), but increasing values of plate stiffness D ($D=1.0$ to 100 Nm) and decreasing values of foam stiffness k ($k=1.0$ to 0.01Nm^{-3}), similar to those used in figure 6.9. This plot is shown in figure 6.10.

Figure 6.10 Effect of varying plate and foundation stiffness on peak stress (Nm^{-2}).



Both figures 6.9 and 6.10 show that for a constant value of l , the peak impact load and stress varies significantly depending on the relative stiffness of the foam (k) and the shell (D). Observation of figure 6.9 shows that increasing D to maximise l

causes the peak impact load to increase as the impulse duration becomes shorter. This result is supported by the experimental results presented in chapter 4, for the 115 kgm³ foam coupled with the 4 mm polycarbonate shell and the carbon fibre laminate ('bottoming out' in the cases of the 2 and 3mm polycarbonate shell means these particular tests do not reproduce this behaviour). The result of decreasing k in relation to D , is to cause the peak load to decrease significantly. These results are consistent with the experimental results presented within chapter 4, for tests concerning the range of foam densities coupled with the carbon fibre.

Considering the graph in figure 6.10, it can be seen that the consequence of minimising k is again to diminish the stress levels, but for constant values of characteristic length, the lowering of k causes a much bigger reduction in stress levels than a proportional increase of D . Again, this behaviour is observed experimentally within chapter 4. Essentially, this graph shows that to minimise stress levels beneath the foundation material (which would ultimately be the stress levels imparted on the leg beneath a shin pad) is best achieved through the minimisation of the foam stiffness k .

These results suggest that the stiffness of the shell material has little effect on the characteristic equations and increased shell stiffness causes the peak impact load to increase, a characteristic that is undesirable in terms of injury prevention as highlighted in chapter 2. However, it must be remembered that these equations hold only for the situation of foam dominated behaviour where no 'bottoming out' occurs. Reference back to the experimental results presented in chapter 4 shows the importance of the stiffness of the shell material. All tests conducted with the lowest

stiffness 2 mm polycarbonate shell displayed the 'bottoming out' effect irrespective of the foam stiffness of the supporting medium. As a result of which both the peak impact load and stress levels induced were extremely high in comparison to results where no 'bottoming out' occurred.

The purpose of this section has been to analyse the equations that explain shin pad behaviour. Through the minimisation of the modulus of the elastic foundation, the peak load and consequently the peak bending moment may be reduced. Care must be taken to ensure k is not reduced excessively causing the 'bottoming out' effect, it is anticipated that this may be avoided by increasing the value of the shell stiffness.

Substituting 6.16 for α_1 in equation 6.12 gives:

6.7 Adding criteria to the solution to obtain optimum material properties.

It is clear that in the design of a shin pad it is desirable to minimise the modulus of the foundation as much as possible, to cause the peak impact load to be as low as possible. This section deals with the introduction of criteria to achieve this minimisation, while ensuring the 'bottoming out' effect described in chapter 4 does not occur in the load range anticipated.

6.7.1 The first criterion

The first criterion is that the foam must not crush by more than 80% of its thickness. This is important for three reasons. Firstly, the materials exhibit two modes of behaviour experimentally. At relatively low compressive strains the behaviour is foam dominated, at high strains; shell dominated. For the purpose of developing the theory, tests exhibiting foam dominated behaviour has exclusively been used.

Therefore, if the foam strains over 80% the shell dominated behaviour becomes predominant, and the equations calculated would be unlikely to hold. If the foam is highly compressed, it has been experimentally shown in chapter 4, that the stresses beneath the foam become extremely large, leading to an increased possibility of fracture. Most importantly, by obtaining the largest deformation possible without 'bottoming out' occurring, the deceleration properties of the foam material are utilised to their fullest potential. In effect, the stiffness of the foam material (represented by k) is minimised as much as possible, a characteristic which has been proven to minimise the peak load and peak pressure occurring during impact in section 6.6.1.

Substituting $0.8h$ for w_0 in equation 6.12 gives:

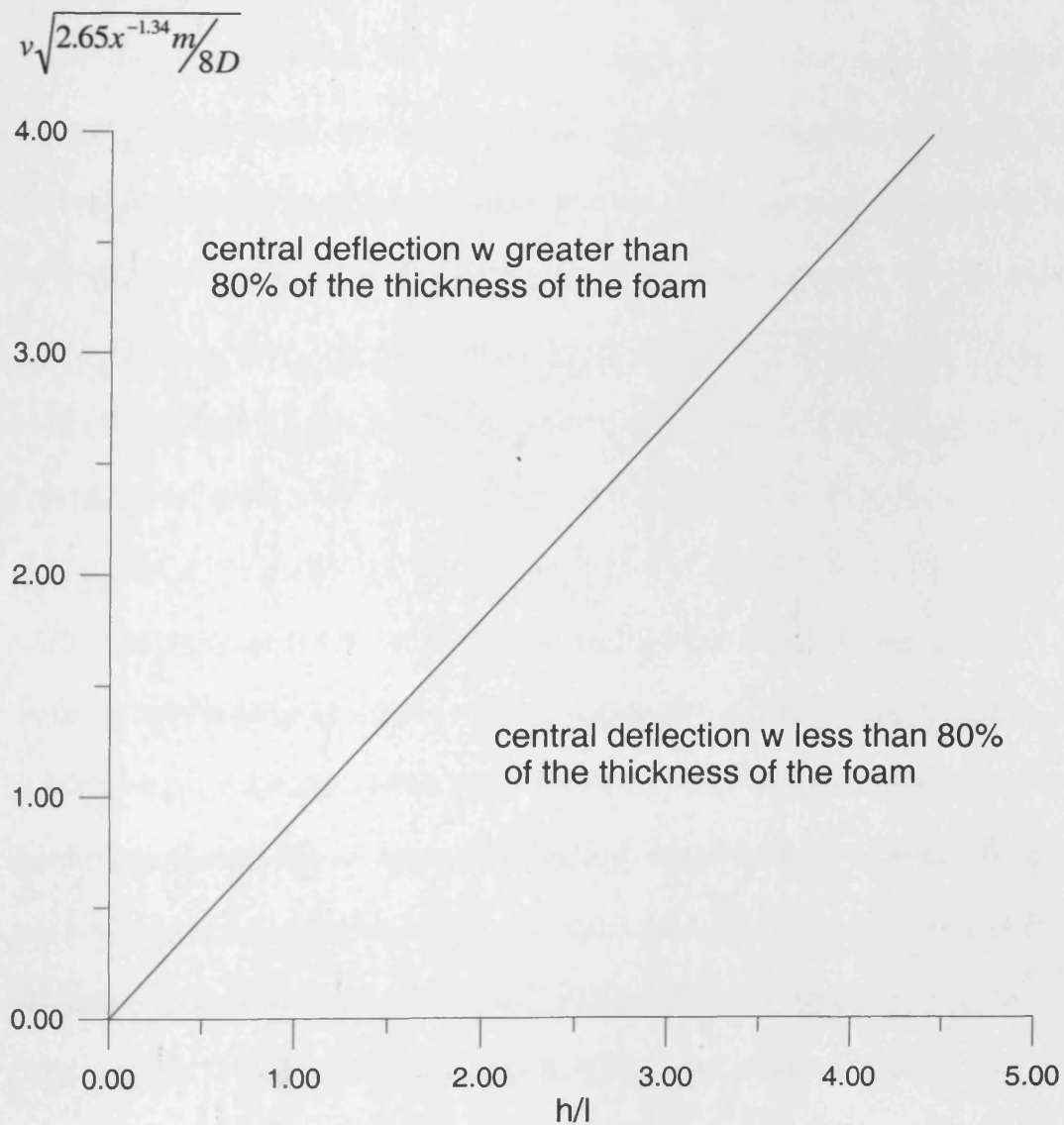
$$0.8h = 0.88vl\sqrt{\frac{2.65x^{-1.34}m}{8D}} \quad \text{equation 6.13}$$

expressing non-dimensionally:

$$\frac{h}{l} = 1.1lv\sqrt{\frac{2.65x^{-1.34}m}{8D}} \quad \text{equation 6.14}$$

Plotting this we obtain the following solution:

Figure 6.11 Graphical solution for first criterion



The following equation satisfies the first criterion.

$$\frac{h}{l} = 1.11v \sqrt{\frac{2.65x^{-1.34}m}{8D}} \quad (6.14)$$

Equation (6.14) provides a threshold for any impact factors (such as impactor mass or velocity) and any preference to favour given as shell thickness or mobility of the foundation, for any given velocity (impact factor) or form thickness. Such a formula has been derived in section 5.3, a further threshold criteria has also been added in section 6.1.4, which is given in equation 6.15 above. This equation may be rearranged to give equation 6.14 below, by inserting values for the impactor mass (m), velocity (v), shell thickness (D). Correspondence (D) calculated up to a limit of 10% using the method detailed in section 6.1.3 to obtain a weight (m) and give radius (r) using equation 6.14. The thickness of shell required to obtain a strain of 10% may

be calculated by equation 6.15, which is equation 6.14 rearranged to give:

$$\left(\frac{Dh}{l}\right)^2 = \frac{1.11^2 v^2 m}{8D} \quad (6.15)$$

Before proceeding further, it must be noted that this equation gives an accurate representation of what is occurring approximately. To obtain complete equivalence to the model, further FEA simulations have been carried out which extend beyond the limits of the original work, by modelling different material and geometries of more varying impact velocities. The form model has been changed to thickness of density 70 kg/m³ which has been successfully modelled by Williams (1971) as discussed in section 5.3.3. It must be noted that for the modelling of the form, the FEA model is based on the model as shown

6.7.2 Proof by application of equation derived using first criterion.

The aim of organising the Timoshenko solution into non-dimensional groups was to obtain a relationship that holds for any input factors (such as impactor mass or velocity) and any performance factors (such as shell stiffness or modulus of the foundation), for any geometry (plate radius or foam thickness). Such a formula has been derived in section 6.5, a further behavioural criteria has also been added in section 6.7.1, which is given in equation 6.14 above. This equation may be rearranged to give equation 6.15 below, by inputting values for the impactor mass (m), velocity (v), shell stiffness (D), foam modulus (E , calculated up to a strain of 80% using the method detailed in section 6.4.1 to obtain a straight line equivalent) and plate radius (a) into equation 6.14. The thickness of foam required to obtain a strain of 80% may

then be calculated by iteration.
$$\frac{h}{\left(\frac{Dh}{E}\right)^{\frac{1}{4}}} = 0.639v \sqrt{\frac{m}{\left(\frac{a}{\left(\frac{Dh}{E}\right)^{\frac{1}{4}}}\right)^{1.34} D}} \quad \text{equation 6.15}$$

Before going any further, it must be verified that this equation gives an accurate representation of what is occurring experimentally. To ensure complete confidence in the formula, further FEA simulations have been carried out which extend beyond the limits of the original tests, by modelling differing materials and geometries at more testing impact velocities and mass. The foam material has been changed to Microvon of density 70 kgm^{-3} which has been successfully modelled by Williams (1995)^[5.1], as discussed in section 5.3.2. It must be noted that for the modelling of this foam, the Poisson's ratio was defined within the model as lateral

strain. All values were taken directly from William's thesis. Microvon behaves as a typical elastomeric foam, as introduced in chapter 4 section 4.1, a brief introduction to the material is given in appendix E4.

The original FEA model discussed in chapter 5 was defined using a range of data. A fairly varied range for the density of foam ($34\text{--}115\text{ kgm}^{-3}$) and shell stiffness ($1.6\text{--}62.89\text{ Nm}$) was used. However, the mass (1.3 kg), velocity (4ms^{-1} and 8ms^{-1}) of the impactor and radius of the plate (50 mm) have been kept at constant values. Subsequently, these values have been varied within three further case studies carried out using FEA simulation techniques. The basic methodology is the same as that described in chapter 5, with an axisymmetric model of a shell material on a foam substrate. The theoretical model, given by equation 6.15, is used first to find out the thickness of foam required to obtain 80% foam compression under specified loading conditions. This same impact situation is then modelled using FEA incorporating the foam thickness calculated using the formula. If the formula is correct, the computer simulation should provide a central deflection of 80% of the foam thickness. A summary of the results is given below in table 6.4. Full details of the three case studies may be found in appendix E.4.

Table 6.4 results of case studies expected to produce 80% compression.

	Case study A	Case study B	Case study C
Foam used	Microvon 70 kgm^{-3} $E=5.35 \text{ MPa}$	Microvon 70 kgm^{-3} $E=5.35 \text{ MPa}$	Microvon 70 kgm^{-3} $E=5.35 \text{ MPa}$
Impactor velocity (v)	12 ms^{-1}	16 ms^{-1}	16 ms^{-1}
Impactor mass (m)	2 kg	2 kg	3 kg
Plate radius (a)	50 mm	50 mm	120 mm
Plate stiffness (D)	62.89 Nm	15.78 Nm	62.89 Nm
Hypothesised foam thickness required for 80% compression (obtained using equation 6.15)	15.7 mm	31 mm	13.5 mm
Maximum deflection obtained in simulation	13.4 mm	26.6 mm	12.7 mm
Actual strain experienced by foam	85 %	86 %	94 %

As can be seen from table 6.4, the strains occurring in the simulation are consistently higher than the expected 80 %. This is particularly true for case study C, the instance where the radius of the plate is significantly increased. As can be seen from equation 6.15, the radius of the plate is raised to the power of 1.34 and is the most significant individual factor in the equation. From these results, it appears probable that the initial curve fit for the non-dimensional plot given in figure 6.1 is slightly inaccurate. This exaggerated deflection is fortunately offset by the inaccuracy in the modelling as a result of the assumption of a rigid surface.

It was hypothesised in chapter 5 that the simulated peak displacement would be expected to be larger than that occurring experimentally. This hypothesis was proven in section 6.3, where the 'bottoming out' effect for the combination of a 2 mm polycarbonate shell with 12 mm thickness 34 kgm^{-3} foam, clearly occurred within the simulation but not the experiment. In chapter 5, simulation results were on average 13 % shorter in duration and had a peak load 9 % bigger than that which occurred

experimentally. It is not unreasonable to assume the displacement has a similar percentage difference as that occurring for the peak load and total duration for the two methods. Effectively, if we assume the simulation deflects 11 % more than actually occurs experimentally, the deflection occurring for case studies A, B and C are 76 %, 76 % and 84 % respectively which compare well to the desired 80%.

It remains most likely to occur,

The most comprehensive blast impact test results are provided by Karam et al. (1997) as discussed in chapter 2. The paper addressed the problem of pedestrian in urban traffic accidents. It is particularly applicable to the football impact situation as it simulates our blower impact on the distal end of the lower leg. The paper is particularly significant as over 200 subject responses were recorded over an age range of 20 to 70 years of age. According to the literature, and as per bench loading calculations also discussed in chapter 2, a value of 3000N may be considered as the maximum tolerable load.

Re-examining our first criterion:

$$\frac{F}{1000} = 12.15 \sqrt{\frac{2.55 \times 10^6}{80}} \quad (6.14)$$

With our dynamic solution:

$$F = 12.15 \sqrt{\frac{2.55 \times 10^6}{80}} \quad (6.15)$$

Introducing $\alpha = 0.1$

$$F = 12.15 \sqrt{\frac{2.55 \times 10^6}{80 \times 0.1}} \quad (6.16)$$

Substituting $\alpha = 0.1$ into 6.16 we obtain:

$$F = 12.15 \sqrt{\frac{2.55 \times 10^6}{80 \times 0.1}} = 12.15 \sqrt{31875} = 12.15 \times 178.53 = 2170.5 \text{ N}$$

6.7.3 The second criterion

A second criterion which considers the peak load the tibia can withstand without fracture will now be applied. This complements the first criterion by ensuring that the 80% compression occurs at the maximum tolerable load for the tibia.

Therefore, the peak deceleration capacity of the materials occur at the instance when fracture is most likely to occur.

The most comprehensive tibial impact test results are provided by Kramer et al^[2.30], as discussed in chapter 2. The paper addressed the problem of pedestrians in urban traffic accidents. It is particularly comparable to the football impact situation as it simulates car bumper impact on the distal third of the lower leg. The paper is particularly significant as over 200 subject cadavers were tested over an age range of 20 to 90 years of age. According to this literature, and simple beam bending calculations also considered in chapter 2, a value of 5000N may be considered as the maximum tolerable load.

Re-arranging our first criterion:

$$\frac{h}{l} = 1.1lv\sqrt{m}\sqrt{\frac{2.65x^{-1.34}}{8D}} \quad (6.14)$$

From our dynamic solution:

$$P = \frac{v}{l}\sqrt{\frac{8Dm}{2.65x^{-1.34}}} \quad (6.10)$$

rearranging gives:

$$v\sqrt{m} = Pl\sqrt{\frac{2.65x^{-1.34}}{8D}} \quad \text{equation 6.16}$$

substituting 6.16 into 6.14 we obtain:

$$\frac{h}{l} = \frac{0.367 Plx^{-1.34}}{D} \quad \text{equation 6.17}$$

If we substitute the maximum tolerable load of 5000N for P_{\max} as stipulated by our second criterion and recalling:

$$l = \sqrt[4]{D/k}$$

$$k = E^f / h$$

$$x = a/l$$

Substituting these into equation 6.17, we are left with a relationship which defines the behaviour of an idealised shin pad to conform with the two criteria in terms of the thickness of the foam padding h , the thickness of the external shell D , the width of the pad a , and the elastic modulus of the foam padding E^f , shown in equation 6.18.

$$2070 = D^{0.165} h^{0.165} E^{f 0.835} a^{1.34} \quad \text{equation 6.18}$$

$$2070 = D^{0.165} h^{0.165} E^{f 0.835} a^{1.34} \quad \text{equation 6.18}$$

This equation may now be used as a conceptual design tool in the creation of a prototype. This equation simply provides a balance for which the maximum deceleration capabilities of the foam coincide with the load at which the tibia is likely to fracture. For loads higher than the 5000N, fracture is highly probable as the foam will compress more than 80% and the shell material will become dominant in the deceleration process.

It has been highlighted in chapter 2 that the value of 5000N for the maximum tolerable load for the tibia may be rather conservative due to the degeneration of bone associated with age and cadaver storage techniques. The lack of published evidence to suggest a higher tolerable load, effectively means this value has to be adhered to. If in

the light of subsequent research a differing value is obtained the method applied above would still apply, however this value should be substituted for the 5000N which would result in a revised numerical constant in equation 6.18 above.

6.8 Adjustments required to make equation 6.18 applicable to human tibia.

As detailed within section 3.8, all research has been carried out based on testing with the pad materials supported by a medium that may be considered infinitely stiff. In reality, the pad would be supported by a human tibia and this has been shown to have a significant influence on the characteristics of the impact.

Referring back to section 3.8, the peak impact load is given by:

$$\frac{P_{\max}}{P_{\max E \rightarrow \infty}} = \sqrt{\frac{1}{1+X}} \quad (3.6)$$

where X for the tibia is given by:

$$X = (31.6 \times 10^{-6})kab$$

From our original dynamic solution:

$$P = \frac{v}{l} \sqrt{\frac{8Dm}{2.65x^{-1.34}}} \quad (6.10)$$

and:

$$w_0 = vl \sqrt{\frac{2.65x^{-1.34}m}{8D}} \quad (6.9)$$

Recalling our solution is for the case where the pad is supported by an infinitely stiff medium the expression in equation 6.10 may be substituted for $P_{\max E \rightarrow \infty}$ in equation 3.6 which gives the following:

$$P_{\max} = \sqrt{\frac{1}{(1+X)}} \left(\frac{v}{l} \sqrt{\frac{8Dm}{2.65x^{-1.34}}} \right) \quad \text{equation 6.19}$$

Rearranging equation 6.19 gives

$$v\sqrt{m} = Pl \sqrt{\frac{(1+X)2.65x^{-1.34}}{8D}} \quad \text{equation 6.20}$$

Substituting equation 6.20 into 6.9 gives:

$$w_0 = Pl^2 \frac{2.65x^{-1.34}}{8D} \sqrt{1+X} \quad \text{equation 6.21}$$

Substituting for X in equation 6.21. Setting $w_0 = 0.8h$ to comply with first criterion

and $P_{\max}=5000$ to comply with the second and recalling:

$$l = \sqrt[4]{D/k}$$

$$k = E^f/h$$

$$x = a/l$$

the following equation is obtained:

$$.8h = \frac{1656.25 \left(\frac{Dh}{E} \right)^{.5} \left(1 + \frac{.316 \cdot 10^{-5} E a b}{h} \right)^{.5} \left(\frac{1}{\left(\left(\frac{a}{\left(\frac{Dh}{E} \right)^{.25}} \right)^{1.34} D \right)} \right)^{.5}}{\left(D \left(\frac{a}{\left(\frac{Dh}{E} \right)^{.25}} \right)^{1.34} \right)^{.5}} \quad \text{equation 6.22}$$

As can be seen, equation 6.22, which defines the behaviour of an idealised shin pad to conform with the two criteria for a human leg, is considerably more complex than that for a stiff supporting medium. The implications of the discrepancy between the two formulae on the ultimate design of the pad are considered in more detail in chapter 7.

Experimental deflection under a defined load, in terms of the geometry and material properties of the supporting medium. Comparison of equation 6.22 with the experimental data has shown a good correlation up to a certain point, at which the two relations then diverge. This divergence is consistent with the assumption of an infinitely large elastic foundation and occurs as the values of δ increase. It is therefore concluded that the model is valid for relatively low values in the experimental range.

By assuming a constant foundation for the conditions and dimensions specified, a dynamic solution is arrived at that modifies the above-mentioned relationship to include impact velocity and mass. Plotting of experimental data has shown the modified equation to be reasonably accurate, although slight modification to the form of a constant coefficient is required to achieve a better fit to the data. It is concluded that the model is valid for the range of conditions specified.

Analysis of the derived formulae, with respect to the variation of δ , suggests the augmentation of the model to take into account the variation in the geometry of the shin pad. To achieve this, a further assumption is made that the geometry of the shin pad is constant. It is concluded that the model is valid for the range of conditions specified.

6.9 Conclusions.

Using the basic Timoshenko theory for the behaviour of an elastic plate on an infinite elastic foundation, a set of non-dimensional variable groupings has been obtained. Application of experimental data through non-dimensional plots has yielded a relationship for the experimental deflection under a defined load, in terms of the geometry and material properties of the constituent components. Comparison of experimental to theoretical behaviour has shown a good correlation up to a certain point, at which the two solutions then diverge. This divergence is consistent with the assumption of an infinitely large elastic foundation and occurs as the volume of foamed polymer contributing to the impact drops to relatively low values in the experimental case.

By assuming a sinusoidal relationship for the load/time and deflection/time histories of the impact, a dynamic solution is arrived at that modifies the aforementioned relationship to involve impactor velocity and mass. Plotting of experimental data has shown the manipulated equation to be reasonably accurate, although slight modification by the insertion of a numerical constant was required to ensure accurate correlation.

Analysis of the derived formulae, with respect to the causation of injury, suggests the augmentation of the impact load / time history offers the best option in preventing tibial fracture. To achieve this, maximisation of the shell stiffness and minimisation of the foam stiffness is required. Spreading the impact over a larger area does not have a particularly significant effect on the overall bending moment applied

to the tibia, but is again achieved through similar methodology, namely shell stiffness maximisation and minimisation of the foam stiffness.

The addition of two criterion for desirable behaviour characteristics for maximum deformation (not more than 80% of the foam thickness) and peak tolerable load (not more than 5000N) allows the definition of a single equation that outlines the behaviour of an idealised shin pad. This equation gives an optimum condition where a load of 5000N coincides with the maximum foam deflection allowable, without risking onset of 'bottoming out' effects. The equation is defined in terms of the thickness of the foam padding, the stiffness of the outer shell, the radius of the pad, and the elastic modulus of the foam padding. This equation has been verified by comparing the deflections predicted for a range of different materials under increased load cases to those obtained by computational FEA under the same conditions.

References

- [6.1] Timoshenko
Theory of Plates and Shells
McGraw-Hill 1959
Chapter 8 pp 259-281

Chapter 7

Development and Manufacture of Prototype.

7.0 Introduction.

Following on from the theoretical work carried out in chapter 6, we now have a method of predicting the behaviour of any combination of materials under an impact situation similar to that which occurs in the game of soccer. The next logical step is to use this method to select the optimal material combination to protect against injury caused by a football tackle. In essence, we have an equation that sets the maximum possible deformation to coincide with the maximum tolerable load in terms of four basic quantities, thus making the optimum possible use of the decelerating properties of the foam material.

Returning to the equation derived in the previous chapter:

$$2070 = D^{0.165} h^{0.165} E^{0.835} a^{1.34} \quad \text{equation (6.18)}$$

As can be seen from equation 6.18 the behaviour is dependant principally on the radius of the plate, and then in order of reducing influence, E^f , D and h . Within the equation, the radius of the plate is basically defined by the average length of the shin, and the thickness of the foam padding (which as can be seen in equation 6.18 is not as influential as either foam stiffness or pad size) is controlled by practicality. This leaves us with the dominant design factors of D , the stiffness of the outer shell, and more importantly, E^f , the modulus of elasticity of the foam. This chapter addresses how to use this equation to arrive at the optimum material combinations; materials that fit the equation, but are also realistically priced and easily manufactured, to ensure the final product may be viably mass produced. Equation 6.22, which

describes the pad behaviour when supported by the tibia is also analysed within this section to determine optimum material combinations for actual use. Once the material selection process has been finalised, the chapter ultimately addresses the production of a prototype. The prototype produced within this chapter is based on the equation (6.18) derived using an infinitely stiff supporting medium rather than the tibia. This has been carried out to allow the experimental proof of principle for the theoretical work, and is dealt with in detail in chapter 8.

7.1 Design Considerations.

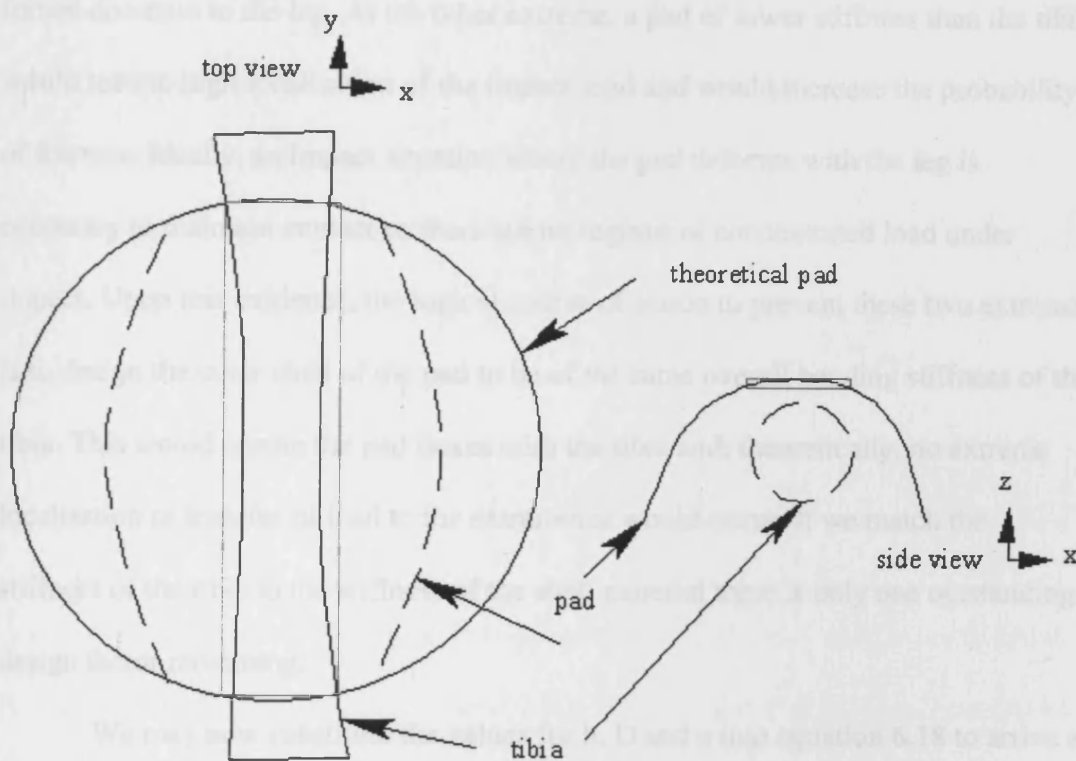
The definitive equation (6.18) has been developed assuming a 'flat symmetrical plate' situation, a condition that is clearly not the case for a shin pad which has a curved outer shell and a length substantially greater than its width to follow the contour of the shin. With respect to the theory addressed in chapter 6, the characteristic length ($l = 4\sqrt{\frac{D}{k}}$) which is fundamental in describing pad behaviour, would now vary from the original circular region as a result of the alternative geometry and the associated variation of shell stiffness D with location on the pad shell. This would be further complicated as the natural flexure under impact loading would cause the outer flanges of the pad to move upward and away from the leg. It is therefore extremely difficult to calculate what overall geometry the new characteristic length would acquire under these circumstances, to allow a 'global' definition of pad behaviour. Effectively the removal of the flatness and symmetry of the shell means equation 6.18 may no longer be used to describe the behaviour of the whole guard, as the characteristic length now has a directional dependency. However, if we

concentrate on a single plane within the pad of a constant, or alternatively, an experimentally determined stiffness, the theoretical solution should still be valid.

Consider the diagram shown in figure 7.1. Along the plane designated as y, roughly represented by the region enclosed by a red box (labelled as top view), there is a similar geometry for both the actual and theoretical pad. Over this region there is only a slight deviation from a level surface, and behaviour may be assumed to be similar to that occurring in the flat plate situation from which the theory is derived. This is also the zone over which an impact is most likely to cause fracture due to the lack of flesh protecting the bone, and is therefore the region of most interest.

In assuming that along the plane parallel to the tibia the pad behaves as a flat plate, it must be recognised that the bending stiffness is defined by the whole geometry of the pad, and not just that enclosed by the box in figure 7.1. To address this problem, the stiffness of any prospective material must be accurately measured for a curved plate of the approximate geometry of the proposed shin pad. By forming the shell material into a curved plate of the approximate dimensions of a shin pad and applying a central load, the bending stiffness in the plane parallel to the long axis of the tibia may be measured and substituted into equation 6.18. A detailed consideration of the experimental procedure used to achieve this is discussed in more detail in section 7.2.2.

Figure 7.1 Actual geometry for shin pad compared to theoretical geometry.



As detailed in chapter 4, the stiffer the outer shell material the larger the area over which the impact is spread. However, referring back to chapter 2, it is clear that if the stiffness of the pad is greater than the stiffness of the tibia, a bolster effect is a plausible outcome which has been proven to lead to knee and ankle ligament damage. This is supported by work by Viano et al^[2.34] (this work is considered in detail in section 2.8) in which a bolster impact was carried out on the lower leg of seven cadavers (4 male, 3 female). All female cadavers exhibited fracture of the tibia and fibula, however, none of the male legs were fractured. Two male subjects showed no serious injury, but the other two showed tears and avulsions of the posterior cruciate ligament. This is potentially a more serious injury than fracture of the tibia and the

bolster impact test method may be considered very similar to a stiff shin guard being forced down on to the leg. At the other extreme, a pad of lower stiffness than the tibia would lead to high localisation of the impact load and would increase the probability of fracture. Ideally, an impact situation where the pad deforms with the leg is necessary to maintain contact so there are no regions of concentrated load under impact. Upon this evidence, the logical course of action to prevent these two extremes is to design the outer shell of the pad to be of the same overall bending stiffness of the tibia. This would ensure the pad flexes with the tibia and, theoretically, no extreme localisation or transfer of load to the extremities would occur. If we match the stiffness of the tibia to the stiffness of the shell material there is only one outstanding design factor remaining.

We may now substitute the values for h , D and a into equation 6.18 to arrive at an idealised E^f . Realistically, the value of the thickness of the foam material must be limited to 6 mm thickness to prevent the pad becoming too cumbersome thus reducing the performance level of the wearer. The radius of the outer shell is also governed by practicality. In available literature (Yamada, 1970)^[2,29] the length of the tibia ranges from between 35 and 45 cm. In previous work (Cattermole et al, 1996)^[2,10] it was shown nearly all (93%) of the fractures initiated in the distal third of the tibia and this is clearly the area which the pad must protect. Consequently, a pad of length 200 mm would protect this vulnerable area for all tibia lengths, and the radius of the pad may be set at 100 mm. As previously discussed, the stiffness of the outer shell must be equivalent to the stiffness of the tibia (EI) which has been calculated to be approximately 900 Nm (this is considered in detail later within this

chapter) Substituting $h=0.006$ m, $a=0.1$ m and $D=900$ Nm into equation 6.18 we obtain an idealised E^f of 0.28 MPa.

This is the optimum for a pad supported on a stiff medium. As discussed in chapter 6 section 6.8, the relationship for a pad supported by the tibia is rather more complicated and is given by:

$$.8 h = 1656.25 \frac{\left(\frac{Dh}{E}\right)^{.50} \left(1 + .316 10^{-5} \frac{E a b}{h}\right)^{.5} \left(\frac{1}{\left(\frac{a}{\left(\frac{Dh}{E}\right)^{.25}}\right)^{1.34} D}\right)^{.5}}{\left(D \left(\frac{a}{\left(\frac{Dh}{E}\right)^{.25}}\right)^{1.34}\right)^{.5}} \quad (6.22)$$

Again, substituting foam thickness $h=0.006$ m, pad radius $a=0.1$ m, pad width $b=0.1$ m and $D=900$ Nm into equation 6.22 we obtain an equation that requires iteration to solve for E^f .

$$.0048 = .65 \times 10^{-5} \left(\frac{1}{E}\right)^{\frac{167}{200}} \sqrt{.1 \times 10^{15} + .1 \times 10^{10} E}$$

To satisfy this equation, an E^f value of 0.16 MPa is required.

The combination of the theoretical and experimental work has provided an explicit solution for the stiffness of the foam material of 0.28 MPa for the idealised impact situation, and a predicted value of 0.16 MPa for the true impact situation. The non-linearity of the stress / strain curves for cellular materials again provides a problem in defining a singular elastic modulus for the foams. Once more, the method defined in chapter 6 section 6.4.1 may be used. Summarising this method, the area

beneath the stress/ strain curve, up to 80%, is re-plotted as a straight line, with the E value calculated as the gradient of this equivalent plot. Effectively by using this method, the two plots provide identical strain energies for the same deflection, but a definite elastic modulus is now defined.

Most of this work was carried out using data from the Cambridge Material Selector (CMS) programme (written by Peter Smith). Further potential materials outside the scope of this package were also tested under compression. A number of potential designs fitted the criteria, along with a further substance called Plastica.

Although essentially a cellular material, Plastica is basically a high strength bubble wrap (typically used as a packaging material, with a bubble diameter of 10mm). A picture of a piece of Plastica is shown below in figure 7.2.

Figure 7.2 Plastica, bubble radius 5mm



The graph below shows up to 80% compression for Plastica with a bubble radius of 5mm. The graph shows a linear relationship between stress and strain, indicating a definite elastic modulus.

C

7.2 Material selection

7.2.1 Cellular material selection

A comparison of available cellular materials was carried out to allow selection of a material that fitted the required E^f value. Most of this work was carried out using data from the Cambridge Material Selector (CMS) programme foamed polymer database. Further potential materials outside the scope of this package were also tested under compression. A number of potential foams fitted the criteria, along with a further substance called Plastica.

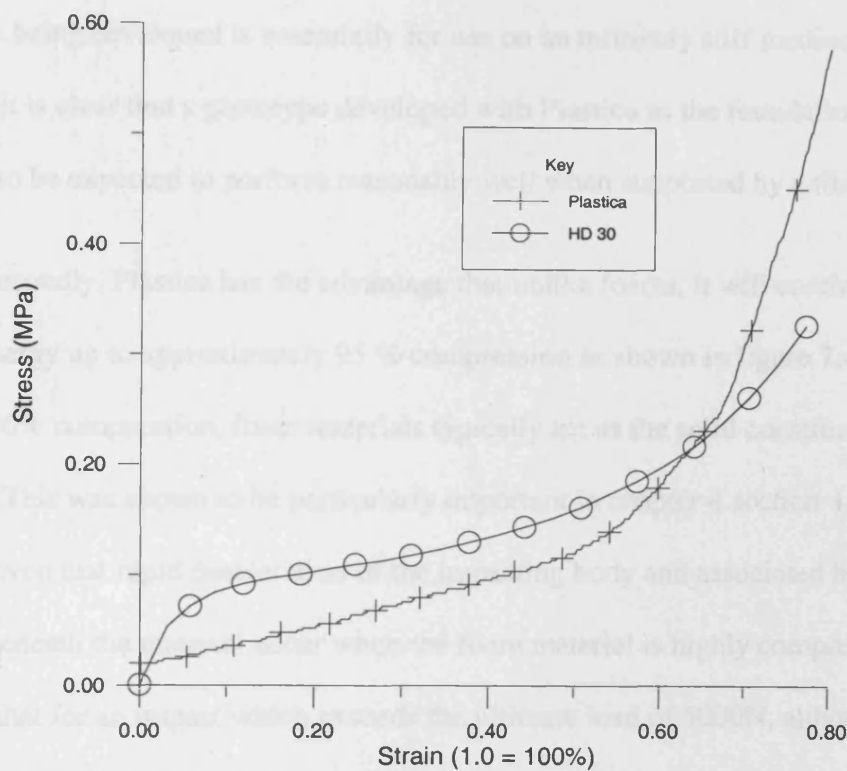
Although essentially a cellular material, Plastica is basically a high strength 'bubble wrap' typically used as a packaging material, with a bubble thickness of 400 microns. A picture of a piece of Plastica is shown below in figure 7.2.

Figure 7.2 Plastica. Bubble radius 5 mm.



The stress / strain curves up to 80% compression for Plastica and one of the suitable foams (HD30) is shown in figure 7.3 below.

Figure 7.3 Comparison of stress strain curve for Plastica and HD 30.



As can be seen, the areas beneath the curves are almost identical up to a strain of 80% and, although the individual path characteristics vary, both show the desirable attribute of progressive strain hardening. Plastica has been selected above the foam materials for three basic reasons.

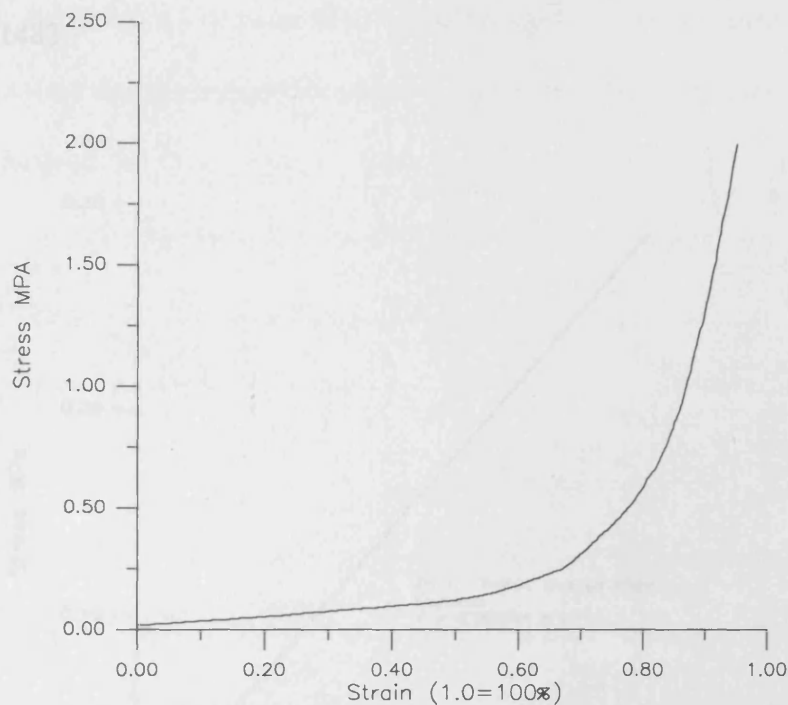
As discussed in section 7.1, where the pad is to be supported by the tibia the optimum modulus of elasticity for the foam is predicted to drop to 0.16 MPa. Using the curve linearisation method first introduced in chapter 6, the Plastica has an E value of 0.16 MPa for a compression of 67 %, whereas the foam material has a comparable E value for 45 % compression. Although the Plastica material does not accurately fit the criteria for the tibia supported pad, it would be expected to perform considerably better than the HD 30. The material of lesser stiffness (Plastica) would

produce the lowest deceleration and therefore the longest response times. The prototype being developed is essentially for use on an infinitely stiff medium, however it is clear that a prototype developed with Plastica as the foundation material would also be expected to perform reasonably well when supported by a tibia.

Secondly, Plastica has the advantage that unlike foams, it will continue to absorb energy up to approximately 95 % compression as shown in figure 7.4 below. Beyond 90% compression, foam materials typically act as the solid constituent polymer. This was shown to be particularly important in chapter 4 section 4.4, where it was proven that rapid deceleration of the impacting body and associated high stresses beneath the material occur when the foam material is highly compressed. This suggests that for an impact which exceeds the ultimate load of 5000N, although a fracture is the likely outcome, the fact some of the energy will continue to be absorbed and the 'bottoming out effect' discussed in chapter 4 will therefore be delayed, may lessen the severity of the injury.

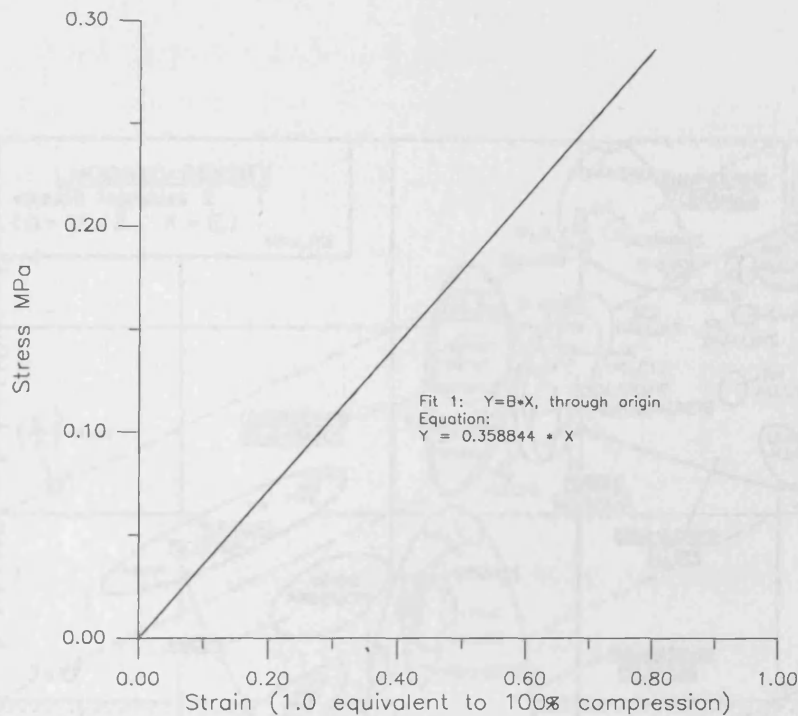
Thirdly although the foams are closed cell, they will still take on moisture from the environment. This could be a particular problem when playing in excessively wet conditions where moisture absorption would lead to an increase in pad weight and, more importantly possibly affect the stress / strain characteristics of the foam. This problem can not occur with Plastica as all cells are isolated completely from the outside environment.

Figure 7.4 Full stress / strain curve for Plastica.



The area beneath the stress / strain curve for Plastica up to 80 % compression (shown above in figure 7.3) has been measured as 0.11483 Nm^{-2} . Re-plotting this curve as a straight line, as shown in figure 7.5 below, by equating strain energy potential (the method introduced in chapter 6 section 6.4.1) a single modulus of elasticity may be defined. As can be seen the E^f for Plastica is 0.359 MPa which compares well to the calculated optimum of 0.28 MPa.

Figure 7.5 Equivalent plot for Plastica strained to 80% compression. Area under curve = 0.11483.



7.2.2 Outer Shell material selection.

For the shell material, it is required that the stiffness to weight ratio is high to obtain the required stiffness whilst keeping the thickness and weight of the pad to a minimum. Considering the Ashby diagram shown below in figure 7.6, the optimum material group to obtain this ratio is the engineering composites and, in particular, the carbon fibre laminates. However, the cost and moulding time, which requires the use of an autoclave, makes the use of this material unviable for a mass produced pad at a

Figure 7.6 Ashby diagram reproduced from ‘Material Selection in Mechanical Design’ M Ashby^[7.1]



The outstanding material in this group is called Twintex which is made up of woven polypropylene and glass fibres. The material properties for both the basic balanced weave and a specially produced directionalised weave, with a ratio of four fibres in the x direction and one in the y direction are shown in table 7.1 below.

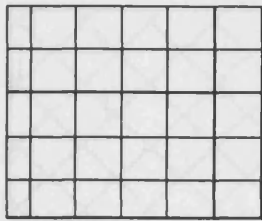
Table 7.1. Twintex composite mechanical characteristics.

Characteristic	Tested to specification	Units	balanced weave	directionalised weave 4:1
Tensile strength	(ISO 527)	MPa	350	400/130
Tensile modulus		GPa	15	28/6
Tensile strength	(ISO 178)	MPa	280	380/160
Tensile modulus		GPa	13	18/6
Charpy impact unnotched	(ISO 178)	kJm^{-2}	220	330/90
Izod impact notched	(ISO 180)	kJm^{-2}	180	260/95
Glass content in weight		%	60	60
Glass content in volume		%	35	35

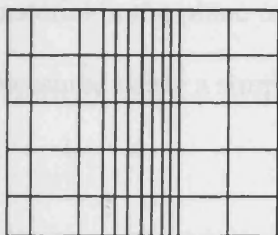
The material is inexpensive at 3.00 pounds sterling per square meter and, crucially, will form to shape within seconds at both low temperature (180-230 degrees centigrade) and pressure (approximately 1 bar), to allow ease of mass production.

Because Twintex is a laminate material and therefore non isotropic, there are difficulties in defining a modulus of elasticity. As highlighted in section 7.1, it is also being used to form a curved shell to fit the shin, thus causing a variety of loading conditions in terms of both magnitude and direction, depending on the location within the shell. To deal with bending, tests have been conducted on a curved plate (comparable in size, 220 mm length, to that required for a shin pad) made from various Twintex composite lay ups to discover an approximate elastic modulus. A 3 inch diameter cylinder was used to provide a mould for the various lay ups which were as follows:

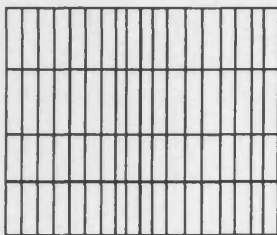
Laminate 1 basic balanced weave orientated at 0, and 90° to the axis of loading.



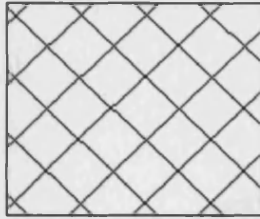
Laminate 2 basic balanced weave orientated at 0, and 90° to the direction of loading,
with central strips of directionalisised 4:1 weave.



Laminate 3 directionalised weave in the ratio of 4:1.



Laminate 4 basic balanced weave orientated at $\pm 45^\circ$ to the axis of loading



A special tool made of two basic parts was manufactured from aluminium.

These are shown below in figure 7.7a and 7.7b. The idea being that the stiffness of the material in the plane of interest (parallel to the long axis of the tibia) may be measured using a simple modified bending test.

Figure 7.7b Tool placed mid span on the upper surface of the curved plate



The first part shown in figure 7.7a acts as a rigid support for the plate, maintaining contact at the upper and lower ends of the plate. The second part (7.7b) is placed centrally on the upper surface of the plate, again ensuring contact. Loading is applied using a mechanical fixture with two pneumatic cylinders, a cross beam

Figure 7.7a Base upon which the curved plate is placed.

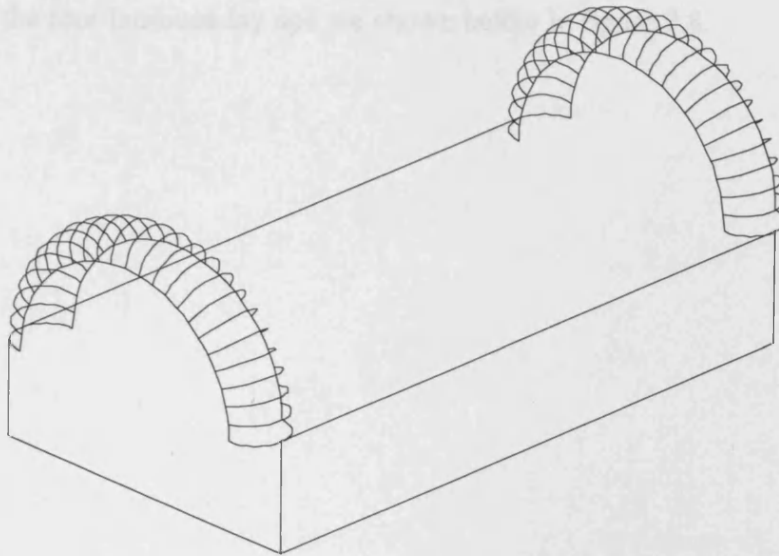
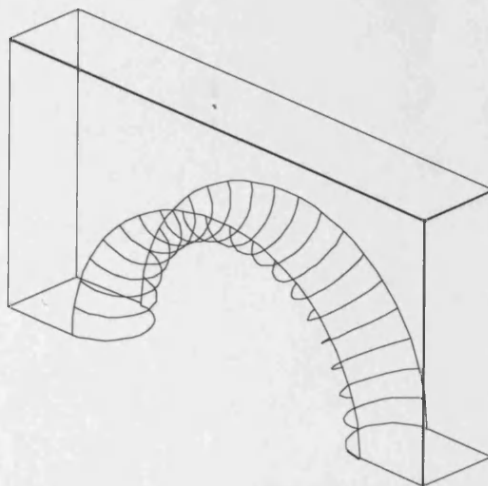


Figure 7.7b Tool placed mid-span on the upper surface of the curved plate.



The first part shown in figure 7.7a acts as a rigid support for the plate, maintaining contact at the upper and lower end of the plate. The second part (7.7b) is placed centrally on the upper surface of the plate, again ensuring continuous contact. Loading is applied using a Houndsfield tensometer, and the central deflection is measured

Figure 7.7a Base upon which the curved plate is placed.

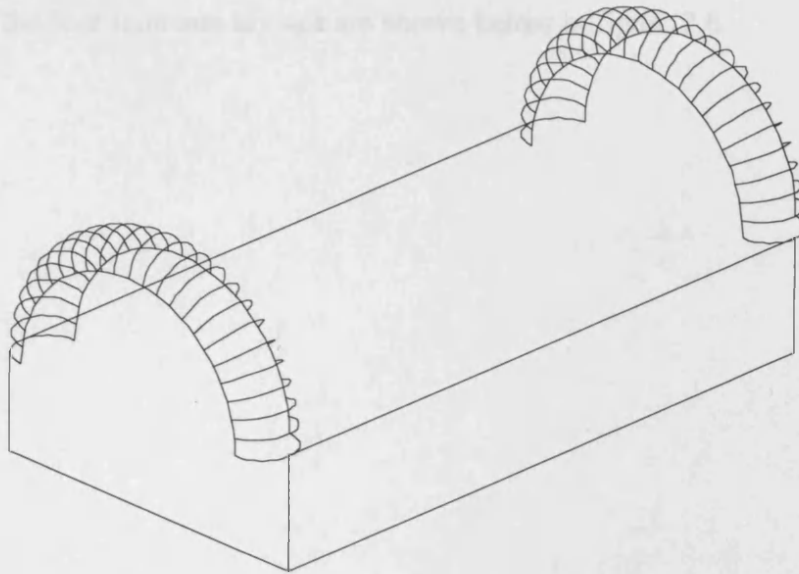
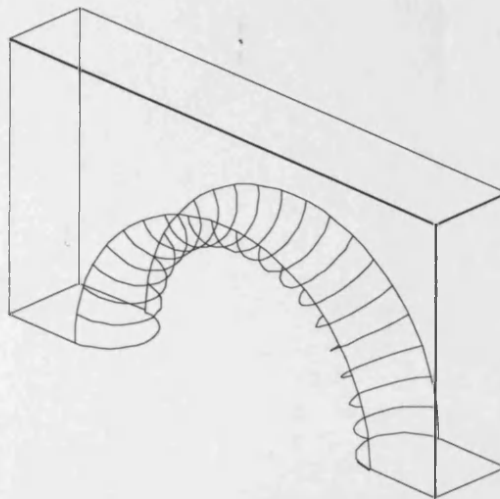


Figure 7.7b Tool placed mid-span on the upper surface of the curved plate.



The first part shown in figure 7.7a acts as a rigid support for the plate, maintaining contact at the upper and lower end of the plate. The second part (7.7b) is placed centrally on the upper surface of the plate, again ensuring continuous contact. Loading is applied using a Houndsfield tensometer, and the central deflection is measured

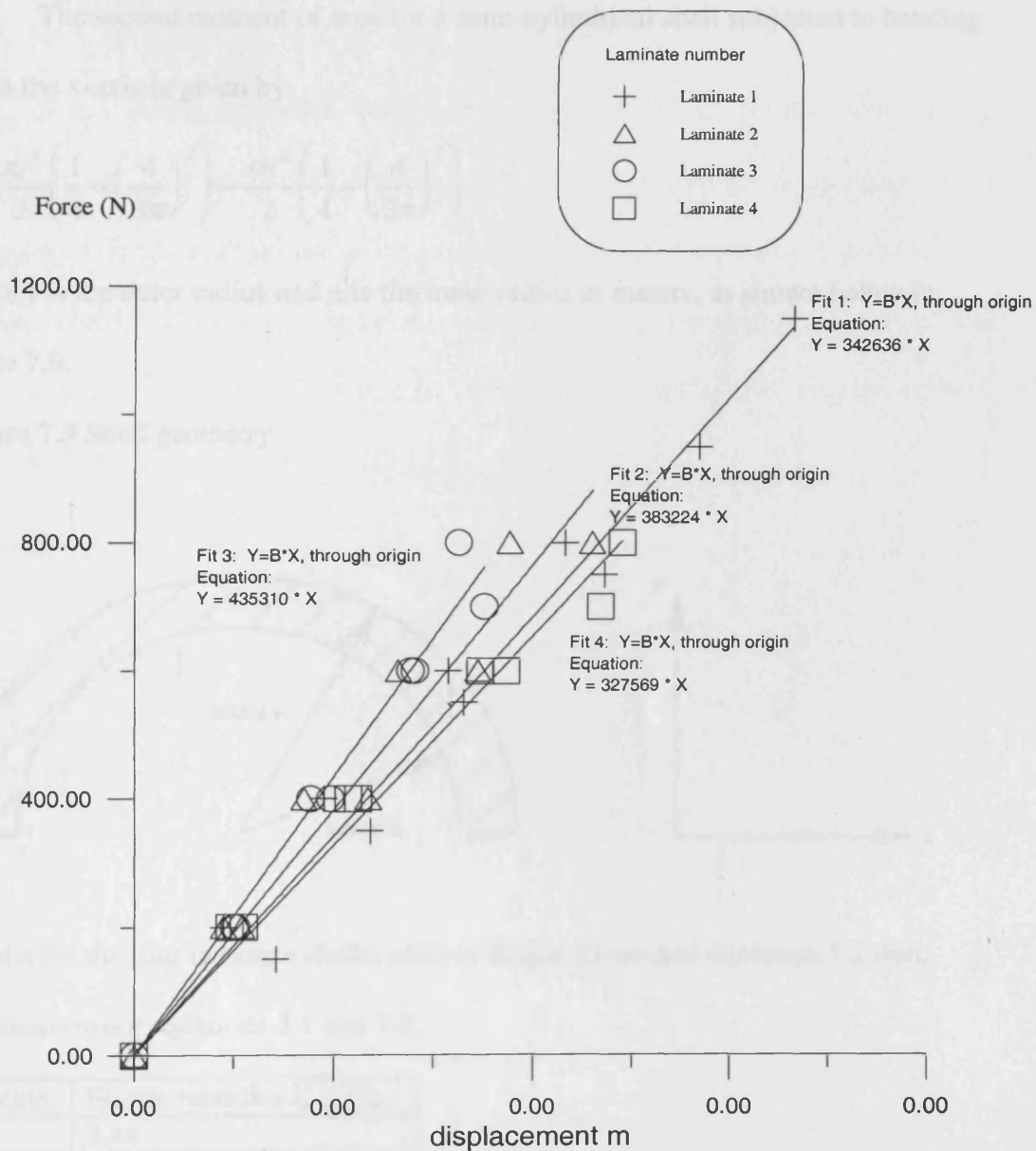
using a micrometer. Full diagrams with dimensions may be found in appendix F1.

Results for the four laminate lay ups are shown below in figure 7.8.



The elastic modulus was calculated using the standard result for a simply supported beam with a central bending load applied, which is given below in equation

Figure 7.8 Load displacement curves for the four laminates.



The elastic modulus is calculated using the standard result for a simply supported beam with a central bending load applied, which is given below in equation 7.1.

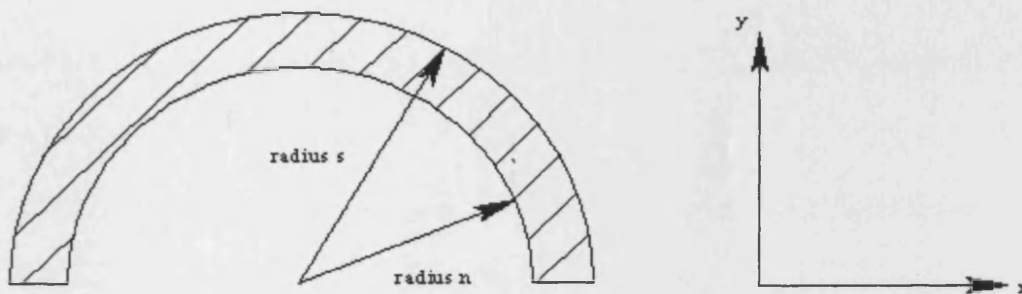
maximum deflection $d = \frac{PL^3}{48EI}$ equation 7.1

The second moment of area for a semi-cylindrical shell subjected to bending about the x-axis is given by:

$$I = \frac{\pi s^4}{2} \left(\frac{1}{4} - \left(\frac{4}{3\pi} \right)^2 \right) - \frac{\pi n^4}{2} \left(\frac{1}{4} - \left(\frac{4}{3\pi} \right)^2 \right)$$

where s is the outer radius and n is the inner radius in meters, as shown below in figure 7.9.

Figure 7.9 Shell geometry.



Results for the four laminate shells, each of length 23 cm and thickness 1.2 mm, calculated using equations 7.1 and 7.2.

laminate	Elastic modulus E (GPa)
1	2.84
2	3.18
3	3.61
4	2.72

The directionalised weave is significantly more expensive than the balanced weave but, as can be seen, little benefit is achieved in increasing the elastic modulus, so the balanced weave has been selected as the outer shell material.

As previously discussed, the second moment of area for the tibia varies along the length of the leg, and therefore the bending stiffness of the tibia also varies. In both cases the stiffness is equal to the product of the Elastic Modulus E , and the Second Moment of Area relative to the axis of bending I . The second moment of area at six intervals along the tibia of subject D. Davey, obtained by analysing the output from an MRI scan, are shown in table 7.2.

Table 7.2 Required I_{xx} to maintain identical peak tibial bending stiffness.

Distance from knee joint (cm)	Bending stiffness of tibia $E I_{xx}$ (Nm ²)	Required I_{xx}
8	9770.0	8.36 E-6
12	7280.0	1.29 E-5
13	1901.0	6.71 E-7
24	943.0	1.49 E-7
30	430.0	1.67 E-7
36	411.0	1.45 E-7

Using the outer radius of the shell as a clearance of 1 cm (allow for finish painting of 0.5 mm and the thickness of the shell material), again obtained from the results in Appendix A.1, and Appendix C.2 above, the second moment of area for a

Table 7.2 Second Moment of Area for tibia at six intervals.

Distance from knee joint (cm)	Second moment of area (m ⁴) of tibia
8	6.38 E-7
12	2.44 E-7
18	1.27 E-7
24	6.60 E-8
30	2.80 E-8
36	2.75 E-8

The full calculations to obtain these values, along with the MRI scans of these specific cross sections, may be found in Appendix A1.

Various literature summarised by Currey(1970)^[2,14] gives the Elastic modulus of bone as 15 GPa. The required second moment of area for the prospective guard may be obtained by equating EI_{tibia} per unit length to EI_{pad} at the six intervals along the tibia.

Table 7.3 Required I_{pad} to maintain identical pad and tibial bending stiffness.

Distance from knee joint (cm)	Bending stiffness of tibia EI (Nm)	Required I_{pad}
8	9570.0	3.36 E-6
12	3660.0	1.29 E-6
18	1905.0	6.71 E-7
24	990.0	3.49 E-7
30	420.0	1.47 E-7
36	412.5	1.45 E-7

Using the outer radius of the shin (with a clearance of 1 cm to allow for foam padding of 6 mm and the thickness of the shell material), again obtained from the scans in Appendix A1, and equation 7.2 above, for the second moment of area for a

semi-cylindrical shell, the required thickness of the guard using the Twintex may be calculated.

Table 7.4 Twintex pad thickness.

Distance from knee joint (cm)	Approximate radius of shin (and 10 mm extra) a (mm)	Required thickness of pad to equate stiffness a-b (mm)
8	82.5	19.54
12	85	5.02
18	78	3.54
24	65	3.12
30	60	1.72
36	60	1.60

Considering the results shown in table 7.4, we can see that to ensure identical bending stiffness both for the pad and the tibia would require the construction of a pad that had varying thickness along its length. However, if a thickness of 2 mm is selected for the shell, the bending stiffness for the tibia and leg are adequately close. This is particularly true lower on the tibia where impact is most likely to occur and the tibia is correspondingly most vulnerable. This suggests a shell thickness of approximately 2 mm manufactured from woven balanced Twintex would be suitable for the prototype pad.

C

7.3 Manufacture of prototype

Following the selection of the two materials to fit the criteria, a prototype may now be fabricated to allow comparative testing between the new pad and those commercially available.

To create a tool to mould the preferred laminate, a plaster cast was taken of subject D. W. Davey's legs, as shown below in figure 7.10.

Figure 7.10 Creation of casts for subject D. W. Davey.



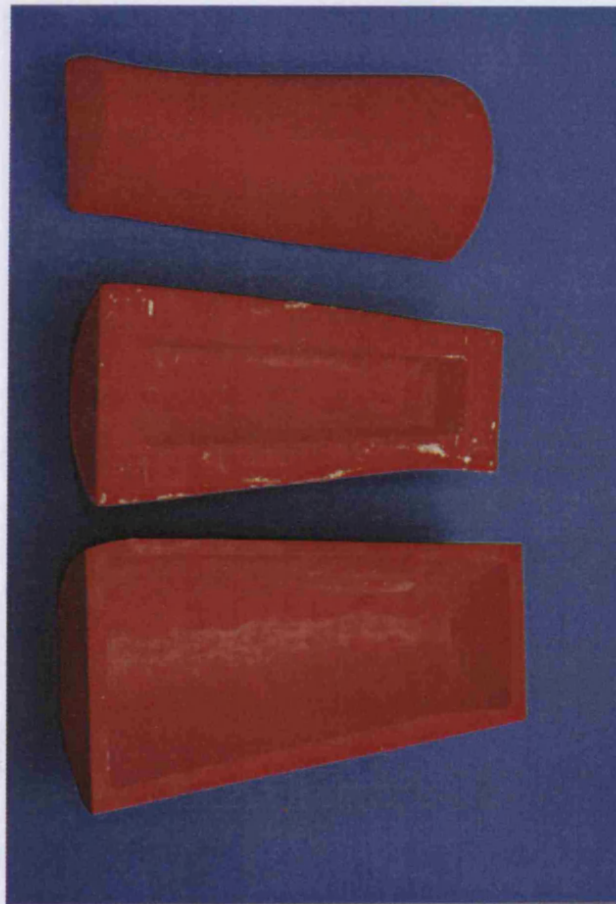
The casts were allowed to dry and were then carefully removed by cutting them vertically downwards into two halves. The halves were then reassembled and sanded. These shells were used as a mould for a further 'male' cast for each leg using a filler material called Tetrion. These blocks were then sanded and painted to obtain a smooth surface which follows the contours of the lower leg. They are shown as the top two items in figure 7.11. A layer of plastercine of 2 mm thickness was applied to the outer surface of the moulds, and a further Tetrion cast was taken for each leg to create a 'female' mould into which the initial 'male' blocks may be placed with a clearance of 2 mm. One such cast is shown as the bottom item in figure 7.11. This allows the Twintex to be placed between the 'male' and 'female' moulds to create the outer shell. For the purpose of mass production a more durable moulding tool would be required. Using the Tetrion moulds shown in figure 7.11, aluminium tools have been manufactured using the standard sand casting method.

A sheet of Twintex was heated in an oven until the polypropylene became suitably flexible and was quickly inserted in the aluminium moulding tools. The sheet was placed between the halves and a small pressure was applied for a few seconds. Once the part had set in the polypropylene it was released and a layer of Plaster was added.

To manufacture the final prototype the shell of 2 mm thickness between Twintex, with a layer of Plaster beneath. The finished cast is shown in figure 7.12.

C

Figure 7.11 Moulds used for sand casting



A sheet of Twintex was heated in an oven until the polypropylene became suitably flexible and was quickly transferred to the aluminium moulding tools. The sheet was placed between the tools and a manual pressure was applied for a few seconds. Once the pad had set to the required shape it was trimmed and a layer of Plastica was added.

To summarise, the final prototype has a shell of 2 mm thickness balanced Twintex, with a layer of Plastica beneath. The finished pad is shown in figure 7.12.

C

Figure 7.12 Final Prototype design.



7.4 Conclusions

The theoretical work addressed in chapter 6 defined an equation that describes the response of a two phase material (consisting of a stiff shell with a foam substrate) to satisfy two desirable behaviour criteria. This theory has been developed through an idealised condition of a flat circular geometry. There are concerns in applying the equation derived for a flat plate condition to the comparatively complex shape of a shin pad. It has been argued within this chapter that over the region that covers the tibia, the geometry of the pad shows only a slight curvature, and would be expected to behave in a similar way to the idealised flat plate condition. It is required that the stiffness of the shell in the plane, parallel to the long axis of the tibia, is experimentally measured for the complete geometry of the pad, as the full form contributes to the stiffness. This has been achieved by modifying the basic simply supported beam bending test, and applying the standard theory. The construction of a prototype relying on this assumption has been carried out. Impact testing of this curved pad must be carried out to confirm the experimental results follow those predicted theoretically, and consequently that the assumption is a reasonable one. This will be the main concern of the following chapter.

The defining equation has two variables; the stiffness of the shell and the stiffness of the foam. Essentially one needs to be set before the other may be calculated. Evidence presented by Viano et al^[2,34] has shown that if the impact load is transferred to the knee and ankle joints, ligamentous damage is possible. On this premise it has been decided to set the stiffness of the shell material to be the same as that for the tibia which, at its weakest point, is approximately 900 Nm. When this

value is substituted into equation 6.18, along with the other variables that are set by practicality, a modulus of elasticity for the cellular material of 0.28 MPa is realised. A search for material has been undertaken to obtain a shell material that has a high stiffness to weight ratio, that is inexpensive and easy to mould, to allow for possible mass production. The optimum material found is Twintex, a glass fibre laminate. A further search was carried out to find a foam material that exhibited the desired material properties. A candidate that fitted the equation well, and also had other attributes that propelled it above the other candidates, was a cellular material called Plastica. It must be stated that these materials may not be the absolute optimum, but they do fit the equation well, and are cheap and easy to work with. A prototype has been constructed from these materials so that testing may be carried out.

References

[7.1] Material Selection in Mechanical Design
Ashby M
Second Edition
Published By: Butterworth-Heinemann

Chapter 8

Testing of prototype and comparison with commercially available shin pad performance.

8.1 Introduction.

The prototype has now been designed and manufactured with the optimal materials available to fit the model, as defined in chapter 6. This prototype must now be given an exacting test at impact velocities and mass close to those expected to cause tibial fracture. Building on the experimental set up discussed in chapter 3, a more realistic impact velocity may be achieved.

The key concern of this testing is to observe if a curved plate on an elastic foundation, in the shape of a shin pad, behaves in a manner comparable to a flat plate on an elastic foundation, for which the governing behavioural equations have been derived. If this is the case, the equations obtained in chapter 6 section 6.7 may be confidently used in the design of new shin pads.

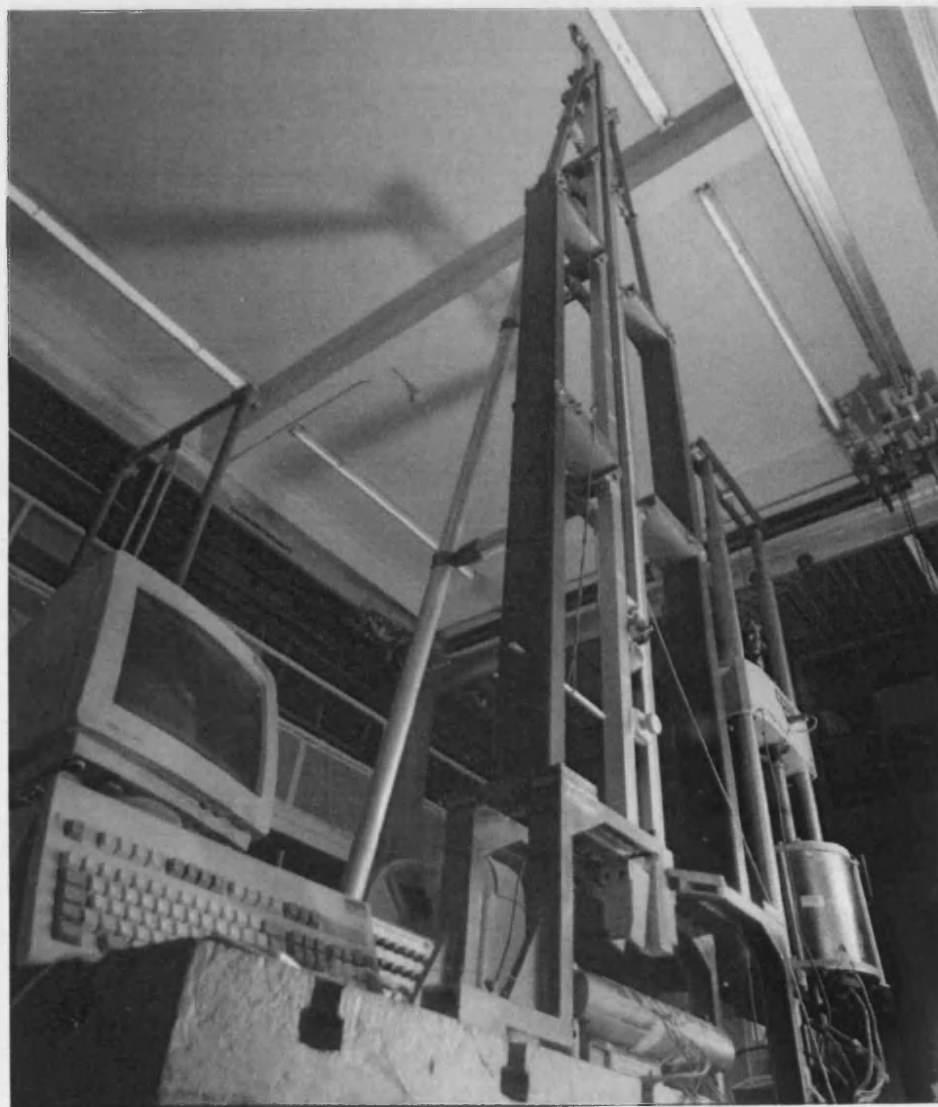
The test has also been conducted on a range of seven commercially available shin pads to achieve a direct comparison between the engineered pad and those currently in general use by the public. These tests will indicate just how much better the level of performance obtained from the prototype is in comparison to an ordinary pad. It also allows an evaluation of other pads which may be used to outline good and bad design traits in modern shin pads. This may be a useful guide for players looking to obtain the best possible level of protection in the current market, who are unsure of the type of pad to purchase.

8.2 Revised test method

The minimum impact velocity from literature required to cause tibial fracture with an effective impact mass of approximately 1.3 kg has been calculated to be 12 ms^{-1} . This is clearly unachievable using the small drop weight tower described in chapter 4. Considerable improvement must be made to the height of the tower to achieve more realistic velocity.

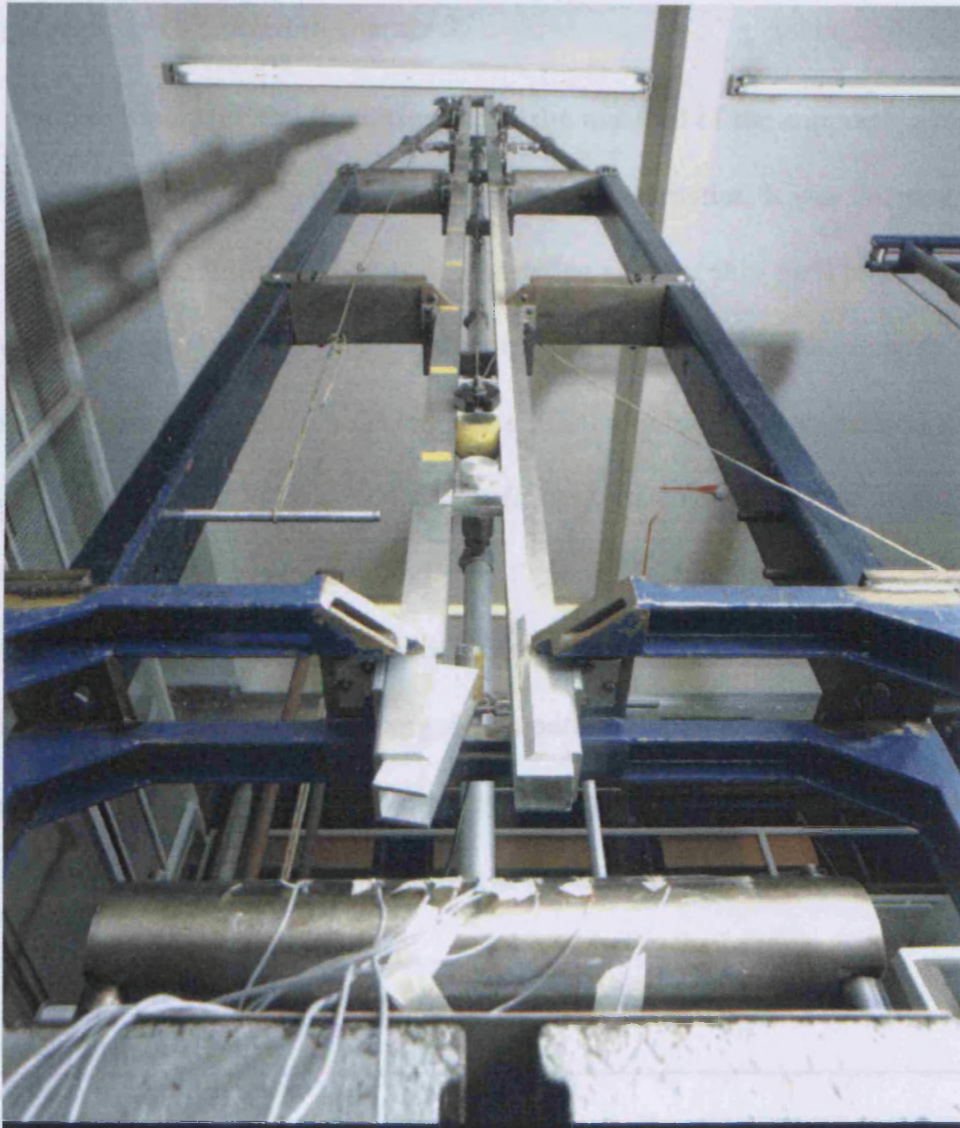
The apparatus constructed is shown below in figures 8.1a and 8.1b. It consists of a much improved 3.5 meter drop weight tower (the height of the tower being limited by the height of the laboratory) which allows a maximum impact velocity of 8 ms^{-1} . This value is much closer to the minimum velocity expected to fracture the tibia of 12 ms^{-1} , calculated in section 2.7.

Figure 8.1 Improved apparatus.



C

Figure 8.1b

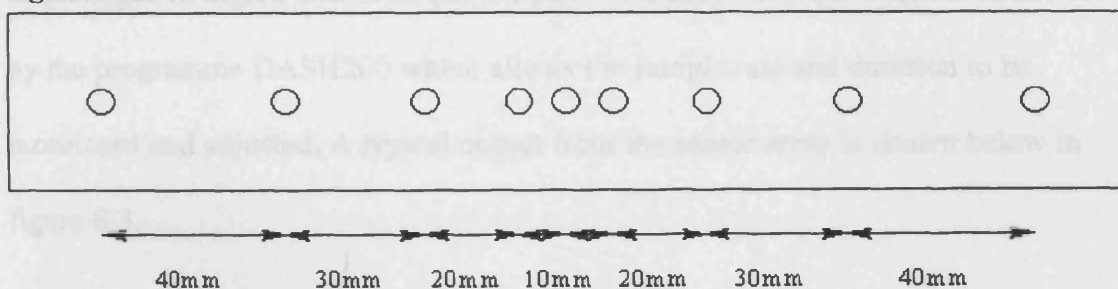


The impactor which screws into the slider is a spherical resin filled 'ball' of a radius similar to that of the boot tip used in the original test. A Kistler load cell (type 9021A) is sandwiched between the boot tip and the slider and connected via an amplifier (Kistler type 5011) to an oscilloscope, allowing the force at the point of impact to be calculated. Again, a suitable correction must be made to the results due to significant mass both above and below the load cell, using the calculation described in chapter 3 section 3.8. The combined mass of the ball, slider and load cell is 0.82 kg

which is slightly lower than the effective mass of the lower leg, when occupied in a kicking action, as calculated in chapter 2.

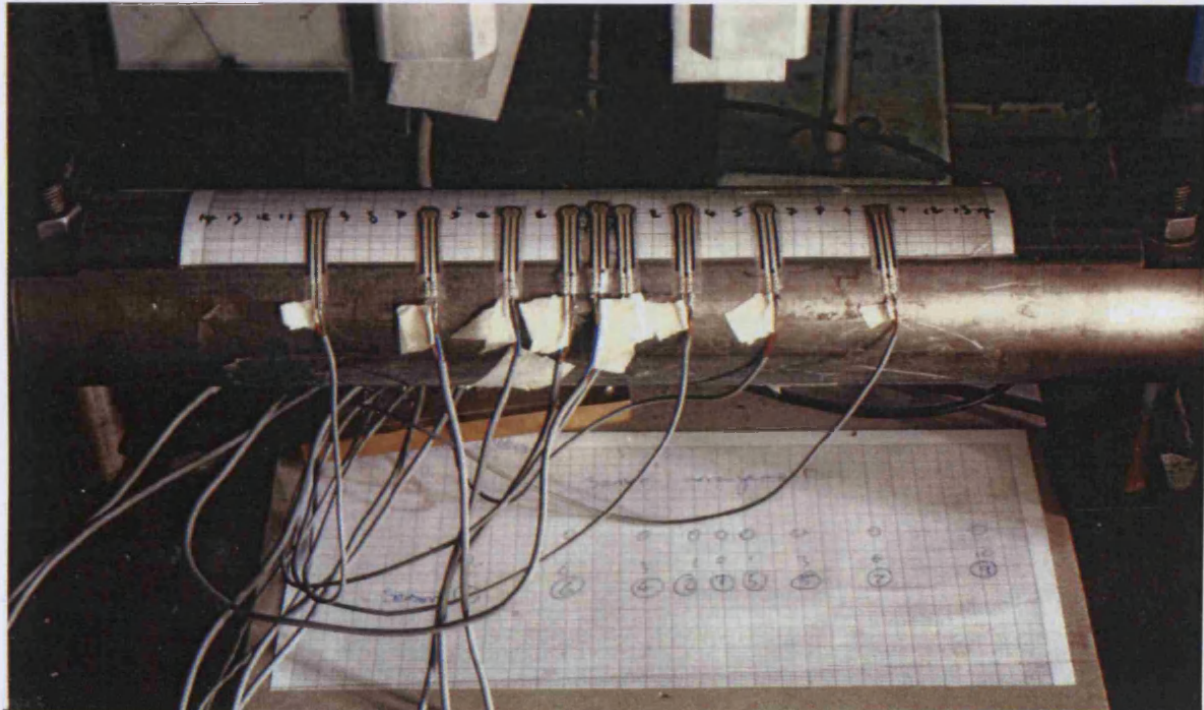
As previously proven in section 4.2.1, the material of the supporting medium does have a significant effect on the key impact characteristics. It was decided to use a three inch diameter aluminium bar as a dummy leg as most shin pads and the prototype fitted this shape very well, ensuring proper contact with the sensing devices (FSR's). The stiffness of the bar (EI) is also sufficiently high, in comparison to the pad stiffness, to allow it to be assumed as infinitely stiff. The FSR's are arranged in a horizontal line of 9 sensors (shown in figure 8.2a and 8.2b) along the bar where the tibia would be imagined to be, with the central sensor located directly beneath the point of impact. The sensors are arranged in a pattern which concentrates on the loading at the mid point of the tibia, directly beneath the point of impact as shown below in figure 8.3, but also takes readings at the extremities of the tibia to monitor possible ligament threatening impacts.

Figure 8.2a Sensor location.



C

Figure 8.2b

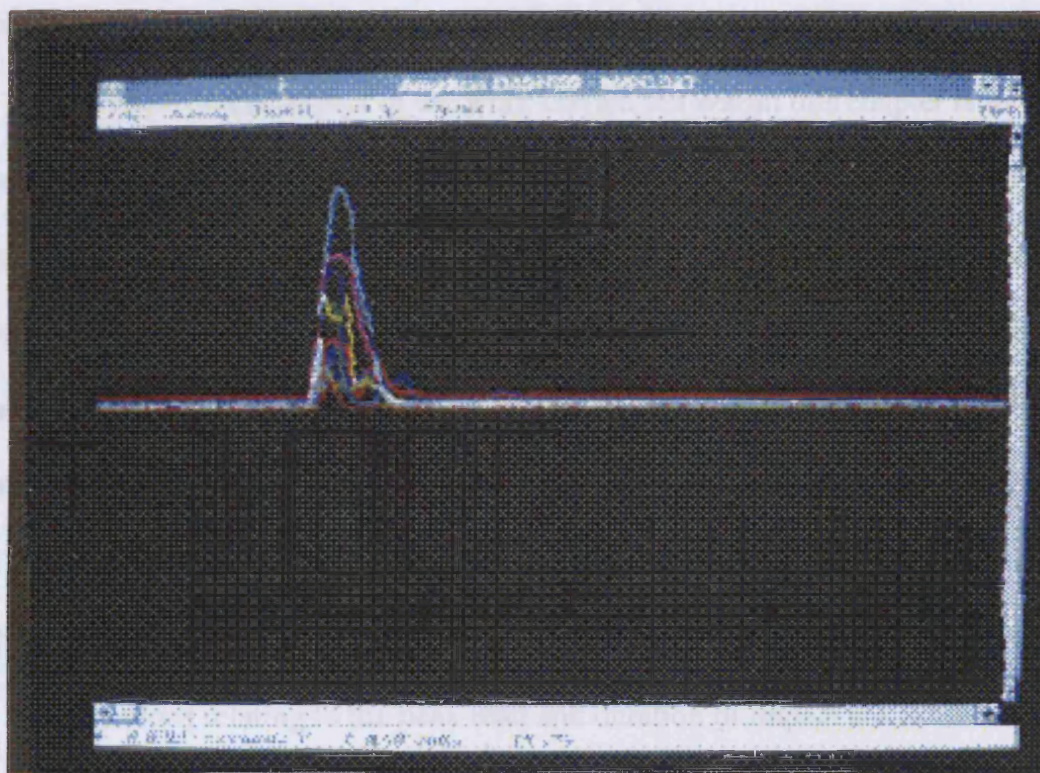


The sensitivity of each individual sensor was controlled using the amplifier especially designed for use with the FSR's, as described in chapter 3.

As pressure is applied normal to the sensor, the device resistance decreases and thus the voltage applied across the sensor is varied. The voltage is recorded using an analogue to digital converter (an Amplicon PC226). The A/D board is controlled by the programme DASH200 which allows the sample rate and duration to be monitored and adjusted. A typical output from the sensor array is shown below in figure 8.3.

C

Figure 8.3 Dash 200 on screen display.



The data is converted from a voltage/time history to a pressure/time history using previously obtained calibration data for each individual sensor. Essentially, this experimental set up allows us to monitor how the pads affect the impulse at the point of impact, and also how the material combination transmits and spreads the load along the tibia.

Pictures and brief descriptions of the seven pads, made by leading sport manufacturers, which will be tested may be found in appendix G1.

8.3 Analysis of performance of prototype by comparison of experimental results to behaviour predicted using theoretical solution.

The most crucial aspect of the work carried out within this chapter is to compare the experimental results to those predicted using the equations derived in chapter 6. Although the theoretical behaviour is derived from experimental results generated in chapter 4, and has been shown in section 6.7.2 to be able to predict the characteristic behaviour for any material impacted at any mass or velocity, all this has been achieved using the idealised condition of a flat outer shell. It has been assumed that the flat plate situation will be applicable in the plane parallel to the tibia as long as the bending stiffness for the curved plate is used as detailed in chapter 7 section 7.1. The equations relating to the peak load and duration of impact are as follows:

$$P = \frac{v}{l} \sqrt{\frac{8Dm}{2.65x^{-1.34}}} \quad (6.10)$$

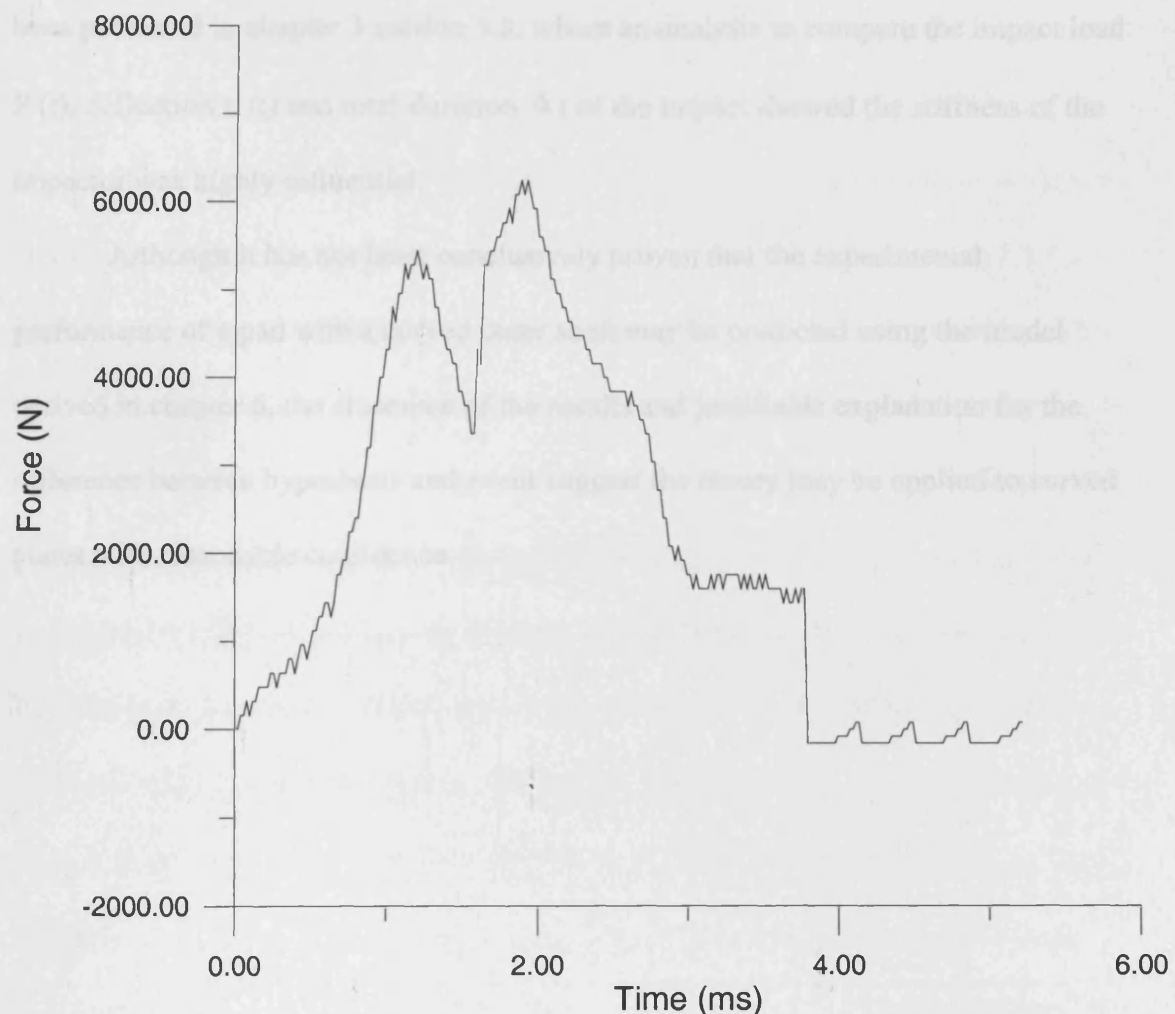
$$\Delta t = \pi \sqrt{\frac{2.65x^{-1.34}m}{8D}} \quad (6.11)$$

Substituting experimental values for impact velocity $v=8 \text{ ms}^{-1}$, plate radius $a=0.1 \text{ m}$, impactor mass = 0.82 kg , plate stiffness $D=900 \text{ Nm}$, foundation stiffness $k = 0.35 \text{ Nm}^{-3}$ and pad thickness $h=0.006$ we obtain the following theoretical solution:

$$P= 8240\text{N and } \Delta t = 2.5 \text{ ms}$$

These values may be compared to the output from the load cell in the experimental situation described in section 8.2, as shown in figure 8.4 below.

Figure 8.4 Experimental output from load cell for prototype.



As can be seen, the output from the experiment does not accurately follow the results predicted using the theoretical solution. However, they are reasonably close with a peak load of 6240N c.f. 8240N and impact duration of 3.78 ms c.f. 2.5 ms. It is hypothesised that this difference is caused by a degree of flexibility within the impactor. The theoretical solution was derived primarily through results obtained by computer simulation, where the impactor was infinitely stiff. In the experimental situation, although the impactor is primarily made from the same stiff resin used in initial testing, which followed the simulation results much more closely, there is now

an outer layer of deformable material which is influencing the results. This effect has been predicted in chapter 3 section 3.8, where an analysis to compare the impact load $P(t)$, deflection $x(t)$ and total duration Δt of the impact showed the stiffness of the impactor was highly influential.

Although it has not been conclusively proven that the experimental performance of a pad with a curved outer shell may be predicted using the model derived in chapter 6, the closeness of the results and justifiable explanation for the difference between hypothesis and event suggest the theory may be applied to curved plates with reasonable confidence.

Table 8.1

pad name	condition after impact	peak load at foot tip (N)	peak pressure between pad & foot (Pa)
Standard pad over shoe	deformed	2408	15.7
San-Fee Pad Gascongne	cracked	3734	24.3
Mini Tectonic	deformed	7307	47.1
Deception	intact	7535	48.4
Mike Ah	cracked	7110	45.6
Urban Gel Sock	cracked	9072	58.6
Mini Libre	cracked	4309	27.8
Prototype	intact	1500	9.6

The peak loads occurred at the point of impact for selected pads (shown in figure 8.3) and how performance is shown graphically in figure 8.5.

8.4 Summary of key results obtained from pad tests.

Testing, using the method described in section 8.2, has been carried out on the prototype and the seven pads produced by leading sports manufacturers. The key results for peak impact load and peak stress recorded for the central sensor are given in table 8.1 below. The full results are given in appendix G1. Observation of the condition of the pad after impact testing has also been made. The structural integrity of the pad is meaningful in its ability to deal with further impacts and also understanding the response of the pad, a cracked shell would considerably lower the stiffness reducing the value of the characteristic length and therefore increasing the peak load for subsequent impacts. A permanently deformed pad would cause the foam material to be constantly stressed, and in the event of a further impact at the same location on the pad, the declarative effect of the foam would be reduced. Pictures and brief descriptions of the seven pads tested may be found in appendix G1.

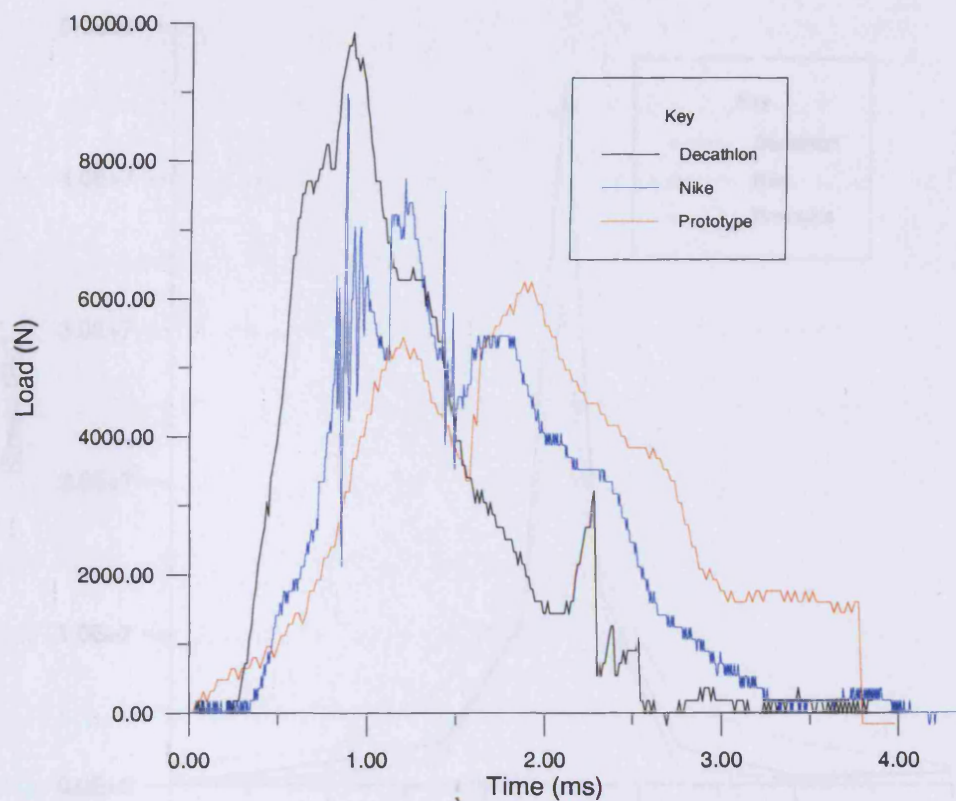
Table 8.1

pad name	condition after impact	peak load at boot tip (N)	peak pressure beneath pad (MPa)
Sondico cool max pro	deformed	8448	38.7
Sondico Paul Gascoigne	cracked	8751	39.9
Mitre Tectonic	deformed	7347	37.7
Decathlon	intact	9856	46.4
Nike Air	cracked	7216	32.0
Umbro Gel Safe	cracked	9072	44.6
Mitre Libero	cracked	8760	28.8
Prototype	intact	6240	26.9

The peak loads obtained at the point of impact for selected pads (poorest, typical and best performance) are shown graphically in figure 8.5.

C

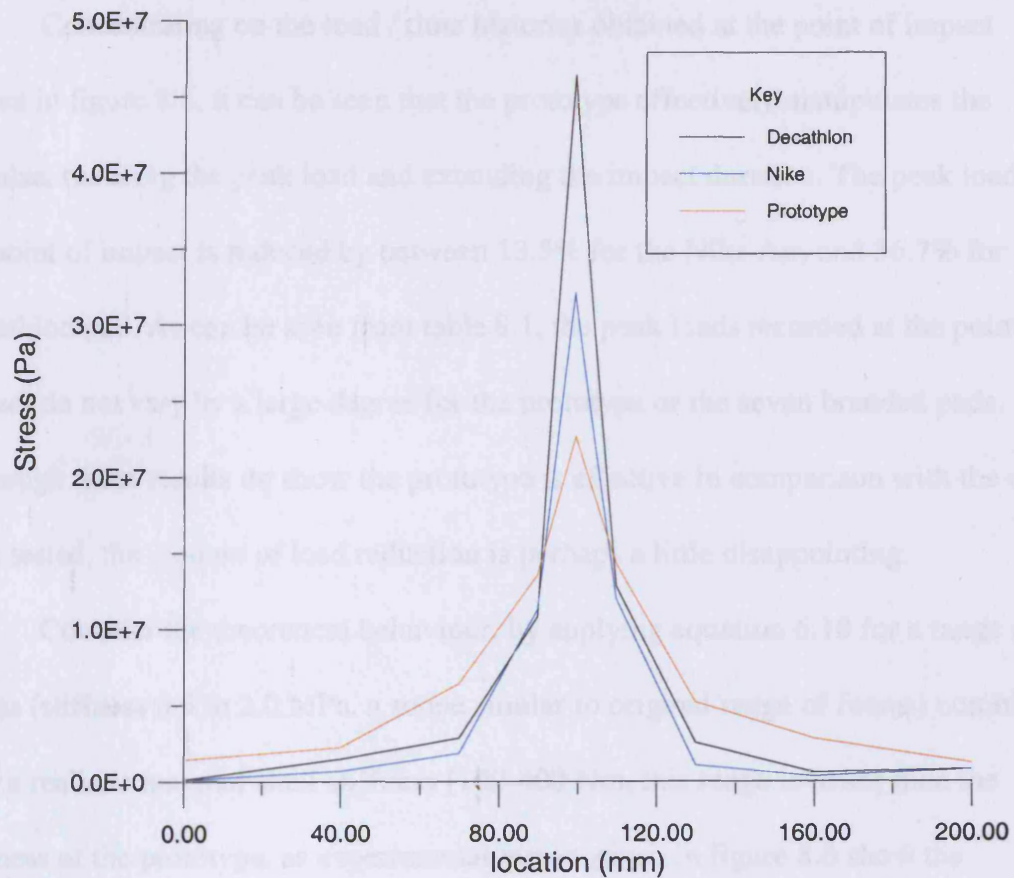
Figure 8.5 Comparison of impulses for a selection of pads



The stresses recorded by the sensor array at their maximum for selected pads (worst, typical and best performance) is shown in figure 8.6.

C

Figure 8.6 Stress distributions for selected pads



Maximum Force (N)	10.5 MPa	14.6 MPa	20.0 MPa
100 Nms	peak load 7927	peak load 9456	peak load 14230
200 Nms	peak load 8477	peak load 11102	peak load 13068
300 Nms	peak load 8946	peak load 11946	peak load 13755

8.5 Analysis and comparison of shin pad performance.

Concentrating on the load / time histories obtained at the point of impact shown in figure 8.5, it can be seen that the prototype effectively manipulates the impulse, reducing the peak load and extending the impact duration. The peak load at the point of impact is reduced by between 13.5% for the Nike Air, and 36.7% for the Decathlon pad. As can be seen from table 8.1, the peak loads recorded at the point of impact do not vary by a large degree for the prototype or the seven branded pads. Although these results do show the prototype is effective in comparison with the other pads tested, the amount of load reduction is perhaps a little disappointing.

Consider the theoretical behaviour, by applying equation 6.10 for a range of foams (stiffness 0.5 to 2.0 MPa, a scope similar to original range of foams) combined with a realistic range of shell stiffness (100-400 Nm, this range is lower than the stiffness of the prototype, as experimental results given in figure 8.6 show the prototype has the largest distribution of load, and therefore the stiffest shell medium) as given in table 8.2 below.

Table 8.2

Modulus of foam / shell stiffness combination	0.5 MPa	1.0 MPa	2.0 MPa
100 Nm	peak load 7977	peak load 10654	peak load 14230
200 Nm	peak load 8447	peak load 11282	peak load 15068
400 Nm	peak load 8944	peak load 11946	peak load 15955

Equation 6.10 predicted a peak load of 8240N, whereas 6240N was obtained experimentally for the prototype pad. Assuming this overestimation (approximately 25%) is consistent for all pad materials considered in table 8.2, it is evident that all

the commercially available shin pads experimentally fall within the material boundaries tabulated above. This shows that for reasonably large variations in material properties, the overall effect on the peak load is not overly appreciable. This indicates a huge improvement in performance would be unlikely. It also must be remembered that the thickness of the pad must be limited to a maximum of approximately 8-10 mm thickness for the sake of practicality. Realistically, the amount of load attenuation (or any other significant impact characteristic) that is achievable using materials of such thickness is always going to be finite, and in real terms a reduction in the peak load of 13.5% may be the crucial difference between severe bruising and a leg fracture.

Of the seven pads purchased, four pads developed cracks, two sustained damage in the form of permanent deformation, but with no outer shell fracture. Only one maintained full structural integrity. The numerical results tabulated above indicate the Decathlon pad displayed the poorest performance, however this was the only pad that showed no permanent damage, other than the prototype. These results indicate little thought has been put into the development of the majority of the pads, with a brittle plastic material being chosen for two thirds of those tested. It would be expected that once a crack has initiated within the pad, the overall stiffness would be much reduced leading to larger localised deformations and increased probability of injury. This effect would be exaggerated at higher impact loads. It also suggests the highly undesirable 'bottoming out effect' first discussed in chapter 4 is occurring, and the shell material has become the main decelerator of the impact, and therefore is undergoing large deformation leading to fracture.

Interestingly, Cattermole's study (1996)^[2,10] highlighted a correlation between tibial fracture and shin pad breakage, with 16.9% of the pads having fractured or been penetrated when tibial fracture occurred. Whether the cracking of the pads actually causes loading that is significant in the causation of tibial fracture, or we are simply seeing the results displayed above; namely that commercial shin pads are made from materials that rupture under high loading, and the tibial fractures would be likely to occur under the magnitude of load irrespective of the integrity of the pad, is a matter of conjecture. It must be stated that all impact tests carried out within this chapter would produce tibial fracture if the peak tolerable load is 5000N, as discussed in chapter 2. In particular, the prototype has been designed to perform at an optimum level for a peak load of 5000N. It would be expected that within the impact testing of the prototype (to a peak load of 6240N) the onset of the 'bottoming out' effect is likely to be occurring, but encouragingly, there was no accompanying evidence of lasting damage to the shell material or rupture of the Plastica cells.

Of the seven pads, five were of the typical solid shell, and two (Nike Air and Umbro Gelsafe) were made up of several individual splints, with the Gelsafe containing an energy absorbing gel material. Although both performed averagely according to the numerical results, both cracked under impact. This is to be expected, as the splints which are in effect a series of flat plates have a much lower overall stiffness than a curved plate manufactured from the same material. Clearly these tests show that it is inadvisable to use the pads that are made up of separate splints. Care must also be taken to try to ensure brittle pads are avoided. Although there is no direct

evidence that pad fracture has a direct link to tibial fracture, it is implicated within preceding research.

Concentrating on the pattern of stress distribution beneath the pads shown in figure 8.6, it can be seen that the prototype effectively manipulates the loading over a larger area, and therefore has a lower peak stress. The peak pressure beneath the pad varies slightly more than the load at the point of impact, with the prototype reducing the peak by between 21.5% for the Mitre Libero and 51.3% for the Decathlon pad. It is interesting to note that the pad that reduces the peak load by the largest percentage (Nike Air) does not have the corresponding largest reduction in peak pressure. The most important aspect of these results is that none of the pads appear to cause a bolster effect of note which could possibly cause ligament damage at ankle or knee joints. Ligament damage was the principal reason for setting the shell stiffness to 900 Nm, as evidence discussed in chapter 2 section 2.10, suggested impact loading could possibly lead to ligament damage if the shell material was stiffer than the tibia. Therefore, the shell stiffness may be increased, which in turn would allow the substrate material to be of a lower stiffness and further improvement is possible on the shin pad design. However extreme caution must be taken with respect to this option. Referring back to chapter 3 section 3.8, analysis shows the stiffness of the impacting body is extremely important in defining the impact characteristics. In the event of a shin on shin impact, a reasonably common event within a football match, the wearer of the high stiffness guard (greater than the originally designated upper limit of 900 Nm) although personally better protected against the impact, may be causing increased possibility of injury to the opposing player.

Essentially, the results from the sensors imply the stiffness of the pad may be greatly increased without risking ligamentous damage, but any such increase would increase the risk of injury to other players. This suggests the choice of 900 Nm for the shell stiffness should not be significantly increased.

8.6 Conclusions

The key issue dealt with in this chapter is whether or not the prototype pad behaves as anticipated using the model for a flat plate situation. Results indicate there is a reasonable correlation, with the peak impact load experimentally measured being within 25% of the value obtained using the predictive model.

Comparative tests for a range of leading manufacturers' shin pads and the prototype have shown the peak impact load, and therefore the peak bending moment, is reduced by between 13.5 and 36.7 % by the engineered pad. The corresponding peak stress is reduced by between 21.5 and 51.3 %. These results prove the performance of the prototype to be superior to that of the established commercially available pads, and the redesign of pads undertaken within this thesis to be a success.

Of the pads tested, those with a shell made from a number of splints were unable to maintain structural integrity, which has been associated with tibial fracture in published literature ^[2,10], although this link has not been categorically proven. The cracking of the shell material also occurred in the majority of single curved plate type designs, and indicates that the pads had not been tested at high impact loads within the design process. Consequently the shell materials selected are inappropriate for dealing with an impact event of a magnitude able to fracture the tibia.

Chapter 9

Concluding remarks and suggestions for further work.

9.1 Conclusions

This thesis has approached the problem of designing a new soccer shin guard with the ultimate aim of specifically reducing the incidence of tibial fracture within the game of soccer. The work of Cattermole et al has shown a surprisingly high level of tibial fracture in soccer, something that had previously been overlooked. In their study they investigated the cause of all tibial fracture in the Leicestershire area; over one third of all such injuries were as a result of soccer. Extrapolating their results, an estimated 3000 soccer players suffer a fractured tibia annually throughout the UK at a cost of £7,700,000, in terms of initial treatment, sick pay and loss of productivity.

Considering the size and financial implications of the problem, a literature search showed a relative lack of previous work into the prevention of the injury. All published reports in the area are limited to simplistic testing methods, comprising of shin pads mounted on a prosthetic leg instrumented with a load cell. Although these studies are valuable in showing the importance of wearing a guard, they do not attempt to suggest improvements in design. The problem has been exacerbated by the mistake in classification of shin pads as personal protective equipment of 'simple design' by the European Union. This means that each individual shin pad manufacturer may use their own test standard that does not necessarily involve an impact, before releasing a potentially hazardous product on the market with the CE mark for assurance of safety attached. However, the imminent reclassification by the

EU, which will require an approved independent body to test the pads to a yet to be defined standard, adds extra significance to this thesis.

Work into understanding the behaviour of the lower leg with particular reference to the tibia indicates the reasons for the high incidence of tibial fracture in soccer as reported by Cattermole (1996)^[2.10]. The minimum second moment of area for the tibia naturally coincides with the centre of the football when at a players feet. This causes a missed tackle to impact at the specific point on the tibia where the resistance to bending is at a minimum. Cattermole also classifies the fracture patterns of broken tibias occurring in the game of soccer in terms of the loading history to failure..

Fracture patterns for 100 participants proved the tibia fractured predominantly as a result of bending loading with initiation of fracture occurring on the side subjected to tensile loading. This study also showed fracture occurred at the point of impact on the tibia, suggesting a quasi-static response. Intuitively, if the fracture of the tibia was due to wave phenomena the break would occur mid-span. This supposition is corroborated by subsequent work carried out at the University of Leicester which showed oscillations in the tibia are quickly arrested naturally. Additional work considering the tibia as a simply supported beam, coupled with published literature, suggests a bending moment of 320 Nm and an ultimate bending strength of approximately 5000 N for the tibia loaded at the point of minimum resistance to bending loading.

Analysis of the biomechanics of kicking concludes a maximum impact velocity approaching 30 ms^{-1} is attainable with an effective impactor mass of

approximately 1.3 kg. This potentially relates to very high energy impacts in the game of football. Clearly, a typical pad thickness of 6-8 mm is not going to enable the absorption of such a significant impact energy. This is especially true when considering a shin pad is a product that is used repeatedly. Most materials absorb energy through sustaining damage and this is not a practical option for a shin pad as they need to be durable.

Instead the problem was approached from the perspective that if the impulse at the point of impact on the guard could be understood and controlled, the probability of fracture could be much reduced. To obtain this understanding, a test method was developed that was more comprehensive than those previously performed by other investigators. Initially, a flat plate test was carried out on a simple material combination typically used in shin pads, of a stiff outer shell with a foam layer beneath. A drop weight tower was used to provide the impact and the impulse imparted to the pad was measured using a load cell. The use of pressure sensitive semiconductor films with a fast data logging system also provided valuable insight into the maximum stresses experienced beneath the pad and also the distribution of pressure.

These preliminary experiments demonstrated, in simple circumstances, the range of response which may occur. The key discovery from this analysis was the stress levels imparted to the leg become extremely high if the foam material crushes to high strain levels. They also indicated that as the pad becomes stiffer the impulse duration becomes shorter and thus the peak load is higher. It is evident that a balance between two extremes is necessary. If the pad is too flexible, high localised

compression of the foam material occurs, too stiff and enlarged peak loads occur. A further simple dynamic analysis showed that the construction of a limb that exactly imitates the behaviour of the human leg is a prerequisite to the attainment of accurate results. These experiments provided useful data for a combination of prospective materials for impacts of low velocity (4 ms^{-1}), but not at realistic velocities approaching 30 ms^{-1} . To achieve high speed testing computational Finite Element Analysis has been used.

An axisymmetric model of the impact situation was created which reproduced results obtained experimentally. The simulation allowed verification of the hypothesised behaviour, whereby the high stresses were caused in low stiffness material combinations by the straining of foam in excess of 90%. Results for experiment and simulation followed each other closely, both in terms of impact loads and duration. However, in situations where the foam material strained more than 90% there were considerable differences in measured and simulated stresses incurred beneath the material combination. This anomaly clearly arose from the assumption that the foams tested have a Poisson ratio of zero. At low strains this has been proven to be a reasonable assumption, but at high strains (80% and above) the foams would be expected to act as a solid with a Poisson ratio approaching 0.5.

To ensure the problem associated with the Poisson ratio was not encountered for further tests at higher velocities, simulations were carried out on components with unfeasibly (in terms of use in a shin pad) thick foam substrates. The purpose of this was solely to achieve more data at more realistic impact velocities to allow a conceptual model to be developed.

A behavioural model has been created based on classical theory derived by Timoshenko for an elastic plate supported on an infinite elastic foundation. Using the experimental and simulation results, a non dimensional solution has been obtained which predicts the behaviour of a shell material covering a foam substrate. By adding two simple criterion; firstly that the foam material must not compress more than 80%, ensuring no excessive stresses occur, and secondly the load at the point of impact does not exceed the predicted maximum tolerable load for the tibia, a simple equation may be defined. The equation which comprises of terms for both the shell and foam materials effectively extracts the best usage of the two component materials; the stiffness of the outer shell and the cushioning effect of the foam.

Further work was carried out to discover the ideal materials which displayed the material characteristics required. The equation comprised of, the outer shell stiffness, the foam thickness, the foam's Modulus of Elasticity and the size of the pad. Realistically, the size of the pad and allowable foam thickness are defined by practicality, and the stiffness of the pad is required to be the same as the tibia to maintain proper contact between pad and leg. This leaves a singular design variable which may be calculated by substituting suitable figures for the other variables. The ideal cushioning material is provided by a robust 'bubble wrap' called Plastica. This is combined with a suitable shell material called Twintex, a glass fibre laminate which has been chosen because of its low cost and ability to mould at relatively low temperature and pressure.

Following the manufacture of the prototype from the materials stipulated, it was put through a rigorous test regime. To gauge the effectiveness of the prototype

performance, seven commercially available pads were also tested. In comparison with the branded shin pads the prototype responded well reducing the peak load at the point of impact by between 13.5 and 36.7%, and the peak pressure experienced beneath the pad by between 21.5 and 51.3%. It was also noted that of the seven purchased shin pads, six sustained irreversible damage at loads in the range required to fracture the tibia. It was also discovered that damage was more likely to occur in pads that were made up of individual splints rather than a singular shell. Fractured shin pads have been linked to tibial fracture in published research.

9.2 Suggestions for further work.

Intuitively, there are two key areas that offer potential for further work; specifically continuation of work on football shin pads and the exploitation of the basic design method for use on other body parts.

9.2.1 Suggestions for further work on shin pad design.

Considering the work to date, there are clearly areas which could be expanded upon and other new domains which could be researched. The pad has been developed specifically along the lines of finding a compatible pair of materials to fit two criterion specified by the tolerance level of the tibia and the characteristics of cellular materials. An alternative avenue would be to look at including energy absorbing mechanisms in the structure of the pad. This could be taken further with a pad that specifically fractured as the load reaches the critical value at which the tibia fractures thus absorbing a proportion of the energy. Further design work could also be carried out to improve on the ergonomics of pads in an attempt to deflect impact away from the tibia.

Concentrating on the work already carried out, further investigation into literature concerning the ultimate tolerable load the tibia is able to withstand would allow the estimated value currently used of 5000N either to be confirmed or modified. This is particularly important since any significant variation in this load will affect the ultimate material properties obtained from the derived equation. There is also a void of available literature that relates stress patterns applied to the lower leg with injury mechanisms. The design process in this thesis is based on the peak impact load to cause fracture, which is monitored by measuring the impulse at the point of impact. It

has been experimentally shown that similar impact impulses can produce very different stress patterns beneath the pad materials. It is these stress patterns that the lower leg is directly experiencing and the ability to interpret this data would give more significance to the sensing equipment developed within this thesis. A design methodology based on the actual load the leg is experiencing beneath the pad materials rather than the load at the point of impact would be a significant improvement.

Improvements could also be applied to the experimental set up. The impact velocity, even with the improved 3.5 meter drop weight tower, is well below that which may occur in the game of soccer. It is necessary to instrument the impactor since the sensor array cannot be relied upon for extreme accuracy, and the stress patterns are difficult to interpret in terms of potential injury causation. Again, if the stress patterns could be categorised in terms of injury potential, the load cell could be removed from the equipment. This would allow the drop weight tower to be eliminated from the equipment and a discharged projectile could be used in its place to provide testing at higher velocities.

Another area where improvements can be made is the computational FEA. In particular, the problem associated with the variable Poisson's ratio for the cellular material. As the model stands, it is inadvisable to test pads of a realistic thickness since the stresses produced are much larger than those obtained experimentally. A totally representative model could possibly negate the need for experimental testing and allow all evaluations to be carried out through simulation.

More work may also be carried out to determine the exact influence the curvature of the shin pad has on the equations in chapter 6 which were derived from an idealised situation of a flat circular shin pad. Experiments, as detailed in chapter 8, showed the theoretical load and impact duration was within 25 % of those occurring experimentally and this difference was hypothesised to be caused by a small degree of flexibility within the impactor. The 25 % difference was felt to be small enough to avoid detailed analysis of the cause of this irregularity, however a definitive factor that took account of the geometry of the pad within the theoretical equations would be an extremely useful addition.

9.2.2 Suggestions for other work.

The effectiveness of this method of design has been shown by the prototype results. Clearly, there is scope for applying the same procedure to any body part in situations where thick energy absorbent materials are impractical. In sport alone rugby, hockey, cricket, American football and ice hockey instantly spring to mind. This method could also possibly be applied to packaging fragile or expensive items when in transit.

Summary of symbols used within thesis.

Chapter 3

Calculating effect of location of load cell within impactor.

C is a numerical constant of proportionality

F_m is the measured load in Newtons (N)

F_m^{\max} is the measured peak impact load in Newtons (N)

F_a is the actual load in Newtons (N)

F_a^{\max} is the true peak impact load in Newtons (N)

M_1 is the mass beneath the load cell in kilograms (kg)

M_2 is the mass above the load cell in kilograms (kg)

Effect of stiffness of supporting medium on measured characteristics presented within chapter 3.

P_{\max} is the peak impact load in Newtons (N)

y_{\max} is the peak total deflection in meters (m)

Δt is the total duration of the impact in seconds (s)

L is the length of the tibia in meters (m)

k is the Modulus of the Foundation which is given by the Elastic Modulus of the foam material in Newtons per meter squared divided by the thickness of the foam material in meters. (Nm^{-3})

$2a$ is the length of the pad outer shell material in meters (m)

b is the width of the pad outer shell material in meters (m)

$(EI)_L$ is the minimum value for the Modulus of Elasticity for the supporting medium in Newtons per meter squared (Nm^{-2}) multiplied by the minimum moment of area in meters to the fourth power (m^4) over the length of the beam (Nm^2)

X is a non dimensional group given by $X = \left(\frac{2L^3 kab}{48(EI)_L} \right)$

Further symbols used in full analysis in Appendix B3.

P is the impact load in Newtons (N).

y is the total deflection (pad and beam) in meters (m).

w is the bad deflection in meters (m).

v is the impactor velocity in meters per second (ms^{-1}).

v_0 is the terminal impact velocity and rebound velocity of the projectile in meters per second (ms^{-1}).

m is the impactor mass in kilograms (kg)

Effect of stiffness of impactor on measured characteristics presented within chapter 3 and Appendix B4.

z is the impactor deflection in meters (m)

k_1 is a linear constant of proportionality between load in Newtons and deflection in meters.

y_1 is the total deflection (pad and impactor) in meters (m).

Description of piezoresistivity in appendix B1

μ is the mobility (velocity per unit field) in meters squared per volt second ($\text{m}^2\text{V}^{-1}\text{s}^{-1}$)

ϵ is the electric field strength in Volts per meter (Vm^{-1})

v is the velocity in meters per second (ms^{-1})

q is the charge in Coulombs (C)

τ is the probability of an electron collision (numerical constant)

ϕ is the effective mass of electrons in kilograms (kg)

Chapter 6

Timoshenko's theory.

A, B, G and H are constants

w is the deflection of the plate in meters (m).

w₀ is the central deflection of the plate in meters (m).

w_{inf} is the central deflection in meters (m) for a plate of infinite size

r is the radial distance from the centre of the plate in meters (m).

a is the radius of the circular plate in meters (m).

x is a non-dimensional term which is given by the radial distance **r** from the centre of the plate, divided by the characteristic length **l**

$$x = \frac{r}{l}$$

l is the characteristic length in meters (m) and is given by:

$$l = 4\sqrt{\frac{D}{k}}$$

D is the stiffness of the plate in Newton meters (Nm) and is given by:

$$D = \frac{E^p t}{12(1 - \nu)}$$

E^p is the elastic modulus of the plate in Newtons per meter squared (Nm⁻²)

t is the thickness of the plate in meters (m).

ν is the Poisson's ratio of the plate.

k is the modulus of the foundation in Newtons per cubic meter (Nm^{-3}) and is given by:

$$k = \frac{E^f}{h}$$

E^f is the elastic modulus of the foam in Newtons per meter squared (Nm^{-2})

h is the thickness of the foam in meters (m).

P is the applied load in Newtons (N).

P_{max} is the peak applied load in Newtons (N).

Applying a dynamic solution to the Timoshenko solution.

v is the terminal velocity of the impactor in meters per second (ms^{-1}).

m is the mass of the impactor in kilograms (kg).

p is the reaction of the subgrade in Newtons per square meter (Nm^{-2})

p₀ is the central reaction of the subgrade in Newtons per square meter (Nm^{-2}).

Chapter 7

s is the outer radius of a hemispherical shell in meters (m).

n is the inner radius of a hemispherical shell in meters (m).